Alma Mater Studiorum
Università degli Studi di Bologna

Facoltá di Scienze Matematiche, Fisiche e Naturali

Dipartimento di Astronomia

DOTTORATO DI RICERCA IN ASTRONOMIA

Ciclo XXI

SHOCKS AND TURBULENCE

IN SIMULATED LARGE SCALE STRUCTURES

Dottorando:

FRANCO VAZZA

Coordinatore:
Chiar.mo Prof.
LAURO MOSCARDINI

Relatore:
Chiar.mo Prof.
GIANCARLO SETTI

Co-relatore:
Dr. **GIANFRANCO BRUNETTI**

Co-relatore:
Dr. **CLAUDIO GHELLER**

Settore Scientifico Disciplinare: Area 02 - Scienze Fisiche

FIS/05 Astronomia e Astrofisica

Esame Finale Anno 2009

QUESTA TESI E' STATA SVOLTA

NELL'AMBITO DELLE ATTIVITA' DI RICERCA

DELL' ISTITUTO DI RADIOASTRONOMIA

DELL' ISTITUTO NAZIONALE DI ASTROFISICA

(BOLOGNA)

Contents

Chapter 1

Abstract

In this thesis we study shocks and turbulence in large scale structures and their connection with accretion processes in the Intra Cluster Medium. We use cosmological numerical simulations with the goal to explore their application in the modeling of non–thermal phenomena in galaxy clusters. Shock waves and turbulent motions that follow merger events and matter accretion in large scale structures are expected to inject or re-energize a sizable amount of relativistic particles during the lifetime of galaxy clusters. These *Cosmic Rays* (CR) are responsible for the diffuse non-thermal emission, which is mostly observed at Radio frequencies, in a number of galaxy clusters in the nearby Universe. The sizable number of radio observations of non-thermal emission from galaxy clusters and the incoming future instruments that are expected to shed new light on these phenomena makes the application of numerical simulations of these issues particularly timely. At the same time the complexity of the physics involved in these processes also requires exploratory studies in order to understand the capability of present cosmological simulations and the future numerical developments that are required to approach this problem.

This thesis is therefore devoted to follow, in the most physically meaningful way, the dynamics of the intra cluster plasma in response to merger and accretion events, and to highlight the connection of this processes to the injection and evolution of CR particles stored in galaxy clusters. We extensively use two of the most widespread cosmological numerical codes on the market (the Lagrangian code GADGET and the Eulerian code ENZO) combined with a number of original implementations developed during this thesis, and take advantage of their best performances in different regimes: GADGET is an ideal tool to study the innermost region of

galaxy clusters (due to the high spatial resolution that it allows to achieve), while ENZO allows to study in detail shocks and turbulent motions (due to the high order numerical scheme adopted to model fluid-dynamics).

The Chapters of this thesis are organized as follows:

- in the Introduction, Chap.2, we give a brief summary of the various phenomena taking place at different scales in galaxy clusters, and we review the established picture of thermal and non thermal phenomena in galaxy clusters. For both of them, we also highlight the most relevant open issues.

- In Chap.3, we present results for the characterization of shock waves in a large simulated volume of the Universe, and discuss in detail their role in injecting CR. Simulations are performed using the Eulerian cosmological code ENZO and shocks are identified by using an original detecting scheme which analyzes the velocity field of the gas component; we compare this method to others present in literature. The properties of shocks and of CR acceleration in galaxy clusters is discussed in detail, and a comparison with present upper limits on the energy budget of CR is presented. The main results of this Chapter can also be found in Vazza,Brunetti & Gheller (2008) and Vazza, Brunetti & Gheller (2009).

- In Chap.4, we present the results of an ongoing project of comparison between three cosmological numerical codes. Starting from identical initial conditions, a large volume of the universe is simulated using three complementary numerical approaches, and the results are compared in detail. We discuss the differences found in various statistics related to Dark Matter and gas matter (e.g. mass functions of halos, density and temperature distributions, baryon fraction of halos) and we also investigate the reasons for them. A preliminary extended study of shock waves in the various codes is presented, with the aim of assessing the level of agreement (or disagreement) among the simulations. The main results of this Chapter will appear in Dolag et al.(2009) and Vazza et al.(2009).

- In Chap.5, we study turbulent motions in simulated galaxy clusters and their connection with the dynamical processes. A recipe is presented to detect chaotic small scale motions in Lagrangian and Eulerian simulations, and the budget of the kinetic energy in turbulent motions is studied as a function of

clusters masses and distance from cluster centers. Using a large sample of galaxy clusters simulated with the Lagrangian code GADGET, we show that a scaling is found between turbulent energy and the cluster mass. The measured amount of turbulent energy and its connection with mergers is found in line with the expectations from a theoretical model which assumes turbulent re-acceleration as the origin of the emitting particles present in galaxy clusters with diffuse radio emission. Then by using a set of re-simulations of a fiducial galaxy cluster with the Eulerian code ENZO, we focus on the detailed spatial modeling of turbulent motions up to large distance from the cluster center; this is done through the implementation of a new adaptive mesh refinement criterion that increases the numerical resolution of the simulation in regions of shocks and chaotic gas motions. Time dependent spectral properties of the gas velocity field are studied in detail, in connection with the evolution of shock-energy in the simulated intra cluster medium. The main results of this Chapter can be found in Dolag et al.(2005), Vazza et al.(2006) and Vazza et al.(2009).

- In the Conclusions, Chap.6, we summarize the most important results of this thesis and present some of the necessary numerical implementations required in the future.

- In the Appendix, Chap.7, we report additional tests and applications of the study of shocks and turbulent motions.

Chapter 2

Introduction

Understanding in the complex interplay of physical scales which govern the formation and the evolution of Galaxy Clusters (GC) in the Universe is still a challenge. Despite the great number of sophisticated techniques of analysis so far employed to tackle this topic (e.g. multi–wavelength observations from ground and from the Space, analytical models, semi-analytical and fully numerical methods using the biggest super computer on the Earth) a self–consistent picture describing all scales involved in the evolution of GC is still missing. However, an epoch of "precision cosmology" is now possible, due to the large number of telescopes, arrays and satellites that will shortly provide an overwhelming amount of data with unprecedented spatial and spectral resolution (such as FERMI, LOFAR, SKA, ALMA, JWST, XEUS, NEXT, Constellation-X). This will likely provide an amount of information which cannot be fruitfully compared to theoretical expectations unless by using cosmological numerical simulations in an extensive way. Indeed, the strength of numerical methods is that the basic gas and dark matter dynamical processes which determine the evolution of cosmological structures (e.g. galaxies, DM halos, galaxy clusters and groups) can be coupled with semi-analytical recipes following the most relevant astrophysical processes at scales below the numerical resolution limit (e.g. star formation, plasma processes, radiative processes, CR dynamics etc). The outputs of cosmological simulations can then be post processed producing virtual observations at all wavelengths, by means of pipelines mimicking those employed in real observations, and statistical comparisons can be performed with real data. However, present day cosmological numerical simulations are far from being self-consistent, in the sense that a number of *ad hoc* prescriptions are adopted

in a semi-empirical way, in order to fit a number of observational constraints.

At any rate, the synergy between a next generation of cosmological numerical simulations and new experiments will hopefully produce a giant step forward in our understanding of the formation and evolution of all matter constituents of GC.

Here below we summarize the main physical mechanisms acting at the various scales of interest in GC, that observations and theoretical methods must necessary take into account while studying this topic.

2.1 GC at different scales.

At the largest cosmic scales, the evolution of GC is tightly connected to that of the *smooth* Universe inside the cosmological horizon. GC form at the over-density peaks of a continue distribution of baryonic and dark matter component, which evolves according to the Friedman metric in a Universe (e.g. Padmanabhan 1993) characterized by cosmological parameters of a ΛCDM model ($\Omega_\Lambda > \Omega_{DM} > \Omega_b > \Omega_R$ at present epoch, with Λ referring to the cosmological constant, DM referring to Cold Dark Matter, b referring to baryons and R referring to radiation). The tight connection existing between the epoch of formation of GC, the evolution of their abundance in time and their spatial distribution are all important proxies which can be used to determine the exact values of many cosmological parameters (see Fig.2.1, e.g. Reiprich & Böhringer 2002, Evrard et al. 2007), often providing complementary constraints with respect to other independent techniques, such as the study of primordial CMB radiation and the study of high-z supernovae. On the other hand, the details of the GC evolution are closely connected with the exact values of the cosmological parameters, which act like boundary conditions. For instance, Lacey & Cole (1993) showed that the merger rate within structures has a slight dependence on Ω_{DM}, and this in turn would affect the merging history of a GC, in a statistical sense. The thermal properties of the "smooth" Universe at scales of the order of hundreds of Mpc can also affect the properties of GC at present epoch: the presence of a re-ionization background produced by Active Galactic Nuclei, AGN, or massive primordial stars in the early Universe (i.e. $z > 6$) and the spatial distribution of its sources play an important role in setting the thermal properties of baryons in the outer region of GC at $z = 0$ (e.g. Fukugita & Kawasaky 1994).

At scales of the order of tens of Mpc's the direction of large scale filaments

of matter and voids can produce detectable effects in the final distributions of galaxies within GC, by determining preferential direction for clustering (e.g. White et al.1987).

At scales of the order of ~ 1 Mpc, the ensemble of ram pressure stripping, tidal disruptions and large scale shocks plays a primary role in setting and modifying the thermal structure in GC via multiple mergers (e.g. Moore, Katz & Lake 1996; Röettiger; Loken & Burns 1997; Ricker & Sarazin 2001). The same mechanisms are also found to be primary responsible for the chemical enrichment of the Intra Cluster Medium, ICM, (e.g. Gnedin 1998; Schindler et al.2005), for the establishment of the entropy distribution in GC (e.g. Mitchell et al.2008 and references therein), and for Cosmic Rays (CR) injection processes during GC mergers (e.g. Roettiger et al.1999; Takizawa & Naito 2000). At the scale of $\sim$ 1Mpc, also the injection of turbulent eddies and the amplification of ICM magnetic field during mergers are basic processes likely driving the formation of Giant Radio Halos in GC (e.g. Brunetti 2004 and references therein).

At scales of the order of hundreds of kpc's, the variety of phenomena which governs the evolution of the ICM increases significantly. The dynamical feedback from AGN in the innermost regions of GC is powerful enough to modify the central temperature, density and entropy distribution of GC (e.g. Churazov et al.2001), possibly balancing cold gas deposition in cooling flow clusters (e.g. Brighenti & Mathews al.2003 and references therein). The possible mechanisms of energy interchange with AGNs at these scales are many: the interaction of radio jets with the resident ICM, the PdV work by raising bubbles of relativistic particles, the heating by shock waves driven by X-ray cavities, fluid instabilities at the interfaces between bubbles and the ICM, powerful galactic winds (e.g. Quills et al.2001; Fabian et al.2003; Borgani et al.2004; Omma et al.2004; Mc Namara et al.2005; Sijacki et al.2007). At similar scales, galaxies chemically pollute the ICM through release of elements from supernovae and stellar winds (e.g. Borgani et al.2008 and references therein). At these scale, the motion of stripped satellites mainly composed of DM is also expected to cause the appearance of cold fronts and to inject small scale turbulence (e.g. Markevitch & Vikhlinin 2007 for a review).

At scales of $\leq$ 10 kpc, plasma processes become fundamental players which set the properties of the ICM. Tangled magnetic field determine the properties of

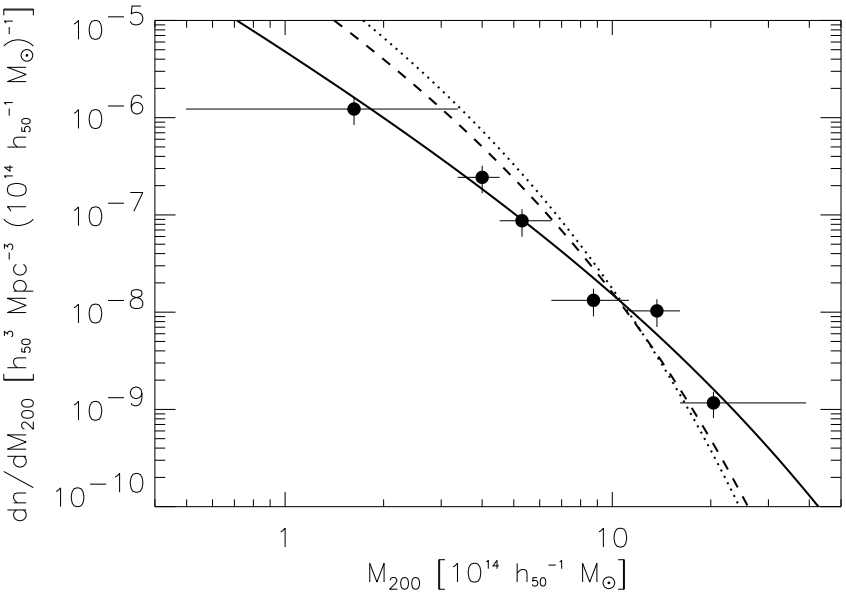

Figure 2.1: Mass function of the HIFLUGCS X-ray clusters (dots with error bars). The solid line is the best fit with $\Omega_m = 0.12$ and $\sigma_8 = 0.98$. The dashed and dotted lines are the best fits with $\Omega_m = 0.5$ or $\Omega_m = 1.0$ held fixed, which yield $\sigma_8 = 0.60$ and $\sigma_8 = 0.46$, respectively. From Reiprich & Böringer(2002).

thermal conduction and viscosity in the ICM (e.g. Schekochihin & Cowley 2006 for a review), and are efficient in deflecting and trapping relativistic particles in GC with energies below $< 10^7$ GeV (e.g. Berezinsky, Blasi & Ptuskin 1997). CR hadrons and electrons are likely accelerated within the thin magnetized layer at shocks in the ICM (e.g. Bykov et al.2008 and references therein for a review). High energy collisions between hadrons generate a cascade of high energy particles and high energy emissions in GC (e.g. Blasi & Colafrancesco 1999). Resonant and non–resonant coupling between relativistic and thermal particles and MHD waves governs the dissipation of turbulent eddies at sub–kpc scales and re-accelerate CR particles in a stochastic way (e.g. Brunetti & Lazarian 2007 for a review). At sub-kpc's, also the bulk of interesting star formation processes, accretions onto Black Holes and energy release from supernovae takes place.

2.2 Thermal Phenomena in GC.

Rather than focusing at the physical scale of interest, an alternative to broadly classify the ensemble of phenomena in GC is to distinguish between *thermal* and

non–thermal phenomena.

Indeed the bulk of GC radiating properties depends on the properties of baryons in (approximate) thermal equilibrium with the potential well determined by the total (baryon plus DM) matter in GC. On the other hand, an interesting number of observations, mostly in the radio, soft and hard-x wavebands, suggest that a number of phenomena occur in GC, which cannot be modeled without considering the existence and evolution of a sub-population of relativistic baryons in the ICM. Therefore understanding in detail most of the long standing, or new questions arisen by GC observations, should involve the simultaneous modeling of the interplay between thermal and non-thermal populations (plus DM).

Clusters of galaxies are self-gravitating systems of mass $\sim 10^{14} - 10^{15} h^{-1}$ $M_\odot$ and size $\sim 1 - 3h^{-1}$ Mpc. Their mass consists of Dark Matter, hot diffuse intra cluster plasma and a small fraction of stars, dust, and cold gas, mostly locked in galaxies. In most clusters, the existence of scaling relations between their properties (like mass, galaxy velocity dispersion, X-ray luminosity and temperature) testifies that the cluster components are in approximate dynamical equilibrium within the gravitational potential well. However, observations of spatially inhomogeneous thermal and non-thermal emissions of the ICM, show the signature of non-gravitational processes, ongoing cluster merging and interactions taking place at several different physical scales. Both the fraction of clusters with these features, and the correlation between the dynamical and morphological properties of irregular clusters and the surrounding large-scale structure are found to be increasing with redshift (e.g. Diaferio, Schindler & Dolag 2008 for a review).

The existence of hot diffuse X-ray emitting gas (e.g. Gursky et al.1972) implies the presence of a deep gravitational potential well that maintains the gas confined in the cluster. By assuming hydrostatic equilibrium and spherical symmetry, the cumulative mass within radius r is

$$M(< r) = -\frac{kTr}{G\mu m_{\rm p}} \left(\frac{{\rm d}\,\ln \rho_{\rm gas}}{{\rm d}\,\ln r} + \frac{{\rm d}\,\ln T}{{\rm d}\,\ln r} \right) , \qquad (2.1)$$

where μ is the mean molecular weight, $m_{\rm p}$ the proton mass and $\rho_{\rm gas}$ the gas mass density.

The origin of the X-ray emission (whose luminosity is referred as L_X) was very early interpreted as thermal Bremsstrahlung emission from a hot intra cluster

plasma:

$$L_X = \int n_{\rm e}(\mathbf{r}) n_{\rm ions}(\mathbf{r}) \Lambda[T(\mathbf{r})] {\rm d}^3\mathbf{r} \ , \tag{2.2}$$

where $n_{\rm e}$ and $n_{\rm ions}$ are the electron and ion number densities in the ICM and $\Lambda(T)$ is a cooling function. For temperatures $kT > 2$ keV (k is the Boltzmann constant), when the ICM is almost fully ionized, we have $\Lambda(T) \propto T^{1/2}$.

By assuming that virialization occurs within GC, also the observation of the dynamics of cluster galaxies is a viable tool to measure the total mass within GC. If the cluster is an isolated, spherically symmetric system in dynamical equilibrium, the virial theorem gives the total mass

$$M = \frac{3\sigma_v^2 R}{G} \ , \tag{2.3}$$

where G is the gravitational constant, σ_v is the dispersion of the galaxy velocities along the line of sight, and R is the cluster size. More recently, complementary approaches have been applied to measure the total GC mass: through weak and strong gravitational lensing (e.g. Schneider 2006), and by analyzing the distribution of galaxies in redshifts space through the caustic technique (e.g. Diaferio 1999). Also the measure of the gas mass in GC is possible by measuring the Sunyaev-Zeldovich signal (e.g. Bartlett 2006).

All the mass estimation methods used to date indicate that the DM contributes $\sim 80\%$ of the total cluster mass, the ICM contributes $\sim 20\%$, and the galaxies contribute less than a few percent, as already inferred in early observations of the Coma Cluster by Zwicky (1937).

The total cluster mass is an extremely relevant quantity to constrain the cosmological model, because clusters populate the exponential tail of the mass function of systems of galaxies. If the power spectrum of the primordial perturbations of the density field is a power law with index n, the number of galaxy systems per unit volume $[{\rm d}n(M)/{\rm d}M]dM$ with total mass in the range (M, $M+dM$) is (Press & Schecter 1974):

$$\frac{{\rm d}n(M)}{{\rm d}M}{\rm d}M = \frac{1}{\sqrt{\pi}} \frac{\bar{\rho}}{M^2} \left(1 + \frac{n}{3}\right) \left(\frac{M}{M_*}\right)^{(n+3)/6} \exp\left[-\left(\frac{M}{M_*}\right)^{(n+3)/3}\right] {\rm d}M \ , \tag{2.4}$$

where $\bar{\rho}$ is the (constant) comoving mean mass density of the universe and M_* is a parameter depending on the normalization of the power spectrum σ_8 and on the

structure growth factor, which in turn, depends on time, on the cosmological density parameter Ω_m and the cosmological constant Ω_Λ. M_* increases with time when $n > -3$, and it is $M_* \sim 10^{14} h^{-1}$ $\mathrm{M}_\odot$ at the present epoch. Since the exponential cut off dominates the mass function above $M \sim M_*$, the evolution of the cluster number density is a very sensitive indicator of the power spectrum normalization and of the cosmological parameters. The application of this idea requires modern versions of the Press-Schechter mass function which are more sophisticated than Eq. (2.4) and take into account the triaxiality of halos (Sheth & Tormen, 1999).

If clusters are in virial equilibrium, we can derive simple relations between their global properties, namely mass, galaxy velocity dispersion, number of galaxies, X-ray luminosity, ICM temperature, and so on.

The simplest model to predict observable properties of the ICM assumes that gravity alone determines the thermodynamical properties of the hot diffuse plasma (Kaiser 1986). By considering the virial relation $3kT/(2\mu m_\mathrm{p}) = GM/R$, one can derive the scaling relation between the total mass M and the gas temperature kT:

$$kT = 3.229 \left(\frac{\mu}{0.6}\right) \left(\frac{\delta}{500}\right)^{1/3} \left(\frac{M}{10^{14} h^{-1} \mathrm{M}_\odot}\right)^{2/3} \mathrm{keV} \tag{2.5}$$

where δ is the average cluster over-density with respect to the critical density $\rho_{cr} \equiv 3H_0^2/(8\pi G)$ of the universe, with $H_0 = 100h$ km s^{-1} Mpc^{-1} being the Hubble constant at the present time. Quantities in equation (2.5) are normalized to typical observed cluster values.

The total X-ray luminosity can also be written in a similar way:

$$\begin{aligned} L_X &= 1.327 \times 10^{43} \left(\frac{f_\mathrm{gas}}{0.1 h^{-3/2}}\right)^2 \left(\frac{0.6}{\mu}\right) \left(\frac{n}{10^{-3} h^2 \,\mathrm{cm}^{-3}}\right) \left(\frac{T}{\mathrm{keV}}\right)^{0.4} \times \\ &\times \left(\frac{M}{10^{14} h^{-1} \mathrm{M}_\odot}\right) h^{-2} \,\mathrm{erg\,s}^{-1} \,, \end{aligned} \tag{2.6}$$

where the cooling function Λ can be approximated as $\Lambda(T) = 0.843 \times 10^{-23} (kT/\mathrm{keV})^{0.4}$ erg cm^3 s^{-1} at $kT \geq 1$ keV, which holds for gas with poor metallicity, and assumed $n_\mathrm{e} = n_\mathrm{ions} \equiv n = f_\mathrm{gas}\rho/(\mu m_\mathrm{p})$, where f_gas is the fraction of the cluster total mass in the ICM and ρ is the cluster total mass density.

Another useful quantity characterizing the thermodynamical properties of the

ICM is the gas entropy (e.g. Voit 2005) which is customary defined as

$$s = \mathrm{k_B} \ln K^{3/2} + s_0 \tag{2.7}$$

where s_0 is a constant and $K = \frac{\mathrm{k_B} T}{\mu m_\mathrm{p} \rho_\mathrm{gas}^{2/3}}$. Another quantity, often called "entropy" in the cluster literature, which we will also use in the following, is

$$S = \mathrm{k_B} T n_\mathrm{e}^{-2/3} \tag{2.8}$$

where n_e is the electron number density. According to the self–similar model, this quantity, computed at a fixed over-density Δ_c, scales with temperature and redshift according to

$$S_{\Delta_\mathrm{C}} \propto T(1+z)^{-2}\,. \tag{2.9}$$

Finally, quite recently Kravtsov et al.(2006) proposed an additional scaling law relating an X–ray observable related to pressure, and cluster mass. They introduced the quantity $Y_X = M_\mathrm{gas} T$, defined by the product of the total gas mass times the temperature, both measured within a given aperture; using this definition, Y_X represents the X–ray counterpart of the Compton-y parameter, measured from the SZ effect. By computing Y_X for a set of simulated clusters and for a sample of nearby GC observed with Chandra, Kravtsov et al.(2006) showed that Y_X has a very tight correlation with the cluster mass, with a remarkably small scatter of only 8 per cent.

All the above scaling relations provide a powerful method to estimate the cluster mass from the X-ray related quantities. However the assumption of dynamical equilibrium is crucial for obtaining these estimates. Even if quantities related to X-ray observations are robust and relatively simple to correlate (Rosati et al.2002), a number of observational facts from X–ray data points against the simple self–similar picture.

For instance, a large fraction of clusters shows the presence of substructures both in their galaxy distribution and in their X-ray emission morphology. X-ray observations typically show patchy temperature (Belsole et al.2005) and the X-ray morphology is found to be on average increasingly irregular with increasing redshift (e.g. Jeltema et al.2005); this is consistent with the framework of a hierarchical building of GC through a sequence of mergers between substructures.

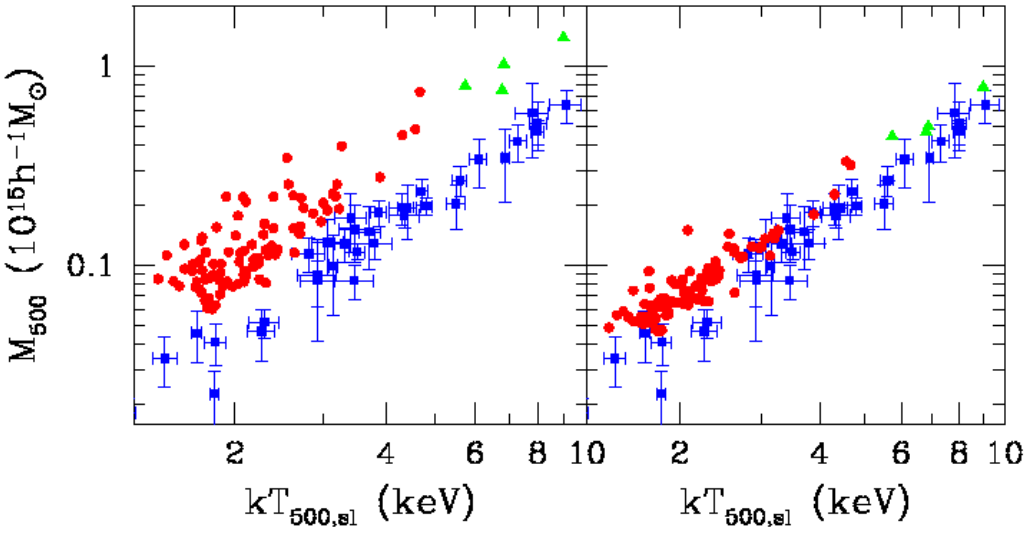

Figure 2.2: The relation between mass and spectroscopic-like temperature within r_{500}. *Red circles* and *green triangles* are for simulations, which include cooling, star formation and feedback from galactic winds, while *squares with error bars* are the observational data by Finoguenov et al.(2001). *Left panel:* M_{500} exactly computed by summing the mass of all particles within r_{500}. *Right panel:* M_{500} estimated as in the observational data, by using the equation of hydrostatic equilibrium for a polytropic β-model. From Rasia et al.(2005).

2.2.1 Open Problems in Thermal Phenomena

The Breaking of Self–Scaling Laws

A sizable amount of observations has shown that expectations based on simple self-similar scaling are at variance with real GC. In the observed L_X–T relation, a steeper slope is measured with respect to the expectations from self–similar scalings (e.g. Markevitch 1998): $L_X \propto T^{\alpha}$ with $\alpha \simeq 3$ for GC with intermediate mass and possibly larger for groups. This clearly suggests the breaking of the similarity in GC for some critical mass.

The excess of entropy in poor clusters and groups (e.g. Cavagnolo et al.2009 and references therein) and the decreasing trend of the gas mass fraction in poorer systems (e.g. Sanderson et al.2003) also points towards the presence of some mechanism, other than the pure gravitationally driven shock heating, which significantly affects the ICM thermodynamics.

The first mechanism introduced to break the ICM self–similarity is the non–gravitational heating (e.g. Evrard & Henry 1991). Indeed by increasing the gas entropy with a given extra heating energy per gas particle $E_{\rm h}$, it is possible to prevent gas from sinking to the center of DM halos, thereby reducing gas density and X–ray emissivity. This effect will be large for small systems, whose virial temperature is $\mathrm{k_B}T < E_{\rm h}$, while leaving rich clusters with $\mathrm{k_B}T \gg E_{\rm h}$ almost unaffected. Therefore, one would expect that the X–ray luminosity and gas content are relatively more suppressed in poorer systems, leading to a steepening of the L_X–T relation.

The implementation of heating by non-gravitational processes in cosmological numerical simulations (e.g. Borgani et al.2002) has been proposed by injecting extra entropy or extra energy at high redshift (aiming at mimicking the rate of explosion of SN from an external model of galaxy formation). This heating scheme is effective in reproducing the observed L_X–T relation (breaking self–similarity by the presence of an entropy floor of 50keV cm^2), but it also produces too large isentropic cores and this prediction is found to be in disagreement with observations (e.g. Donhaue et al.2006).

Radiative cooling has been also suggested as a viable alternative to non–gravitational heating: indeed cooling provides a selective removal of low–entropy gas from the hot X–ray emitting phase (e.g. Voit & Brian 2001). In this way, while the global entropy of the baryons decreases, the entropy of the X–ray emitting

gas increases and only gas having a relatively high entropy will be observed as X–ray emitting. This analytical prediction has been indeed confirmed by radiative hydrodynamical simulations, which found that the entropy level is well above the prediction of the self–similar model, by a relative amount which increases with decreasing temperature, and in reasonable agreement with the observed entropy level of poor clusters and groups. However, problems arise even in this case because a too large fraction of gas is converted into stars: observations in fact show that only about 10 per cent of the baryon content of a cluster is in the stellar phase (Lin et al.2003), whereas radiative simulations typically convert into stars up to ~ 50 per cent of the gas (e.g. Davé et al.2002). In addition, cooling has the effect of steepening the temperature profile in the innermost region of simulated GC (due to the lack of pressure support that it causes, and to the subsonic inflow of gas from surrounding regions, which causes additional adiabatic compression), while leaving unchanged the temperature profile at the outermost region (e.g. Tornatore et al.2003, see also Left panel in Fig.2.3 and 2.2.1). This results is also found to be at variance with current observations of cool core GC.

The steepening of the central temperature profiles and overcooling are likely two aspects of the same problem. One would expect that this problem could be solved by providing a mechanism to heat the gas and to simultaneously regulate star formation, while maintaining pressurized gas in the hot phase. Interesting attempts to do that were presented in Borgani et al.(2003), using simulations which include cooling, star formation and feedback in the form of galactic winds powered by SN explosions. In this work, it is suggested that the injection of entropy at relatively high redshift, the observed slope of the L_X–T relation can be reproduced. These simulations showed an other paradoxical results: in the same way that cooling causes an increase of the temperature of the hot phase, supplying energy with an efficient feedback causes a decrease of the temperature. This happens because the extra energy compensates radiative losses, thereby maintaining the pressure support for gas which would otherwise have a very short cooling time, thereby allowing it to survive on a lower adiabat.

The relation between total collapsed mass and temperature has also received much consideration both from the observational and the theoretical side, in view of its application for the use of galaxy clusters as tools to measure cosmological

parameters (e.g., Voit 2005). The relation between ICM temperature and total mass should be primarily dictated by the condition of hydrostatic equilibrium. For this reason, the expectation is that this relation should have a rather small scatter and be insensitive to the details of the heating/cooling processes.

Mazzotta et al.(2004) pointed out that the thermal complexity of the ICM is such that the overall spectrum is given by the superposition of several single–temperature spectra, each one associated to one thermal phase. When fitting it to a single–temperature model in a typical finite energy band, where X–ray telescopes are sensitive, the cooler gas phases are relatively more important in providing the high–energy cut–off of the spectrum and, therefore, in determining the temperature resulting from the spectral fit. Therefore Mazzotta et al.(2004) introduced a spectroscopic–like temperature, $T_{\rm sl}$, which adopts the weight $w_i = \rho_i m_i T^{\alpha-3/2}$ to filter the information of projected temperature from simulations. By using $\alpha = 0.75$, this expression for $T_{\rm sl}$ was shown to reproduce within few percent the temperature obtained from the spectroscopic fit, at least for clusters with temperature above 2–3 keV. Rasia et al.(2005) showed that using the spectroscopic–like definition, $T_{\rm sl}$, leads to a mass underestimate of up to $\sim$ 30 per cent with respect to the true cluster mass (see Fig.2.8). They suggested that the difference between "true" and "recovered" masses is partly due to the violation of hydrostatic equilibrium, associated to subsonic gas bulk motions (e.g., Nagai et al.2007), and partly to the poor fit provided by the β–model (e.g.,Ascasibar et al.2003) when extended to large radii.

The Inner Thermal Profiles of GC

Despite their relatively modest spatial resolution, early ASCA observations established that most of the clusters show significant departures from an isothermal profile, with negative temperature gradients characterized by a remarkable degree of similarity, out to the largest radii sampled (e.g.,Markevitch et al.1998). With Beppo–SAX observations it was then shown that the above gradients do not extend towards the innermost cluster central regions, where instead an isothermal profile is observed, possibly followed by a decline of the temperature towards the center in the case of relaxed clusters (De Grandi 2002). More recent Chandra and XMM-Newton observations basically confirmed this picture, providing more detailed picture of the

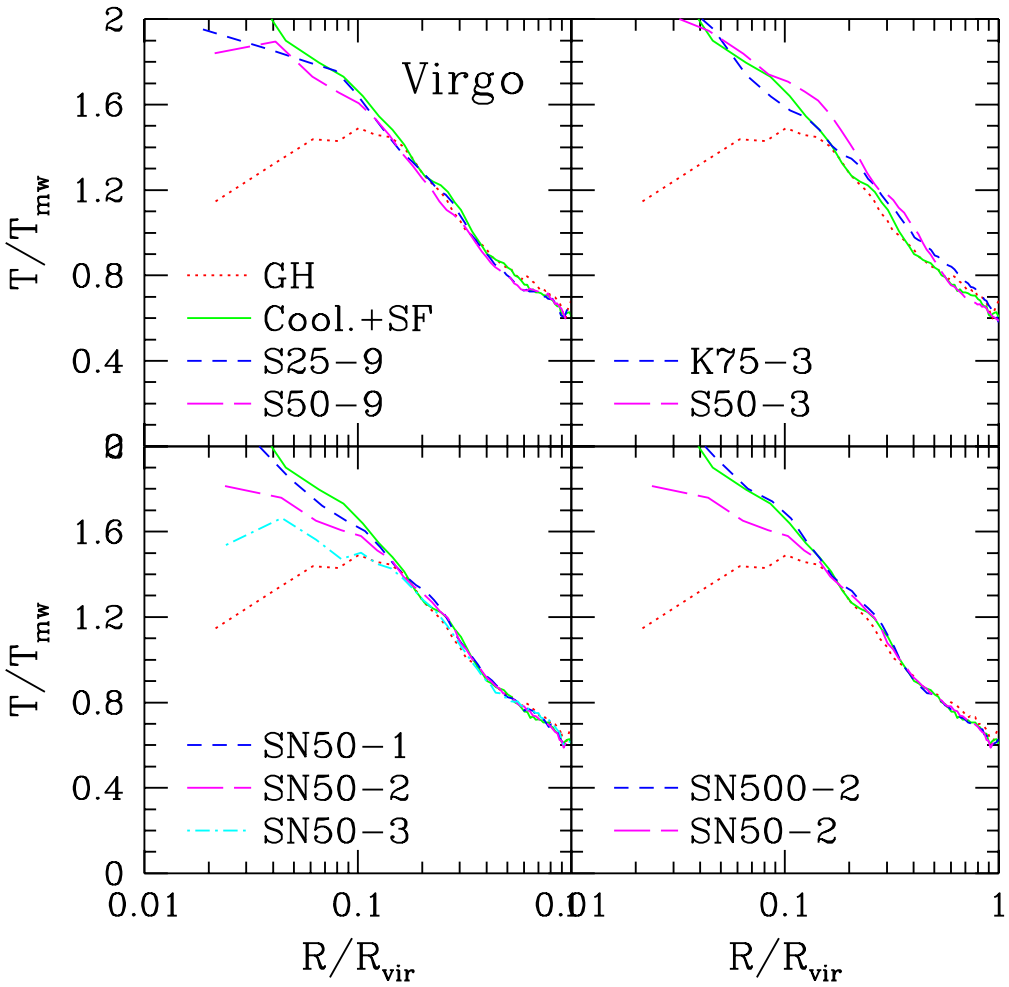

Figure 2.3: Temperature profiles from hydrodynamical simulations of a $\sim$ 3 keV galaxy cluster. In all panels the dotted and the solid curves correspond to a non radiative run and to a run including cooling and star formation. The other curves are for different recipes of gas heating (from Tornatore et al.2003).

central temperature profile for a number of GC (Pratt et al.2007). Relaxed clusters are generally shown to have a smoothly declining profile toward the center, with values about half of the overall virial cluster temperature in the innermost sampled regions. Non–relaxed clusters, instead, have a larger variety of temperature profiles. The emerging picture suggests that gas cooling is responsible for the decline of the temperature in the central regions, while some mechanism of energy feedback should be responsible for preventing overcooling, thereby suppressing the mass deposition rate and the resulting star formation.

On the other hand, including gas cooling has the effect of steepening the T–profiles in the core regions, in clear disagreement with observations. The problem of the central temperature profiles in radiative simulations has been consistently found by several independent analyzes (e.g. Valdarnini 2003; Borgani et al.2004; Nagai et al.2007; Burns et al.2007) and is likely due to the difficulty of implementing feedback schemes which balance the cooling runaway in a stable fashion, see Fig.2.3.

Resolving this would require that simulations are able to produce the correct thermal structure of the observed "cool cores", meaning that a suitable feedback should compensate the radiative losses of the gas at the cluster center, while keeping it at about $\sim 1/3$ of the virial temperature. AGN might represent the natural solution to this problem, even if only quite recently these studies have been extended to clusters forming in a fully cosmological context (Heinz et al.2006; Sijacki et al. 2007).

Simulations have also difficulties in accounting for the observed entropy structure, mainly because the ICM thermodynamics is sensitive to complex physical processes in the core regions. Ponman et al.(2003) and Voit et al.(2003) suggested that the entropy excess in poor clusters an groups may be the effect of entropy amplification due to shocks from smoothed gas accretion. Indeed, accretion shocks taking place at a lower density are more efficient in generating entropy, and in the hierarchical scenario for structure formation, a galaxy group is expected to accrete from relatively smaller filaments and merging sub–groups than a rich cluster does. Therefore if the gas is heated with a fixed amount of specific energy (or entropy), such a diffuse heating will be more effective to smooth the accretion pattern of a group than that of a rich cluster, due to the lower virial temperature of the accreted structures. While the semi–analytical approach by Voit et al.(2003)

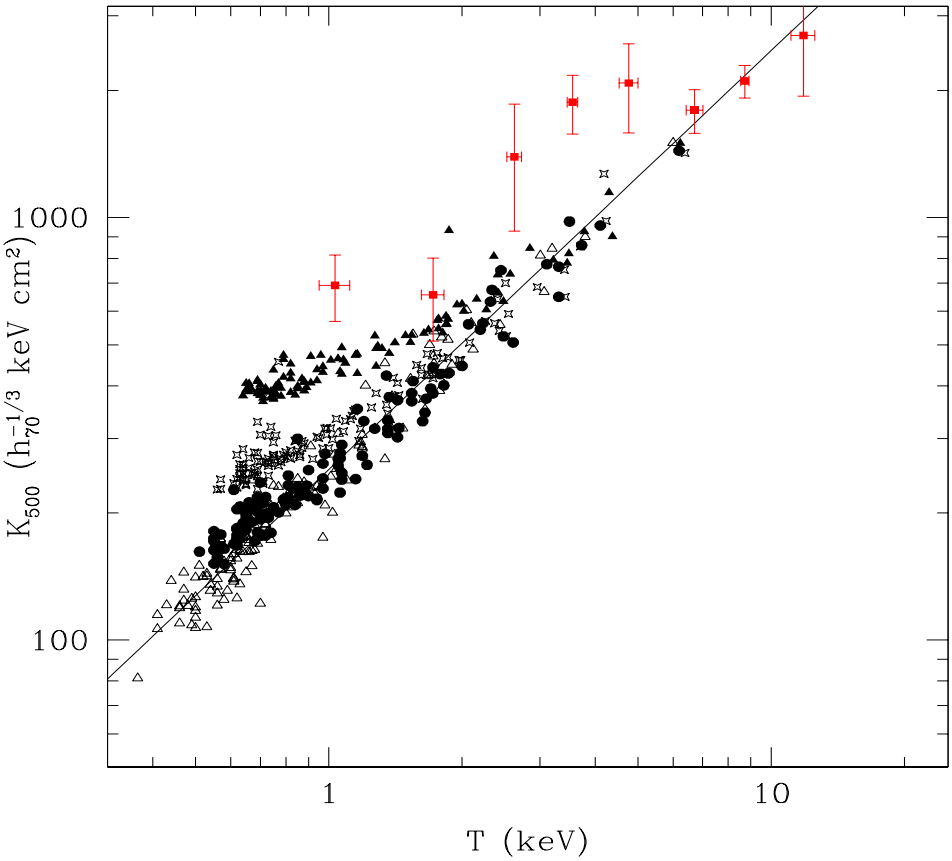

Figure 2.4: The relation between entropy computed at r_{500} for clusters and groups identified in AMR ENZO cosmological simulations (from Younger & Bryan 2007), compared with the observational results by Ponman et al.(2003); symbols with error bars. Shown are four different cases of entropy injection at $z = 10$: no pre-heating (open triangles), 78 keV cm^2 (filled circles), 155 keV cm^2 (stars), 311 keV cm^2 (filled triangles). The solid line is a power–law fit to the self–similar prediction from the simulations.

was promisingly in agreement with observational results, tests employing full hydrodynamical simulations showed that the addition of an entropy floor at high redshift provides an efficient smoothing of the gas accretion pattern, but the level of entropy is substantially increased in the central regions (Borgani et al.2005, Younger & Bryan 2007, see also Fig.2.4). This is again inconsistent with high–resolution Chandra measurements of low entropy gas in the innermost cluster regions, where it reaches values as low as ~ 10 keV cm^2 (Donahaue et al.2006).

The Baryon Fraction of GC

Measuring the the baryon mass fraction in nearby galaxy clusters is a powerful method which allows to measure the cosmological density parameter (e.g. White et al.1993); in addition, its evolution with redshift while provides constraints on the dark energy content of the Universe (e.g. Ettori et al.2003). A number of observational evidences shows that the gas mass fraction is smaller in lower temperature systems (Sanderson et al.2003), and thus that not all cosmic structures retain the universal cosmic baryon fraction as evolution goes on. In addition, since X–ray measurements of the gas mass fraction are generally available only out to a fraction of the cluster virial radius, the question then arises as to whether the gas fraction in these regions is representative of the cosmic value.

Hydrodynamical simulations offer a way to check how mass of the gas component is distributed within individual clusters and how it depends on the total cluster mass. Kravtsov et al.(2005) and Ettori et al.(2006) performed similar tests using high resolution cosmological simulations with both radiative and non–radiative physics, using complementary numerical approaches (i.e. Eulerian and Lagrangian simulations). They found that the inclusion of various feedbacks and additional physical mechanisms different from pure non-radiative physics, has a substantial effect on the total baryon fraction in the central cluster regions, where it is found to be even larger than the cosmic value. On one hand, these works suggested that the baryon fraction in simulated GC is generally a stable measurement if computed at large enough radii, $\geq r_{500}$; on the other hand they also showed that changing the description of the relevant ICM physical processes modeled in the simulations (e.g. radiative processes, star formation) has an effect of the extrapolation of the baryon fraction from the central regions to the virial radius of the GC, and thus that a viable comparison with observations is still unfeasible.

In addition, the above works also found that small, but systematic differences exist when comparing the baryon fraction resulting from Eulerian and Lagrangian approaches, which still need to be understood appropriately.

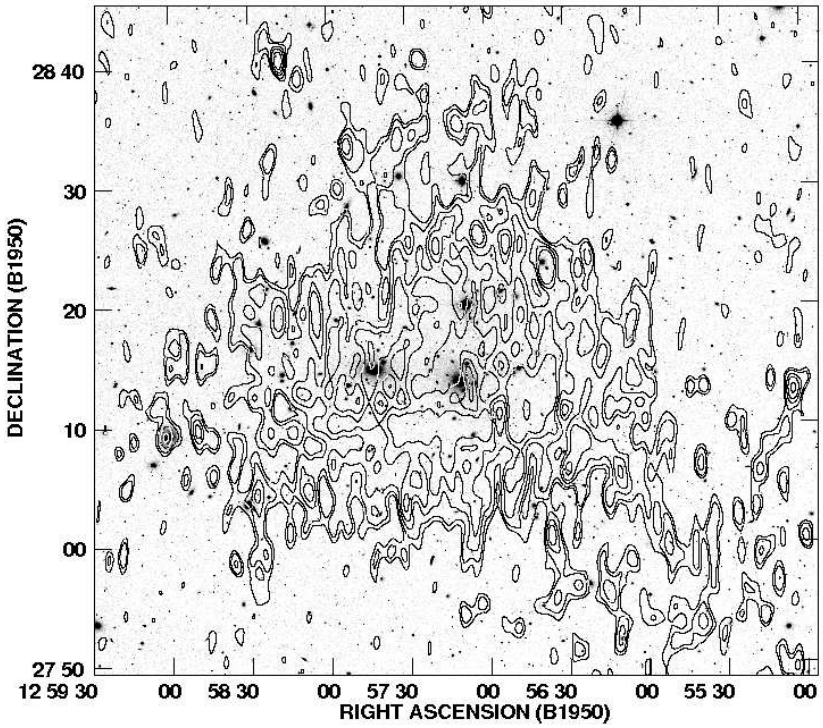

Figure 2.5: 90 cm contours of the radio halo in the Coma cluster ($z = 0.023$) are overlaid on the DSS optical image. Radio point sources have been subtracted. Taken from Feretti et al.2001.

2.3 Non-Thermal Phenomena in GC.

Accretion of matter from smaller sub–units is a necessary process in the growth of GC according to the hierarchical framework, and this is expected to cause most of the turbulence in the ICM (e.g. Schuecker et al.2004) and generate shock waves crossing the cluster volume (e.g. Bykov, Dolag & Durret 2008 for a review).

In addition, cluster mergers are also believed to be the most important sources of non-thermal energy components in GC: a fraction of the energy dissipated during these mergers could be channeled into the amplification of the magnetic fields (e.g. Dolag et al.2008 for a review) and into the acceleration of high energy Cosmic Rays particles via stochastic mechanism (e.g. Petrosian et al.2008 for a review).

In general, non-thermal components are expected to mix with the thermal IGM inside GC, and they may drive still unexplored physical processes modifying our simplified view of the IGM itself (Schekochihin et al. 2005; Subramanian et al. 2006; Brunetti & Lazarian 2007; Guo et al. 2008).

Since the last twenty years, Radio observations have discovered an increasing number of Mpc-sized emissions from the ICM: Radio Halos, at the cluster center, and Radio Relics, at the cluster periphery (e.g. Ferrari et al. 2008 for a review). These sources are likely due to synchrotron emission from ultra relativistic electrons diffusing in a turbulent magnetic field at μG level. Additionally, the possible detection of diffuse emissions in the hard-X band (e.g. Fusco-Femiano et al.2007) suggests the existence of a budget of relativistic electrons emitting via the Inverse Compton (IC) mechanism; yet the existence of this emission is still object of debate (e.g. Rossetti & Molendi 2004).

Apart from their common properties (nature of the emission, steep radio spectra), diffuse and extended radio sources in clusters differ in a number of physical properties, in particular: size, position in the host cluster, intensity of polarized signal, morphology and association to other cluster physical properties (e.g. dynamical state, presence of a cooling flow). In a schematic way, they can be divided into

- *radio halos*: extended (~ 1 Mpc) diffuse radio sources at the center of clusters, with a quite regular morphology, similar to the clusters X-ray morphology;
- *radio relics*: with similar extensions and also detected in merging clusters, but

usually located in the cluster outskirts and showing an elongated morphology;

- *radio mini-halos*: smaller sources (< 500 kpc) located at the center of cooling flow clusters, and surrounding central radio galaxies.

2.3.1 Radio Halos

All detected radio halos are located in the center of clusters with a disturbed dynamical state and without a cooling core. However, not all merging clusters host a radio halo and indeed they are found only in a fraction of X-ray luminous GC. (e.g. Giovannini et al.1999, Venturi et al.2007).

Coma C is the prototype of the low surface brightness ($\sim \mu$Jy arcsec^{-2} at 1.4 GHz) and extended (≥ 1 Mpc) radio halos (e.g. Feretti 2002); interestingly enough, several authors also reported on the detection of diffuse hard-X ray excess (respect to the extrapolated Bremsstrahlung emission) whose source can be IC emission from the same population of relativistic electrons emitting at radio frequencies (e.g. Rephaeli et al.1999; Fusco-Femiano et al.1999).

In recent years, many observational efforts have been devoted to multi-frequency observations of radio halos, in order to get more and more accurate determinations of their radio properties and of their connection with the hot thermal gas in GC. These studies are limited however by the capability of current instruments to do multi-frequency observations at the sensitivity required for studying radio halos ($\sim$ Jo $- \mu$Jy arcsec^{-2} going from the MHz to the GHz range). In a few cases, a steepening of the halo spectrum at high frequency has been detected: Coma (Thierbach et al.2003) and A 521 (Giacintucci et al.2005; Brunetti et al.2008).

Spectral studies of radio halos combined with X-ray observations have explored the connection between thermal and non–thermal components and found that flatter radio spectral indexes are usually associated with regions of high temperature of X-ray emitting gas (Orrú et al.2007). The radio power of radio halos if found to correlate with the X-ray emissions, temperature and mass of the host GC (e.g. Cassano 2009 for a review), suggesting that gravity, that drive the thermal properties of the GC on large scales, is also responsible for the observed non–thermal phenomena in GC.

Recently, Cassano et al.(2007) pointed out that the fraction of the radio emitting cluster volume significantly increases with the cluster mass. This break of self-

similarity can give important constraints on the physical parameters entering the hierarchical formation scenario, since it suggests that the distributions of the magnetic field and relativistic electrons change with cluster mass.

Future low frequency radio observations are expected to shed new light on our understanding of radio halos. A large number of radio halos is expected at fainter radio fluxes by simply considering the extrapolation of their 1.4 GHz number counts through the radio power–X-ray luminosity correlation (Enßlin & Röttgering 2002). These faint radio halos are hardly detectable with present facilities at 1.4 GHz, but since they have steep radio spectra they should appear more luminous at lower frequencies (e.g. Cassano 2009).

Formation Scenarios for Radio Halos

The observed connection between the non–thermal emissions in GC and cluster mergers suggests that a fraction of the energy dissipated during these mergers is channeled in non–thermal components of the GC. Once injected in the ICM, relativistic particles are subject to energy losses. Relativistic electrons with momentum $p_e = m_e c\gamma$ lose energy through ionization losses and Coulomb collisions, which dominate for $\gamma < 100$, and via synchrotron and IC scattering off the Cosmic Microwave Background photons, which dominate at higher energies (*e.g.,* Sarazin 1999). On the other hand relativistic protons lose energy mainly through proton–proton inelastic scattering, while Coulomb losses become important at lower energies. Relativistic protons are long living ($> 10^9$ yr) and accumulate in GC so that the emissions from the secondary products generated through the collisions between these protons and the thermal protons can be thought as a "stationary" signal (e.g. Blasi, Gabici & Brunetti 2007).

On the other hand, relativistic electrons are short living particles that radiate their energy in the region where they are produced (e.g. Jaffe 1977). Specifically, electrons emitting synchrotron radiation around ~ 1 GHz have an energy of the order of $\approx 7\, B_{\mu G}^{1/2}$ GeV and a life-time of $\approx 10^8$ yr. During this timescale electrons can only diffuse for a few tens of kpc, which is very small compared with the observed $\sim Mpc$ scale common for Radio Halos. This lead to the requirement that the electrons responsible for the radio emission in Radio Halo should be generated or accelerated everywhere in the cluster: either secondary electrons from *pp* collisions

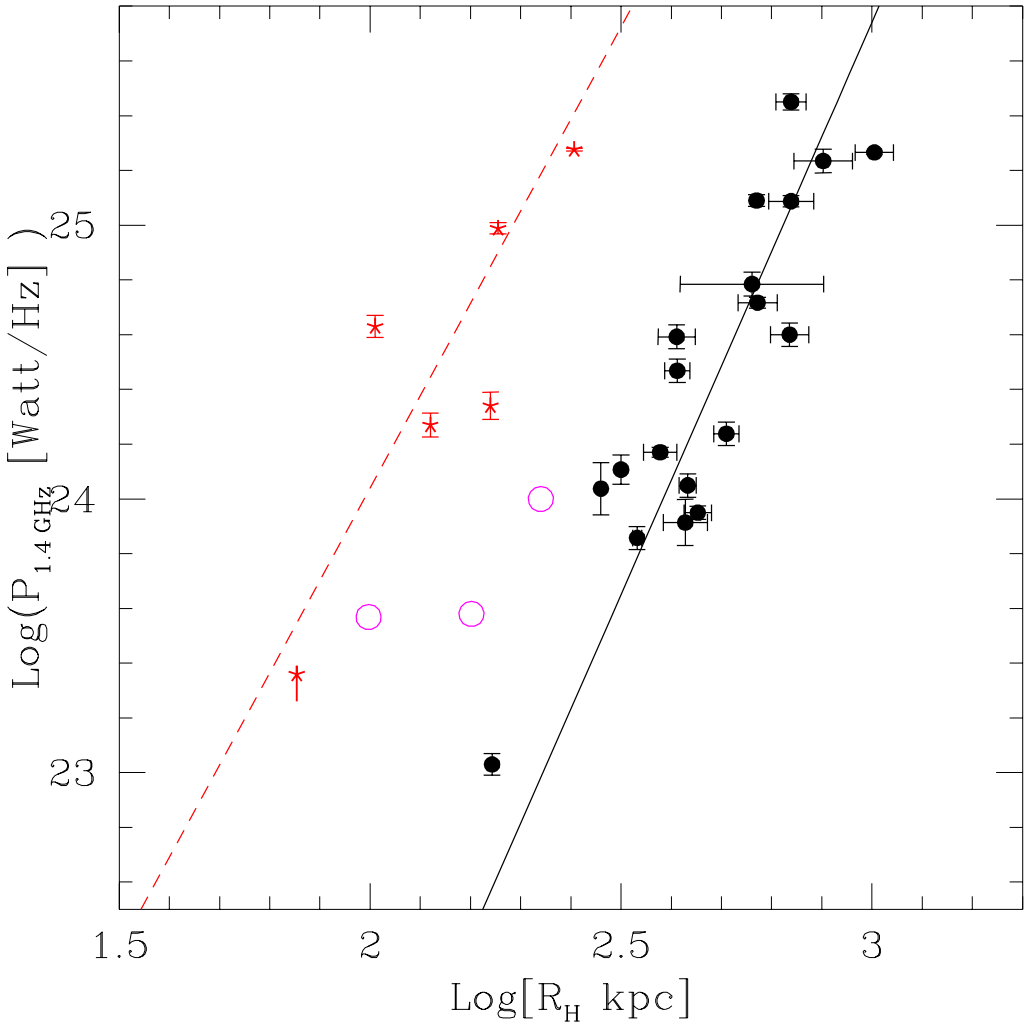

Radio power at 1.4 GHz versus radio size of GHs (black circles) and MHs (red asterisks), and small-scale radio emissions (magenta open circles). The black solid line and the red dashed line are the best-fit correlations for GHs ($P_{1.4} \propto R_{\rm H}^{4.18}$), and for MHs ($P_{1.4} \propto R_{\rm H}^{3.4}$), respectively. Taken from Cassano, Gitti & Brunetti (2008).

(Dennison 1980; Blasi & Colafrancesco 1999), or electrons re-accelerated *in situ* through second order Fermi mechanisms by ICM turbulence during cluster mergers (Brunetti et al. 2001; Petrosian 2001).

In the first scenario, an extended and fairly regular diffuse synchrotron emission is expected from secondary electrons, and also some level of γ-ray emission from secondary π^0 must unavoidably be present. However recent observational data point against this scenario: first, the non detection of diffuse emission from secondary electrons in the majority of clusters (Brunetti et al.2007) put strong upper limits to CR hadrons in these GC; second the detection of steep spectrum of the radio halos (e.g. in A 521, Brunetti et al.2008) is inconsistent with secondary models which would require an unrealistic energy budget in terms of relativistic protons in order to explain radio halos with spectrum significantly steeper than ≈ 1.5 (Brunetti 2004). The historical motivations for the turbulent re-acceleration scenario were the connection observed between Radio Halo and cluster mergers (e.g. Buote 2001), and the steepening at high frequency observed in the spectrum of the Radio Halo in Coma (e.g. Schlickeiser et al. 1987), that suggests a stochastic, poorly efficient particle acceleration mechanism for the origin of the emitting particles. According to this model, the statistical properties of radio halos depend on the interplay between the rate of cluster-cluster mergers and the fraction of the energy that is channeled into MHD turbulence and in the can re-accelerating of high energy particles. This connection has been investigated through Montecarlo procedures (Cassano & Brunetti 2005), and despite the wide range on uncertainty about the physics of turbulence at small $< kpc$ scales, this model predicts some basic features of the statistical properties of radio halos. In this framework, only massive and merging clusters, where enough energy can potentially be channeled into particle re-acceleration, are expected to host radio halos. Also, because the turbulent energy injected during mergers is expected to scale with the cluster thermal energy, the fraction of clusters with radio halos should increase with the cluster mass (or X-ray luminosity); that remarkably is in line with recent radio surveys (Cassano et al. 2008; Venturi et al. 2008). At the same time, protons are believed to be the most important non-thermal particle components, and the final picture is very complex: the ICM should contain a mixed population of relativistic particles (protons, secondary and primary electrons/positrons, re-accelerated particles) which

coexist in the ICM together with turbulent magnetic fields and thermal particles.

The predicted broad band non–thermal spectrum is very complex, and originate from two main components: a long-living one that is emitted by secondary particles (and by π_0 decay), and a transient component due to particles re-accelerated in cluster mergers (e.g. Brunetti 2008). The first component is presently constrained by radio and γ-ray observations of GC (Reimer et al. 2003, Brunetti et al. 2007, Aharonian et al. 2009), while the second component, that should be connected with cluster mergers, may explain Radio Halos. Observations from the new generation of high energy experiments (e.g. FERMI/GLAST and Cherenkov telescopes) will likely provide much more stringent constraints to the energy budget stored by relativistic hadrons, thus improving the theoretical understanding of this complex picture.

2.3.2 Radio Relics

Radio relics are elongated radio sources with a steep spectrum usually located at the boundary of the X-ray emission of host GC (e.g. Kampner et al.2004). These sources are polarized at the level of about $10 - 30$ % and so far, there are ~ 20 clusters of galaxies with radio relics. Some of the most extended and powerful giant relics are located in clusters with central radio halos (e.g. A2256, Clarke & Ensslin 2006, and A512, Giacintucci et al. 2005). In a few cases, two symmetric relics have been detected within the same clusters (e.g. Rottgering et al.1997; Bagchi et al.2006, see also Fig.2.6; Bonafede et al.2008). Radio relics are found in merging clusters, and, in some cases, they suggest a spatial correlation with shocks in the thermal gas has been pointed out (e.g. in the case of A 520, Markevitch et al.2005). Yet, due to low X-ray brightness at the cluster periphery, a comparison of relic properties with the surrounding medium (i. e. temperature and brightness gradient induced by shock waves) is not obvious. For instance, Feretti & Neumann (2006) did not find any evidence of a temperature jump nearby the Coma cluster relic.

Formation Scenarios for Radio Relics

Due to the connection detected between relics and merger shocks in some cases, it is believed that shocks play an important role in the origin of these emissions. Several models, all requiring the presence of a shock wave, have been proposed to explain the origin of radio relics. They can be divided into 2 classes:

- Diffusive Shock Acceleration by Fermi-I process (Ensslin et al. 1998; Roettiger et al. 1999; Hoeft & Brüggen 2007).
- Shock-reacceleration of emitting particles due to adiabatic compression of fossil radio plasma (Ensslin & Gopal-Krishna 2001).

The second one requires the presence of a relatively nearby radio source to provide the fossil radio plasma which can be re-energized by the shock wave. In favor of this second scenario there is the observational evidence that relics resemble individual objects and do not trace the entire shock front (Hoeft et al. 2004). However, a major difficulty in this scenario come from the fact that ghost radio plasma should be well confined into the ICM to keep the internal sound speed at the level of the speed of light, in order to experience adiabatic compression and not shock acceleration: in this respect, as soon as the ghost relativistic component is mixed with the ICM, diffusive shock acceleration come into play as leading mechanism for the acceleration of particles.

Roettiger et al. (1999) were able to reproduce the main features of the relic radio emission in A3667, by combining a single merger simulations with a model for shock acceleration. Relativistic electrons were injected with a power-law spectrum with slope dependent on the shock Mach number, and the aging of the radio plasma were include in their simulation. They found that the observed distribution of the spectral index of the relic were reproduced by adopting a shock velocity of the order of $v_{\rm s} \approx 700 - 1000$ km s^{-1} and a magnetic field of $\approx 0.6\mu$G at the position of the radio relic.

More recently, Hoeft et al.(2004) investigated Ensslin & Gopal-Krishna (2001) model by using the SPH code *GADGET* to simulate a merging galaxy cluster within a cosmological environment. This work showed that the probability for a shock wave to flare the ghost radio plasma is reduced in the central regions of galaxy clusters, where the radio plasma ages much faster due to the fact that the pressure of the radio plasma is kept higher by the external medium and the magnetic field is larger. Moreover, the compression ratio of the shock wave is much higher in the low-density peripheral regions than in the cluster center and this would explain why radio relics are more common in these regions. On the other hand, the increasing rate of detection rate of double relics in the last years seems to disfavor the scenario of Ensslin & Gopal-Krishna (2001), because of the low probability to find two

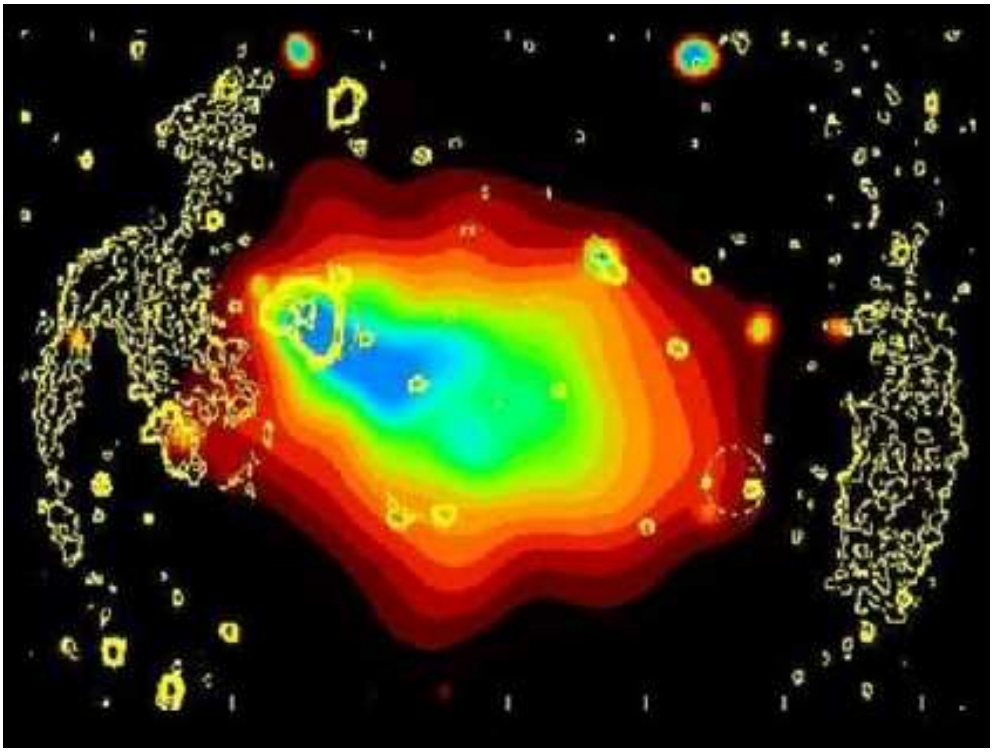

Figure 2.6: Colors: X-ray emission of A 3376 in the energy band 0.14-2 keV from from ROSAT PSPC observations. Contours: radio emission detected with VLA-1.4GHz observations. Taken from Bacghi et al.2006.

symmetric regions with fossil radio plasma (e.g. Bonafede et al.2008).

2.3.3 Mini Radio Halos

The so-called "mini radio-halos" differ from radio halos not only because of their smaller size (few 10^2 kpc), but also mini-halos are usually found around powerful radio galaxies at the center of cooling core clusters and their total size is comparable to that of the cooling region. Due to the their smaller angular size and the strong radio emission of the central radio galaxy, the detection of mini-halos requires a much higher dynamic range and resolution than those in available surveys, and this complicates their detection. As a consequence, our current observational knowledge on mini-halos is limited to less than ten known sources (e.g. Ferrari et al.2008 for a review).

Major mergers are thought to be powerful enough to disrupt cluster cooling flows (e.g. Buote & Tsai 1996), thus they cannot play a major role in the origin of mini halos. For example, signatures of merging activity are found in A 2142 (Giovannini

& Feretti 2000) and RXJ 1347.5−1145 (Gitti et al.2007). Recently, Cassano, Gitti & Brunetti (2008) suggested a possible connection between mini halos and "moderate" merger events in the host cool-core clusters. In this work, evidences were also shown for a P_ν-$L_{\rm X}$ and P_ν-$R_{\rm H}$ (where R_H is the radio halo radius) trends for mini-halos. Mini–halo clusters share the same region of giant halo clusters in the $(P_{1.4}, L_X)$ plane, whereas they are clearly separated in the $(P_{1.4}, R_H)$ plane (see Fig.2.3.1). Compared to radio halos, a more efficient source of injection of particles, (likely connected with the central radio galaxy) which takes part in the re-acceleration process, is required in mini-halos, that indeed have a synchrotron emissivity much larger than that of giant halos.

2.3.4 Open Problems in Non Thermal Phenomena

The Origin of Magnetic Fields in GC

Measurements of synchrotron radio emission at several frequencies provide the evidence for the presence of a significant population of relativistic electrons and magnetic fields. However, the magnetic field strength and relativistic electron density cannot both be determined from radio measurements alone. The presence of magnetic fields in GC can be estimated by measuring the statistical depolarization and Faraday Rotation (FR) of the plane of polarization of radiation from background radio sources seen through clusters (e.g. Kim et al.1991), and also from radio sources in the cluster. FR samples the line of sight component of the randomly oriented magnetic fields, weighted by the gas density, yielding a mean weighted value, $B_{\rm fr}$. This quantity was estimated by analyzing the rotation measure (RM) distribution of individual radio sources in several clusters (e.g. Rephaeli et al.2008 and references therein). Analyzes of RM typically yield values of $B_{\rm fr} \sim 1 \div 10$ μG (e.g. Murgia et al.2004). The major uncertainty in the RM procedure is related to the several contributions to the total RM (including that intrinsic to the radio source), the unknown tangled morphology of magnetic fields and their spatial variation across the cluster volume (e.g. Murgia et al.2004).

From a theoretical point of view, the magnetic field is believed to be injected in GC and amplified in a second phase by mechanisms probably connected with the formation process of thermal gas in GC (e.g. Dolag et al.2008 for a review).

Initially, magnetic fields can be produced either at relatively low redshift

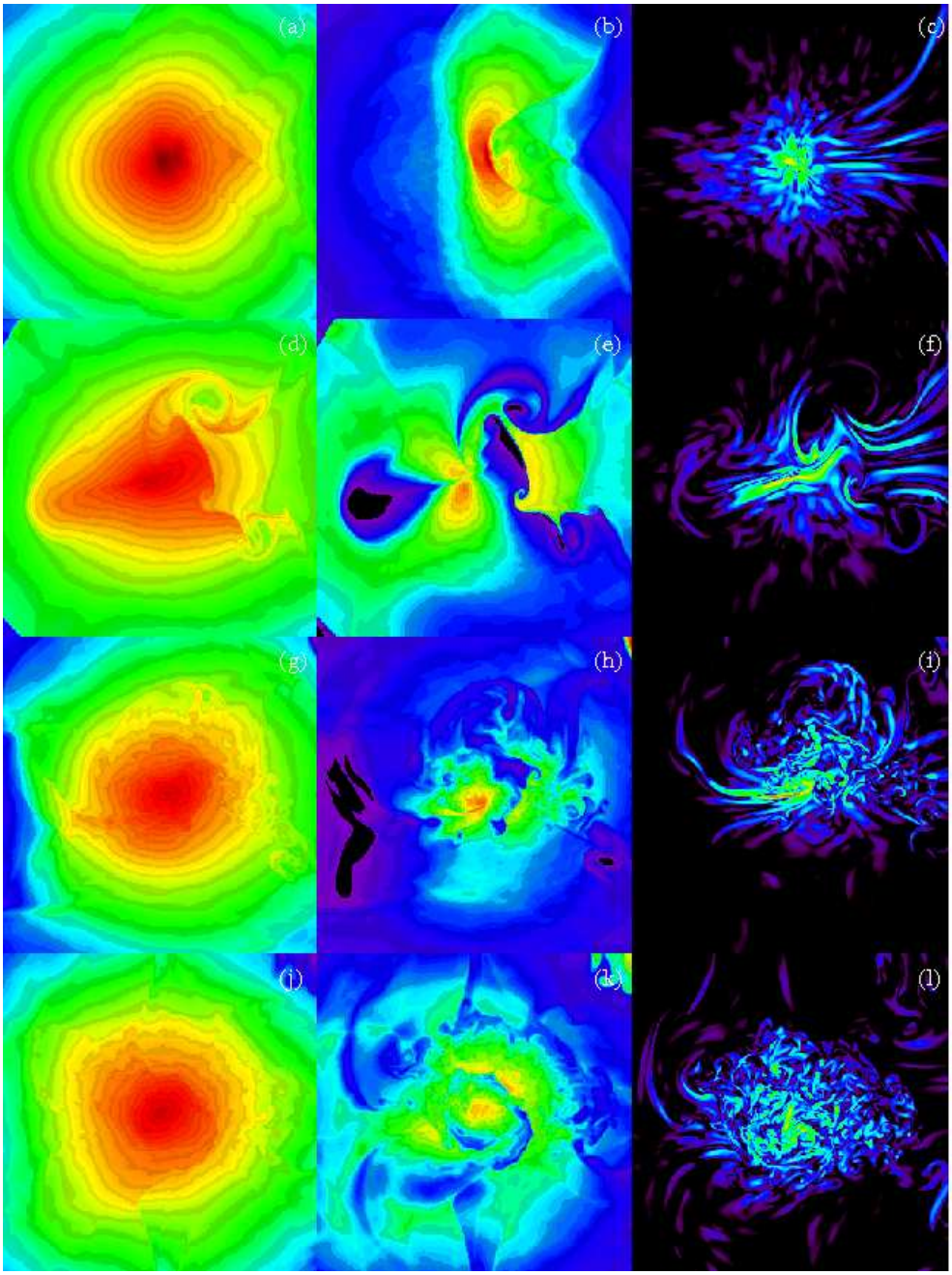

Figure 2.7: The evolution of (the logarithm of) the gas density (left column), the gas temperature (central column), and (the logarithm of) the magnetic pressure (right column) in two-dimensional slices taken through the core of a cluster in a major merger phase in the plane of the merger. Each row refers to different epochs: $t = 0$ (i.e. the time of the core coincidence), $t = 1.3$, $t = 3.4$, and $t = 5.0$ Gyr, from top to bottom. Each panel is 3.75×3.75 Mpc. The merging sub-cluster enters from the right. From Roettiger et al.(1999).

($z \sim 2-3$) or at high redshift ($z > 4$). In the former case, galactic winds (e.g. Volk & Atoyan 2000) or AGN ejecta (e.g. Enßlin et al.1997) produce magnetic fields 'locally' within the proto-cluster region. In the latter case, the magnetic field seeds can also be produced by an early population of dwarf star-burst galaxies or AGN before galaxy clusters form gravitationally bound systems.

One of the main arguments in favor of the 'low-redshift' models is that the high metallicity observed in the ICM suggests that a significant enrichment occurred in the past due to galactic winds or AGN. Winds and jets should carry magnetic fields together with the processed matter, and it has been shown that magnetic fields produced by the ejecta of star-burst galaxies can be as large as 0.1 . Clearly, this class of models predicts that magnetic fields are mainly concentrated in and around galaxies and within galaxy clusters. If the magnetic pollution happens early enough (around $z \sim 3$), these fields will be amplified also by the action of shear flows, turbulent motions, and merging events during the formation of the cluster. Shocks too are expected to be produced copiously during the non-linear stage of the LSS formation, and a class of specific instabilities driven by energetic accelerated particles (e.g. Vladimirov et al.2006).

According to 'high-redshift' models, the strength of the field seed is expected to be considerably smaller than in the previous scenario, but the adiabatic compression of the gas and the shear flows can still give rise to a considerable amplification of the magnetic fields. In these models the magnetic field seeds are supposed to be expelled by an early population of AGN or dwarf star-burst galaxies at a redshift between 4 and 6 (Kronberg et al.1999), which magnetize a large fraction of the cosmic volume.

Early extensive numerical simulations following the generation and evolution of magnetic field during a merger event were presented in Roettiger et al.(1999) by using the Eulerian code ZEUS. These authors demonstrated that the field initially becomes quite filamentary, as a result of stretching and compression by shocks and bulk flows during infall. Then when the bulk flow is replaced by turbulent motions, the field amplification is more rapid and located in particular regions (see Fig.2.7).

By using the *GrapeMSPH* code (e.g. Dolag et al.1999) and assuming that a small initial magnetic field seed exists before structure formation, the first self-consistent simulation able to follow the magnetic field amplification during the cosmological evolution of GC have been performed by Dolag et al.(1999,2002, see also

Fig.2.8). These simulations demonstrated that the contribution to the amplification of magnetic fields by shear flows (and by its induced turbulence) is significant and, for the first time, a consistent picture of the magnetic field in galaxy clusters could be constructed. The amplification predicted by the simulations allows to link the strength of the seed magnetic field at $z \approx 3$ to the observed magnetic field strength in GC.

A general predictions of the above simulations is that the final structure of the the magnetic field in GC reflects the process of structure formation, and no memory on the initial magnetic field configuration survives: this relaxes the constraints on the models for amplification of the seed magnetic field. These conclusion were enforced by recent results from numerical MHD simulations using an implemented version of GADGET2 (Donnert et al.2008), where different models of seed magnetic fields were assumed, with no relevant consequence on the final level of magnetic field within formed cluster. In general, such models predict a magnetic field profile that is similar to the density profile. Complementary numerical method of Eulerian simulations with FLASH, performed by Brüggen et al.(2005), produced results in agreement with GRAPESPH.

Another interesting quantity to look at is the slope α of the magnetic field power spectrum ($\propto k^{-\alpha}$, with k being the wave vector). Within galaxy clusters, α is predicted by the SPH simulations to be slightly lower, but still very close to 11/3, which is the expected value for a Kolmogorov-like spectrum in 3D. The AMR simulation by Brüggen et al.(2005) nearly perfectly matches the Kolmogorov slope.

The Origin of CRs

The origin of relativistic particles within GC is still debated. Many are the possible contributors to cosmic rays in the ICM: AGN activity in cluster galaxy, strong accretion shocks at the outskirts of GC, internal merger shocks in GC with moderate Mach numbers, proton–proton collision that inject secondary relativistic electrons, resonant and non-resonant coupling between turbulent MHD waves and mildly relativistic particles and secondary electrons in GC.

AGN outflows dissipate their kinetic energy into the ICM providing non-gravitational ICM heating (e.g. Churazov et al.2003). Relativistic outflows are likely important sources of supra-thermal particles in clusters. A powerful relativistic AGN

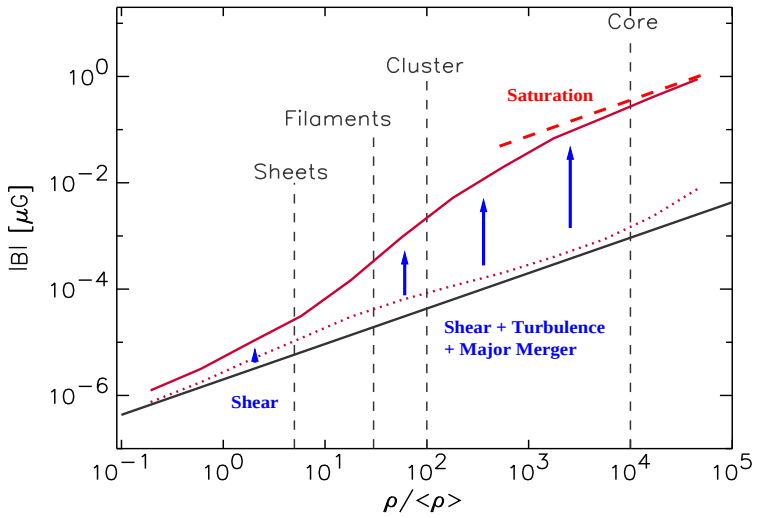

Figure 2.8: The strength of the magnetic field as a function of baryon over-density within a cosmological simulation. The straight line shows the expectation for a purely adiabatic evolution, the solid line gives the mean field strength at a given over-density within a cosmological simulation (Dolag et al.2005).

jet could deposit up to 10^{62} erg into a pool of relativistic particles pool during a duty cycle of ~ 50 Myr, and a sizable fraction of the energetic particles could escape the flows and avoid fast cooling that typical occurs in the central parts of the cluster.

Star formation activity in galaxies is another source of CRs in clusters of galaxies (e.g. Völk et al.1996), by means of the combined action of supernovae and winds of early-type stars leading to the formation of a hot, X-ray emitting and slowly expanding super bubbles filled with large-scale (tens of parsecs) compressible MHD motions. Bubbles may eventually expand beyond the disk of the parent galaxies and produce a super wind that supplies the ICM with metals and CRs ejected by supernovae. Non-thermal particle acceleration can occur in supernovae events and powerful stellar winds (e.g. Bykov 2001). This mechanism provides efficient injection of non-thermal nuclei and this population can transport a substantial fraction ($\sim$ 10%) of the kinetic energy released by the supernovae and by the winds of young massive stars.

A bright phase in the galaxy evolution can be the source of the relic CRs in clusters, where they can be stored in cluster magnetic field for several Hubble times (Berezinsky et al.1997). These nuclei can produce a diffuse flux of high-energy γ and neutrino radiation due to the interaction of the CRs with the ICM (e.g. Enßlin

et al.1997), depending on the ICM baryon density.

Shocks occurring during the formation of GC are also believed to be powerful injectors of relativistic particles in the ICM. The sub-cluster merging processes and the supersonic motions of DM halos in the ICM are accompanied by the formation of shocks, large-scale flows and broad spectra of MHD-fluctuations in a tenuous intra-cluster plasma with frozen-in magnetic fields. The free energy available for the acceleration of energetic particles is in the ram pressure of the shocks and in the large-scale motions.

The most studied way to transfer the power of the MHD motions to the energetic particle population is the Fermi-type acceleration (see e.g. Blandford & Eichler 1987). An important ingredient of the energetic particle acceleration by shocks and large-scale MHD motions is the presence of small-scale MHD turbulence, which is necessary to scatter relativistic particles and to make their pitch-angle isotropic. The scale of the fluctuations required for the resonant scattering of a particle of energy ~ 1 GeV is about $3\times\ 10^{12} B_{-6}^{-1}$ cm, where B_{-6} is the local mean magnetic field in μG. The scale is some 10–11 orders of magnitude smaller than the basic energy scale of the systems, thus the origin of such small scale turbulence is a serious issue; in non-linear models of particle acceleration by strong MHD shocks the presence of turbulence could be supported by the CR instabilities themselves (e.g. Vladimirov et al.2006).

The non-linear effect of the back-reaction of accelerated particles on large-scale plasma flows result in the modification of the temporal evolution of the particle spectra. Moreover, thanks to the conversion of a fraction of the shock ram pressure into magnetic field energy, an efficient acceleration of baryons by MHD shocks in a turbulent cosmic plasma may result also in the strong amplification of the magnetic field in the shock upstream. Non linear interaction between particles and turbulent motions in the collision-less regime provides a source of stochastic particles in GC (e.g. Brunetti & Lazarian 2007 for a review). This mechanism is poorly efficient to extract particles out of the thermal pool, yet it plays an important effect in modifying the energy distribution of relativistic particles in the ICM, and this in turn may greatly affect the non-thermal emissivity properties of GC.

Some processes related to CRs were implemented in fully cosmological simulation codes. For instance, *COSMOCR* is a numerical code for the investigation of CRs in

computational cosmology (Miniati 2001), that includes a number of prescriptions to account for the diffusive shock acceleration, the mechanical and radiative energy losses and the spatial transport of the energetic particles into the cosmic environment. In this numerical approach however, the back-reaction of the non-thermal components (CRs and magnetic fields) caused by their pressure contribution to the thermal gas is neglected.

To study the impact of CRs on galaxy and cosmic structure formation and evolution, Pfrommer et al.(2006) developed an approximate framework which treats dynamical and radiative effects of CRs in cosmological SPH simulations. These authors included some approximate prescriptions for CR injection and acceleration by shocks, as well as CR transport and energy losses due to Coulomb interactions, ionization losses, Bremsstrahlung losses, and hadronic interactions with the background matter. Although in such implementation the description of the CR population is more simplistic than in the work described earlier, the dynamical influence of the CRs onto the underlying hydrodynamics is no longer neglected. This is not only important for the dynamics of the ICM itself but also for the injection of the CRs by shocks, which are altered by the presence of the non-thermal pressure support of the CRs themselves. However, the bulk of results from the above approaches, such as distribution of CR hadrons in the innermost region of massive GC, is found to be in disagreement with recent observations (see Fig.2.9).

The simulation of CR injection is one of the main goal for the present PhD thesis, and we will discuss in detail this issue and all related uncertainties in Chapters 3 and 4.

Turbulence in the ICM

During their growth, GC continuously accrete other structures including objects with similar mass (major mergers). Together with the diffuse accretion and the generation of turbulence by hydrodynamic instabilities induced by these bulk motions, the gas in GC generally contains an amount of kinetic energy which is not negligible compared to the amount of thermal energy (e.g. Bryan & Norman 1999).

Different simulation methods reach good agreement in predicting that the ratio of bulk kinetic energy to thermal energy is up to 15% in galaxy clusters (e.g. Frenk et al.1999). Based on cosmological hydrodynamic simulations, (Sunyaev, Bryan &

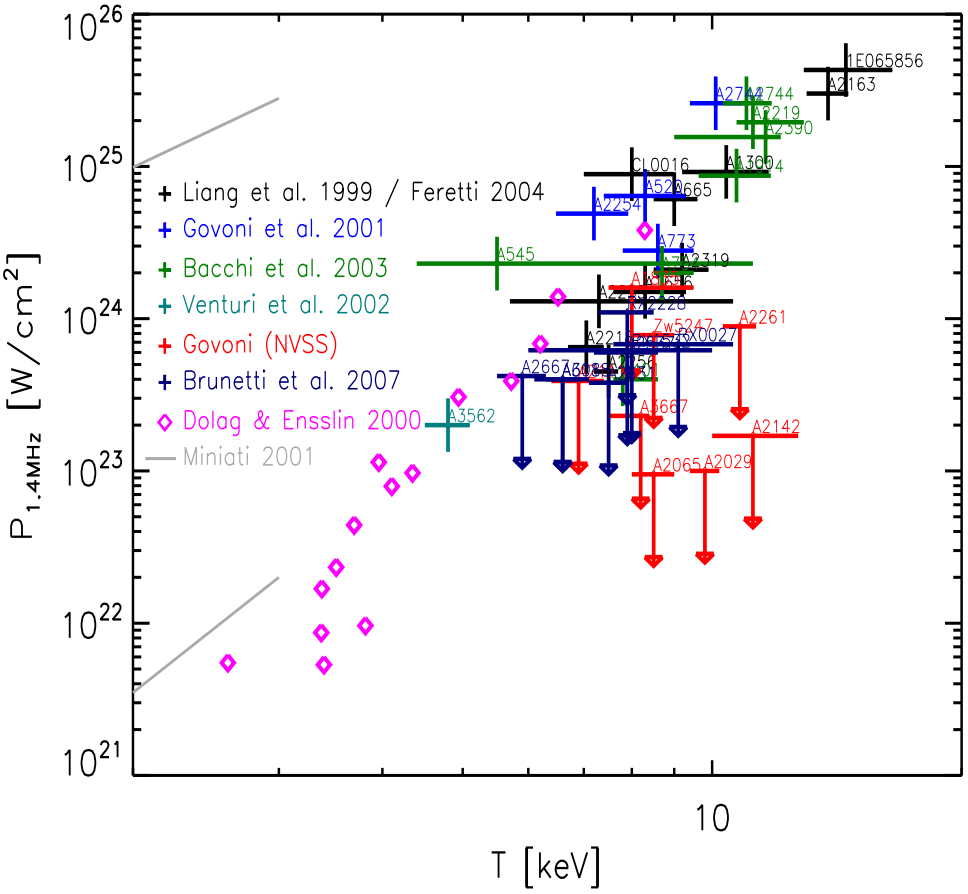

Figure 2.9: Total power of radio halos at 1.4MHz vs. cluster temperature. Data are taken from various surveys, and additional upper limits from Brunetti et al.(2007) are shown. A secondary model from Dolag & Ensslin (2000) is applied to calculate radio emission from simulated galaxy clusters (*squares*) and additional lines are shown for expected emission from primary (*upper line*) and secondary (*lower line*) electrons from Miniati et al.(2001). Note that the values for the luminosities of primary electrons should be scaled with the electron to proton injection radio $R_{e/p}$. Taken from Dolag et al.(2008).

Norman 2001) pointed out that the broadening of the emission lines in the X-ray band (e.g. the iron K line) due to these expected bulk motions is appreciably larger than the broadening due to thermal motions. Thus, future instruments like XEUS or NEXT will be hopefully able to infer such bulk motions from the analysis of the line shapes. Although large-scale bulk motions will be the main contributor to the deformation of the line shapes, the imprint of small scale turbulence might be more subtle to infer from the line profiles.

Using a mosaic of XMM-Newton observations of the Coma cluster, Schuecker et al.(2004) were able to produce spatially-resolved gas pressure maps which indicate the presence of a significant amount of turbulence. Performing a Fourier analysis of the data reveals the presence of a scale-invariant pressure fluctuation spectrum in the range between 40 and 90 kpc which is well described by a projected Kolmogorov turbulence spectrum; at least 10 percent of the total ICM pressure is in turbulent form (see Fig.2.10).

Alternatively, following a less direct approach by using Faraday rotation measurements, Ensslin & Vogt (2006) argue that observed magnetic field spectrum in cool core galaxy clusters (e.g. Hydra cluster) has Kolmogorov-like spectrum. Faraday rotation within non-cooling flow clusters with multiple extended radio sources (which therefore probe the magnetic field structure at different radii) can give complementary constraints on the magnetic field power spectra (e.g. Murgia et al.2004; Govoni et al.2006) and thus on the underlying turbulence in the ICM.

Yet the total energy budget in form of turbulent motions inside GC, as well as their distribution and their connection with cluster dynamics and non gravitational process in GC are sill open fields of research.

In Chap.5 of the present PhD thesis we report on first extensive cosmological simulations that study turbulence in GC and its connection with cluster dynamics.

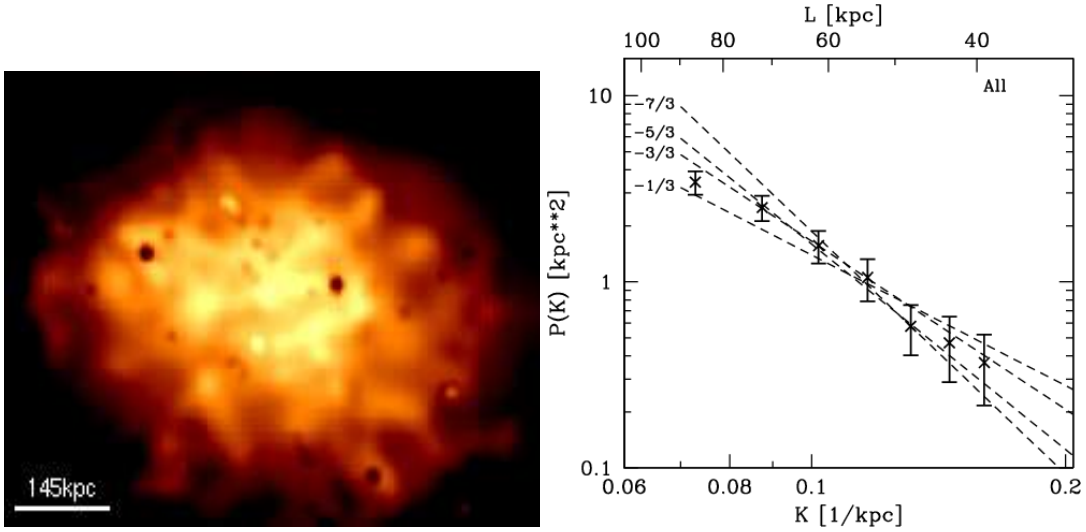

Figure 2.10: *Left:* XMM pseudo-pressure map of the innermost region of the Coma cluster. *Right:* observed projected power spectral densities as inferred from XMM observations of the Coma cluster, after subtraction of the shot noise; the dashed lines are model predictions (from Schuecker et al.2004)

Chapter 3

Shocks and Cosmic Rays in ENZO Simulations.

3.1 Introduction

The detection of shocks in Large Scale Structures (LSS) is still observationally challenging since they usually develop in the external regions of galaxy clusters, where the X–ray emission is faint. Moreover, projections and mass-weighting effects along the line of sight are expected to smooth most of possible temperature gradients in observed galaxy clusters. In a few cases, however internal shocks driven by the merging events have been discovered with typical Mach numbers $\approx 1.5 - 3$ (e.g. Markevitch et al. 1999; Markevitch et al. 2002; Belsole et al.2004; Markevitch & Vikhlinin 2007).

As stressed in the Introduction (Sec.2.3.4), shocks are important not only to understand the heating of the ICM but also because they may be efficient accelerators of supra–thermal particles (e.g. Sarazin 1999; Takizawa & Naito 2000; Blasi 2001), which are likely connected to the appearance of diffuse non–thermal emissions in galaxy clusters.

The energetics associated with the population of cosmic ray particles (CR) accelerated at shocks depend on the Mach number of these shocks (e.g. Kang & Jones 2002). The Mach number distribution of cosmological shocks is thus important to understand cosmic rays in galaxy clusters. Semi–analytical studies pointed out that shocks that form during cluster mergers are weak, $M \sim 1.5$, being driven by sub-clumps crossing the main clusters at the free-fall velocity (Gabici & Blasi 2003, Berrington & Dermer 2003). These approaches however are limited as

they treat cluster mergers as binary encounters between ideally virialised spherical systems. Therefore cosmological numerical simulations represent a necessary avenue to address this issue in more detail. First attempts to characterize shock waves in cosmological numerical simulations were produced by Miniati et al.(2000), by employing a set of eulerian simulations and a shock detecting scheme based on jumps in the temperature variable. Later works adopted more refined shock-detecting schemes and were more focused onto the distribution of energy dissipated at shocks (Keshet et al.2003; Ryu et al.2003, Hallman et al.2003, Pfrommer et al.2006). Ryu et al. and Pfrommer et al. basically confirmed that the bulk of shocks in the universe is made of relatively weak shocks, but they also allow to constrain the population of stronger shocks that form in the external regions of galaxy clusters. In these environments, strong shocks are frequent and may provide the bulk of the acceleration of CR in large scale structures (Ryu et al. 2003; Pfrommer et al. 2006; Skillman et al. 2008). On the other hand, the identification and characterization of shocks, as well as the calculation of the energy injected in the form of CR at these shocks, is difficult because of the complex dynamics of large scale structures and because of the severe limitations in terms of physics and numerical resolution that affect present cosmological simulations.

In this Chapter we will use cosmological numerical simulations performed with the ENZO code in order to describe cosmological shocks in LSS. The outline of this Chapter is the following: In Sect.3.2 we provide a brief introduction to the ENZO Code, in Sect.4.3 we present our cluster sample and the main properties of cosmological structures in our simulations, and in Sect.3.4 we discuss the effect of re-ionization on the thermal properties of simulated cosmic structures. In Sect.3.5 we provide the different methods to characterize shocks in post processing and in Sect.3.6 we discuss their main source of uncertainties in the cosmological framework. In Sect.3.7 we present our results about the main shocks properties and about the injection of CR. The main conclusions of this work are given in Sect.3.8. In the Appendix (Ch.7) we discuss the the effect of spatial the resolution and of σ_8 on our results.

Table 3.1: Main characteristics of the simulations.

Volume	Resolution	physics	ID
$(145Mpc)^3$	$125kpc$	adiab.	**AD125**
$(145Mpc)^3$	$250kpc$	adiab.	**AD250**
$(145Mpc)^3$	$500kpc$	adiab.	**AD500**
$(145Mpc)^3$	$800kpc$	adiab.	**AD800**
$(80Mpc)^3$	$125kpc$	cool. + reion.	**CO125**
$(80Mpc)^3$	$250kpc$	cool., reion. and $\sigma 8 = 0.74$	**S8250**
$(80Mpc)^3$	$250kpc$	cool.+reion.	**CO250**

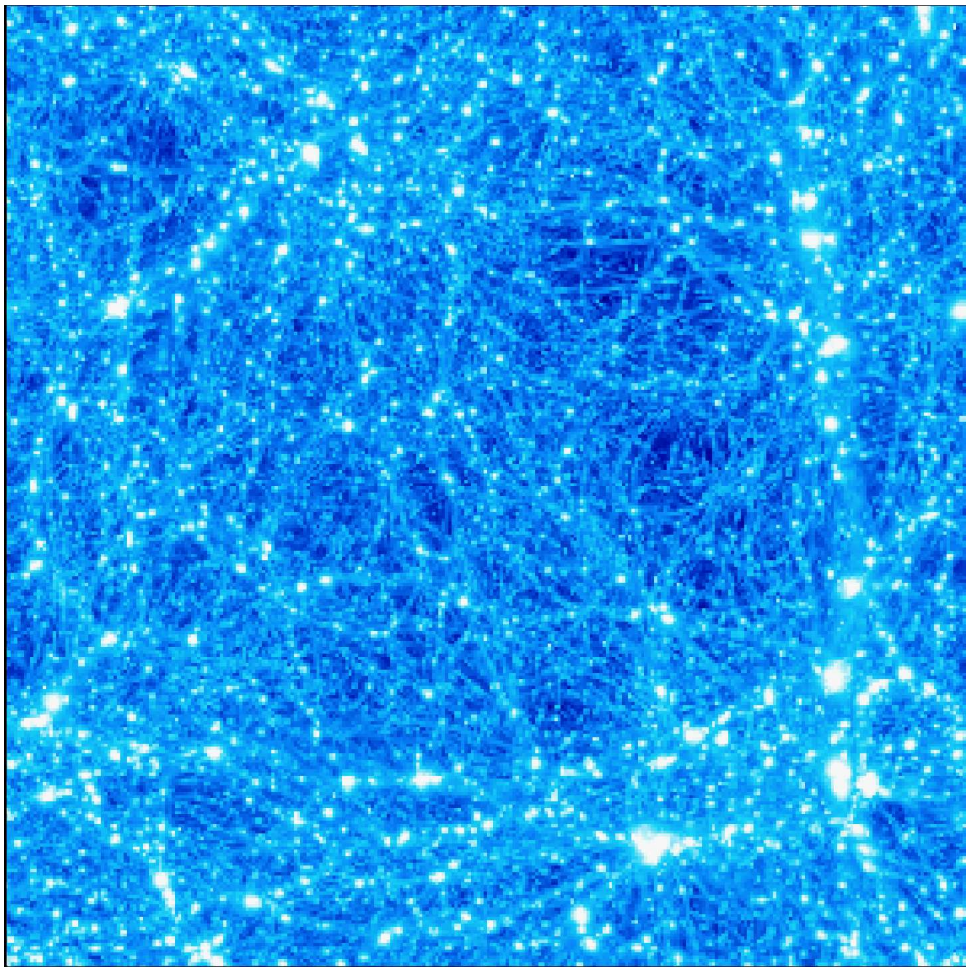

Figure 3.1: Map of projected gas density for one simulated volume of the sample. The line of sight and the side of the image are $80Mpc$.

3.2 Numerical Code - ENZO.

A precise description of the behavior of the bayonic gas is crucial for the goals of the present work. In particular, the numerical code adopted for our simulations must support an accurate treatment of the dynamics of high supersonic flows and the formation and propagation of strong shock waves during the process of cosmological structures formation. The ENZO code supports such description. ENZO is an adaptive mesh refinement (AMR) cosmological hybrid originally written by Greg Bryan and Michael Norman (Bryan & Norman 1997, 1998; Norman & Bryan 1999; Bryan, Abel, & Norman 2001, Norman et al.2007). It couples an particle-mesh solver with an adaptive mesh method for ideal fluidynamics (Berger & Colella, 1989).

ENZO uses a particle-mesh N-body method (PM) to follow the dynamics of collision-less systems. This method computes trajectories of a representative sample of individual DM particles and it is much more efficient than a direct solution of the Boltzmann equation in most astrophysical situations.

DM particles are distributed onto a regular grid using the cloud-in-cell (CIC) interpolation technique, forming a spatially discretized DM density field. After sampling dark matter density onto the grid and adding baryon density (calculated in the hydro method of the code), the gravitational potential is calculated on the periodic root grid using Fast Fourier Transform algorithms, and finally solving the elliptic Poisson's equation.

The effective force resolution of a PM calculation is approximately twice as coarse as the grid spacing at a given level of resolution. The potential is solved in each grid cell; however, the quantity of interest, namely the acceleration, is the gradient of the potential, and hence two potential values are required to calculate this.

As hydrodynamical solver, ENZO adopts the Eulerian Piecewise Parabolic Method (PPM, Woodward & Colella, 1984). The PPM algorithm belongs to a class of schemes in which an accurate representation of flow discontinuities is made possible by building into the numerical method the calculation of the propagation and interaction of non–linear waves. It is a higher order extension of Godunov's shock capturing method (Godunov 1959). It is at least second–order accurate in space (up to the fourth–order, in the case of smooth flows and small time-steps) and second–order accurate in time.

The PPM method describes shocks with high accuracy and has no need of artificial viscosity, leading to an optimal treatment of energy conversion processes, to the minimization of errors due to the finite size of the cells of the grid and to a spatial resolution close to the nominal one. In the cosmological framework, the basic PPM technique has been modified to include the gravitational interaction and the expansion of the universe (e.g. Bryan et al.1995)

In order to more accurately treat situations involving bulk hypersonic motion, where the kinetic energy of the gas can dominate the internal energy by many orders of magnitude, both the gas internal energy equation and total energy equation are solved everywhere on the grid at all times. This *dual energy formulation* ensures that the method produces the correct entropy jump at strong shocks and also yields accurate pressures and temperatures in cosmological hypersonic flows.

In this work, in order to keep our study of LSS shocks as simple as possible, we use ENZO with a fixed spatial resolution without the application of AMR techniques.

AMR simulations performed with ENZO and focused on high resolution simulations of turbulence and shocks in galaxy clusters are subject of Chapter 5.

3.3 Cosmological Simulations and Tests.

3.3.1 General Properties

In our simulations we have assumed a "Concordance" model, with density parameters $\Omega_0 = 1.0$, $\Omega_{BM} = 0.044$, $\Omega_{DM} = 0.226$, $\Omega_\Lambda = 0.73$, Hubble parameter $h = 0.71$, a power spectrum produced according to the Eisenstein & Hu (1999) fitting formulas with a primordial spectrum normalization $\sigma_8 = 0.94$, and an initial redshift of $z = 50$. In order to have a large cluster statistics we simulated a total volume equivalent to $(145Mpc)^3 \approx (103Mpc/h)^3$ at the fixed numerical resolution of 125 kpc. This total volume was obtained by combining together six (independent) simulated boxes of 80 Mpc per side.

Fig.3.1 shows the projected gas density across one of the simulated volume of 80Mpc per side.

A list of all simulations run used in our study with their main properties is listed in Tab.3.1. The goal of this study is to investigate cosmological shocks with the most simple physical and numerical treatments. Cosmological shock waves are supposed to be mainly driven by the assembly of cosmic structures, and therefore

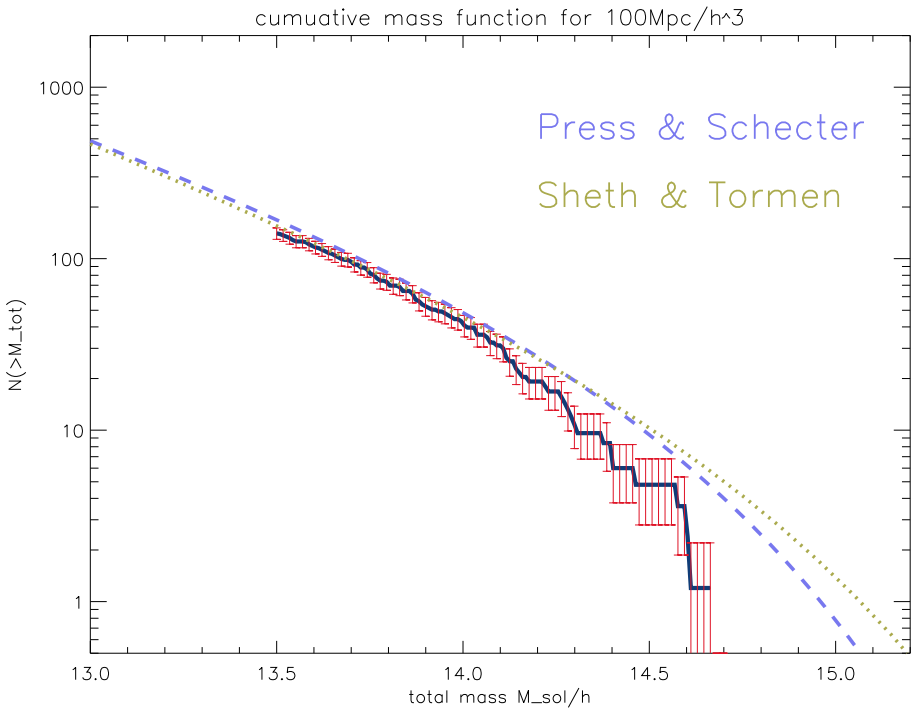

Figure 3.2: Cumulative Mass Function for the total matter of all simulated halos, with poissonian errors. Press & Schechter (*dashed*) and Sheth & Tormen (*dotted*) mass functions are reported for comparison.

gravity should be the principal ingredient to model. Therefore we made massive use of "adiabatic" simulations at various resolutions (*AD125, AD250, AD250, AD800*): these simulations contain only "adiabatic" physics, i.e. they do not have radiative cooling, UV photo-ionization at early epochs, thermal conduction and magnetic fields. These simulations are the starting point to investigate the effects on the properties of shocks driven by the adoption of a more complex physical modeling. In particular, the re-ionization process has the important effect of increasing the temperature (and the sound speed) of cosmic baryons in the low temperature regions, and thus this is the first additional ingredient to take into account. Therefore we re-simulated one of our six 80 Mpc boxes at two different resolutions with the Haardt & Madau (1996) re-ionization model plus radiative cooling (*CO125, CO250*) and used the outputs of these simulations to derive a recipe to mimic the effect of re-ionization in post-processing in adiabatic simulations. Finally, we perform simulations with a different σ_8 parameter, in order to study how this parameter can affect our results (*S8250* simulation, see the Appendix).

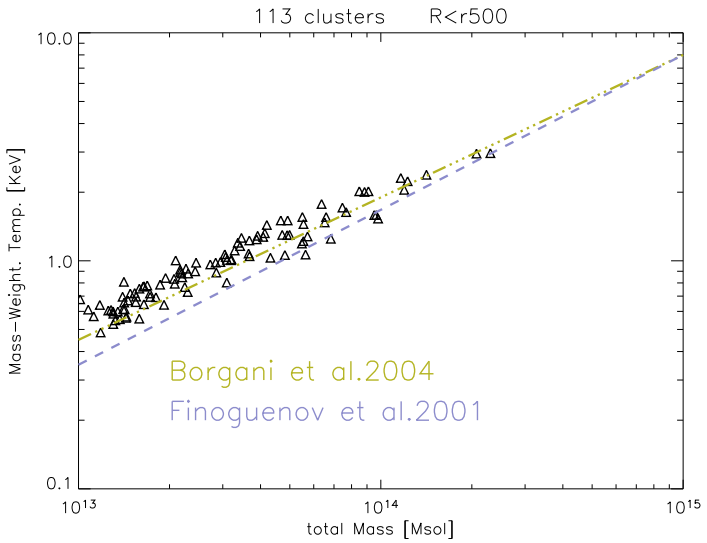

Figure 3.3: Total Mass versus Emission–Weighted Temperature for the all the simulated galaxy clusters of the sample. Best fit relations for these samples are drawn (*solid line = AD125, dashed = CO125*), and also a comparison with the results of Borgani et al.2004 (*yellow line*).

3.3.2 Properties of the Simulated Galaxy Clusters

The aim of this Section is to present the sample of galaxy clusters obtained from our simulations and to briefly discuss their main properties.

A cluster reconstruction procedure, based on total over density criteria (e.g. Gheller, Moscardini & Pantano 1998), has been applied to the outputs of the simulations at different cosmological times, providing a population of synthetic galaxy clusters which can be followed during time. The overall *AD125* simulation at $z = 0$ consists of 113 galaxy clusters with total virial masses $\geq 3 \cdot 10^{13} M_{\odot}/h$.

The cumulative mass function of all the halos of our sample is reported in Fig. 3.2 and shows an overall good agreement with the expected Sheth & Tormen (1999) mass function for masses $M < 3 \cdot 10^{14} M_{\odot}/h$. The deficit of halos with masses $\geq 3 \cdot 10^{14} M_{\odot}/h$ in our sample is likely due to the fact that single runs in our sample are only $80 Mpc$ in size, implying a cutoff in the over density power spectrum at long wavelengths. This is a known drawback of the procedure, which is commonly found in cosmological numerical simulations (Bagla & Ray 2005; Bagla & Prasad 2006). Massive galaxy clusters are expected to be the most important regions where the kinetic energy is dissipated (in thermalization and CR acceleration) by shocks.

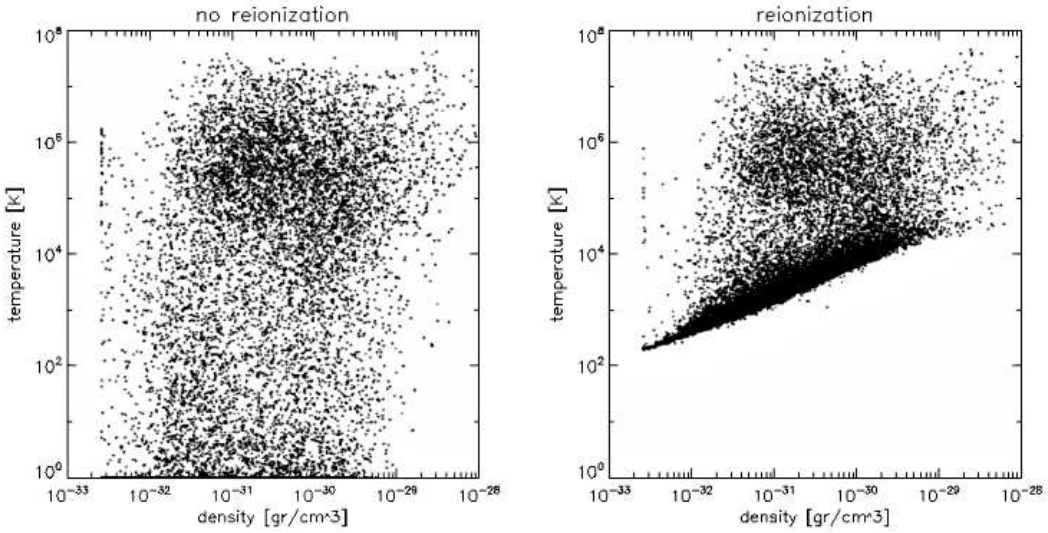

Figure 3.4: Phase diagrams for a box of $80Mpc$, from the *AD125* run (*left*) and from the *CO125* re-simulation*right*.

Thus a deficit in massive cluster halos may cause a deficit in the energy processed by shocks in the total simulated volume, which should be taken into account when our results are compared with previous studies (e.g. Ryu et al. 2003; Pfrommer et al.2006; Kang et al.2007).

In Fig.3.3 we report the scaling between the total mass and the emission–weighted temperature within r_{500} for our clusters population [1]. Points are slightly above (but they are consistent within a ~ 15 per cent scatter) the self similar scaling found by Borgani et al.(2004).

Overall Figs.3.2–3.3 show that the basic statistical properties of our galaxy clusters are in line with those from other cosmological numerical simulations, and that our sample is reliable for statistical analysis.

3.4 Phase Diagrams and re–ionizing background.

Shocks and compressions driven by the gravitational force are the only sources that increase the thermal energy of cosmic baryons in our adiabatic simulations. Baryons far away from collapsing regions have the lowest temperature that can be potentially affected by the process of re-ionization which occurred between $z \sim 30$ and $z \sim 6$ (e.g. Fan, Carilli & Keating 2006). This process heats up the medium, increasing

[1] r_{500} is the radius encompassing a mean total over density of 500 times the cosmic mean density, and roughly corresponds to 0.48 the virial radius of galaxy clusters in a ΛCDM cosmology.

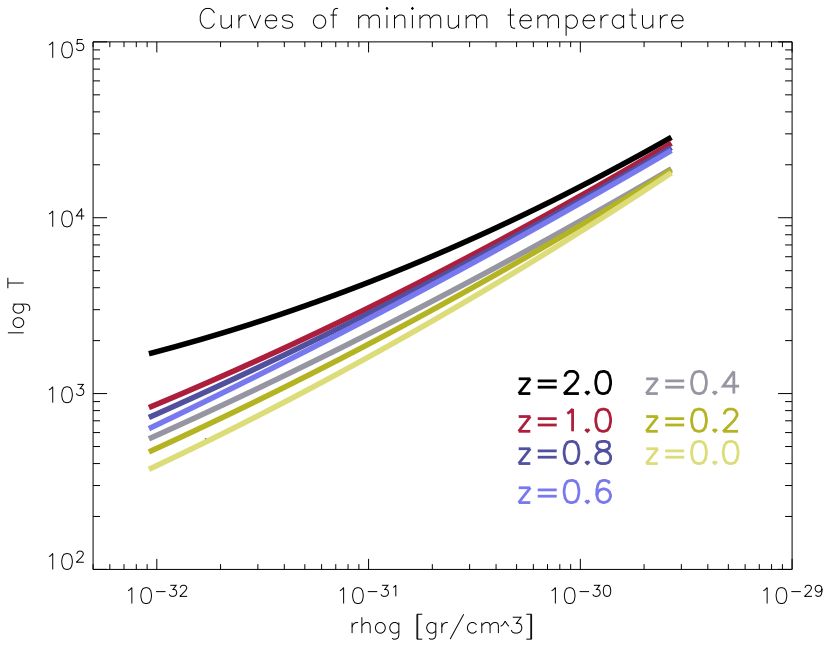

Figure 3.5: Evolution of the best–fitting relation for the minimum temperature of the *CO125* run, from $z = 2$ down to $z = 0$. Best fit parameters for these curves are reported in Tab.2.

the speed of sound in the lowest temperature regions and this affects our estimate of the Mach number of shocks. Therefore a study of cosmological shock waves must deal with the influence of a re–ionizing background (Haiman & Holder 2003; Loeb & Barkana 2005; Mellema et al.2006).

The re-ionization scheme available in ENZO is linked with a treatment of radiative cooling, which is computed by assuming an optically thin gas of primordial composition, in collisional ionization equilibrium, following Katz, Weinberg & Hernquist (1996). The time–dependent UV background is introduced according to Haardt & Madau (1996), where a model is introduced for the population of quasars that re-ionizes the universe at $z \approx 6$. The implementation of run–time re-ionization is more expensive in terms of memory usage compared to non–radiative simulations, and thus we applied it only in two re–simulated data–sets (*CO125, CO250*). The effect of a re–ionizing background can also be modeled in the post–processing phase by increasing the temperature of each cell in the simulation. This has been done in Ryu et al.(2003), where a constant value of $T = 10^4 K$ is imposed to the simulated volume at $z = 0$, and this may correctly reflect the complete re–ionization inside halos at present epoch (Haiman & Holder 2003) but it overestimates the mean

temperature of baryons far away of the most massive cosmic structures. Figure 3.4 shows the phase diagram in one $(80Mpc)^3$ simulation from the *AD125* data set, and in its re-simulation with cooling and re-ionization, *CO125*. Re–ionization efficiently removes the coldest phase of the baryons and a forbidden region in the $\log T - \log \rho$ space forms (where T and ρ are gas temperature and density, respectively), which actually traces the lower bounds of the Warm Hot Intergalactic Medium (Katz, Weinberg & Hernquist 1996; Cen & Ostriker 1999; Valageas, Schaeffer & Silk 2002; Regan, Haehnelt & Viel 2007). This lower bound is evolving with time, as shown in Fig.3.5 where we report fits to the value of the 15 per cent percentile in the distribution of temperature in the cells for different density bins; we checked that variations in the percentile (up to ~ 50 per cent) does not significantly affect the results. By restricting to baryon densities in the range $10^{-32} \leq \rho \leq 3 \cdot 10^{-30} gr/cm^3$ we obtain best fits to the minimum temperature with a second order polynomial :

$$\log(\frac{T_{min}}{T_0}) = c_1 \log(\frac{\rho}{\rho_0}) + c_2 (\log(\frac{\rho}{\rho_0}))^2, \tag{3.1}$$

where $\rho_0 = 10^{-32}$gr cm^{-3}. The best fit parameters for each redshift are reported in Table 3.4 At moderate redshift ($z \leq 1$) all curves can also be approximated with a simple power law, $T_{min} \propto \rho^{0.6}$ (consistent with Valageas et al.2002), and with a normalization decreasing with time. In particular, at $z = 0$ the minimum temperature of baryons is given by:

$$T_{min}(K) = 450 \ (\frac{\rho}{\rho_0})^{0.60}, \tag{3.2}$$

which is consistent with Eq.21 in Valageas et al. (2002); by using the *CO250* data set we also verified that these fits do not change with spatial resolution.

We use the formulas in Tab.3.4 to increase the temperature of baryons in our adiabatic simulations in the post-processing analysis. In Fig.3.6 we show the evolution with time of the temperature distribution function of the cells in a sub–sample of the *AD125* simulation with post–processing treatment and in the case of *CO125* simulation. The agreement between the two distributions demonstrates the validity of our post–processing approach that will be applied in the following to the full set of our adiabatic simulations (*AD125, AD250, AD500* and *AD800*).

Table 3.2: Fit parameters for the minimum temperature for the outputs of the *Co125* run.

Redshift	$LogT_0$	c1	c2
$z = 2.0$	3.2383 ± 0.0032	0.3198 ± 0.0061	0.0749 ± 0.0025
$z = 1.0$	2.9388 ± 0.0010	0.5056 ± 0.0020	0.0335 ± 0.0008
$z = 0.8$	2.8846 ± 0.0009	0.5358 ± 0.0016	0.0361 ± 0.0007
$z = 0.6$	2.8288 ± 0.0011	0.5773 ± 0.0022	0.0267 ± 0.0008
$z = 0.4$	2.7628 ± 0.0019	0.5437 ± 0.0038	0.0330 ± 0.0015
$z = 0.2$	2.6889 ± 0.0016	0.5517 ± 0.0033	0.0409 ± 0.0013
$z = 0.0$	2.5904 ± 0.0016	0.5711 ± 0.0032	0.0469 ± 0.0001

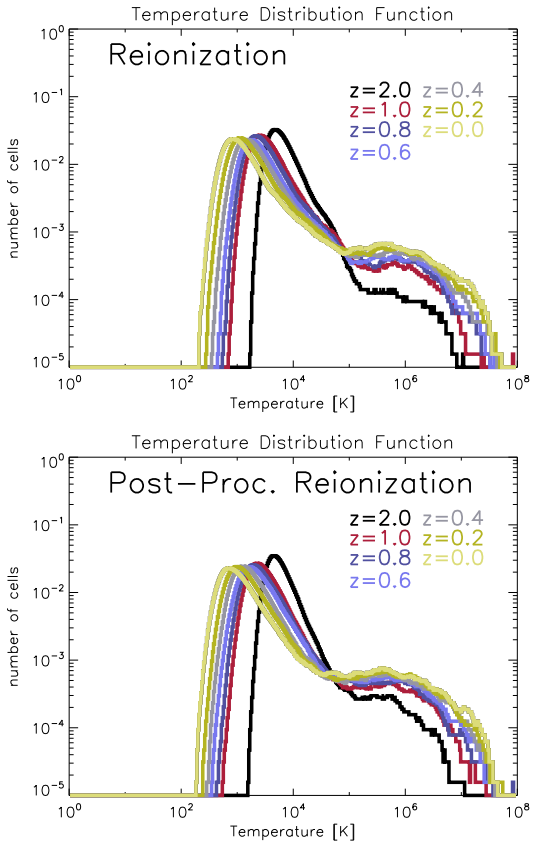

Figure 3.6: Evolution with time of the temperature distribution (see panel for color–coding) from $z = 2$ to $z = 0$, for the *CO125* simulation (*Left*) and for the corresponding adiabatic simulation *AD125* with the post–processing treatment of re-ionization (*Right*).

3.5 Shock–Detecting Methods

3.5.1 Basic Relations

The passage of a shock in a simulated volume leaves its imprint as a jump in all the thermodynamical variables. Under the simple assumption that the pre–shocked medium is at rest and in thermal and pressure equilibrium, the pre–shock and post–shock values for any of the hydrodynamical variables (density, temperature and entropy) is uniquely related to the Mach number, $M = v_s/c_s$, v_s being the shock speed in the region and c_s the sound speed ahead of the shock itself. The Rankine–Hugoniot jump conditions contain all the information needed to evaluate M; if the adiabatic index is set to $\gamma = 5/3$ one has the well known relations (e.g. Landau & Lifshitz 1966):

$$\frac{\rho_2}{\rho_1} = \frac{4M^2}{M^2+3}, \tag{3.3}$$

$$\frac{T_2}{T_1} = \frac{(5M^2-1)(M^2+3)}{16M^2} \tag{3.4}$$

and

$$\frac{S_2}{S_1} = \frac{(5M^2-1)(M^2+3)}{16M^2}\left(\frac{M^2+3}{4M^2}\right)^{2/3}, \tag{3.5}$$

with indices $1, 2$ referring to pre and post–shock quantities, respectively, and where the entropy is $S = T/\rho^{2/3}$.

The Mach number can be obtained from the jumps in one of the hydro dynamical variables (Eqs.3.3–3.5) or from a combination of them.

Fig.3.5.1 shows the behavior of the above Equations in the *"jump"* vs Mach number plane.

Eqs.3.3–3.5 describe shock discontinuity in the case of an ideal shock. In practice measuring the Mach number of the shocks in simulations is more problematic. Matter falling in the potential wells may have chaotic motions and the temperature distribution is usually patchy due to the continuous accretion and mixing of cold clumps and filaments into hot halos. All these complex behaviors establish velocity, temperature and density discontinuities across the cells in the simulated box. In a post-processing analysis this may modify irreparably the strength of the jumps in the thermodynamical variables in the shocked regions with respect to that expected

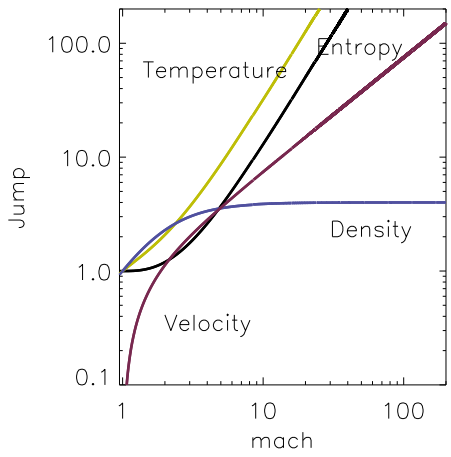

Figure 3.7: Relation between a measured jumps in control variable and the calculated Mach number, according to Ranking–Hugoniot jump conditions. *'Velocity'* stands for the velocity jump used in Eq.3.7 (3.5.3).

in the ideal case (Eqs.3.3–3.5). Consequently the estimate of the Mach number from these equations is subject to unavoidable uncertainties (see Sec.6.1).

3.5.2 The Temperature Jumps Method

The analysis of jumps in temperature is a commonly adopted method to measure the strength of shocks in Eulerian cosmological simulations (e.g., Miniati et al. 2001; Ryu et al. 2003). Cells hosting a possible shock pattern are preliminarily tagged by means of two conditions:

- $\nabla T \cdot \nabla S > 0$;
- $\nabla \cdot \mathrm{v} < 0$;

An additional condition on the strength of the temperature gradient across cells is also customary requested, e.g.

- $\mid \triangle logT \mid \geq 0.11$;

(specifically $\mid \triangle logT \mid \geq 0.11$ filters out shocks with a Mach number $M < 1.3$, Ryu et al.2003); however in the following we neglect this third condition, in order to have a better comparison with the results obtained with the VJ method (see below).

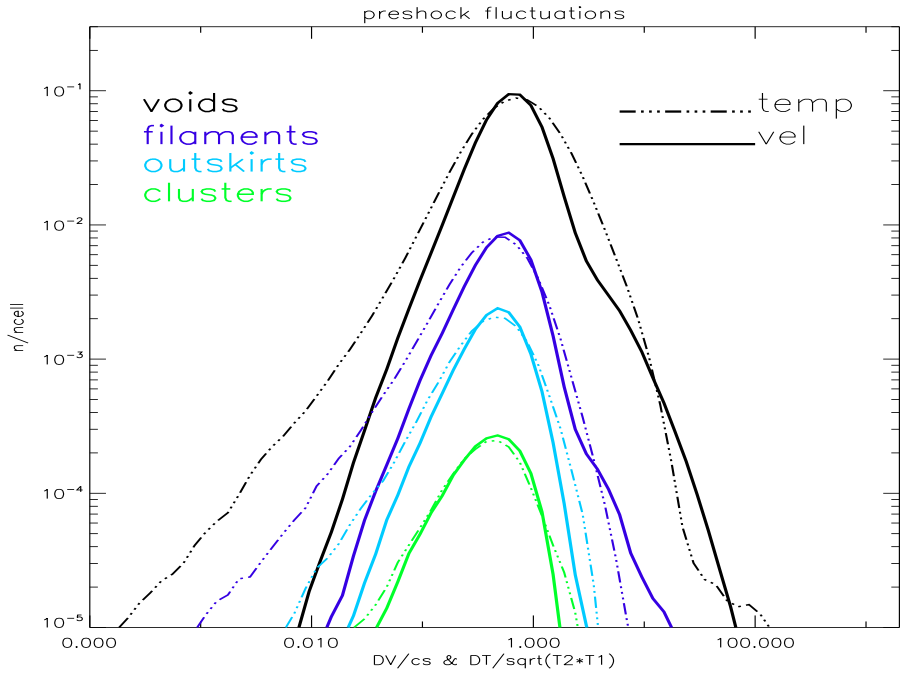

Figure 3.8: Distribution of normalized temperature fluctuations (*dot–dash lines*) and of normalized velocity fluctuations (*solid lines*) for non-shocked cells in the simulation, at four different over density regimes.

Shocks in the simulation are typically spread over a few cells, thus following Hallman et al.(2004) for each 1–D patch of candidate shocks we define the center of the shock with the position of the cell where $\nabla \cdot \mathrm{v}$ is minimum and calculate the Mach number of the shock from Eq.3.4, where T_2 and T_1 are the post and pre–shock temperature across the shock region. More specifically, in the case the shock-jump is assumed to happen in 1 cell, T_2 is the temperature of the shock center, while in the case that the jump is spread over 2, 4, 6, ... 2 n cells T_2 and T_1 are the temperatures of the two cells at distance n (in opposite direction) from the center of the shock.

In the following we will refer to this method as the Temperature Jump (TJ) method.

3.5.3 The Velocity Jump Method.

Conservation of momentum in the reference frame of the shock yields:

$$\rho_1 v_1 = \rho_2 v_2, \tag{3.6}$$

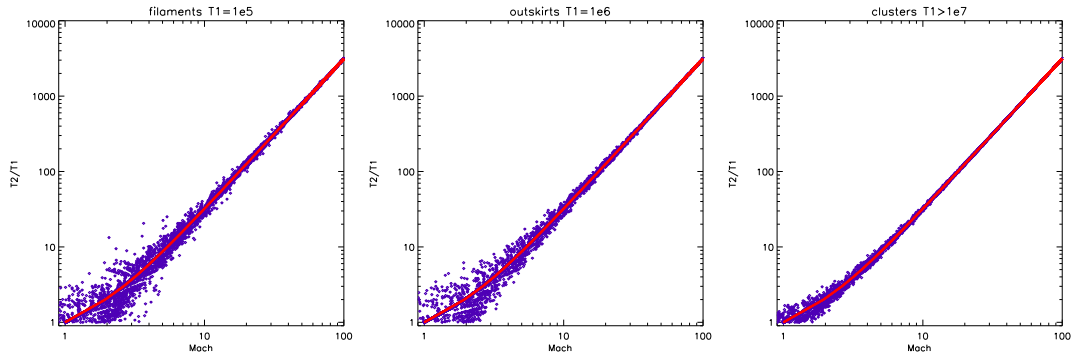

Figure 3.9: Scatter plots for the measured Mach numbers for three Monte Carlo extracted populations of shocked cells, with known pre-shock temperature. Temperature fluctuations are extracted from the corresponding distributions in Fig.3.8. The red curves give the exact solution of Eq.3.4.

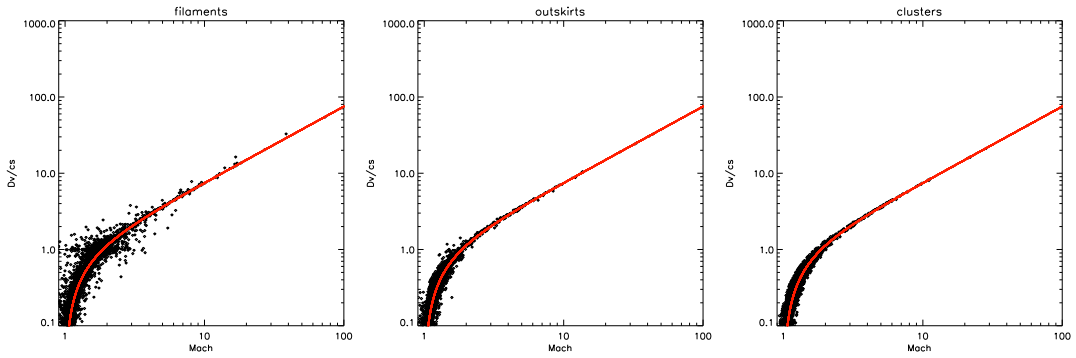

Figure 3.10: Scatter plots of the measured Mach numbers for three Monte Carlo extracted populations of shocked cells, with known pre-shock velocities. Velocity fluctuations are extracted from the corresponding distributions in Fig.3.8. The red curves give the solution of Eq.3.7.

with the same notation used in Eqs.3.3–3.5. In the ideal case in which the pre-shocked medium is at rest and in thermal and pressure equilibrium, the passage of a shock with velocity v_s leaves a clear in-print as a velocity difference, Δv, between the shocked and pre–shocked cells. The relationship between Δv and Mach number in the case of hydrodynamical shocks can be obtained by combining Eq.3.6 with Eq.3.3 and by transforming the velocities from the shock frame to the Lab frame :

$$\Delta v = \frac{3}{4} v_s \frac{1 - M^2}{M^2}. \tag{3.7}$$

where $v_s = M c_s$ and c_s is the sound velocity computed in the pre–shocked cell. The procedure we adopt to reconstruct Mach numbers is the following :

- we consider candidate shocked cells those with $\nabla \cdot \mathrm{v} < 0$ (calculated as 3–dimensional velocity divergence to avoid confusion with spurious 1–dimensional compressions that may happen in very rarefied environments);

- since shocks in the simulation are typically spread over a few cells, as in the case of the TJ method, we define the shock center with the position of the cell in the shocked region with the minimum value of 3–D divergence;

- we scan the three Cartesian axes with a one–dimensional procedure measuring the velocity jump, $\Delta v_{x,y,z}$, between a few cells across the shock center. In the case the shock-jump is assumed to happen in 1 cell $\Delta v_{x,y,z}$ is calculated between the shock center and the pre-shocked cell, while in the case that the jump is spread over 2, 4, 6, ... 2 n cells $\Delta v_{x,y,z}$ is calculated between two cells at distance n (in opposite direction) from the center of the shock;

- the Mach number of the shock is given by Eq.3.7, where the sound speed is that of the pre-shock region (the cell with the minimum temperature);

- we finally assign to shocked cells a Mach number $M = (M_x^2 + M_y^2 + M_z^2)^{1/2}$, that minimizes projection effects in the case of diagonal shocks, and consider only shocked cells with $M > 1$.

In the following we refer to this procedure as the velocity jump (VJ) method.

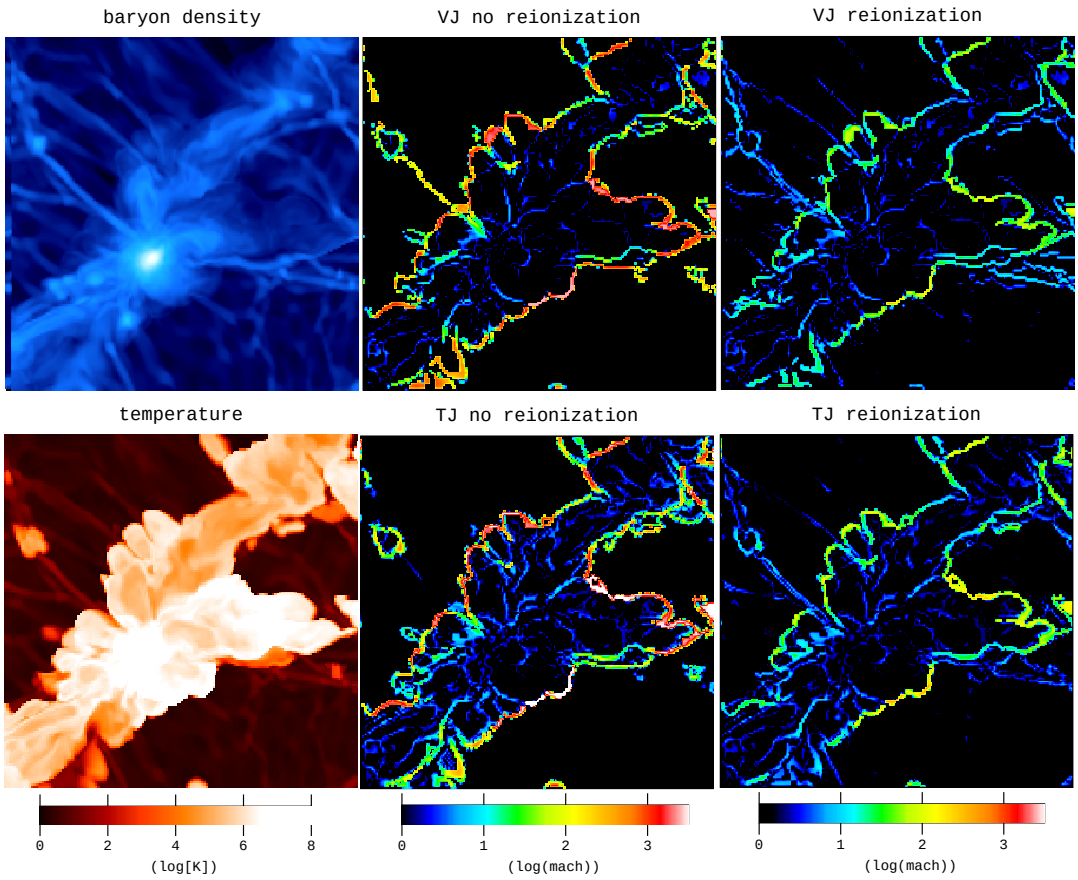

Figure 3.11: Cuts through the center of a $M_{tot} \sim 10^{14} M_{\odot}$ galaxy cluster within a region of $20 Mpc$ and $125 kpc$ of cell resolution (the line of sight width is one cell). Left columns show the baryon density and baryon temperature (for the $CO125$ run); the central and the right column show the maps of Mach number according to the VJ scheme (upper panels) and to the TJ scheme (lower panels). Shocks are shown both in the case of no-reionization ($AD125$) and for the case of reionization ($CO125$).

3.6 Uncertainties in Shock Detecting Schemes

In this Section we discuss the uncertainties of the methods presented in the previous Section, discuss the effect of the re-ionization on the characterization of cosmological shocks and compare results from the VJ and TJ approaches.

3.6.1 Reconstruction of the shock discontinuity

Although the shock discontinuity in ENZO is found to be well reconstructed within 2-4 cells (e.g., Tasker et al. 2008), the risk that comes from the application of procedures based on cell-to-cell jumps (or jumps between several cells) is to underestimate the value of the Mach number of the shock. We performed several shock–tube tests with ENZO with the same numerical setup used in the cosmological simulations, in order to evaluate the convergence of the measure of the shock Mach number with the number of cells used to calculate the jump (Fig.3.12). We find that a reasonable convergence, within 10-40% for Mach ≤ 10, is already obtained with the VJ method in the case that the velocity jump is evaluated across three cells ($n = 1$, where n is the distance between the shock center and the pre or post-shock cells, Sects. 5.2-5.3), and that convergence is reached for $n \leq 2$. On the other hand, the velocity pattern in cosmological simulations is complex and the risk of procedures based on jumps evaluated with large n in these simulations is to mix together signals produced by different shocks, and also to be also affected by gradients in thermodynamical variables that are due to clumps of baryonic matter. In Fig, 3.13 we show maps of Mach numbers obtained with the VJ method in the case of a galaxy cluster taken from the AD125 simulation by assuming a cell-to-cell (two cells) velocity jump, and $n = 1$, 2 and 4 jumps. It is clear that for $n \geq 2$ (jumps based on $\geq$5 cells, $\geq$625 kpc) different shock-patterns start to be mixed together and shocks become poorly characterized.

Similar results are found in the case of the TJ method, thus we conclude that reconstructing the shock discontinuities in our numerical simulations with $n = 1$ (jumps based on 3 cells) provides the best compromise. In Sect.3.7.1 we also show the effect of adopting different values of n on the Mach number statistics.

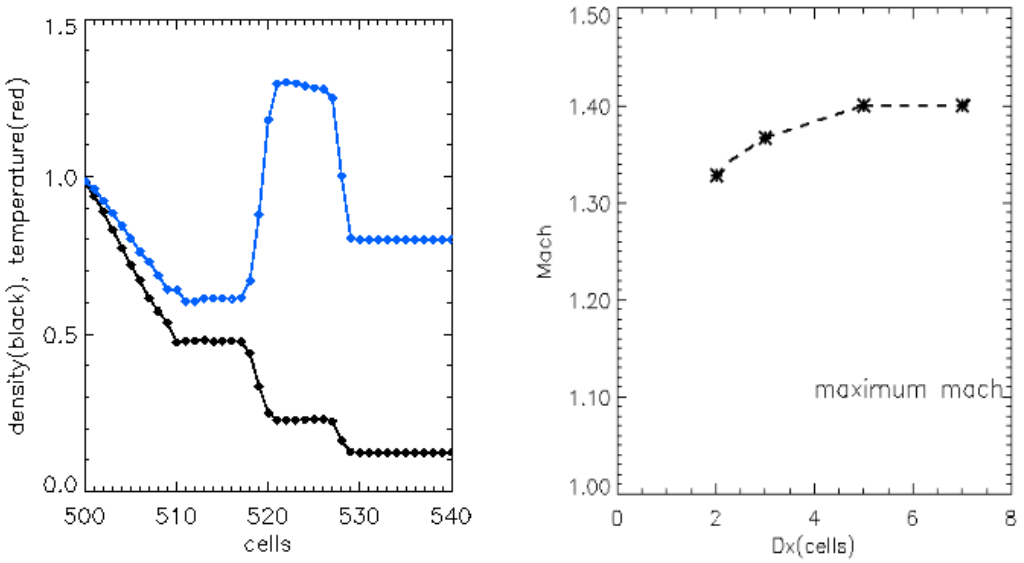

Figure 3.12: *Left:* profile of gas density (black) and gas temperature (blue) for a standard shock tube test on a 1024 grid. *Right:* measured Mach number according to the VJ method, as a function of the number of cells used to evaluate the jump.

3.6.2 Uncertainties in the TJ and VJ methods

As already pointed out in Sect.3.5, a major limitation of the analysis of shocks in post processing comes from the fact that the dynamics and thermodynamics of the gas in the simulations is more complex than in the ideal case in which Eqs.3.3–3.5 and 3.7 are derived. In this sub-Section we discuss the uncertainties that come out; for simplicity here we do not include any modeling of re-ionization in our simulated data.

TJ method

The temperature distribution in simulations is very complex and temperature gradients across non–shocked cells are common by–products of the structure formation process. The passage of a shock in a medium with a complex temperature distribution partially smooths out pre-existing gradients in the thermodynamical variables and creates new shock–induced discontinuities.

One possibility to estimate the level of uncertainties in the application of the TJ method is to introduce a passive modification of the post–shock temperature in Eq.3.4 according to the value of a typical cell to cell temperature jumps across non shocked cells, and to compare the resulting Mach number with that from Eq.3.4 in its

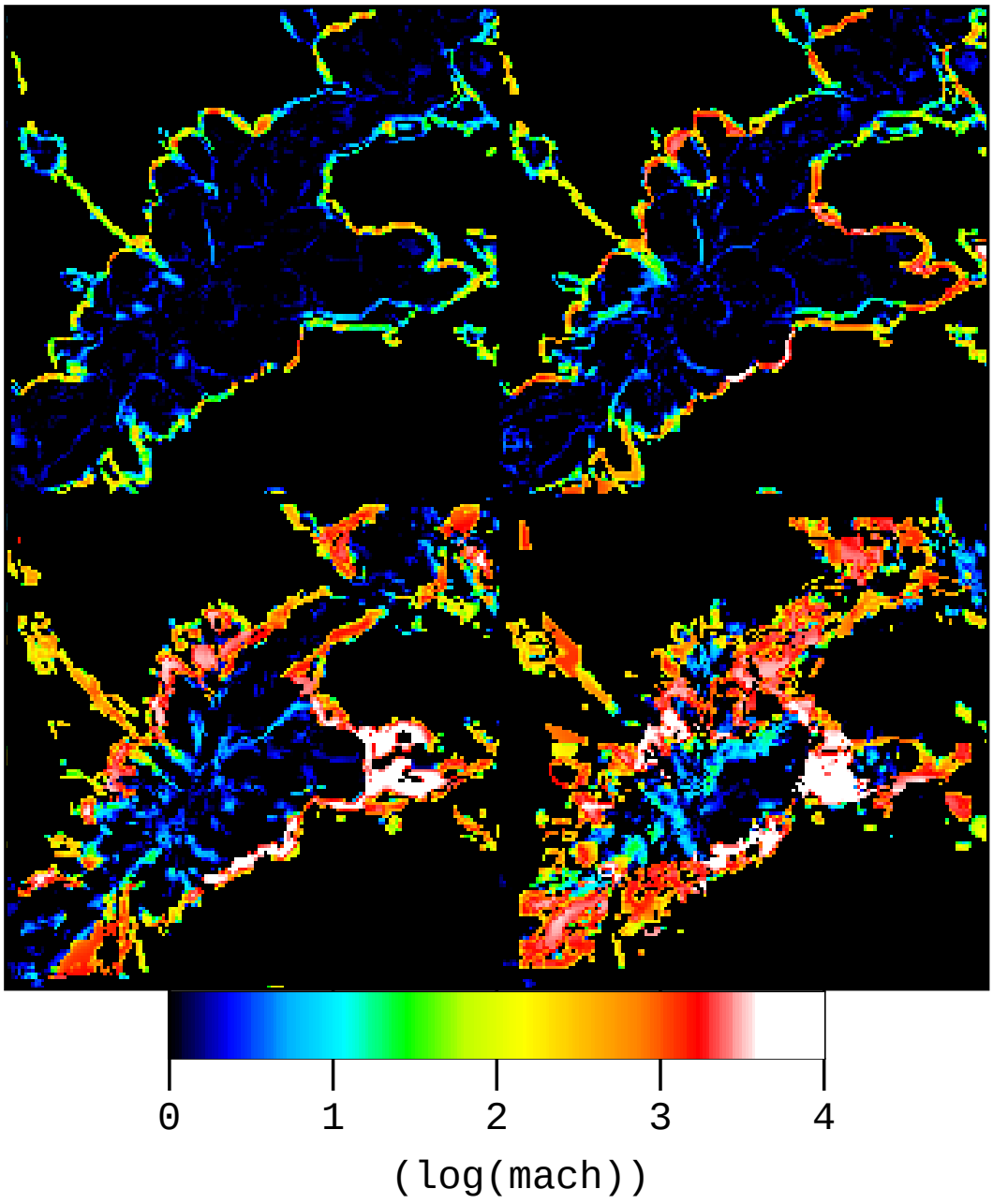

Figure 3.13: Maps of reconstructed Mach numbers using the VJ method based on jumps of 1 cells (upper left), 2 cells (upper right), 4 cells (lower left) and 8 cells (lower right). The side of the image is $20Mpc$ per side, the width along the line of sight is $125kpc$.

original form; obviously this procedure assumes that these jumps are representative of pre-existing temperature gradients, where shocks are presently found, still there is no clear argument for which this unavoidable assumption is not statistically reasonable.

We consider as non–shocked cells those that do not satisfy, at the same time, the TJ and VJ criteria for shocked cells, and extract the values of their cell to cell temperature jumps, δT, in different cosmic environments from the *AD125* simulation at $z = 0$. To follow a very conservative procedure we consider only temperature jumps across a sub–sample of non shocked cells that are at least two cells far away from any post shock cells or shock centers.

We characterize the cosmic environment by means of the total matter density in cells :

- $0.01 \leq \rho_{tot}/\rho_{cr} < 3$: voids and under dense regions,
- $3 \leq \rho_{tot}/\rho_{cr} < 30$: filaments and sheets,
- $30 \leq \rho_{tot}/\rho_{cr} < 50$: cluster outskirts,
- $\rho_{tot}/\rho_{cr} \geq 50$: galaxy clusters.

where $\rho_{tot} = \rho + \rho_{dm}$ is the total matter density and ρ_{cr} is the critical density of the universe. These are expected to mark the different kind of structures of the cosmic web (e.g. Dolag et al.2006; Shen et al.2006).

In Fig.3.8 we plot the differential distribution of (the module of) temperature jumps across the considered sub-sample of non–shocked cells, δT, normalized to a reference value of the local temperature, $\sqrt{T_2 \cdot T_1}$, for the different density regimes. The peak of the distribution is found at $\delta T/\sqrt{T_2 \cdot T_1} \approx 0.5$. In the case of filaments and voids the distributions extend at larger values, although large temperature scatters, $\delta T/\sqrt{T_2 \cdot T_1} \approx 10$, are extremely rare in the case of filaments and are found for only a few percent of the cells in the voids.

For the values of T_1 representative of clusters, outskirts and filaments in our simulation, we allow T_2 to vary and run Monte Carlo extractions of δT extracted across non–shocked cells with temperature T_2 in the same environment. We then compared the estimate of the shock Mach number via Eq.3.4 with that obtained through:

$$\frac{T_2 \pm |\delta T|}{T_1} = \frac{(5M^2-1)(M^2+3)}{16M^2}, \tag{3.8}$$

Figure 3.9 shows the typical scatter introduced in the T_2/T_1 vs M plane by the presence of realistic (i.e. measured in non–shocked cells in our simulations) pre–shock fluctuations in the temperature, for different cosmic environments. The red line shows the ideal case: given a ratio T_2/T_1 the degree of uncertainty on M due to the presence of pre–shock fluctuations in the simulation can be grossly evaluated by an horizontal cut across the distribution of the data points. This scatter increases as the Mach number decreases and, at a given Mach number, it is typically smaller in environments with larger over density.

VJ method

Complex velocity fields arise naturally during the formation of virialised structures in simulations (Bryan & Norman 1998, Sunyaev; Norman & Bryan 2003; Dolag et al. 2005; Vazza et al. 2006; Iapichino & Niemeyer 2008; see also Chap.5 of this Thesis) that however are expected to be smaller than the velocity jumps driven by the passage of a shock across the same regions. A more complex situation is that of non virialised structures where laminar flows may produce relatively strong velocity gradients across the cells. An example is given in Fig. 3.8, where we report the differential distributions of the velocity gradients, δv, normalized to the maximum value of the sound speed in each pair of cells, obtained for the same sub-sample of non-shocked cells considered in the previous sub-Section. The distributions peak at $\delta v/c_s \approx 0.5$, although tails extending towards larger values are found in the distributions of voids and filaments. These tails are mostly due to velocity gradients measured across accelerated laminar flows (where the kinetic energy of the gas may become even larger than the thermal energy) that move from low to higher density regions and are present in a small fraction of the volume of filaments and voids.

In order to grossly estimate the strength of the uncertainties in the case of clusters, outskirts and filaments, we follow a procedure similar to that in Sect.3.6.2. For these different environments we fixed a value of $\Delta v/c_s$, run a Monte Carlo extraction of $\delta v/c_s$ from non shocked cells in the simulations (Fig.3.8) and for each trial calculated the Mach number from :

$$\Delta v \pm |\delta v| = \frac{3}{4} \cdot \frac{1 - M^2}{M} c_s \left(1 \pm \frac{\delta c_s}{c_s}\right), \tag{3.9}$$

That accounts for both pre-shock gradients in the velocity and in the sound speed across non shocked cells. Gradients in c_s are driven by gradients in the temperature distribution of the cells and are evaluated by a Montecarlo extraction of the temperature variations in Fig. 3.8.

In Fig.3.10 we report $\Delta v/c_s$ vs M from our Monte Carlo extraction compared to the calculations in the *ideal case* (Eq.3.7). This result should be compared with that in Fig.3.9, that refers to the TJ method, and the degree of uncertainty on M can be grossly evaluated by an horizontal cut across the distribution of the data points. As expected, in the case of clusters and outskirts the scatter in the two cases is quite similar, although in the case of weak–moderate shocks crossing filaments and outskirts the scatter is less pronounced than that of the TJ method (Fig.3.9).

3.6.3 Modeling the re-ionization.

The role of reionization is of primary importance to study the properties of shocks outside galaxy clusters. In these environments, any additional source of heating (such as reionizing radiation from AGN and/or massive stars feedback) may cause a dramatic increase of the local temperature and sound speed. Thus the temperature distribution across cells in these regions is strongly affected by the modeling of the re-ionization in the simulations, implying an additional uncertainty in the characterization of shocks. This is expected to be particularly relevant in all shock detecting schemes where temperature plays a role.

Therefore before discussing shocks properties in our simulations, we highlight the main effects of cosmic re-ionization on shocks

Fig.3.11 shows the maps of the detected shocks in a $20Mpc$ cubic region extracted from the *AD125* simulation and centered on a $M_{tot} \sim 10^{14} M_{\odot}$ cluster. Results are reported, by calculating shock-jumps in three cells (n=1), in the case of no re-ionization and of a Haardt & Madau (1996) re-ionization scheme. As expected the Mach number of shocks decreases in simulations with re-ionization due to the increase of the sound speed produced by the re-ionization background. This effect is stronger in the cold outermost regions, while the properties of cosmological shocks in galaxy clusters are not affected by the re-ionization background. Re-ionization

also allows to better describe shocks around filamentary structures in low density regions that are not seen in the case of simulations without re-ionization (Fig.3.11). This is because without re-ionization these regions have temperature so small that the temperature floor is artificially put at $1K$ (in the outputting of data) by ENZO¿

In Fig.3.14 we report the kinetic energy flux through shocked cells in the same volume as calculated by means of the VJ method. The kinetic energy flux, $E_{kin} = \rho v_s^3/2$, is reported for different numerical modeling of the re-ionization: three different temperature floors (10^5K, 10^4K and 10^2K), Haardt & Madau (1999) model, and no re-ionization. We find that a fixed temperature floors, which is customary used in several papers to mimic the effect of re-ionization (e.g. Ryu et al. 2003), produces some *artificial* piling up or flattening in the distributions of the energy flux through shocks at large Mach numbers. This is because the temperature background, T_{floor}, changes artificially the speed of the sound in environments with lower temperature and the Mach number of shocks in these environments is affected by T_{floor}, decreasing artificially with increasing T_{floor}. This further supports the requirement of a physically meaningful treatment of re-ionization in a post processing procedure; as already discussed, the post processing fitting procedure described in Sect.3.4 closely resembles the effect of the physically based Haardt & Madau (1999) re-ionization scheme.

3.6.4 Basic Comparison between VJ and TJ methods

In this Section we briefly compare the results obtained from the VJ and TJ approaches, focusing on results obtained with our fiducial numerical treatment of the re-ionization.

In the ideal case the two approaches must select the same population of shocked cells. In reality we find that, when shock-jumps are calculated across 3 cells, about 85 per cent of the shocked cells in our adiabatic simulations are selected at the same time by the conditions in the VJ and TJ approaches. In the case of clusters and cluster outskirts the two approaches select the same population of shocked cells, while these differences typically arise from shocks in low temperature regions.

In the case of clusters and outskirts the velocity and temperature variations across non shocked cells are relatively small (Fig. 3.8) and this allows constraining the Mach number of shocks by means of both the TJ and VJ approach. Still the

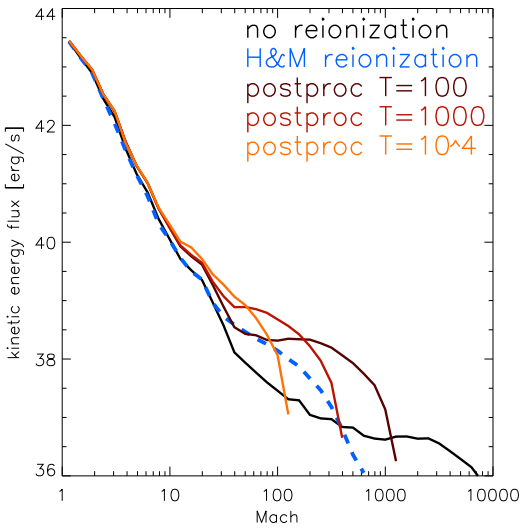

Figure 3.14: Distribution of kinetic energy flux in shocks according to the VJ method, for a cubic volume of side $40Mpc$ and resolution $125kpc$. Fig.3.11. Curves are drawn for the case without reionization (*black solid*), for the Haardt & Madau (1999) reionization scheme applied in post-processing (*blue dashed*) and for different choices of a fixed T_{floor} temperature floor (color coding is labeled in the panel).

statistical uncertainties for weak shocks with the TJ method are expected to be slightly larger than those with the VJ (Figs.3.9 & 3.10).

A comparison between the statistical description of the properties of the shocks obtained with VJ and TJ approaches is shown in Fig.3.15 (top panels), that reports the Mach number distribution of shocks in the *AD250* run (with post-processing re-ionization) and in the *CO250* run. Statistically the results from the two methods are fairly similar in the case of clusters and cluster outskirts, and no remarkable differences are found also in the case of filaments and voids. This suggests the important point that the characterization of shocks in these environments is statistically solid, as two independent approaches lead to basically similar results. Importantly we also notice that the results are similar in the case of AD250 and in the case of CO250, addressing that our post-processing heating model is viable. Larger difference between VJ and TJ methods come out in the lower panels of Fig.3.15, which show the scatter plots for the measured Mach numbers.

In the next Sections we shall use the VJ method to study shocks properties. This is because we believe that the VJ approach is less affected by uncertainties in the case of weak–moderate shocks, especially in lower density regions (e.g., Figs. 3.9-3.10).

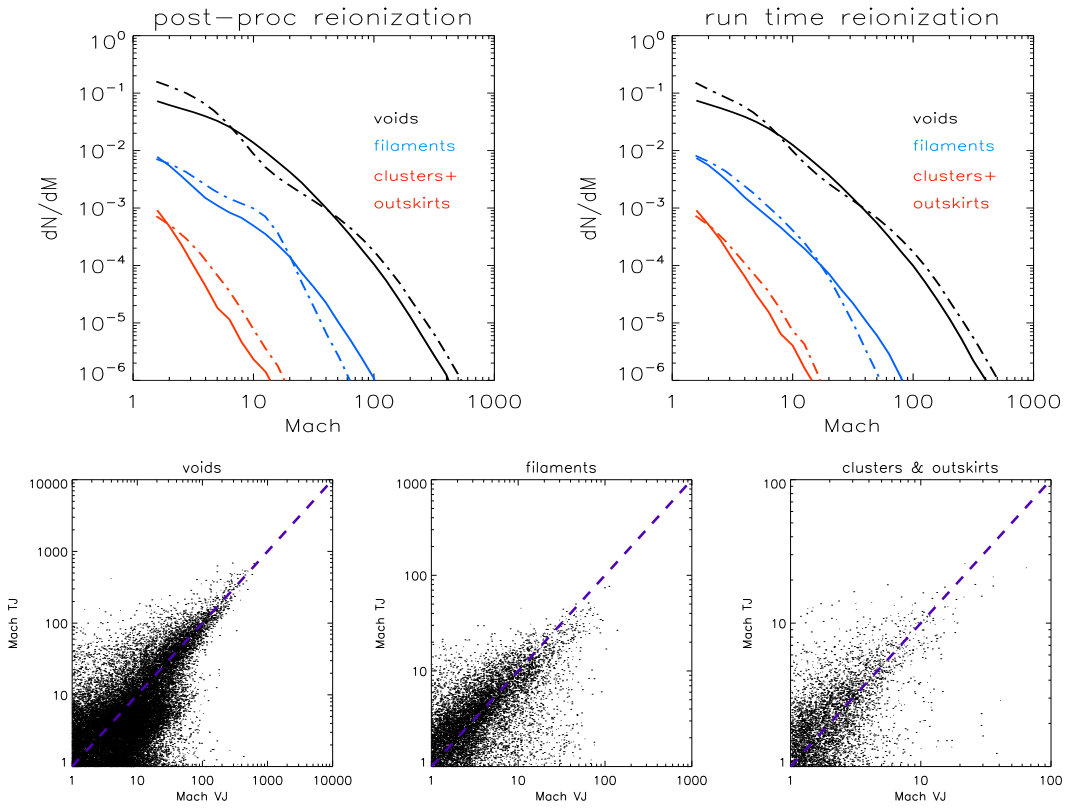

Figure 3.15: Distributions of shock Mach numbers at different cosmic environments, for a $(80Mpc)^3$ volume of the $AD125$ run with post-processing reionization (left) and for the $CO125$ run (right), with the VJ method (*solid lines*) and with the TJ method (*dot-dashed lines*).*Lower panels:* distribution of the Mach number as measured with the TJ and the VJ method for the shocked cells of the $C125$ run, for different cosmic environments.

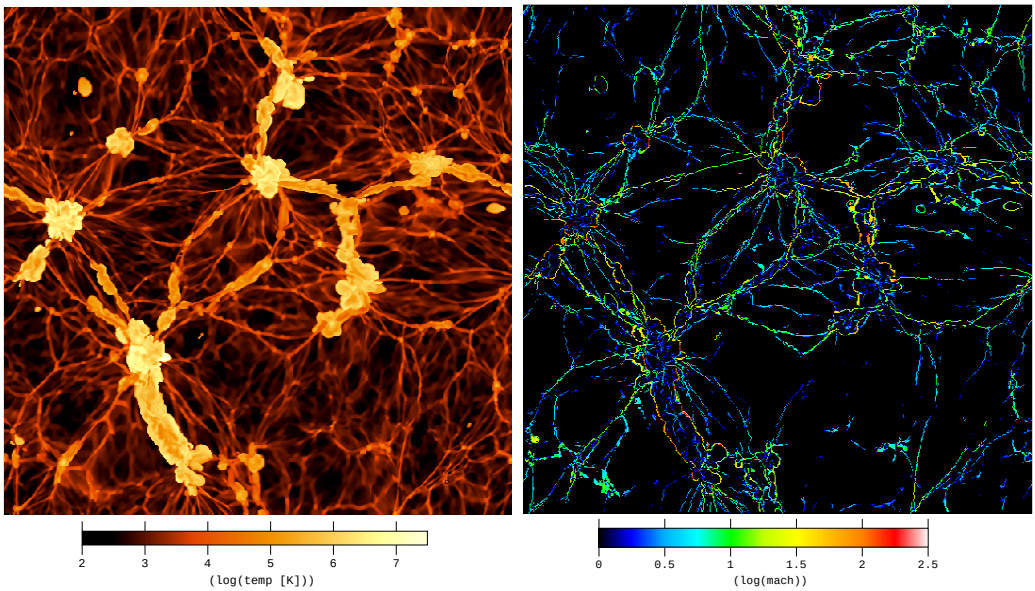

Figure 3.16: 2–dimensional slices for a box of side $80Mpc$ from the *AD125* run with post-processing reionization: gas temperature (*left*) and Mach number measured with the VJ method (*lower right*). The width along the line of sight is $125kpc$.

3.7 RESULTS

In this Section we present the main results obtained for the full set of simulations by making use of the VJ method with shock-jumps calculated across three cells ($n = 1$ unless specified).

3.7.1 Detected shocks and Maps.

Shocks fill the simulated volume in a very complex way (e.g. Miniati et al.2001, Ryu et al.2003). In Fig.3.16 we show a 125 kpc cut of a cubic region of side 80Mpc from the *AD125* run at z=0 with post-processing reionization, showing gas temperature and shocks with Mach numbers reported in color code.

We find that $\sim 10 - 20$ per cent of the cells in the simulated volume host shocks at present epoch, with the percentage of shocked cells increasing in denser environments. Filamentary and sheet–like shocks pattern are usually hosted in low density regions and at the interface of filaments, following the shape of the Cosmic Web. This kind of shocks follows the first infall of baryonic matter onto accreting structures, and generates an abrupt increase in temperature due to the jump from a re-ionization dominated temperature to the gravitationally dominated one. They

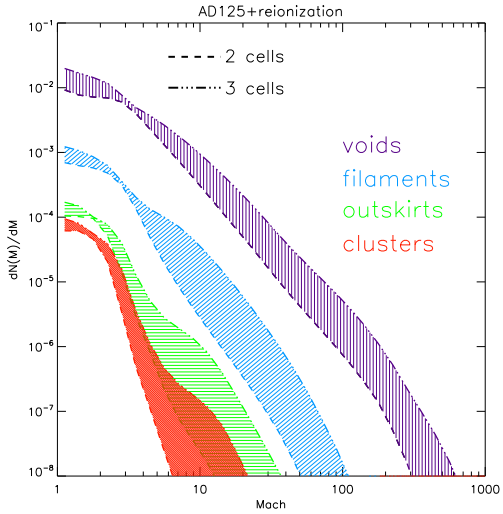

Figure 3.17: Distribution of shocks Mach number for the whole simulated volume of the $AD125$ with post-processing reionization, for different cosmic environments. Dot–dashed lines show the distributions obtained with velocity jumps evaluated across three cells ($n = 1$), while dashed lines shows distributions obtained with cell–to–cell velocity jumps ($n = 0$).

are commonly defined as *"external shocks"* (Miniati et al.2001), and they are the strongest within the simulation, with M$> 10 - 100$. Shocks surrounding galaxy clusters form spherically shaped boundaries at a typical distance of $approx 2R_{vir}$ from the cluster center, while shocks moving inwards the virializing region are found more irregular and weak, with $M < 3$. These shocks is commonly defined as *"internal shocks"* (Miniati et al.2001). Slightly stronger shocks (i.e. $M \sim 3$) inside R_{vir} are episodically found in merging clusters. In this case the violent relaxation due to the fluctuation of the gravitational potential may cause infall of the pre–shocked gas onto the shock discontinuity increasing the Mach number (Springel & Farrar 2007); other strong shocks are the reverse shocks that propagate trough the innermost regions of accreting and cold sub clumps, which keep themselves at the pre–shock virial temperature for several Gyrs during their orbiting around the main cluster (Tormen, Moscardini & Yoshida 2004).

An issue which is still poorly addressed in the literature is the distribution function of shocks with their Mach number; this is reported for our total $145 Mpc$ cubic volume at $z = 0$ in Fig.3.17.

Fig.3.17 also shows the effect of using three cells ($n = 1$) or cell-to-cell velocity jumps to reconstruct the Mach number of shocks. The number of stronger shocks,

that are well reconstructed within 3–4 cells, increases with $n = 1$ producing a flattening of the differential distribution of shocks. As shown in Section 3.5.3, using a larger number of cells to reconstruct the Mach number does not improve the characterization of shocks, yet the risk is to mix different shock patterns and substructures in the simulations.

The overall differential distribution of shocks with their Mach number in the cosmic volume is very steep, with $\alpha \sim -2.6$ (with $dN/dM \propto M^{\alpha}$), and the bulk of the detected shocks at any Mach number is found in the low density regions, which fill the majority of the volume in the simulations; the Mach number distribution becomes increasingly steeper moving towards dense environments: $\alpha \approx -4$ to -5 is found in clusters and their outskirts.

Fig.3.18 the time evolution of the differential Mach number distribution is given for the $CO125$ simulation, that has a suitable time–sampling in the analysis of outputs. We find that before the epoch of re-ionization, $z > 6$, roughly 30% of the simulated volume is shocked. Then, as soon as reionization plays a role, the temperature of the simulated volume increases and the Mach number distribution of shocks at redshift $z \sim 3-6$ undergoes a dramatic change becoming very steep and dominated by weak shocks. With decreasing redshifts, temperature in low density regions gradually decreases and the Mach number distribution becomes gradually flatter with the fraction of shocked cells reaching ~ 15 per cent at present epoch.

3.7.2 Energy Flux and thermalised energy

The energy flux converted into thermal energy of the gas at a shock is given by the Rankine–Hugoniot jumps conditions, which relate the flux of the kinetic energy crossing the shock, E_{kin}, and the resulting thermal flux in the post–shock region, f_{th}. This relation can be expressed by means of a simple $\delta(M)$ parameter (e.g. Ryu et al.2003):

$$\delta(M) = f_{th}/f_{\phi} = v_2 \left[\frac{E_{th,2}}{E_{kin,1}} - \left(\frac{\rho_2}{\rho_1} \right)^{\Gamma} \right] \tag{3.10}$$

where $E_{th,1}$ and $E_{th,2}$ are the thermal energies in the pre– and post–shock regions, $E_{kin,1}$ is the kinetic energy of the shock, and Γ is the adiabatic exponent ($\Gamma = 5/3$). It is useful to express $\delta(M)$ by means of the Mach number (e.g. Kang et al.2007):

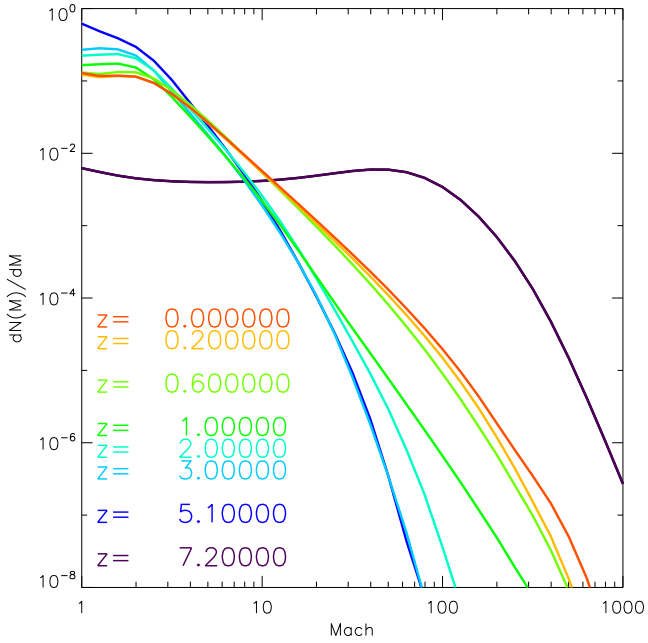

Figure 3.18: Time evolution of the Mach number distribution for the $CO125$ run, from $z = 7.2$ to $z = 0.0$. Only a sub sample of redshifts is drawn for clarity.

$$\delta(M) = \frac{2}{\Gamma(\Gamma-1)M^2 R}\left[\frac{2\Gamma M^2 - \Gamma + 1}{\Gamma + 1} - R^{\Gamma}\right] \tag{3.11}$$

where R is the density compression factor:

$$R = \frac{\rho_2}{\rho_1} = \frac{\Gamma + 1}{\Gamma - 1 + 2/M^2} \tag{3.12}$$

We notice that Eq.3.10 strictly holds only in case of a negligible CR energy density, otherwise the feedback of these CR on the shock itself is expected to severely decrease the efficiency of thermalisation of the kinetic energy flux (see next Section).

Fig.3.19 (Right panel) shows a 2–dimensional cut, with depth=125 kpc, of the measured thermal energy flux in shocked cells, at the present epoch and for a region centered around two massive ($M \sim 4 \cdot 10^{14} M_{\odot}$ and $M \sim 10^{15} M_{\odot}$) galaxy clusters. These clusters belong to a large scale filament (see Left panel of Fig.3.19), for which we provide also a 3–dimensional rendering of the thermal energy flux through shocks (Left panel of Fig.3.20).We generated 3–dimensional distribution of data by means of the visualization tool VISIVO (Comparato et al.2007, http://visivo.cineca.it).

The differential distribution of the thermal energy flux at shocks as a function

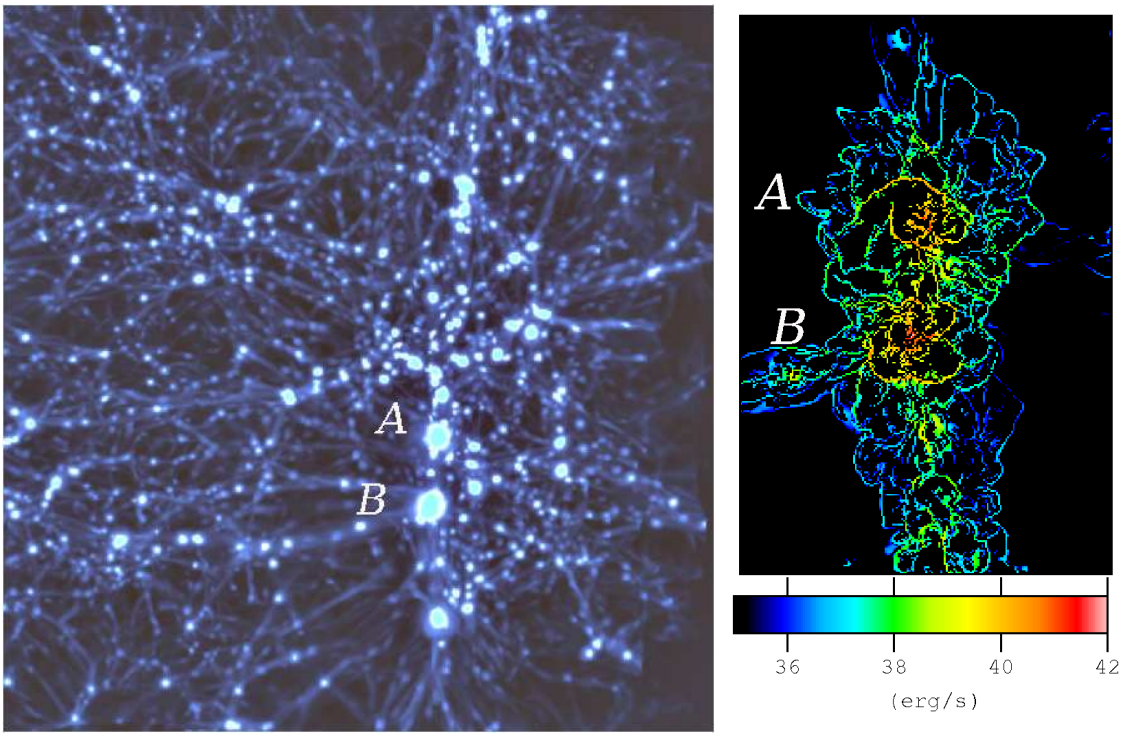

Figure 3.19: *Left:*3–D rendering of baryon density for a cubic region of side $80Mpc$, for the *CO125* re-simulation at $z = 0$. Color coding goes from *dark blue* ($\rho \sim 10^{-31} gr/cm^3$) to *pale blue* ($\rho > 10^{-29} gr/cm^3$). *Right:* thermalised energy flux through shocks, for a slice of depth $125kpc$ and centered to encompass the two massive merging clusters shown in the left panel the letters in the panel show the approximate positions of the two massive clusters.

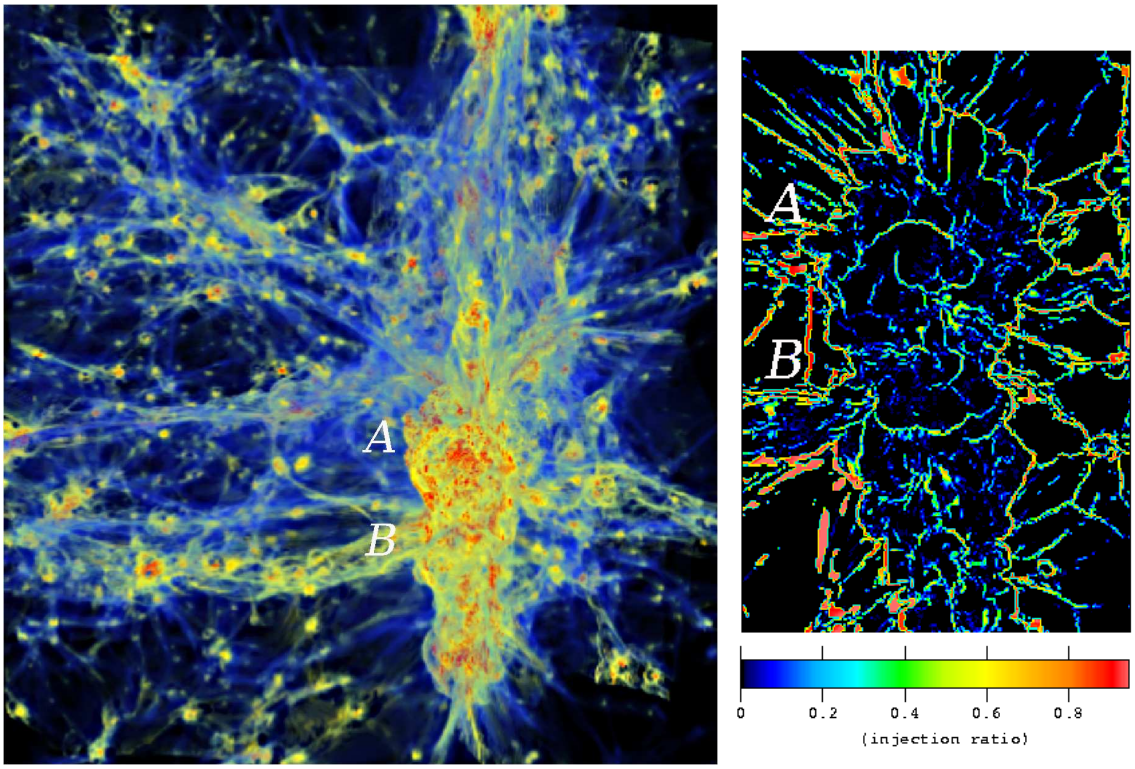

Figure 3.20: *Left:*3–D rendering of the dissipated energy flux for the same region as in Fig.3.19. Color coding goes from *blue* ($f_{th} \sim 10^{33} erg/s$) to *yellow* ($f_{th} \sim 10^{38} erg/s$) to *red* ($f_{th} > 10^{41} erg/s$). *Right:* energy ratio between injected CR energy flux and thermal energy flux in shock waves, for the same slice of right panel of Fig.3.19.

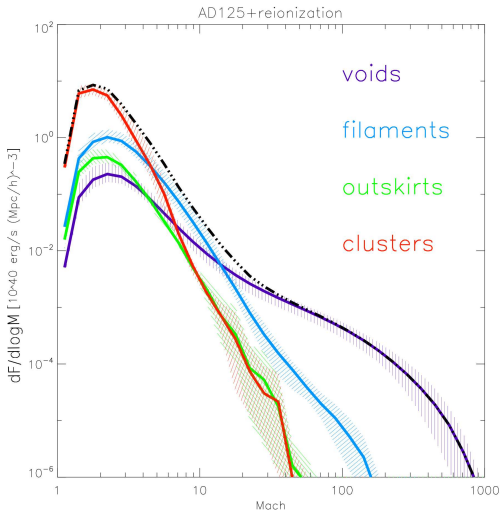

Figure 3.21: Distribution of the thermalised energy flux at different over density bins, for the whole *AD125* and normalized to a comoving volume of $(1 Mpc/h)^3$. The shadowed regions show the cosmic variance within our sample of simulations, while the dot-dash line shows the global average within the sample.

of their Mach number is reported in Fig.3.21. Solid lines give average values, while dashed shadows give the variance spanned by the six different $80Mpc$ cubic sub samples of the AD125 simulation. This variance is fairly small, ~ 30 per cent at the peak, although it increases for the stronger shocks that are rare.

We find that the total processed thermal energy across cosmological shocks in our simulations is $f_{th} \approx 4 \cdot 10^{47} ergs/s$ at the present epoch. This is of the same order of magnitude of the value of the total processed thermal energy found by Ryu et al.(2003) and by Pfrommer et al.(2006), for the same ≈145 Mpc cubic volume. However, as discussed in Sect.3.3.2, the deficit in massive halos in our clusters sample may cause the level of thermalised energy flux in the volume to be slightly smaller.

For Mach numbers ≤20-30 (i.e. those that provide about the 99 percent of the total thermal flux in the simulated volume) the distribution in Fig.3.21 has $\alpha_{th} \approx -2.7$ (with $f_{th}(M)M \propto M^{\alpha_{th}}$). It is steeper than that in Ryu et al.(2003), $\alpha_{th} \approx -2$, while is consistent with that in Pfrommer et al. (2006), $\alpha_{th} \approx -2.5$.

We find that ≈ 70 per cent of the total thermal energy flux dissipated at shocks comes from the virial region of galaxy clusters (because of their large matter density) and that the bulk of the thermalisation happens at shocks with $M \approx 2$ (Fig.3.21). These relatively weak shocks are also responsible for the bulk of the thermalisation in lower density environments, although stronger shocks may provide a sizable contribution in these regions.

The time evolution of the distribution of the thermal energy dissipated at shocks as a function of the shock-Mach number is an important issue. As a relevant example we report in Left panel of Fig.3.22 the distribution of thermal energy flux obtained for the same volume of Fig. 3.18. The evolution of the distributions follows a behavior with cosmic time which is similar to that for the number distribution of shocks, with strong shocks becoming more frequent at evolved times when the energy density of the background becomes lower (see also Pfrommer et al. 2006). The integrated (over cosmic time) thermal energy dissipated at shocks in our $(145\text{Mpc})^3$ volume is $E_{TH} \approx 2 \cdot 10^{64} ergs$ (see Fig.3.22, Right panel), which is consistent with the values reported in Pfrommer et al. (2006) and Ryu et al.(2003), also by taking into account the deficit in the halos mass in our simulations (Sect.3.3.2).

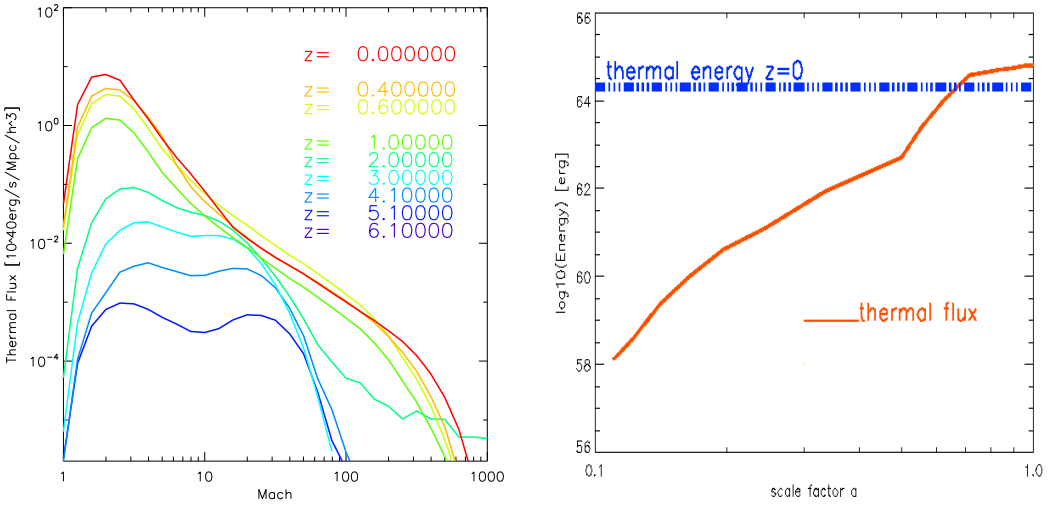

Figure 3.22: *Left:*time evolution of the distribution of thermal energy flux from shocks for the same volume as in Fig.3.18, from $z = 6.1$ to $z = 0.0$. Only a sub sample of redshifts is drawn for clarity.*Right:* integrated thermal energy flux (*red line*) through shocks from $z = 9.2$ to $z = 0$, for the same box as in Fig.3.22. The horizontal blue straight line is the level of the total thermal energy measured for the whole box at final redshift.

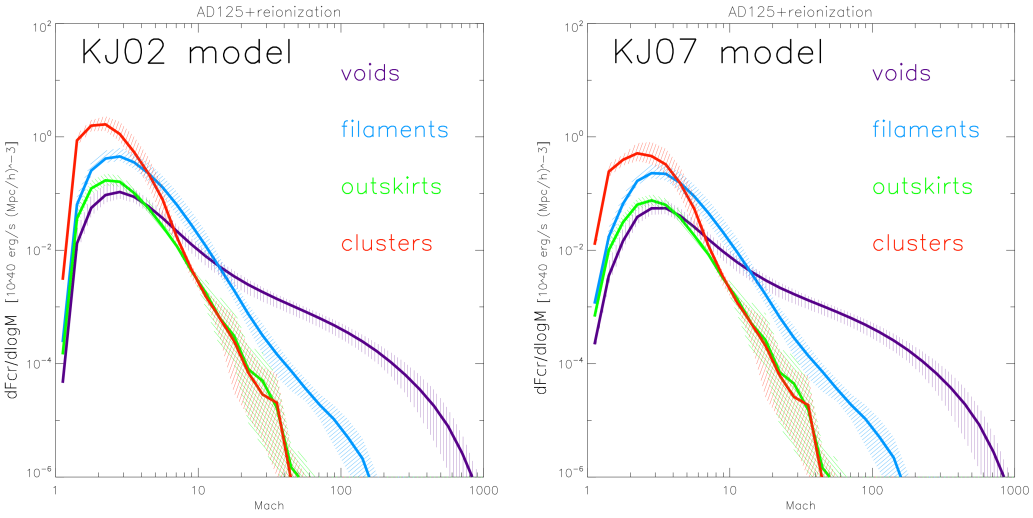

Figure 3.23: Distribution of the injected CR flux at different over density bins, for the whole *AD*125 run with post-processing reionization. *Left* panel shows the measured distribution according to a KJ02 recipe for the CR injection, while *right* panel is for the case of a KJ07 recipe.

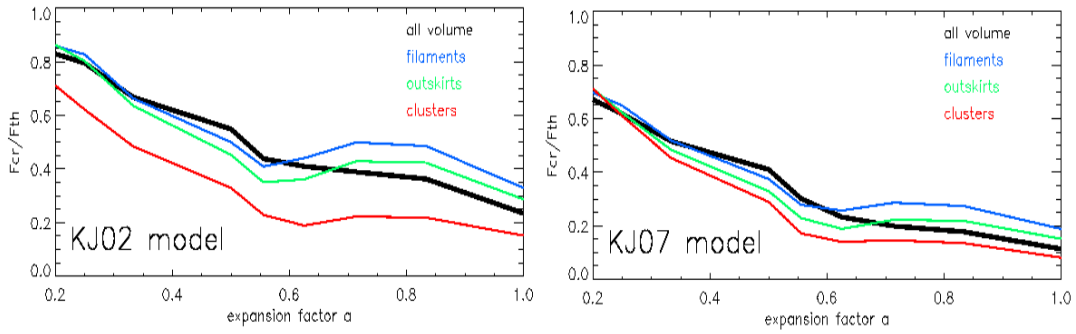

Figure 3.24: Evolution with time of the total injection ratio f_{CR}/f_{TH} for the same sub sample as in Fig.3.22 and in different environments. The upper panel is for the acceleration model outlined in Kang & Jones (2002), while the lower panel is for the acceleration model of Kang & Jones (2007).

3.7.3 Acceleration of Cosmic Rays

The injection and acceleration of Cosmic Rays at shocks is a complex process. It is customary to describe the acceleration according to the diffusive shock acceleration (DSA) theory (e.g. Drury & Voelk 1981; Blandford & Ostriker 1978). That applies when particles can be described by a simple diffusion–convection equation across the shock. There is some general agreement on the fact that strong shocks may channel a substantial fraction of their energy flux into the acceleration of CR which in turn should back react modifying the structure of shocks themselves. Recent advances rely on the theory of non linear shock acceleration, which describes the acceleration of CR in shocks whose structure is modified by the back–reaction of CR energy (e.g., Ellison, Baring, Jones 1995; Malkov 1997; Kang, Jones & Gieseler 2002; Blasi 2002, 2004a; Kang & Jones 2005; Amato & Blasi 2006). The most relevant uncertainty in the description of the particle acceleration at these shocks is the injection model, i.e. the probablity that supra-thermal particles at a given velocity can leak upstream across the sub-shock and get injected in the CR population. This is because even a small variation of the injection momentum, p_{inj}, of supra-thermal particles produces a large difference in the estimate of the injection efficiency at shocks (e.g. Blasi 2004b). An other major hidden ingredient is the amplification of the magnetic field (perpendicular component) downstream, that may be due to CR driven instabilities and adiabatic compression, as this magnetic field self–regulates the diffusion process of CR and supra–thermal particles (i.e. the Larmor radius)

regulating the value of p_{inj}.
An additional difficulty which comes out is that a post–processing approach, as that followed in our paper, does not allow us to account for the dynamical contribution of CR accelerated at cosmological shocks[2].

With all these caveats in mind, we follow the approach adopted by Ryu et al.(2003) in which the thermalisation is calculated by means of the standard Eqs.3.10–3.11 and the CR acceleration at shocks is calculated by making use of numerical results of non linear shock acceleration which adopt a numerical description of the *thermal leakage* to model the injection of particles in the population of CR upstream (Kang & Jones 2002, KJ02). These numerical results provide an estimate of the ratio between the energy flux trough a shock and the energy flux which is channeled into CR acceleration at the shock by means of a simple parameter, $\eta(M) = f_{CR}/f_{\phi}$, which depends on the Mach number of that shock.

Fig.3.20 (Right panel) maps the ratio between CR and thermal energy flux and clearly shows the role played by the Mach number in setting the level of the injection of CR in the various environments. Since the ratio $\eta(M)/\delta(M)$ $(= f_{CR}/f_{th})$ increases with the Mach number of the shocks, the highest values of f_{CR}/f_{th} are found in low density regions, at the interface layers of filaments or in the outermost regions of galaxy clusters, where a substantial population of relatively strong shocks is present. On the other hand the lower values are typically found in galaxy clusters, where the Mach number distribution is steep and strong shocks are rare.

The distribution of the energy flux injected in CR as a function of Mach number is reported in Fig.3.23; this refers to the total simulated volume at the present epoch. We find that the bulk of the CR acceleration happens in galaxy clusters, however also filaments are expected to contribute significantly to the acceleration process. The overall distribution has a well defined peak which is anchored at $M \approx 2$ and has a slope (between $M \sim 2 - 20$) $\alpha_{CR} \approx -2$ (with $f_{CR}(M)M \propto M^{\alpha_{CR}}$).

The value of the Mach number at the peak is close to (slightly smaller than) that found by Ryu et al.(2003) ($M \sim 3$), while the distribution is steeper than that reported in Ryu et al.(2003) (where $\alpha_{CR} \approx -1.5$). Since we use an approach equivalent to that in Ryu et al.(2003) to evaluate the CR acceleration, this difference

[2]Attempts to model this dynamical contribution in cosmological simulations have been recently developed (Pfrommer et al. 2006)

is likely due to our different shock detecting scheme, and to the improved modeling of the re-ionization process in our procedure. A comparison with the results in Pfrommer et al.(2006) is more difficult since these authors use a Lagrangian Smoothed Particles Hydrodynamics code which also include CR dynamics and a completely different approach in the calculation of the CR injection at shocks. The overall distribution of the energy flux injected in CR reported in Pfrommer et al.(2006) has a slope $\alpha_{CR} \approx -1.8$ and is actually in between our results and those of Ryu et al. (2003).

For seek of completeness, in Fig.3.23 (Right panel) we also report the overall distribution of the energy flux injected in CR by adopting the injection efficiency of CR at modified shocks by Kang & Jones 2007 (KJ07). These recent calculations account for the Alfvén wave drift and dissipation in the shock precursor yielding a value of $\eta(M)$ which is smaller than that adopted by Ryu et al.(2003) (at least for $M < 20$). As a consequence the resulting distribution of the energy flux dissipated at shocks into CR acceleration with Mach number of shocks (Fig.3.23, right panel) is flatter than that obtained by adopting KJ02 (Fig.3.23, left panel) and ≈ 50 per cent less energy is expected to be channeled into CR acceleration.

Fig.3.24 shows the evolution with time of the ratio f_{CR}/f_{th} for the same volume considered in Figs. 3.18 and 3.22. The value of f_{CR}/f_{th} as measured at the present epoch, $f_{CR}/f_{th} \sim 0.2$, is a factor $\approx$2 smaller than that found in Ryu et al.(2003); by adopting the injection efficiency of CR of KJ07 the ratio f_{CR}/f_{th} is even smaller, about 0.1. Although Fig. 3.24 shows that CR in dense regions do not provide a relevant back-reaction on the thermal pool during their acceleration (this justifies the use of Eqs. 10–12 in these environments), the larger values of f_{CR}/f_{th} in low density regions and at early cosmic times suggest that following (run-time) the dynamics of CR and the (self consistent) non–linear shock thermalisation and CR acceleration is mandatory in future studies with Eulerian–cosmological simulations.

3.7.4 Shocks in Galaxy Clusters.

In this Section we focus on the shock statistics and CR injection in galaxy clusters and briefly discuss their dependence on the cluster dynamics. We study shocks in four representative massive galaxy clusters extracted from the *AD125* simulation, at $z = 0$:

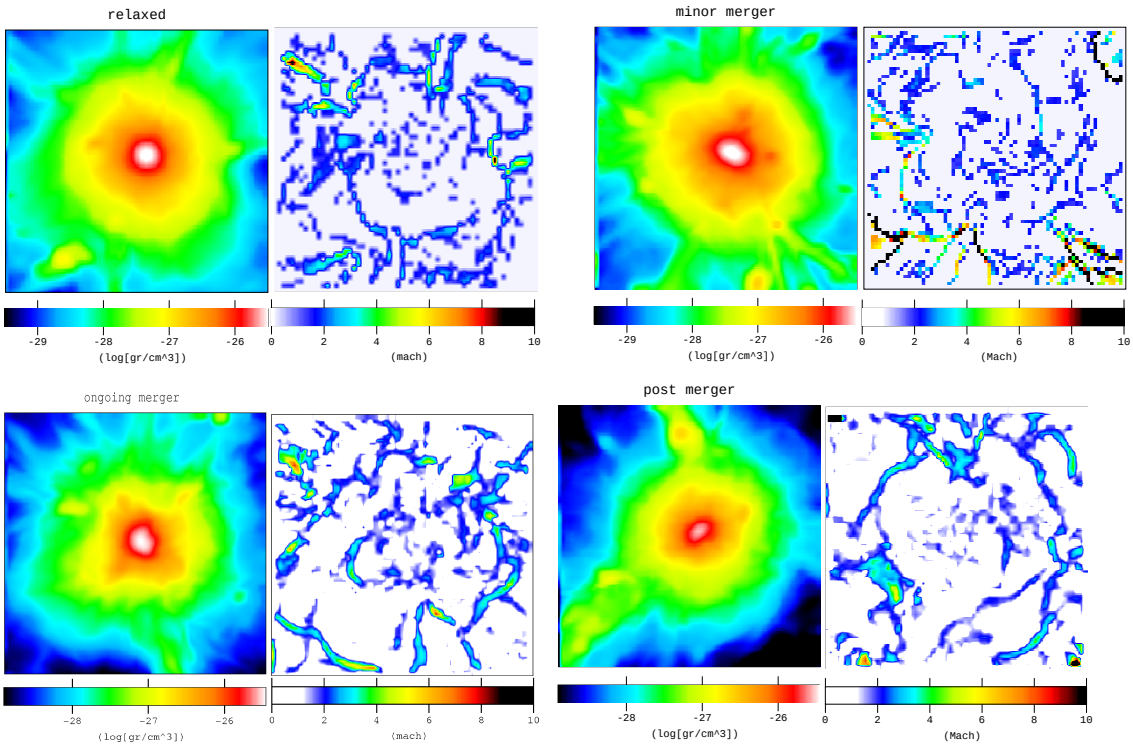

Figure 3.25: *Left panels:* maps of projected baryon density for the 4 galaxy clusters introduced in Sect.3.7.4. Every map has a depth along the line of sight of twice the virial radius of the correspondent cluster.*Right panels:* slabs of 125 kpc along the line of sight, showing the maps of Mach number for the same objects as in left panels.

- **C1**: a $M_{tot} \sim 7 \cdot 10^{14} M_{\odot}$ cluster in a relaxed state;
- **C2**: a $M_{tot} \sim 7 \cdot 10^{14} M_{\odot}$ cluster subject to an ongoing minor merger with a sub clump with mass $M_{tot} \sim 2 \cdot 10^{13} M_{\odot}$;
- **C3**: a $M_{tot} \sim 1 \cdot 10^{15} M_{\odot}$ cluster approaching a major merger with zero impact parameter, with a companion cluster (with $M_{tot} \sim 4 \cdot 10^{14} M_{\odot}$) that is at a distance of $\sim 1.3 R_{vir}$ from the main cluster center;
- **C4**: a $M_{tot} \sim 7.5 \cdot 10^{14} M_{\odot}$ cluster in a post–merging phase (the merger occurs in the simulation ~ 2 Gyr in look back time).

Maps of projected baryon density in a $(4R_{vir})^2$ regions centered on these clusters, and maps of the Mach number measured in slices crossing the same regions are reported in Fig.3.25.

In the case of *C2* (minor merger) and *C3* (major merger) relatively weak, $M \approx 2{-}2.5$, shocks are found inside R_{vir}, while in the case of *C4* (post-merger) merger shocks

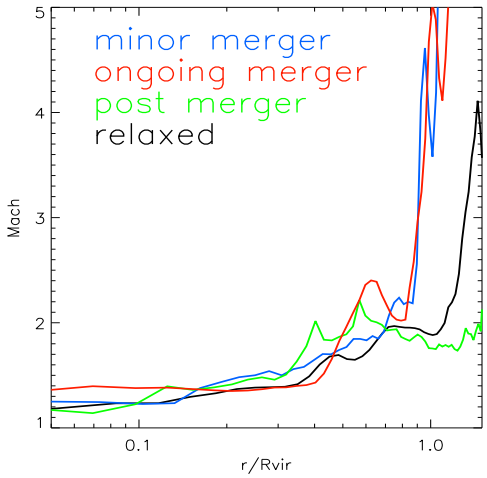

Figure 3.26: Volume averaged profile of the mean Mach number of shocks for the four galaxy clusters of Fig.3.25

have already moved outside the internal region of the cluster, and their strength is increased as the ambient temperature in cluster outskirts decreases.

The volume averaged Mach number of shocks in the four galaxy clusters is reported as a function of distance from cluster centers in Fig.3.26. Within the virial radius shocks are weak in line with expectations from semi–analytical models that indeed found shocks with $M > 3$ extremely rare in galaxy clusters (Gabici & Blasi 2003). This is also highlighted in Fig.3.27, that shows the distribution of the thermal flux dissipated at shocks as a function of shock-Mach number; distributions in different clusters are reported normalized to the volume of the most massive cluster. All distributions are steep, with differences from cluster to cluster due to the effect of their dynamical. Inside R_{vir}, *C1*, *C2* and *C3* have similar distributions, while *C4* shows some excess of rare shocked cells with $M \approx 3 - 7$. On the other hand, an excess of shocked cells with $M \approx 3 - 10$ is found in the external regions of *C3* and *C4*.

Also in the case of clusters our distributions of the thermalised energy flux at shocks are steeper than those reported in other works: we find $\alpha_{th} \approx -4$ to -5, while $\alpha_{th} \approx -3$ to -4 is obtained by Pfrommer et al.(2007), where the Lagrangian SPH code Gadget–2 was employed.

The radial profile of the ratio f_{CR}/f_{th} in our clusters is reported in Fig.3.28. Here we show the results in the case of both the KJ02 (*left* panel) and KJ07 (*right* panel)

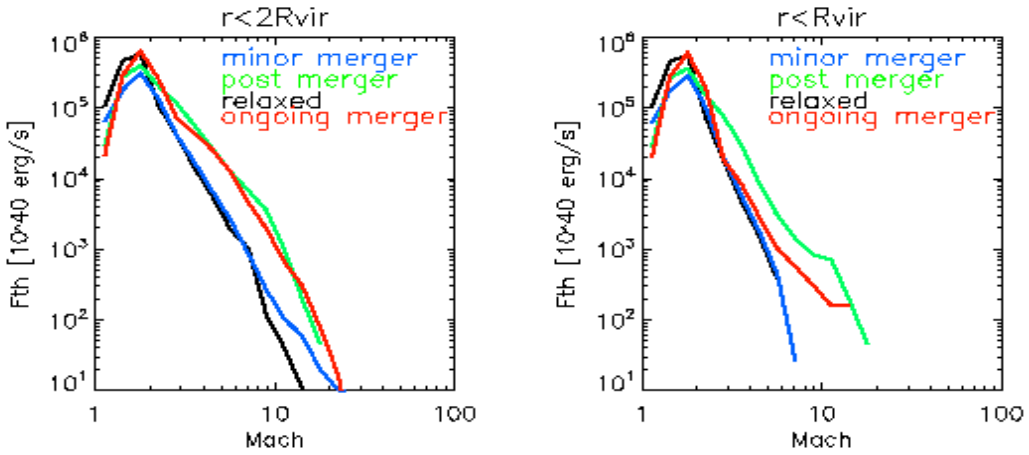

Figure 3.27: Distribution of thermalised fluxes for the four different galaxy clusters presented in the text. Distribution are normalized for the volume of the most massive one, and are taken from spheres of radius $2 \cdot R_{vir}$ and R_{vir} around each galaxy cluster.

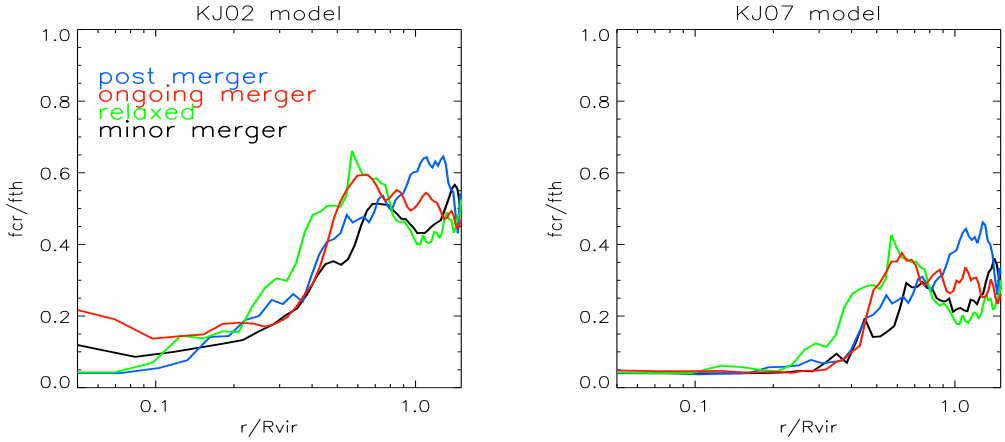

Figure 3.28: Volume averaged profiles of the injection efficiency, f_{CR}/f_{th}, for the four galaxy clusters. *Left* panel is for the KJ02 model and *right* panel is for the KJ07 model.

models. Inside the virial radius we do not find any relevant difference between our clusters. This is because, independently of the cluster dynamical status, the bulk of the energy dissipated in thermal energy and CR flux happens at relatively weak shocks. The maximum value of f_{CR}/f_{th} is found at distance $\geq R_{vir}$ from the cluster center: $f_{CR}/f_{th} \approx 0.5$ and 0.3 using the KJ02 and KJ07 model, respectively.

3.8 Discussion and Conclusion.

In this Chapter we have reported on the results obtained from the study of shocks in cosmological numerical simulations. This subject is particularly intriguing as

shock waves propagating trough LSS are the responsible for the heating of the ICM and may be important sources of CR in the Universe. This subject has been already investigated in several papers under different numerical approaches (Miniati et al.2000; Miniati et al.2001; Keshet et al.2003; Ryu et al.2003; Pfrommer et al.2006; Kang et al.2007; Pfrommer et al.2007, Skillman et al.2008).

We study shock waves by means of a post processing procedure. Although this is similar to Ryu et al.(2003) and Kang et al.(2007), our approach differs from previous ones in several points:

- we use a different numerical codes, the public version of ENZO (e.g. Bryan & Norman 1997), to simulate LSS (Sec.3.2);
- we adopt a more appropriate treatment of the re-ionization in our simulations (Sec.3.4);
- we use a different approach to catch shocks in our simulations and to measure their strength (VJ method, Sect.3.5.3).

3.8.1 Results

We simulated a large cosmic volume, $(145\mathrm{Mpc})^3 \approx (103\mathrm{Mpc/h})^3$, with a fixed grid resolution of 125 kpc. Additional simulations were designed and used to investigate the effect of spatial resolutions and of the σ_8 parameter (see Secs.A and B).

In the following we summarize the main results :

– *Re-ionization*: in Sect.3.6.3 we have shown that a correct treatment of the re-ionization is crucial to have a viable description of shocks with a post processing procedure. We derive formulas giving the typical temperature of the gas as a function of the local density by fitting data obtained from simulations which include a specific modeling of the re-ionization in run–time. These formulas are found to be consistent with Katz et al.(1996) and Valageas et al.(2002) and can be used to model the temperature background of adiabatic simulations in a post processing procedure; importantly in Sec.3.6.3(Fig.3.6) we have shown that our post

processing procedure is indeed consistent with the results from simulations with run–time re-ionization.

– *Methods to derive the Mach number of shocks*: in Sect.3.5.2 and 3.5.3 we have discussed two different methods to catch shocks in simulated data and to estimate their Mach number: the temperature jump (TJ) and the velocity jump (VJ), that rely on jumps in temperature and on jumps of velocity across shocked cells, respectively.

  The shock discontinuity is typically spread over a few cells and the risk in measuring the Mach number of shocks trough cell-to-cell velocity or temperature jumps is to underestimate the Mach number of shocks. To study this point in the context of our numerical simulations we perform several shock–tube tests with ENZO and obtained maps under different approaches (Sect.3.6). We conclude that shocks in our simulations are best characterized from velocity (VJ) or temperature (TJ) jumps taken across three cells centered in the shock centers.

  Both the VJ and TJ schemes use ideal conditions across non shocked cells and this may cause uncertainties in the characterization of the shocks in a post processing procedure (Sect.3.6.2–3.6.2). This is because the velocity field and temperature distributions in the cosmological data sets are very complex and the passage of a shock establishes thermodynamical gradients that are superimposed to already existing ones. We discuss the strength of the uncertainties on the value of the Mach number from the two schemes by means of Monte Carlo extractions of temperature and velocity variations across non shocked cells in our data sets, and show that the VJ method may be more reliable, at least in the case of weak shocks and especially in low density environments (Figs.3.9–3.10).

  Besides these uncertainties we find that the two methods yield statistically similar Mach number distributions of shocked cells in our simulations (Fig.3.15) suggesting that the statistical characterization of shocks in our simulations is fairly solid. In Sects.3.7 and 3.7.2 we adopt the VJ method.

– *Morphology of LS shocks*: in Sect.3.7.1 we discuss the morphology of the shock–patterns detected in our simulated data sets. About 15 per cent of the cells hosts shocks at the present epoch, and this fraction

slightly decreases with look back time for post–reionization epochs. In qualitative agreement with previous studies (Ryu et al. 2003; Pfrommer et al. 2006) we find that shocked cells form spectacular and complex patterns associated with the Cosmic Web: filamentary or sheet–like shocks are found outside the virial regions of clusters and around filaments, while more regular spherical structures surround galaxy clusters.

– *Number Distributions of LS shocks*: we study the number distribution of shocked cells as a function of their Mach number. An important point here is that thanks to the Eulerian scheme of the ENZO code we were able to follow the hydrodynamics of the LS shocks also in very low density regions, whose exploration is challenging for present Lagrangian schemes.

We find that the bulk of cosmological shocks is essentially made by weak $M \leq 2$ shocks and that the number distribution of shocks can be grossly described by a steep power law $N(M) \propto M^{\alpha}$. When considering the Mach number distribution of shocked cells in the total simulated volume we find an overall steep distribution $\alpha \approx -2.6$ which is dominated by the contribution from voids and filaments. This distribution steepens with increasing the cosmic over density and becomes very steep ($\alpha \approx -4$ to -5) in the case of galaxy clusters.

– *Energy dissipated at LS shocks* : the energy dissipation at LS shocks is the main focus of the previous studies on this topic (e.g., Miniati et al.2001; Keshet et al.2003; Ryu et al.2003; Pfrommer et al. 2006; Kang et al.2007; Pfrommer et al.2007). Following Ryu et al.(2003) we calculate the energy rate dissipated at shocks in form of thermal energy, by means of hydrodynamical jump conditions (Eq.3.11). In agreement with these previous studies we find that about $\sim 4 \cdot 10^{47} erg/s$ are dissipated at shocks in a $(103 Mpc/h)^3$ volume in the simulations at the present epoch. The bulk of the energy in our simulations is dissipated in galaxy clusters which indeed contribute to ≈ 75 per cent of the total energy (about 80 per cent if considering also their outskirts), while filaments contribute to a ≈ 15 per cent of the total energy. We calculate the distribution of the energy flux dissipated at LS shocks with shock-Mach number: the distribution is steep, $\alpha_{th} \approx -2.7$ ($f_{th}(M)M \propto M^{\alpha_{th}}$) and peaks at $M \approx 2$. Although in

qualitative agreement with previous studies, we find that the distribution is steeper that obtained by Ryu et al.(2003) that also used cosmological simulations based on a Eulerian scheme. This difference is mostly due to a more solid treatment of the re-ionization background in our case, and also to the use of the VJ scheme to measure the Mach number of shocks.

Following Ryu et al.(2003) we calculate the efficiency of the injection of CR at LS shocks according to Kang & Jones (2002). We obtained Mach number distributions of the energy flux dissipated into CR acceleration in line with previous findings, although we find distributions steeper than those in Ryu et al. and slightly steeper than those in Pfrommer et al.(2006 & 2007).

In agreement with Pfrommer et al. we find that the bulk of the energy dissipated in the form of CR at shocks is shared between clusters and filaments and that CR–acceleration happens in regions broader than those where thermal energy is dissipated at shocks (Fig.3.20). When considering all the shocked cells in our simulations we find that the ratio between the energy dissipated in the form of CR-acceleration and of thermal energy at present epoch is $f_{CR}/f_{th} \approx 0.2$ and that this ratio is smaller in galaxy clusters.

– *Galaxy Clusters*: in Sect.3.7.4 we discuss the case of shocks propagating in galaxy clusters. We find very steep distributions for both Mach number distributions and thermal energy flux at shocks. The typical Mach number of shocks within the virial radius is $M \approx 1.5$, in agreement with semi–analytical studies that provide comprehensive approach to study virialized systems (Gabici & Blasi 2003). At larger distance from the cluster center stronger shocks are found and their presence is correlated cluster dynamics. Remarkably the rarity of moderate–strong shocks in the cluster central regions (within $\approx$ Mpc distance from cluster center) makes the ratio f_{CR}/f_{th} very small, especially when the Kang & Jones (2007) model for the injection of CR at shocks is adopted (Fig. 25).

3.8.2 On the injection of CR

Although we use a different approach with respect to other studies, our findings for the energy dissipated in CR at shocks are grossly consistent with previous studies (Ryu et al. 2003; Pfrommer et al. 2006).

However, the astrophysical problem is extremely complex and several *hidden* ingredients in the adopted procedures are potentially sources of large uncertainties. As discussed in Sect.3.7.3 the efficiency of CR acceleration at shocks is investigated following several approaches. We have adopted the acceleration efficiency resulting from numerical calculations of modified shocks (following Ryu et al. 2003 and references therein). On the other hand Pfrommer et al.(2006) use a linear theory with the efficiency modified to account for saturation effects at large values of the Mach numbers (actually to limit the CR efficiency at ≈ 50 per cent). These two approaches are formally *radically* different, but nevertheless they provide an overall estimate of the CR injection efficiency which is not dramatically different in the case of typical shocks with $M \approx 2-4$. The main *hidden* ingredient in the efficiency of CR acceleration comes from the commonly adopted *thermal leakage injection* scenario which essentially adopts as minimum momentum of the particles that take part in the acceleration process, p_{inj}, a multiple of the momentum of the thermal particles, $p_{inj} = x_i p_{th}$. The choice of x_i is a *guess*, since this depends on physical details which are still poorly known (e.g., Blasi 2004). In Ryu et al.(2003) (and thus in our work) the fraction of protons injected into the CR population at shocks $\approx 10^{-3}$ which is not far from (even if larger than) the resulting efficiency from the assumption of $p_{inj} \approx 3.5 p_{th}$ adopted in Pfrommer et al.(2006). Although this parameter is somewhat constrained by the theory (e.g., Malkov 1998), it should be stressed that having a slightly different value of x_i (e.g. x_i=3.8 instead of 3.5) would have the net effect to reduce the acceleration efficiency by nearly one order of magnitude.

3.8.3 Constraints from observations

As already discussed in the Introduction (Sec.2.3) Theoretical arguments suggest that the bulk of CR in galaxy clusters should be in the form of

supra–thermal protons (e.g. Blasi, Gabici, Brunetti 2007 for a recent review). EGRET gamma ray observations of a few nearby galaxy clusters limit the energy density of CR protons in these clusters to $\approx$ 30 per cent of the thermal energy (Pfrommer & Ensslin 2004; Reimer 2004). More recently deep observations with Cherenkov telescopes have constrained the CR energy in a few galaxy clusters at $<$ 10 per cent of the thermal energy, at least in the relevant case of a flat spectrum of CR protons (e.g. Aharonian et al.2008).

Even more stringent constraints can be obtained from present radio observations. The bulk of galaxy clusters does not show evidence of extended Mpc–scale synchrotron radio emission and this can be used to constrain the population of secondary electrons and thus that of the primary CR protons from which these secondaries would be injected (Brunetti et al. 2007). These limits are very stringent and actually represent a challenge for simulations: in the case that the ICM is magnetized at $\approx \mu$G level (consistent with Rotation Measures, e.g. Govoni & Feretti 2004) the energy of CR should be at $\leq$ few percent of the thermal energy (when the spectrum of CR is fixed at that expected from simulations, i.e. $s \approx 2 - 2.5$, $N(p) \propto p^{-s}$ for $M \geq 3$).

A comparison between our simulations and present limits clearly requires a more detailed study, and to follow the advection and accumulation of CR in galaxy clusters.

However, a simple estimate of the spectral shape of CR injected in our simulations (Fig.3.29) suggests that the bulk of the CR energy in clusters and cluster outskirts is associated with CR populations with relatively steep spectra. In this case both limits from radio observations and from Cherenkov telescopes become less stringent, thus EGRET limits presently represents the most stringent constraints and our results are broadly consistent with these limits.

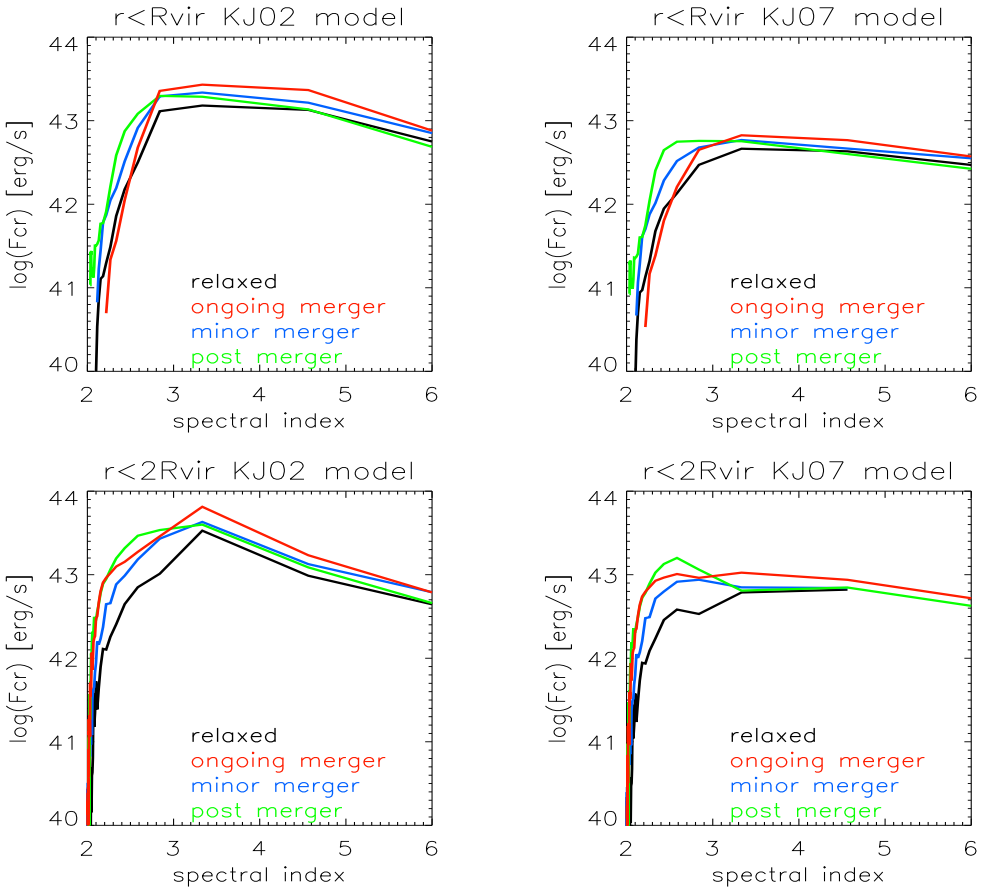

Figure 3.29: Energy distribution of the injected CR for the 4 galaxy clusters presented in the text, as a function of the spectral slope of the energy spectrum of injected protons, $N(p) \propto p^{-s}$. Estimates are shown both in case of the KJ02 and of the KJ07 models. We assume DSA at non–modified shocks (linear theory) according to KJ02, in which case it is $s = 2(M^2 + 1)/(M^2 - 1)$ (e.g. Gabici & Blasi 2003).

Chapter 4

Comparison of Cosmological Codes

4.1 Introduction

In this Chapter we present results from an ongoing comparison project with aim to understand the uncertainties in the characterization of shocks in numerical simulations, through the comparison between different numerical schemes and approaches.

At present, one can divide cosmological codes on the market into two broad classes:

- *grid codes* which use an Eulerian framework to solve hydro equations: the TVD code by Ryu et al.(1993, see also Sec.4.2.2) and Li et al.(2006); the moving mesh scheme (Pen 1998); the piecewise-linear method ART (Kravtsov et al.1997); the PPM codes ENZO (Bryan et al.1995, see also Sec.3.2) and FLASH (Fryxell et al.2000). Most eulerian codes have the possibility of refining the grid resolution, with the *Adaptive Mesh Refinement* (AMR) technique, by means of nested levels of refinement put in region of particular interest (this will be also subject of Sec.5.3).
- *Lagrangian codes* using Smoothed Particle Hydrodynamics (SPH) where the fluid variables are represented with a sampling by particles: GADGET and GADGET2 (Springel 2005, see also Sec.4.2.3), HYDRA (Couchman et al.1995), GRAPE-SPH (Steinmetz 1996).

Dark Matter dynamics is followed in all codes by conceptually similar

approaches, relying on a Lagrangian representation of DM ensembles of particles. An initially regularly distributed population of DM particles (with mass kept constant) in used to sample the DM distributions within the simulated volume; then this ensemble of particles is subject to the gravitational force computed over the DM population and over the baryonic matter component.

Differences from code to code depend on the precise numerical implementations of the gravity calculation: the force of N particles can be computed by means of multipole expansions in a domain decomposed space (*Tree* algorithms), or it can be calculated after interpolation onto a regular mesh and using Fast Fourier Transform algorithms (*PM - Particle Mesh* algorithms). Hybrid combinations of the two, in order to model gravity over a large dynamical range and in case of enormous number of particles (e.g. $N \sim O(10^{10})$), have been also recently developed (e.g. Xu 1995).

Several comparison works (e.g. Kang et al.1994, Frenk et al.1999, O'Shea et al.2004, Heitmann et al.2008) has been successfully done so far, showing that most of the relevant quantities involved in LSS dynamics are generally reproduced within at a ~ 10 percent accuracy if comparing most codes on the market. In general, convergence is reached for the most important statistics involving DM: for instance, the mass function of DM halos, the inner halos DM density profile and the power spectrum of DM density.

On the other hand a relatively poor agreement is found in the case of the properties of the gas: the temperature profiles, the ratio of the specific dark matter kinetic energy and the gas thermal energy and in the entropy profile within clusters (e.g. Frenk et al.1999); remarkably the largest discrepancy observed in Frenk et al.(1999) comparison was in the total X-ray luminosity, because this quantity is proportional to the square of the gas density, and resolving the cluster central region within the core radius is a crucial issue. An other relevant difference between different codes is the predicted baryon fraction and its profile within clusters, and modern schemes still show differences (e.g. Ettori et al.2006, Kravtsov et al.2005).

More recently, also a number of papers showing comparison among different

codes with semi-cosmological initial conditions (e.g. simulating the evolution of galaxy clusters already formed at the beginning of the simulation) has produced interesting insights about how different recipes are able to model complex hydro-dynamical effects (e.g. Agertz et al. 2007, Tasker et al.2008, Mitchell et al.2009).

Agertz et al.(2007) investigated the treatment of hydro instabilities arising in a simulated two-fluid environment (e.g. a gas clump crossing a static ICM), concluding that while in grid codes Kelvin-Helmholtz and Rayleigh-Taylor instabilities agree with analytical expectations, they are inhibited in SPH by artificial extra pressure at fluids boundary, due to the standard implementation of the SPH kernel.

Tasker et al.(2008) presented several tests in order to quantify the differences between 4 widely used numerical codes: the SPH codes GADGET2 and HYDRA, and the Eulerian codes FLASH and ENZO [1]. The main findings of their work are:

- Shock tube tests show that none of the codes produces orientation dependent features in the shock profiles, although a spread of the order ≈ 10 per cent in the values of post-shock quantities.
- Blast wave tests show the good performance of Eulerian codes (except for the ZEUS ENZO) and the production of over-pressurized bubbles in GADGET2, that are caused by time-stepping problems in the extreme case of strong detonation waves.
- Tests on the stability of King halos profiles show the good performance of SPH codes and the need of many levels of refinement for Eulerian methods to recover the correct innermost density profile; otherwise a systematically lower density core is formed.
- Tests on the stability of a translating King profile finally stress the issue of poor Galilean invariance in Eulerian codes (especially in ENZO-ZEUS

[1]Two hydro methods available in ENZO were tested in Tasker et al.(2008). One is the standard PPM method, which is discussed in Sec.3.2 and which does not use any artificial viscosity to solve hydro equations; the second is the so called ZEUS viscosity, which makes use of artificial viscous terms and has been developed mainly for MHD applications. All throughout this thesis, we have made use only of the ENZO-PPM method, which is the recommended one for cosmological simulations.

formulation), which causes a degradation of the halo profile in the direction of translation, at least in the case of high velocity (i.e. $3000 km/s$).
Mitchell et al.(2009) studied in detail the evolution of a system of two colliding galaxy clusters, using FLASH and GADGET2. Their most interesting result is the clear connection between the higher entropy within the cluster in FLASH (which is a general feature of grid codes, e.g. Frenk et al.1999) and the much larger degree of gas mixing during the early phase of the clusters merger found in FLASH simulations, leading to the conclusion that SPH standard implementation for the artificial viscosity is causing most of the difference and preventing efficient gas mixing.

In the last years several groups have studied the problem of shocks in simulated Large Scale Structures and their contribution to the acceleration of CR. Both semi-analytical and numerical approaches concluded that the bulk of energy in virialized structures is dissipated at relatively weak shocks, $M \sim 2 \div 3$ (e.g. Ryu et al.2003; Pfrommer et al.2006; Vazza, Brunetti & Gheller 2009). Less agreement in found in the case of stronger shocks that form in external regions: semi-analytical results cannot be extended to these regions and numerical simulations are sensitive to the details of the hydrodynamics of these regions, that may cause differences in the characterization of shocks. Addressing the process of CR acceleration at these shocks is even more difficult: first, this issue is very sensitive to the properties of shocks, second once their properties are well addressed , important uncertainties still come from our poor knowledge of shock acceleration, especially in the case of weak shocks. In the following the give a list of possible differences among the most relevant groups and the possible reasons of the discrepancies:

* *a different treatment of gas dynamics*: Eulerian TVD method in Ryu et al.(2003) and Kang et al.(2007), Eulerian PPM method in Vazza, Brunetti & Gheller (2009) (and Chap.3) and Skillman et al.(2008) and SPH in Pfrommer et al.(2006) and following works (see Sec.4.2 below for explanation of the different methods);
* *different shock detecting schemes*: Ryu et al.(2003) proposed a post–

processing analysis of temperature jumps (e.g. the "TJ" method discussed in Sec.3.5.2) Vazza, Brunetti & Gheller (2009) (and Chap.3) proposed a post–processing analysis of velocity jumps (VJ), while Pfrommer et al.(2006) analyzed in run time the evolution of entropy for each particle;

* *a different role played by accelerated CR*: in Ryu et al.(2003), Kang et al.(2007), Vazza, Brunetti & Gheller (2009)(and Chap.3) and Skillman et al.(2008) CR particles only enter calculations in a post–processing phase; in Pfrommer et al.(2006) CR have a run–time dynamical back reaction on gas particles, providing extra pressure support;
* *different cosmological setups:* the above papers adopted slightly different cosmological parameters and prescription for re-ionization.

An important step forward would be therefore to produce comparisons using the same set of simulations, with different codes, and with different shock detecting schemes.

A comparison project aimed at addressing the effect of different adopted schemes and recipes on the characterization of shocks and their role on CR accelerations is this timely and in this Chapter we report on the preliminary results from a coordinated effort that has being carried out with K.Dolag, D.Ryu, H.Kang and C.Pfrommer.

In Sec.4.2 we present the details of the numerical codes adopted in this Project, while in Sec.4.3 we present the initial conditions for all simulations Sec.4.4 shows the properties we measure for the DM component in all codes, while Sec.4.5 focuses on the properties of the gas component, by analyzing several statistics across the whole simulate volume. In Sec.4.6 we discuss the characterization of shocks in all codes, using different approaches. Sec.4.7 lists the preliminary conclusions of this Project.

4.2 Numerical Codes

4.2.1 Eulerian methods: ENZO

The technical details of hydro and DM methods in ENZO have already been presented in Sec.3.2, here we just recall some of the most important

Table 4.1: Specifics and performance of the simulations run for the project. Gadget runs were produced with Pentium IV Xeon, 3.06GHz, SPEC 1100. ENZO simulations were produced with AMD Athlon 3400+ (2.4GHz), SPEC 1200. TVD simulations were produced with AMD Operon 250 (2.4GHz), SPEC 1500. *n.s.*=Not specified by the simulator.

Gadget-2 (DM run)					
Run Ngrid	Tcpu [h]	Nproc	Ntstep	Mdm [$M_\odot/h$]	Rsoft [kpc/h]
64	1.2	4	1153	$2.86 \cdot 10^{11}$	31.0
128	19.1	8	1985	$3.57 \cdot 10^{10}$	15.5
256	258.1	16	3035	$4.5 \cdot 10^{9}$	7.75
512	6544.49	64	4943	$5.6 \cdot 10^{8}$	3.775
Gadget-2					
Run	Tcpu [h]	Nproc	Ntstep	Mdm/Mgas [$M_\odot/h$]	Rsoft [kpc/h]
64	4.9	4	2321	$2.4 \cdot 10^{11}$ / $4.55 \cdot 10^{10}$	31.0
128	109.8	8	6346	$3.0 \cdot 10^{10}$ / $5.7 \cdot 10^{10}$	15.75
256	1484.57	32	17205	$3.76 \cdot 10^{9}$ / $7.11 \cdot 10^{8}$	7.875
ENZO					
Run	Tcpu [h]	Nproc	Ntstep	Mdm [$M_\odot/h$]	Grid [kpc/h]
64	0.52	16	241	$2.4 \cdot 10^{11}$	1562.5
128	7.7	16	304	$3.0 \cdot 10^{10}$	781.25
256	1111.46	16	501	$3.76 \cdot 10^{9}$	390.625
512	31961.6	64	950	$4.7 \cdot 10^{8}$	195.31
TVD					
Run	Tcpu [h]	Nproc	Ntstep	Mdm [$M_\odot/h$]	Grid [kpc/h]
64-32	n.s.	2	n.s.	$3..0 \cdot 10^{12}$	1562.5
128-64	n.s.	2	n.s.	$2.4 \cdot 10^{11}$	781.25
256-128	n.s	2	n.s.	$3.0 \cdot 10^{10}$	390.625
(512-256)	200	2	468	$3.76 \cdot 10^{9}$	195.31

features.

ENZO is an adaptive mesh refinement cosmological simulation code developed by Bryan et al.(e.g. Bryan et al.1997, Norman et al.2007 and reference therein).

Summarizing its main features, it employs a high order shock capturing method to model hydrodynamics (PPM) and a particle-mesh method to follow dark matter dynamics (PM).

Even if the use of the adaptive multilevel grids an additional physics (e.g. star formation, re-ionization and cooling processes) are powerful tools in ENZO, we do not use these methods in order to keep simple as possible the comparison with the other codes of the project.

4.2.2 Eulerian methods: TVD code by Ryu.

The cosmological code created by Ryu et al. is based on the Harten (1983) total variation diminishing (TVD) scheme . It is a flux-based Eulerian code with second-order accuracy in space and time. It captures shocks within two to three cells without generating oscillations, but limiting the numerical flux according to the TVD scheme instead of adding a simple artificial viscosity. Several important improvements were made while incorporating the TVD scheme into the cosmological code. The numerical artificial heating around the extremely supersonic flows where the bulk kinetic energy is much greater than the thermal energy is reduced; this was achieved by following the adiabatic changes of the thermal energy using a modified entropy equation instead of using the total energy equation. The leakage of the gravitational energy into the thermal energy in region of supersonic flows was prevented by including the effects of the gravitational force only to the momentum and kinetic energy and keeping the thermal energy rather than solving the conservation of the total energy. Also, a correction due to the mass diffusion under the gravitational field has been added in the gravitational force term in order to obtain better conservation of the total energy and to satisfy the cosmic energy equation. Additional details can be found in Ryu et al.(1993) and Ryu et al.(2003).

The treatment of gravity and DM particles dynamics is completely similar

to what is done in ENZO, provided that a unique resolution level is specified for the whole simulated volume. Additionally, in this code there is the possibility of using a smaller number of DM particles (compared to the standard approach of having a number of DM particles equal to the total number of cells in the grid), in order to spare memory usage. This is motivated by the fact that, as stressed in Sec.3.2, in the PM scheme the effective force resolution is approximately twice as coarse as the mesh spacing. Therefore, adopting a number of DM particles which is $(N/2)^3$ for a N^3 grid, has a very little or negligible difference in the final accuracy of the derived potential and accelerations.

4.2.3 Lagrangian code: GADGET

We compare Eulerian methods with a new version of the parallel TreeSPH code GADGET (Springel 2005), which combines smoothed particle hydrodynamics with a hierarchical tree algorithm for gravitational forces. SPH uses a set of discrete tracer particles to describe the state of a fluid, with continuous fluid quantities being defined by a kernel interpolation technique if needed (e.g. Monaghan 1992). The SPH particles can be thought of as Lagrangian fluid elements that sample the gas. The thermodynamic state of each fluid element may either be defined in terms of its thermal energy per unit mass, u_i, or in terms of the entropy per unit mass, s_i. The latter is used as the independent thermodynamic variable evolved in SPH, as discussed in full detail by Springel & Hernquist (2002). The use of the *entropy formulation* allows SPH to be formulated so that both energy and entropy are manifestly conserved, even when adaptive smoothing lengths are used. The adaptive smoothing lengths h_i of each SPH particle are defined such that their kernel volumes contain a constant mass for the estimated density (e.g. $N = 32$ and $N = 64$ are common choices).

Provided there are no shocks and no external sources of heat, the derivation of equations for the reversible fluid dynamics in SPH is quite simple (e.g. Dolag et al.2008).

However, flows of ideal gases can easily develop discontinuities where

entropy must be generated by micro-physics. Such shocks need to be captured by an artificial viscosity technique in SPH, which is active only when fluid elements approach one another in space, preventing particle interpenetration and transforming kinetic energy irreversibly into heat (e.g. Monaghan & Gingold 1983); additional viscosity-limiters are also introduced in GADGET2 in the presence of strong shear flows to alleviate spurious angular momentum transport.

In GADGET, both the collision-less dark matter and the gaseous fluid are represented by particles, allowing the self-gravity of both components to be computed with gravitational N-body methods. GADGET2 allows the pure tree algorithm to be replaced by a hybrid method consisting of a synthesis of the particle-mesh method and the tree algorithm, with significant reduction of the computational effort. GADGET2's mathematical implementation of this so-called TreePM method is similar to that of Bagla (2002).

Compared with previous SPH implementations, GADGET2 differs significantly in its formulation of SPH, in its time stepping algorithm, and in its parallelization strategy.

4.3 Initial Conditions

We have assumed a "Concordance" model, with density parameters $\Omega_0 = 1.0$, $\Omega_{BM} = 0.043$, $\Omega_{DM} = 0.227$, $\Omega_\Lambda = 0.73$, Hubble parameter $h = 0.70$, a power spectrum with slope $n = 1$ and a primordial spectrum normalization $\sigma_8 = 1.2$ (intentionally kept high in order to have a larger number of collapsed halos). In order to keep the comparison between the different codes the most straightforward as possible, we neglect any modeling of radiative and heating processes for the gas component. The total volume of this data set is that of a cube of side $100 Mpc/h$. The initial displacements and velocities of DM particles were identically initial for all codes; the numbers of DM particles adopted are 512^3, 256^3, 128^3 and 64^3 (except of the case of Gadget, where the 512^3 is neglected). The initial redshift of simulations is computed in order to reach the same growth rate at $z = 0$ for the smallest available density perturbations: $z_{in} = 67.99$,

$z_{in} = 55.92$, $z_{in} = 44.77$ and $z_{in} = 34.63$ for the different resolutions, respectively. The initial conditions used in this Project are public and accessible at: http://canopus.cnu.ac.kr/shocks/case0/.

Typically, the initial conditions in the Eulerian and in the SPH simulations are produced as a set of DM particles with positions and velocities perturbed according to the Zel'Dovich approximation. This perturbation is transferred into the gas component either by perturbing the value of density and velocity within the cells (Eulerian), or by imposing the same displacement and initial velocity to all gas particles (SPH). However, in our case perturbing cells and SPH particles in a consistent way is not trivial, and to avoid the production of initial differences, we simply neglect any initial perturbation of the gas component, and just perturb DM particles.

Table 4.1 lists the amount of computational time and memory usage required for every run to complete. In the case of GADGET, an additional set of DM only runs was produced for comparison. As a general rule, in the following we will refer to a given run accordingly to the number of its gas particles or gas cells; in the case of the TVD code, the number of DM particles is kept 8 times smaller than the number of gas cells (Sec.4.2.2). In the following, we will typically refer to "*self*–convergence" meaning the convergence of a code with respect to increasing resolution, and to "*cross*–convergence" meaning the convergence between different codes, at a given resolution.

4.4 Dark Matter Properties

As discussed in Sec.5.1 the different numerical approach on the market provide a consistent representation of DM, with overall scatter of $\approx 5-10$ percent level in the various quantities. Therefore we just focus on the most important proxies of DM features in our runs.

Several maps of projected positions of DM particles were produced in order to compare by eye the level of "self-convergence" and "cross-convergence" at all resolutions in our different simulations. We find that the "self-convergence" is pretty good in all codes, with mismatches in the positions of the centroid of DM structures within a few hundreds of kpc. On the

other hand the "cross-convergence" is more problematic since mismatches up to $\sim 1Mpc$ are found in the case of the smallest DM halos. No clear trend with resolution or halo masses is found, and it is likely that these differences are caused by different time stepping of codes, as already pointed out in O'Shea et al.(2004) and Heitman et al.(2007).

Figs.4.1 shows the cumulative mass functions calculated for the different runs; results are obtained with a spherical over-density halo finder, that uses the over density from a spherical collapse model. All grid outputs have been converted into a distribution of particles to apply the same procedure halo used in GADGET.

Cumulative distributions obtained with GADGET converge at all resolutions, down to halos containing $\sim 20 - 30$ particles. On the other hand Eulerain codes under-produce halos at all masses, and the "self-convergence" of the results is much slower than that obtained with SPH. The convergence process is particularly slow in ENZO, where convergence is reached only for masses above $\sim 10^{14} M_{\odot}$, with resolutions from 256^3 to 512^3; this trend confirms similar findings reported by O'Shea et al.(2004) and Hetimann et al.(2008).

In order to compare different simulations, we need to assign a formal resolution to each of them. Although the mass functions obtained with GADGET are measured in a stable way down to the smallest halos, containing less than 20 particles, Power et al. (2003) showed that the convergence in resolving the inner structure of halos is reached with at least 500-1000 particles inside R_{vir}. We thus define as "resolved" halos in GADGET those with mass > 500 times the mass of DM particles. In order to have a similar number statistics in the case of Eulerian runs, we assume that the radial profiles inside clusters need at least 5 cells (i.e. at least $\sim 4\pi 5^3/3 \sim 1000$ independent cells) , to be resolved and we use the predicted R_{vir} vs. M_{vir} relation from Dark Matter only runs to assign a formal resolution to grid runs. Therefore, in what follows we discuss only the "cross-convergence" of all codes in the case of halos fulfilling the above mass-resolution criterion. This means, for instance, that only halos with $R_{vir} > 4Mpc/h$ should be considered to explore "self-convergence"

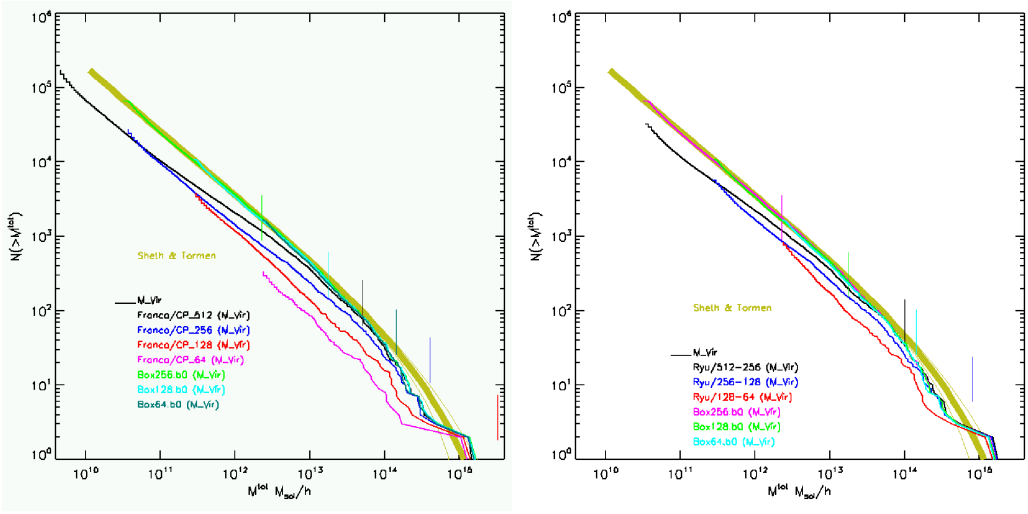

Figure 4.1: Cumulative mass functions of the virialised halos produced in the various runs, shown are GADGET runs (labeled as "Box" in both panels), and ENZO results (*left* panel) and TVD results (*right* panel); GADGET results are shown for reference in both panels (they are labeled as "Box") Additionally, the Sheth & Tormen mass function is shown for reference (bold yellow line) with thin yellow lines showing the Poisson error.

and "cross-convergence" in the case of 128^3 ENZO runs, while those with $R_{vir} > 1Mpc/h$ should considered in the case of 512^3 ENZO runs.

Vertical lines in Fig.4.1 show the value of the mass of halos resolved in grid runs: although in the case of GADGET a good convergence is already reached with a fairly small number of DM particles, in the case of grid codes the minimum number of DM particles to obtain a convergent mass function is larger, of the order of $N \sim 10^4 - 10^5$.

4.5 Baryonic Matter Properties

All simulations neglect radiative cooling, re ionization and heating processes, therefore the thermal properties of baryons are solely due to adiabatic contraction and shock waves. Here we summarize the thermal properties of the simulated volume, and of representative galaxy clusters in the sample, at $z = 0$.

4.5.1 Maps

Figs.5.9 shows projected maps of mass-weighted temperature for the most resolved runs of the project, while Fig.4.3 shows the evolution with spatial

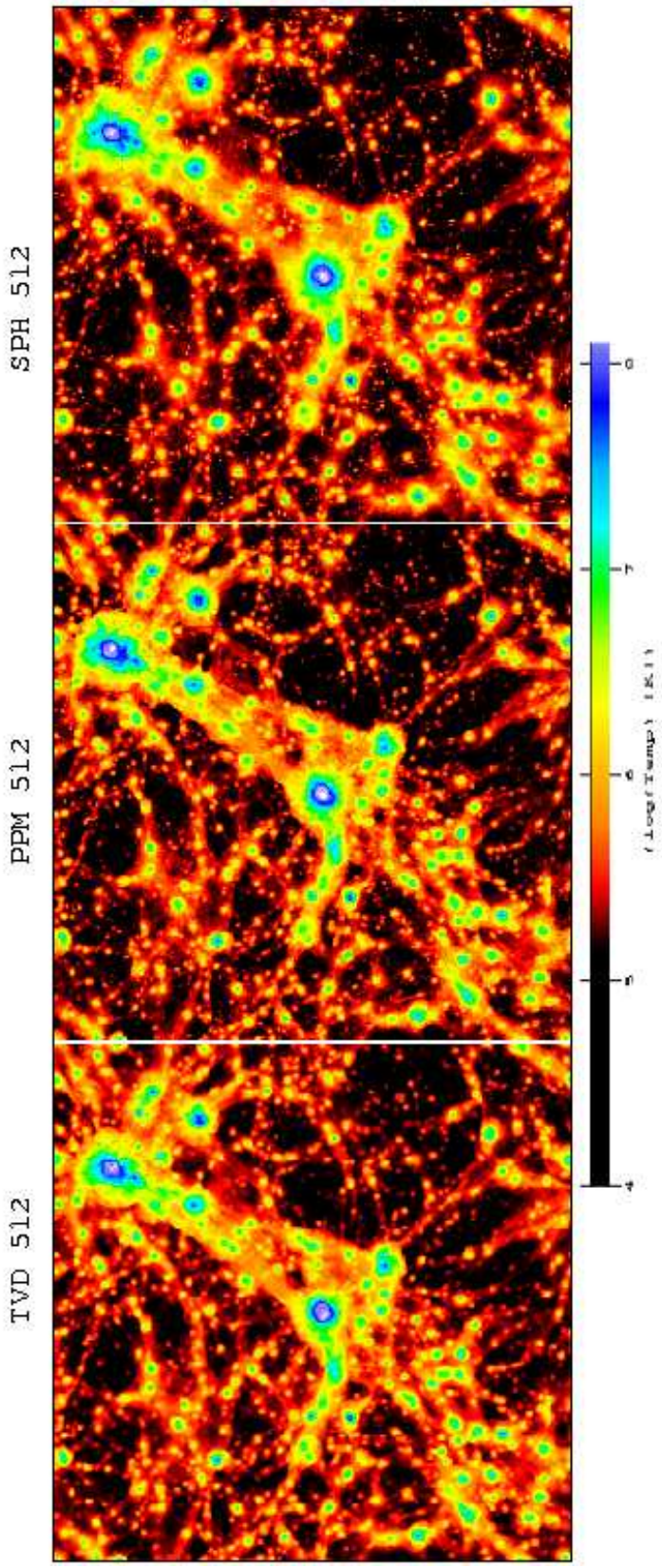

Figure 4.2: Maps of projected Mass-Weighted Temperature for the full simulated volume, at the largest available resolutions in the three codes.

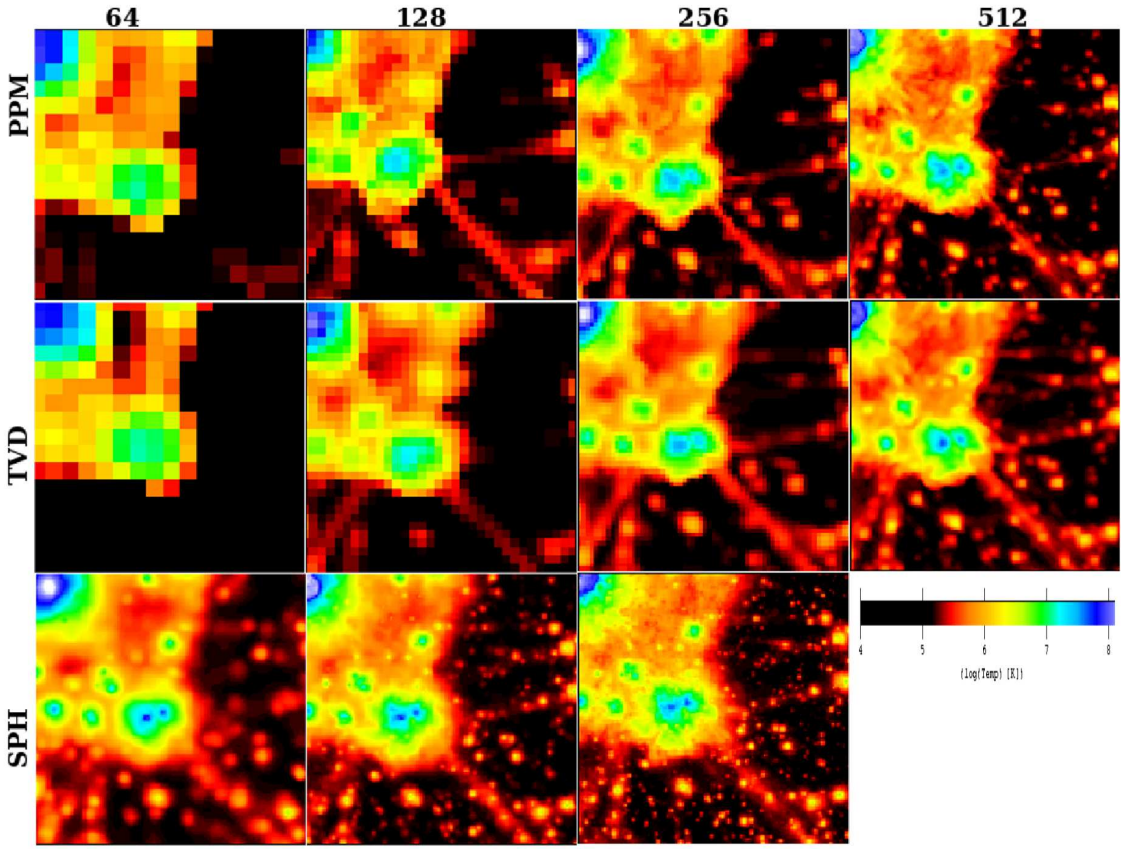

Figure 4.3: Maps of projected Mass-Weighted Temperature for a sub region of side $40Mpc/h$ and LOS depth $100Mpc/h$, for all resolutions and codes.

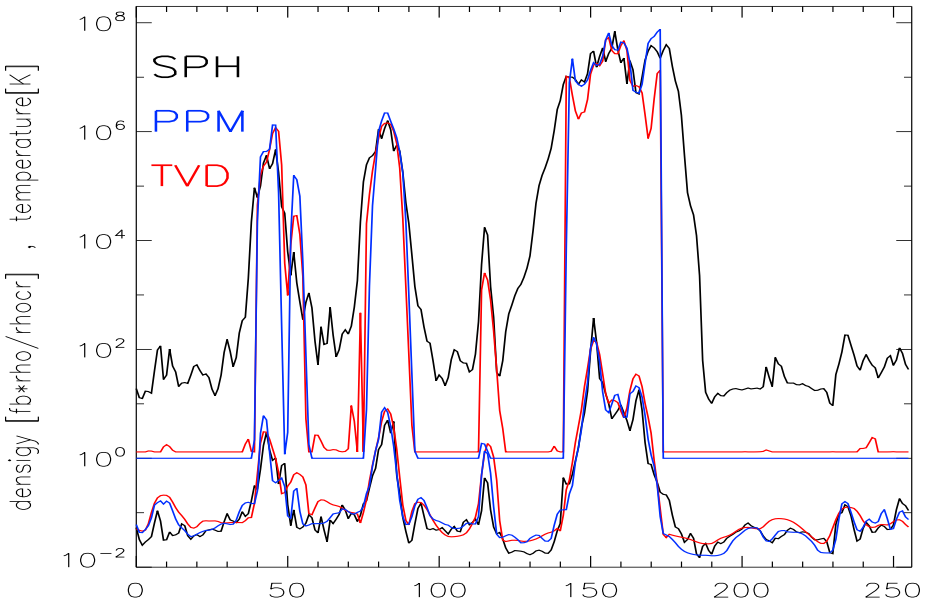

Figure 4.4: 1–D plot of gas density (*lower lines*) and gas temperature (*upper lines*) for all 256^3 runs.

resolution of the mass-weighted temperature map across the outskirt of a galaxy cluster, for all codes; in order to readily compare Lagrangian and Eulerian data, SPH fields have been interpolated onto a regular grid, with resolution equal to that of grid simulations, using the same SPH kernel employed during the simulation.

We find that generally all runs agree very well, and show very similar morphologies. This is also shown in Fig.4.4, that reports 1–D plots of gas density and gas temperature along a line crossing the simulated volume at the position of a massive galaxy cluster, obtained for all 256^3 runs. We notice that the "cross-convergence" is worse in the case of temperature: grid codes show sharp temperature jumps at almost the same locations, while GADGET shows less sharp temperature jumps (obviously due to the spatial smoothing at small over densities in the case of GADGET).

4.5.2 Distribution Functions

A more quantitative analysis of the differences between the codes is reported in Fig.4.5 and Fig.4.6, that show resolution studies of volume

weighted gas density and gas temperature distributions.

Overall GADGET shows the highest degree of convergence in the density distribution and ENZO in the temperature distribution. As expected, the "cross–convergence" between the codes gets better with increasing spatial resolution.

In the case of the density distributions runs with 256^3 DM particles or more (i.e. with mass resolution equal or better than $4.5 \cdot 10^9 M_\odot/h$), show the same average value within a $20-30$ per cent scatter; the largest and the smallest gas densities are different by a factor of ~ 2, with GADGET producing the most extreme values.

Temperature distributions function show a lower degree of "cross-convergence". ENZO has the highest degree of "self-convergence", showing the same average and maximum temperature (within a factor of $\sim 10-20$ per cent at all resolutions). On the other hand, the other two codes show significant differences with resolution, both in the shape and in the average value of the temperature distributions, particularly at lower temperatures, $T < 10^4 \div 10^5 K$. The "cross-comparison" of temperature distributions between the three codes shows that distributions become similar for $T > 10^6 K$, which corresponds to typical virial temperatures of collapsed halos; this is in line with early findings reported in Kang et al.(1994). It is likely that most of the observed differences in temperature are due to different shock heating among the codes.

4.5.3 Baryon Fraction in Halos

In Fig.4.7 we show the baryon fraction within the virial radius of all detected halos (Sec.4.4). As a general feature, most of the resolved halos have a baryon fraction in the range $f_b \sim 0.7 - 1.0 \Omega_b/\Omega_m$. The baryon fraction in GADGET is rather perfectly converged at all resolutions for $M > 5 \cdot 10^{14} M_\odot/h$, with a value of $f_b \approx 0.9 \Omega_b/\Omega_m$.

Overall, for all the codes the resolution criteria outlined in Sec.4.4 are conservative enough to guarantee "self-convergence" if baryon fraction within $\sim 3-5$ per cent level, also considering that slight time stepping delay should cause some spread in the derived halo baryon fraction.

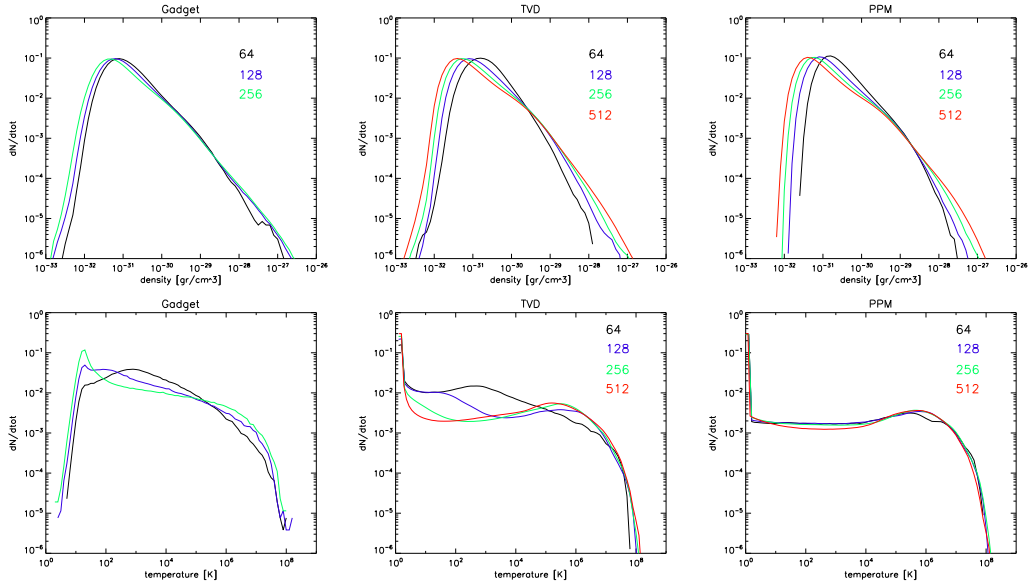

Figure 4.5: Gas density and gas temperature pdf's for all resolutions and all codes.

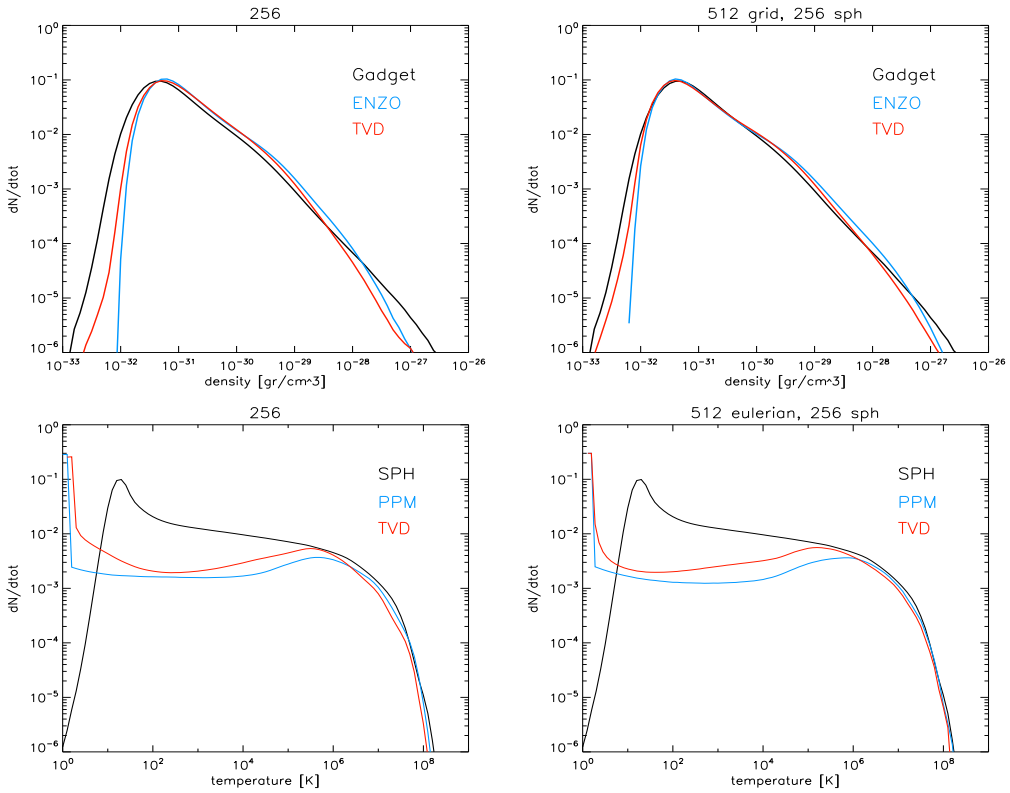

Figure 4.6: Cross convergence of gas density and gas temperature pdf's for the most resolved runs of the project. In the case of GADGET, the run is always the 256^3 one.

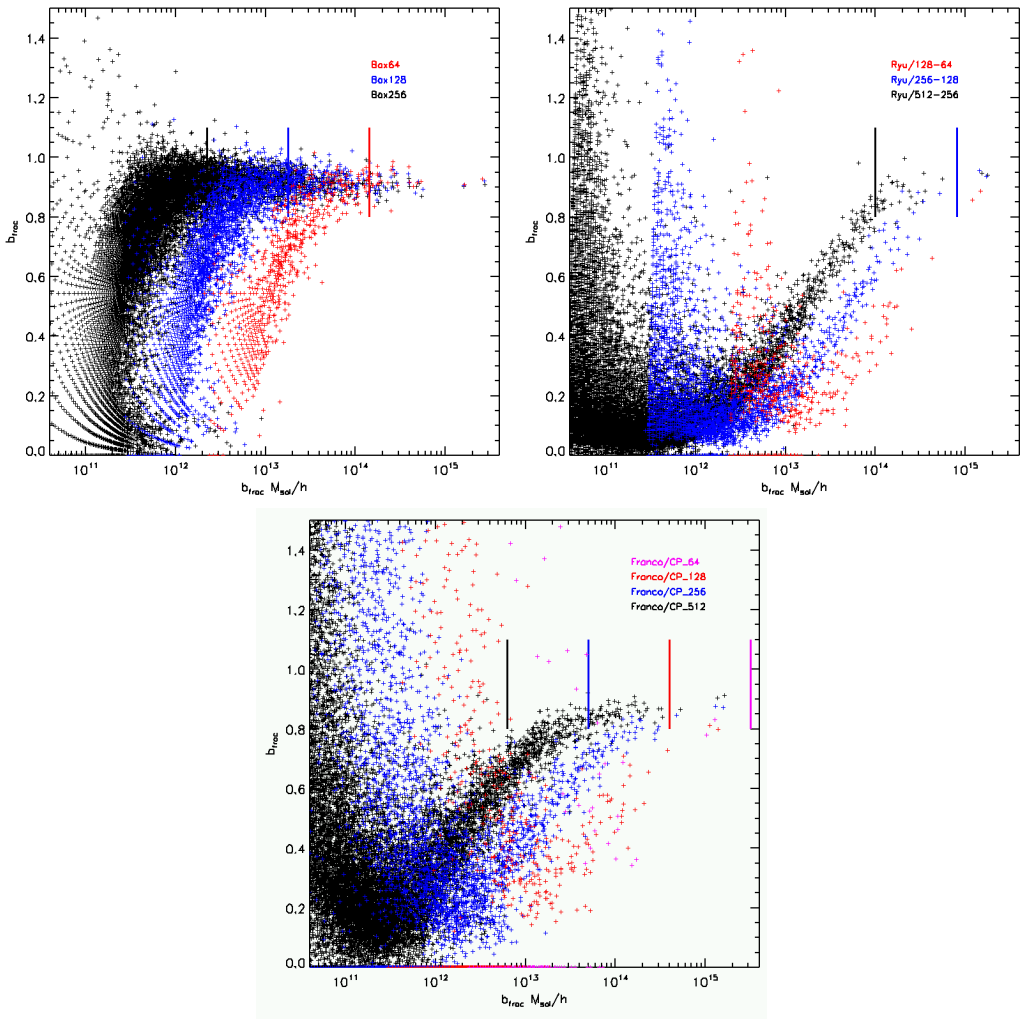

Figure 4.7: Baryon fraction for all halos in the three codes, at all resolutions. The vertical lines marks the minimum mass above which halos are resolved, according to Power et al.2003 and Sec.4.4.

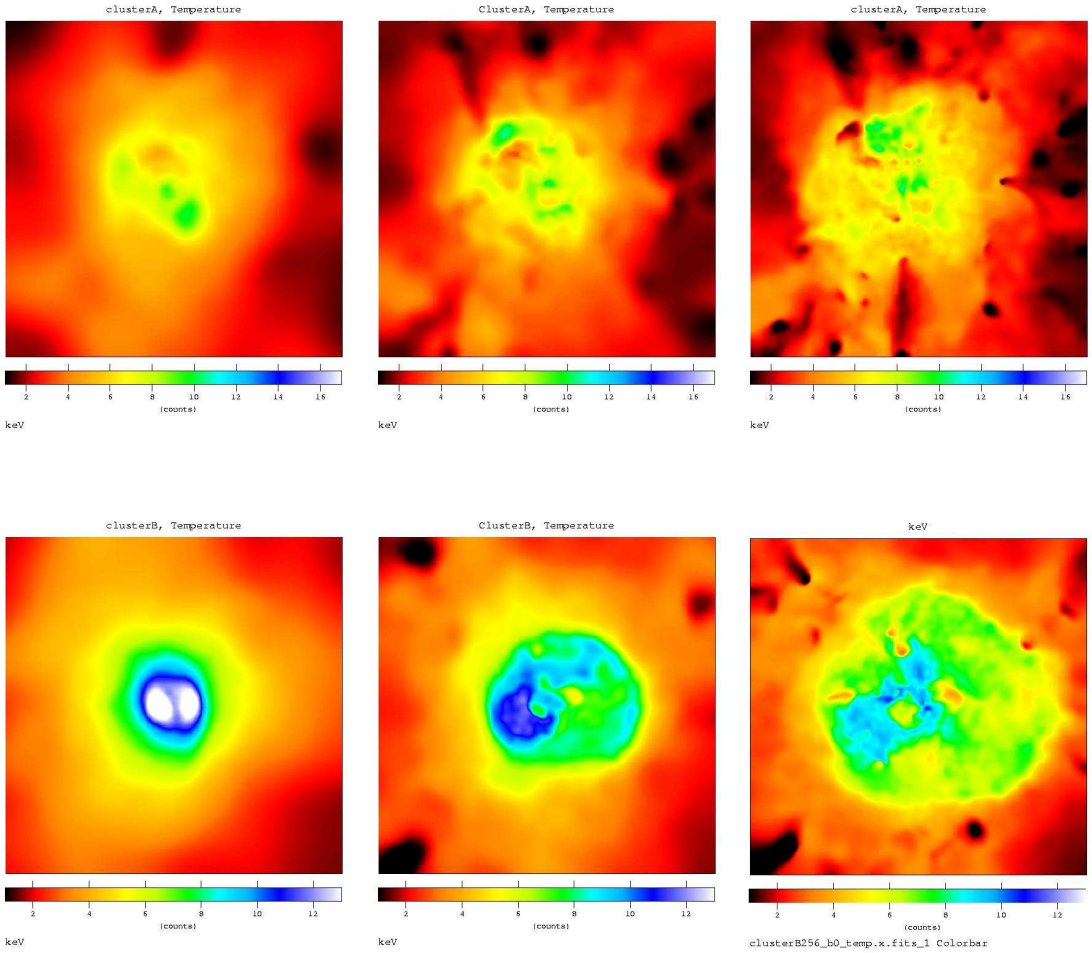

Figure 4.8: Maps of projected mass weighted temperature for cluster A (*upper row*) and cluster B (*lower row*), for a box of side $8Mpc/h$, for the three GADGET resolutions.

What is the reason causing the $\sim 10-20$ per cent larger baryon fraction in grid codes, compared to SPH, at this stage is unclear; however this finding is in quantitatively in line with results presented in literature by Ettori et al.(2004), O'Shea et al.(2004) and Nagai et al.(2005). We will discuss possible explanations to that in Sec.4.7.

4.5.4 Properties of Galaxy Clusters

We carry out "cross-convergence" analysis for the 2 most massive galaxy clusters in our sample:

* a cluster of total mass $M = 1.36 \cdot 10^{15} M_{\odot}/h$ and $R_{vir} = 2.32 Mpc/h$,

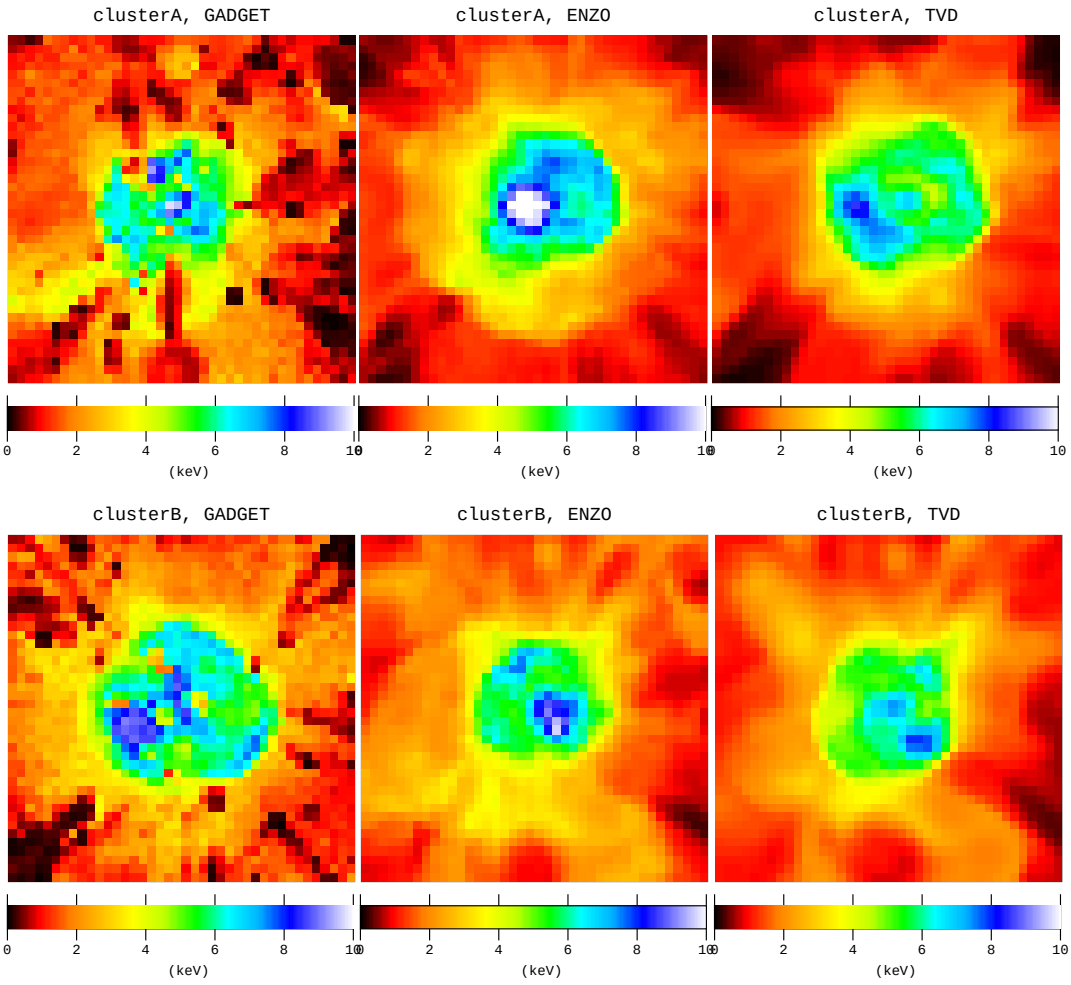

Figure 4.9: Maps of projected mass weighted temperature for cluster A (*upper row*)and cluster B (*lower row*), for the highest resolution runs of the three codes. The volume is as in Fig.4.8; SPH data are interpolated onto a grid of equal resolution of the grid codes.

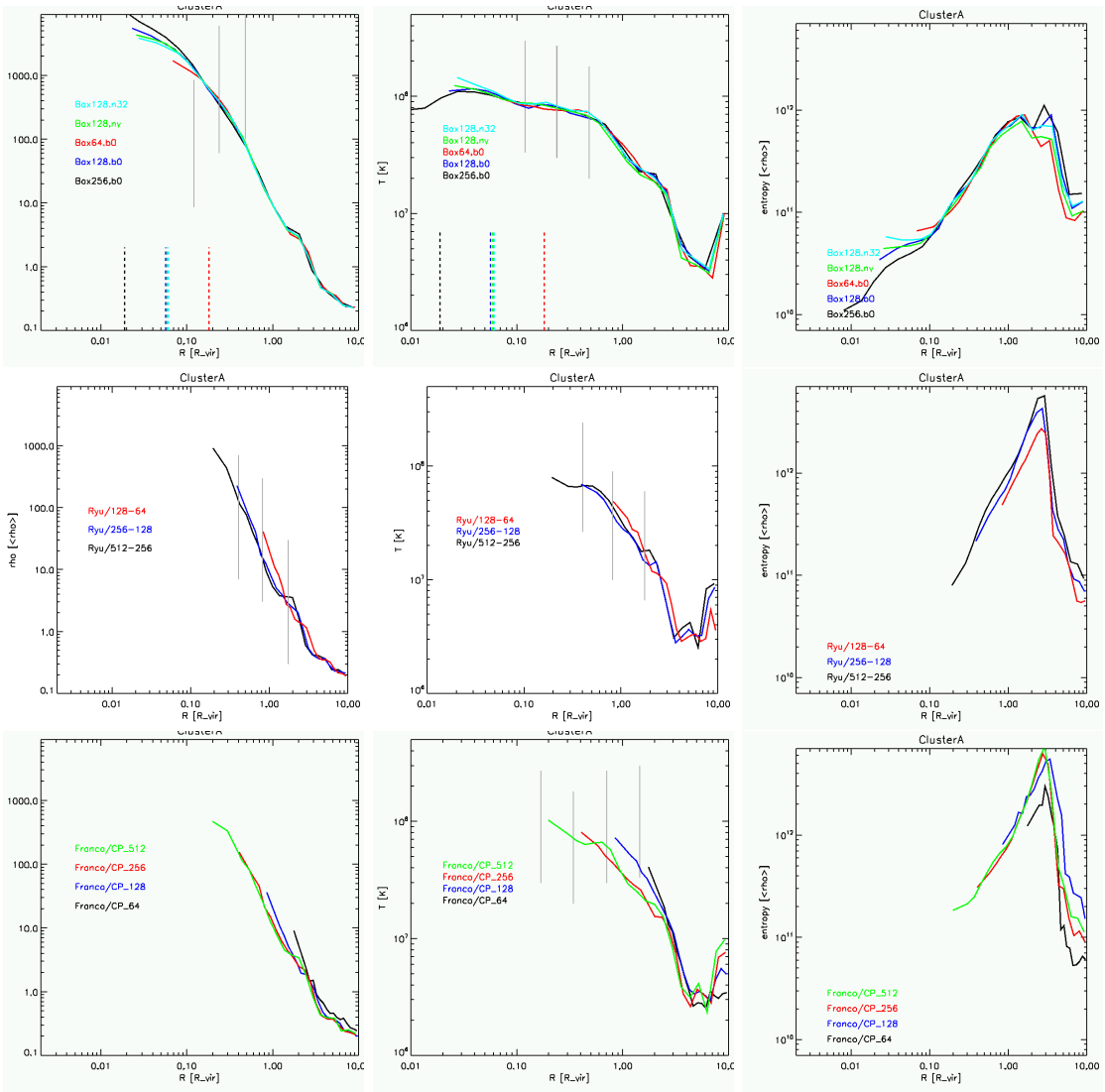

Figure 4.10: Profiles of gas density (*left column*), gas temperature (*center column*) and gas entropy (*right column*) for Cluster A at various resolutions. GADGET runs are in the upper row, TVD runs are in the middle and ENZO runs are in the bottom row. Vertical dashed lines show the minimum radius enclosing 500 gas particles in GADGET runs, while vertical gray lines show the resolution limits of grid codes, according to our criterion exposed in Sec.4.4.

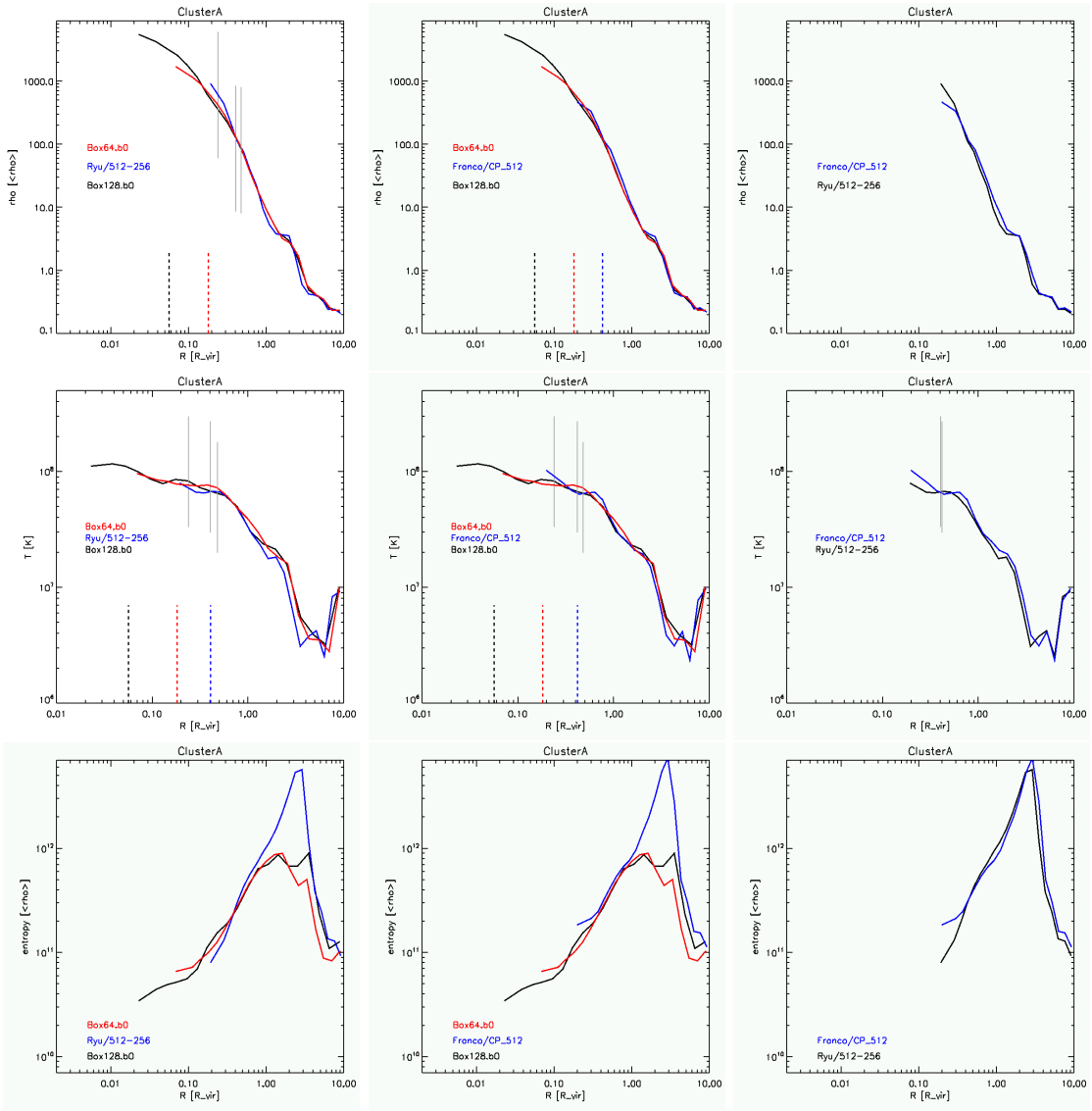

Figure 4.11: Cross comparison of the gas temperature and entropy profiles for the Cluster A.

in a post merging phase(*cluster 'A'*);

* a cluster of total mass $M = 1.64 \cdot 10^{15} M_{\odot}/h$ and $R_{vir} = 2.47 Mpc/h$, in a merger phase (*cluster 'B'*).

where masses are taken from the most resolved GADGET run, with a mass variation across the different runs within a ≈ 6 per cent.

In Fig.4.8 we show projected maps of Mass-Weighted Temperature for clusters A and B at all GADGET resolutions (maps are produced using SPLOTCH ; http://dipastro.pd.astro.it/ cosmo/Splotch).

It should be stressed that different resolutions, even when the same numerical method is applied, produce slightly different timings even when the formal time of the outputs is the same. This is evident in the case of the merging system B, where a rim of hot shocked gas at $T \sim 8 Kev$ in the lower right corner of the cluster locates at a larger distance from the cluster center as resolution is increased, and this seems to reproduce also a time series of the merger in cluster B.

Panels in Fig.4.9 then show the mass weighted temperature maps for clusters A and B, at the highest resolutions from all codes. In this case, the GADGET data have been interpolated onto a regular grid with resolution equal to that of Eulerian runs (by using a Particle In Cell interpolation), to be compared with data from ENZO and TVD. In the "cross-comparison", it is less clear that time stepping issues are responsible for the differences in the innermost structure of clusters.

Fig.4.10 show volume weighted profiles for gas density, temperature and entropy (defined as $S = T/\rho^{2/3}$) in the case of cluster A; in the case of GADGET we also report the additional profile from a run (called *n32*) with a smoothing length computed by 32 SPH neighbors (instead of the standard choice of 64), and from a run (called it nv) where an implemented artificial viscosity is adopted, following Dolag et al.(2005), see also (Sec.5.2.1).

In general, all results show a fairly good "self-convergence" adopting the resolution limit proposed in Sec.4.4; in this case only ENZO runs with the two coarsest resolutions show larger discrepancies in the temperature and entropy profiles.

The "cross-convergence" analysis is reported in the representative case of cluster A, see Fig.4.11. The most striking difference is in the gas entropy profiles: a remarkable difference between grid codes and GADGET, of a factor $\sim 5-6$, is found for the value of the entropy at the distance of $\sim 2R_{vir}$. The shape of the entropy profile in GADGET shows a smoothed behavior rather than the very sharp peak found in ENZO and in TVD; interestingly enough, this difference was not reported in Frenk et al.(1999), because of the different definition of entropy in their comparison ($S \equiv log(T/\rho^{2/3})$ instead of $S \equiv T/\rho^{2/3}$).

An other interesting feature is the hint of entropy floor, within $\approx 0.3R_{vir}$; in clusters simulated with ENZO compared to GADGET runs. The PPM scheme is well known to create entropy floor in cluster cores (e.g. Frenk et al.1999), yet it remained whether this effect is related to the PPM hydro scheme, or to the adoption of AMR techniques (e.g. Tasker et al.2008). Our findings suggest that even without the adoption of AMR, an entropy core is developed inside $< 0.3-0.4R_{vir}$ in our ENZO, simulations. In this respect the analysis of the additional SPH runs, *n32* and *nv*, contribute to shed some light on the reasons that produce the differences: clusters simulated with the *nv* implementation, with reduced artificial viscosity, have somewhat flatter inner entropy profile (see also Dolag et al.2005 and Sec.5.2.4), suggesting that viscosity plays a role. Following Mitchell et al.(2009), the differences could be attributed to the different mixing of high entropy gas in the two codes. Indeed PPM codes are more efficient in mixing plumes of high entropy gas during mergers and accretion events and placing them in the innermost region of clusters in almost hydrostatic equilibrium. On the other hand, this mixing is not efficient in standard SPH implementations, where the artificial viscosity term is modeled in such a way that mixing and turbulence are quickly dampened into heat, even when turbulent motions are subsonic and not followed by shocks (e.g. Dolag et al.2005). When artificial viscous terms in GADGET are modified to reduce this dampening outside shocks, the mixing becomes more efficient and the entropy profile starts flattening qualitatively in the same direction of what happens in the case of PPM.

the entropy profile starts moving qualitatively in the same direction of PPM codes (this work, and also Mitchell et al.2009). However, it is hard to alleviate the discrepancy just by adopting a different SPH implementation of viscosity, and a number of recent works is producing the overall picture that the difference might be much more substantial (e.g. Agertz et al.2007, Tasker et al.2008, Mitchell et al.2009, this work).

The difference in the entropy profiles that are found in the outer regions of clusters are likely due to a different reason. At these distances the only relevant mechanism of entropy production in our grid simulations is the passage of shocks and this lead us to the conclusion that shock heating in the external regions of clusters should work in a remarkably different way in the SPH and Eulerian codes. In the next Section we will thus discuss in detail the properties of shock waves in the different codes.

4.6 Shock Waves

4.6.1 Shock Detecting Schemes

The main goal of our comparison project is to explore the agreement between numerical codes in the characterization of the shock waves in simulated LSS and to investigate the main sources of uncertainties. As already discussed in the previous Chapter, several different shock detecting schemes have been explored in the literature: the TJ method (Ryu et al.2003 and Sec.3.5.2) and the VJ method (Vazza, Brunetti & Gheller 2008 and in Sec.3.5.3), and a *run-time* scheme based on the analysis analysis of entropy jump in SPH particles (Pfrommer et al.2006). In our comparison we adopt these 3 schemes; concerning the TJ method, we use that in its original form (Ryu et al.2003) when applied to TVD simulations.

The Entropy Jumps Method - EJ

In Sec.3.5.2 and in Sec.3.5.3 we already discussed the TJ and the VJ methods, in this Section we describe the EJ method, as presented in Pfrommer et al.(2006). One drawback of SPH is the artificial viscosity which has to deliver the necessary entropy injection in shocks. While the

parametrization of the artificial viscosity can be motivated in analogy with the Riemann problem, the shocks themselves are broadened over the SPH smoothing scale and they are not resolved as true discontinuities, even if post-shock quantities are calculated very accurately.

In the *entropy formulation* adopted in GADGET2 (Springel & Hernquist 2002), it turns natural to use the gas entropy as the main proxy to measure shocks Mach number in SPH. For one particle, the instantaneous injection rate of the entropic function due to shocks is computed, i.e. dA/dt, where A denotes the entropic function $A(s)$, defined by $P = A(s)\rho^{\gamma}$, and s gives the specific entropy. If the shock is broadened over a scale of order the SPH smoothing length $f_h h$ ($f_h \sim 2$ is a factor which has to be calibrated against shock-tubes), one can roughly estimate the time it takes the particle to pass through the broadened shock front as $\Delta t = f_h h/v$, where v can be approximated with the pre-shock velocity v_1. Assuming that the present particle temperature is a good approximation for the pre-shock temperature, it is possible to replace v_1 with $M_1 c_1$.

Based on these assumptions and using $\Delta A_1 \simeq \Delta t dA_1/dt$, the jump of the entropic function of the particle crossing a shock will be:

$$\frac{A_2}{A_1} = \frac{A_1 + \Delta A_1}{A_1} = 1 + \frac{f_h h}{M_1 c_1 A_1}\frac{dA_1}{dt}, \tag{4.1}$$

$$\frac{A_2}{A_1} = \frac{P_2}{P_1}\left(\frac{\rho_1}{\rho_2}\right)^{\gamma} = f_A(M_1), \tag{4.2}$$

where, using Equation 3.3 and 3.4 one has:

$$f_A(M_1) \equiv \frac{2\gamma M_1^2 - (\gamma - 1)}{\gamma + 1}\left[\frac{(\gamma - 1)M_1^2 + 2}{(\gamma + 1)M_1^2}\right]^{\gamma}, \tag{4.3}$$

that combined with Equations 4.1 and 4.2:

$$[f_A(M_1) - 1]\, M_1 = \frac{f_h h}{c_1 A_1}\frac{dA_1}{dt}. \tag{4.4}$$

The right-hand side of Eq.4.4 can be estimated individually for each particle, and Eq.4.4 allows to estimate their Mach number (see Pfrommer et al.2006 for details).

The EJ method is applied to the GADGET runs used in our project by adopting the original code provided by C. Pfrommer.

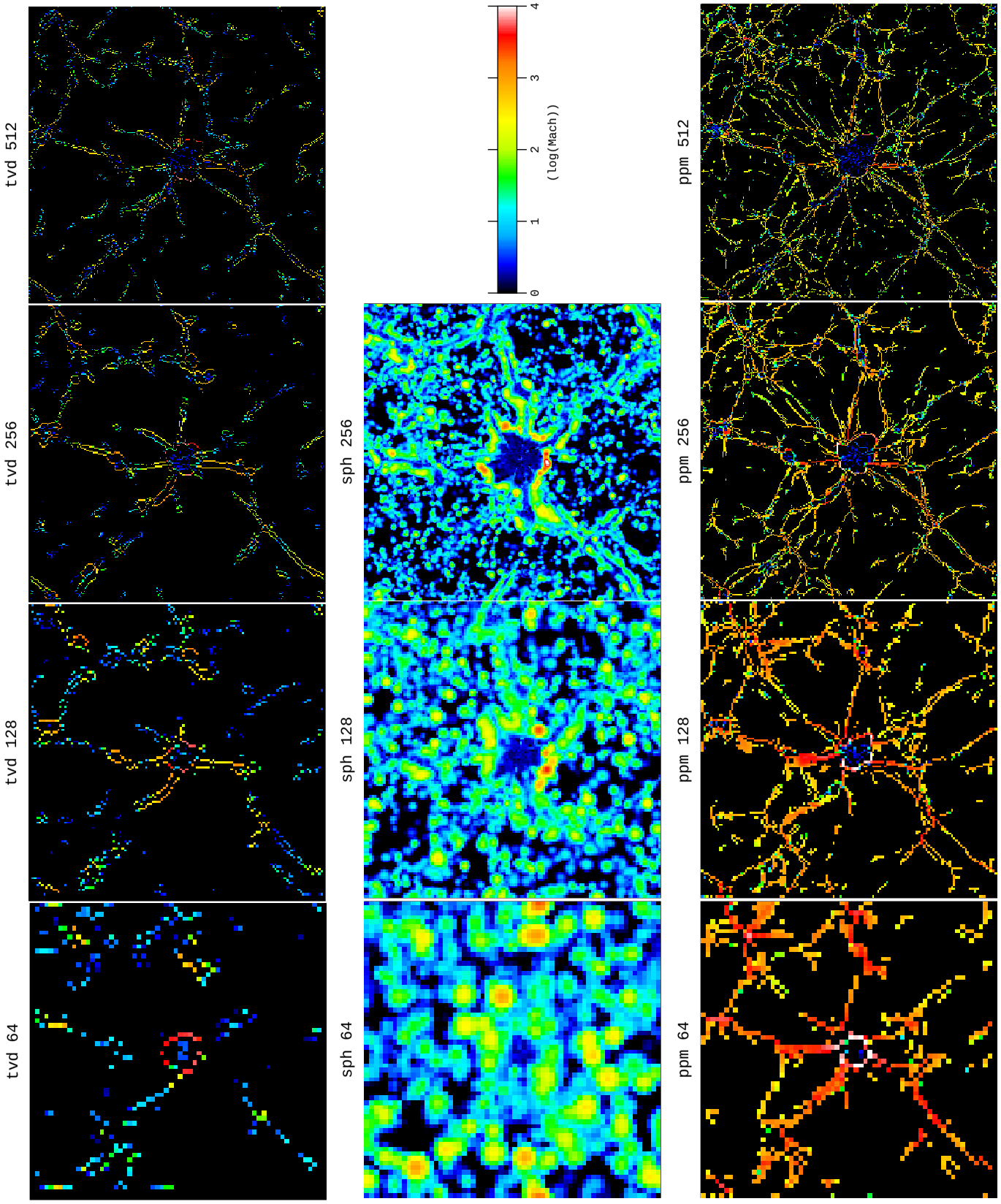

Figure 4.12: Slices crossing the simulated volume, showing maps of Mach number. From the left to right column, the width along the line of sight is 2200, 1100, 550 and 275kpc respectively. SPH data are interpolated as in Fig.5.9.

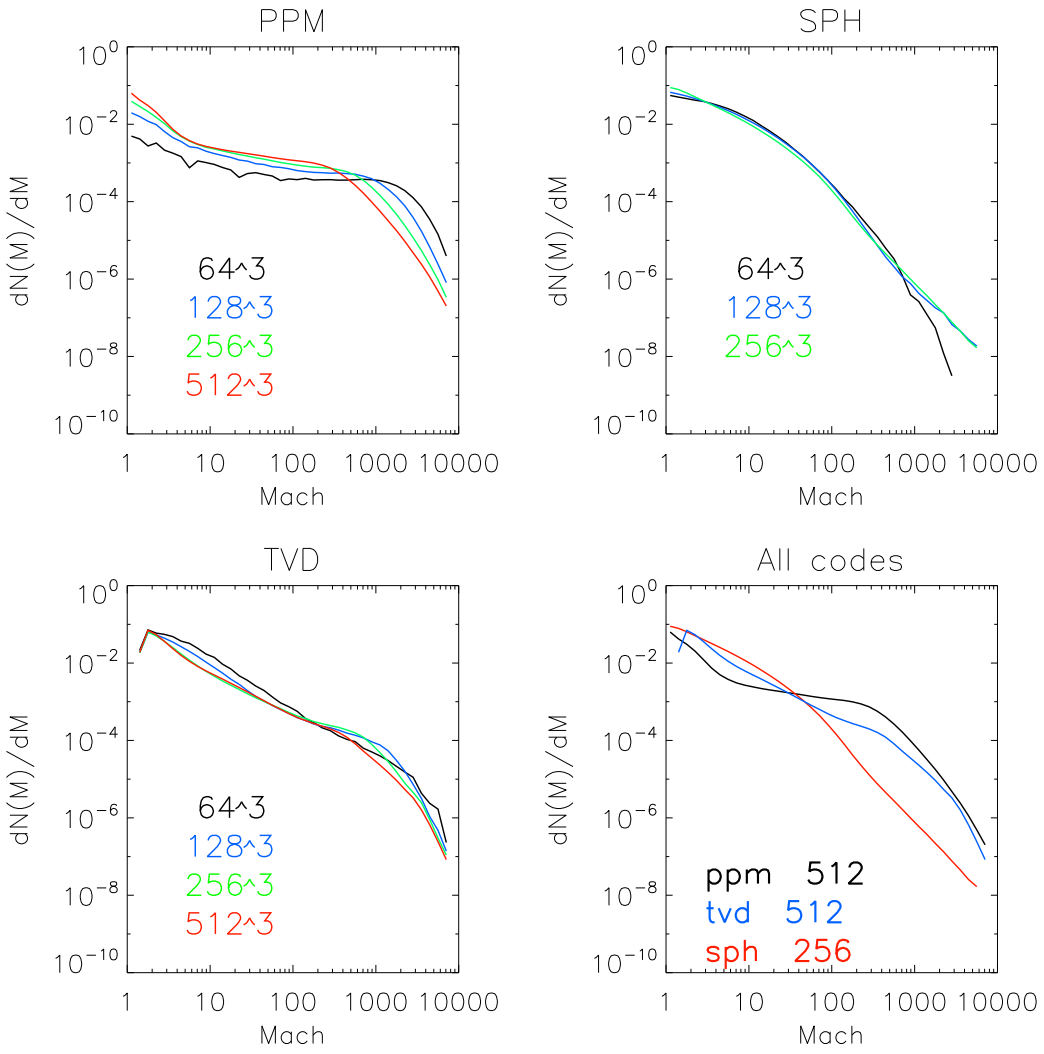

Figure 4.13: Number distribution of shocks at all resolutions and for all simulations. The lower right panel show the cross-convergence for the most resolved runs of all codes.

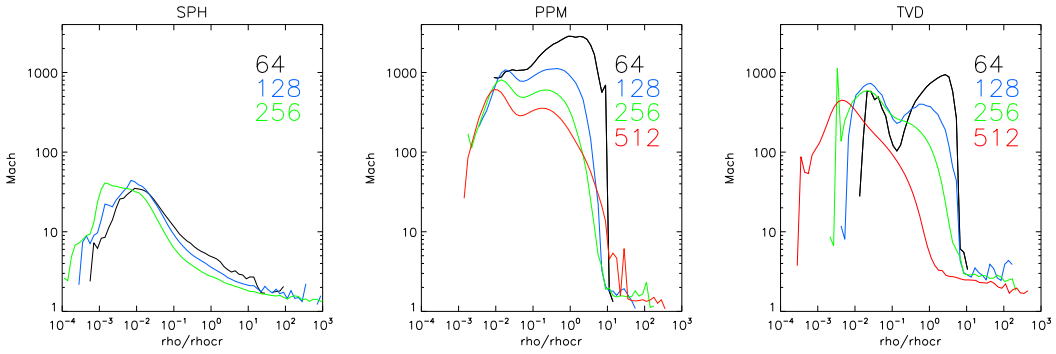

Figure 4.14: Mean mach number as a function of gas density, for all runs of the project.

4.6.2 Shocks Maps and Morphologies

As already pointed out, in order to keep the cross-comparison as simple as possible, the re-ionization background and radiative processes are not included in the simulations. As discussed in Sec.3.6.3, re-ionization is crucial when discussing shocks in the "real" universe, yet the simplification we follow here is aimed at reducing the possible sources of difference between the various runs. ENZO and TVD have a temperature floor at $T = 1K$ and $T = 2K$ in the outputting of data, respectively. The minimum measured temperature in GADGET is $T \sim 10K$, therefore, in all runs we expect to measure very strong shocks in low temperature regions.

Fig.4.12 shows mapping of the measured Mach number at shocks, according to TJ, the EJ and the VJ methods applied to TVD, GADGET and ENZO, respectively; as in Sec.4.5.1, SPH data are interpolated onto a regular grid to be compared with the results from grid codes. While inside clusters shocks look broadly similar when simulated in different codes, outside galaxy clusters differences between grid codes and SPH become very large. Remarkably, shocked particles in GADGET form in clumps, while in grid codes shocks trace sharp surfaces that trace the boundaries between the collapsing and the rarefying universe. In addition, due to the smaller resolution of SPH in external regions, shocks are on averaged more volume-filling than those found in grid codes.

4.6.3 Mach Number Distributions

Fig.4.13 shows the distribution of shock Mach number calculated from all runs using our projects. Distributions from the grid codes are remarkably flat, with an overall slope $\alpha \sim -0.6 \div -1$ (with $\alpha \equiv dlog(N)/dM$) in the range $1 < M < 1000$. GADGET shows much steeper distributions at all resolutions, with $\alpha \sim -1.5 \div -2$, and also presents the best "self-convergence". On the other hand in grid codes the convergence is not yet completely achieved at the cell resolution of 195 kpc, although in both codes there is no large evolution from the case of 256^3 to that of 512^3. Interestingly enough, in the case of SPH the increase in spatial resolution

causes the development of a tail of shocks at $M > 1000$, while an opposite trend is established in the case of grid codes.

The "cross-convergence" between the codes at the best resolutions is unsatisfactory. Differences are highlighted when plotting the volume weighted average Mach number of shocks as a function of gas density (Fig.4.14): the results from different codes become consistent only for $\rho/\rho_{cr} \geq 5 \div 10$, typical of galaxy clusters and clusters outskirts, where $< M > \leq 3$. Remarkably we find a different trend with decreasing density: in SPH $< M >$ is smoothly increasing towards lower density regions, while in grid codes the change in $< M >$ at lower densities is sharp, and depends on resolution (poor "cross" and "self-convergence"). The sharp increase of shock Mach number in the case of grid codes at $\rho/\rho_{cr} \approx 5 \div 10$ marks the difference in catching shocks in the cluster accreting regions between SPH and these codes and together with the morphological difference of shock boundaries between SPH and grid codes (Fig.4.12), and provides a viable explanation for the differences in entropy profiles discussed in Sec.4.5.4.

One of the reasons of the observed discrepancies between grid codes is the temperature floor that mainly affect low density regions. Due to the temperature floor at $T = 2K$ in TVD outputs, the TJ method is unable to measure shocks for lower temperatures. Lower temperature regions are present in ENZO due to the lower value of the temperature floor, $T = 1K$, and this is probably the responsible for the larger number of high Mach shocks observed in ENZO data; in this case temperature plays a role only through the estimate of the sound speed as shocks are characterized with the VJ method.

4.6.4 Energy Distributions.

The efficiency of thermalisation of gas matter at shocks is measured according to Eq.3.11 of Ryu et al.(2003), as a function of M and of pre-shock density and temperature. Panels in Fig.4.15 show the distributions of thermal flux for all simulations of the project (the lower right panel shows the cross-convergence for the most resolved runs). In this case the contribution coming from the low density regions is fairly negligible and

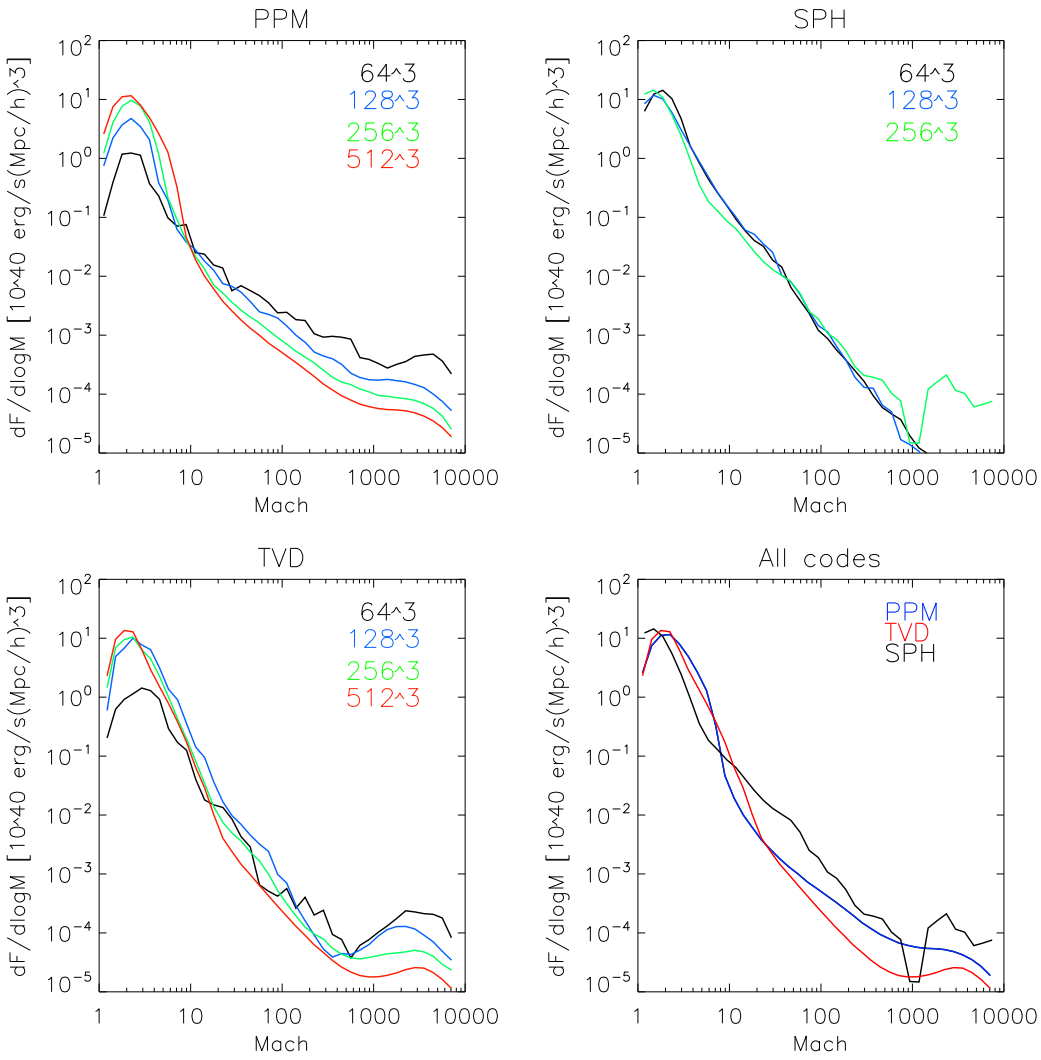

Figure 4.15: Distribution of the thermalized energy flux through shocks at all resolution and for all codes.

results are in better agreement. As for the case of number distributions, GADGET shows the largest degree of self-convergence, and a rather opposite trend with respect to grid codes in the case of strong shocks: in grid codes the energy processed at $M > 50-100$ decreases with increasing resolution, while in GADGET a small tail at $M > 500$ is developed with increasing resolution.

All the codes show a peak of thermalisation efficiency in the range $M \sim 1.5 \div 3$, consistently with previous studies (e.g. Ryu et al.2003, Pfrommer et al.2006, Vazza et al.2009), however "cross-convergence" at strong shocks, $M > 10$, is not yet achieved. We stress that the results reported in Fig.4.15 differ from those reported in Ryu et al.(2003) in the case with TVD and from Pfrommer et al.(2006) with SPH, in particular the slopes of the distribution are steeper. This highlights the effect of different assumptions in these original works (a fixed $T = 10^4 K$ floor in Ryu et al., and a run-time scheme in Pfrommer et al.) respect to our comparison project, where re-ionization is not modeled. In addition, the spatial resolutions achieved in the above works are different (in Ryu et al. the resolution is fixed to $\Delta x = 140 kpc$, while in Pfrommer et al. the peak resolution is as high as $\sim 10 kpc$) and also the assumed cosmology is slightly different (e.g. $\sigma_8 = 0.8$ in Ryu et al. and $\sigma_8 = 0.9$ in Pfrommer et al.).

4.6.5 Phase Diagrams for Shocked Regions.

The above results suggests that different codes and methods are quite consistent in terms of shocks morphologies, mean Mach number and thermal energy flux in the case of the innermost regions of galaxy clusters and filaments, while large discrepancies are found in the case of more rarefied environments.

In order to further clarify these issues we extract the phase diagram of shocked cells and of interpolated particles for the various simulations. Fig.4.16 and 4.6.4 show the flux-weighted mean Mach number and thermal flux (normalized to the total thermal flux in the cosmic volume) for the runs 64^3, 128^3 and 256^3.

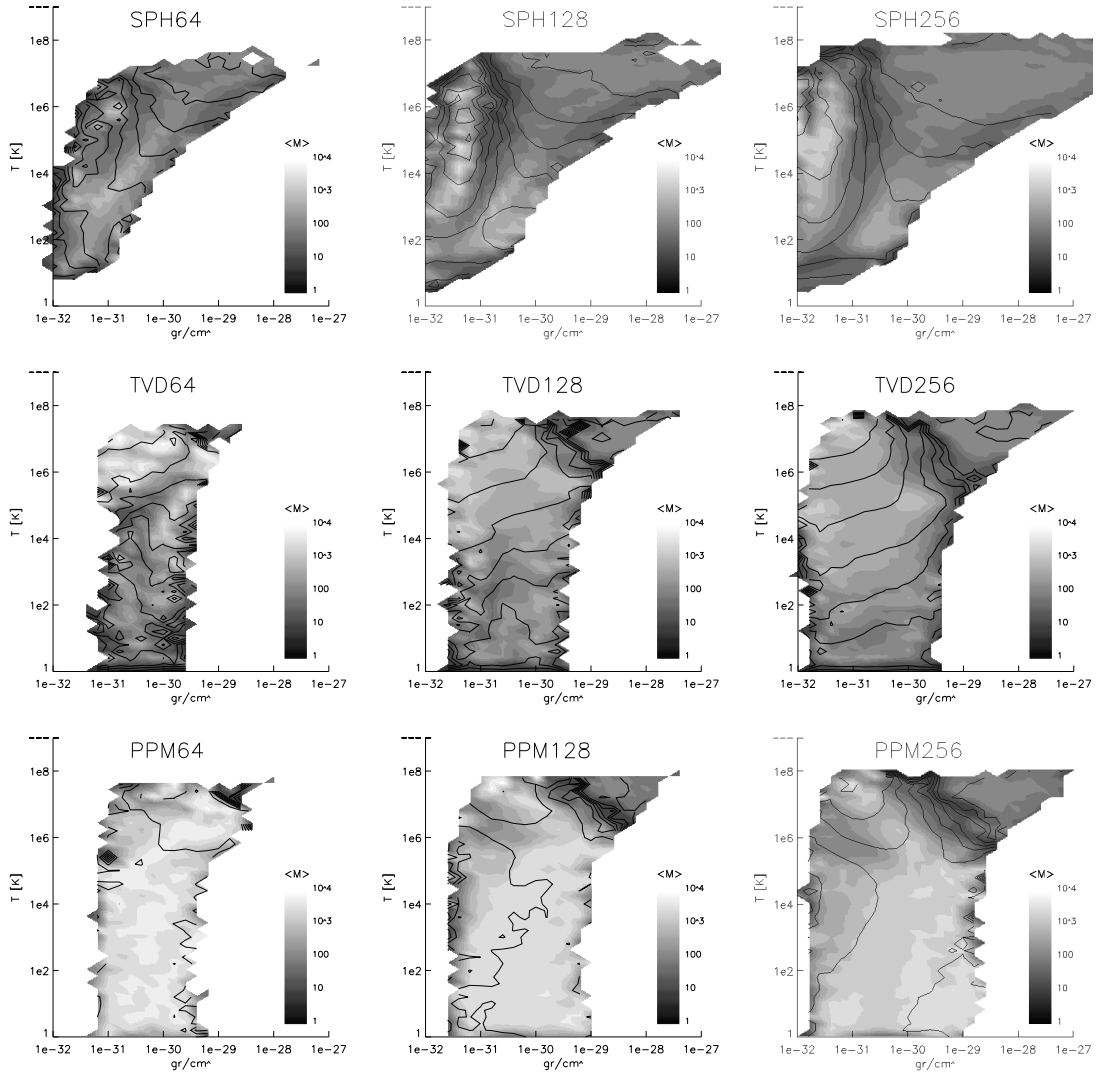

Figure 4.16: Phase diagrams for shocked cells in the simulations, color coding shows the flux-weighted average Mach number. Additional isocontours with a coarse binning in $\sqrt{(} < M >)$ space are shown for clarity.

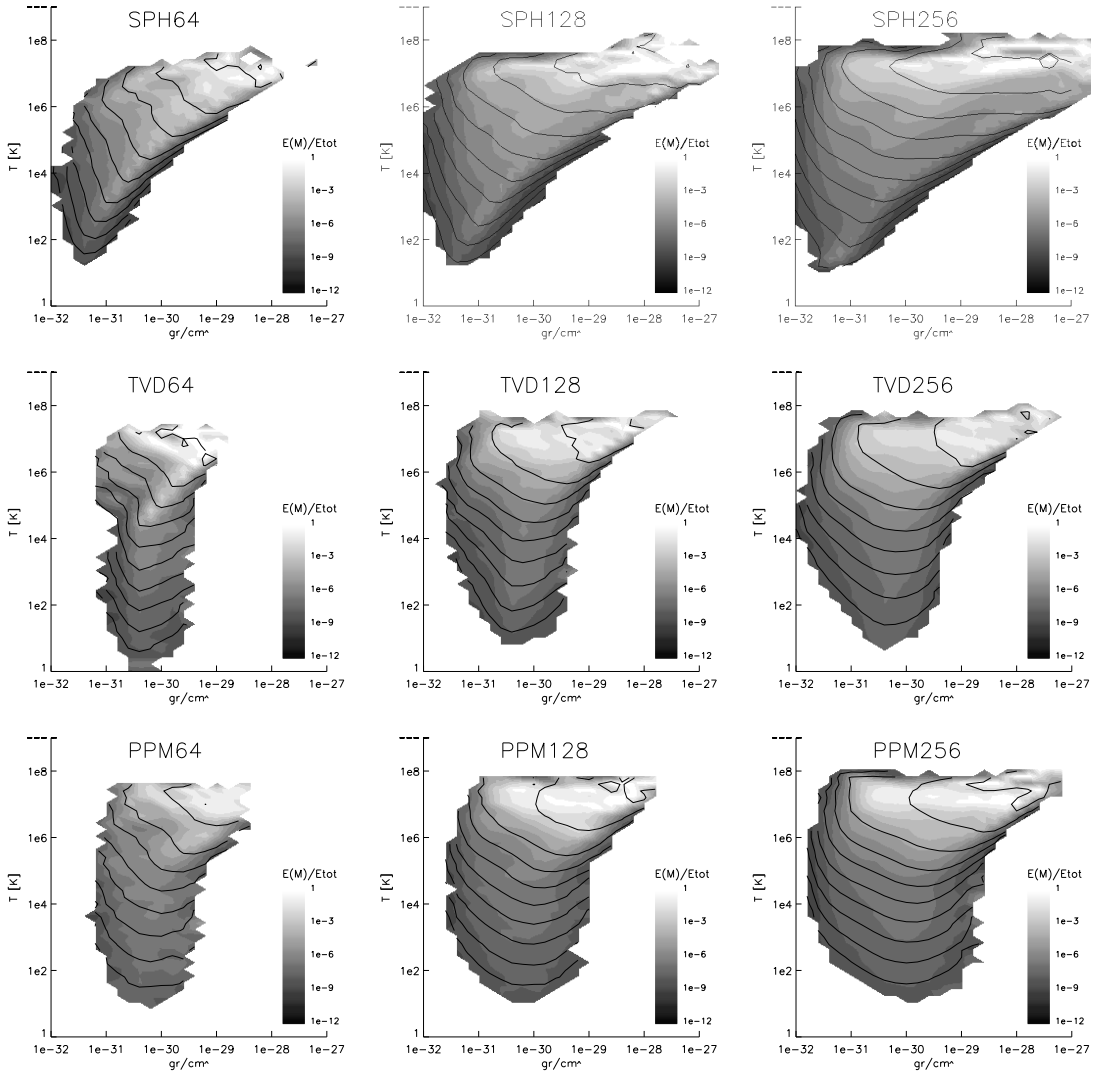

Figure 4.17: Phase diagrams for shocked cells in the simulations, color coding shows the ratio the thermal flux, normalized to the total flux within the simulations. Additional isocontours with a coarse binning in $\sqrt{(}E(M)/E_{tot})$ space are shown for clarity.

Different properties are found in the (ρ,T) plane. In the case of grid codes, as resolution is increased we observe the presence of a cluster of cells with $< M > \leq 10$ at the gas density and temperature typical of galaxy clusters and galaxy groups, while a broad region of strong shocks is found in lower densities. In GADGET, a similar "cluster" is found, but it extends also towards less dense regions, and the region of strong shocks is instead confined at densities in the range $10^{-32} gr/cm^3 < \rho < 10^{-31} < gr/cm^3$. This shows that similar cosmic environments (i.e. similar regions in the phase diagram) host shocks with different properties, depending on the adopted code, but also that the differences among grid codes are less relevant than differences with SPH.

Simulations show a better agreement when the dissipated energy flux is concerned, and roughly the bulk of dissipation is found for $\rho \geq 10^{-28} gr/cm^3$ for $T \geq 10^6$K; yet the region encompassing the bulk of the energy dissipation in the case of SPH is more extended than that in grid codes.

Panels in Fig.4.18 show the scatter plot for the post shock entropy vs M diagram, only for regions with $T > 100$ K in order to avoid artifacts due to the different temperature floor present in the output of the simulations. A concentration of high entropy and low Mach number shocks is common to all the simulated data, and marks the innermost region of galaxy clusters. In grid codes, a second region of concentration is also clearly present, in the range $200 < M < 10^4$, where entropy and Mach number appear correlated. Most of the points in this region trace *external* shocks, for which post shock entropy is correlated with M (Eq.3.5) for strong $M > 10$ shocks. The observed spread around this "power law" is likely due to a broad distribution of values of pre-shock entropy within the cells in the case of the grid simulations. This "phase" of shocked gas is *completely missing* in SPH, independently of the kernel used to interpolate SPH particles on the grid. The connection between the two concentrations observed in the (S,M) plane in the case of the grid codes with external and internal shocks is confirmed from Fig.4.19. In this Figure, we show the temperature map (for a sub volume of the 256^3 runs) and marks cells with

$10^{22} Kcm^2/gr^{2/3} < S < 10^{28} Kcm^2/gr^{2/3}$ and $M < 10$ in red color and cells with $S > 10^{24} Kcm^2/gr^{2/3}$ and $M > 100$ in blue color (see also Fig.4.18 for clear marks of the selected regions in the S vs M plane): only in the case of the grid codes the strong shocks that mark the correlation in the (S,M) plane are located systematically at the outskirts of galaxy clusters and filaments. These findings confirm suggest that a relevant amount of entropy is generated in grid codes as a sharp transition (in both space and time) at strong shocks surrounding clusters outskirts explaining the difference among grid and SPH codes in the case of the entropy profiles (Sec.4.5.4). A possible reason for that is pre-shock entropy generation in SPH (O'Shea et al.2005): since the artificial viscosity term is turned on wherever $\nabla \cdot \mathbf{v} < 0$, entropy in SPH particles can be generated continuously in time, even before an SPH particle crosses a shock region.

4.6.6 Shocks in Clusters and Cosmic Rays Acceleration

We analyze the properties of shock waves in the two massive clusters presented in Sec.4.5.4 and discuss the issue of CR acceleration at these shocks.

Fig.4.20 show maps of Mach number for a slice crossing the center of Cluster A. As in Fig.4.8, in the outskirts of this cluster the differences between grid and SPH approaches are very large, both in the strength of shocks and in their morphologies.

Fig.4.21 shows the flux-weighted mean Mach number profiles for cluster A and cluster B, as expected from all codes (only the best resolution in grid runs are shown). For $r < 0.5 R_{vir}$ the mean Mach number at shocks is similar for all codes, $< M > \sim 2$. At larger distances, the profiles in the case of grid codes sharply rises up to $M \sim 1000$, while a more gentle behavior is observed in GADGET; the profiles for $< M >$ are tightly connected with the entropy profiles shown in Sec.4.5.4.

Galaxy Clusters are important sources of CR in the universe through shock acceleration mechanism (see Sec.3.7.3). In order to explore the effect due to the uncertainties on the profile of shocks on the CR energy flux in different simulations, we apply the same recipe of Sec.3.7.3 and

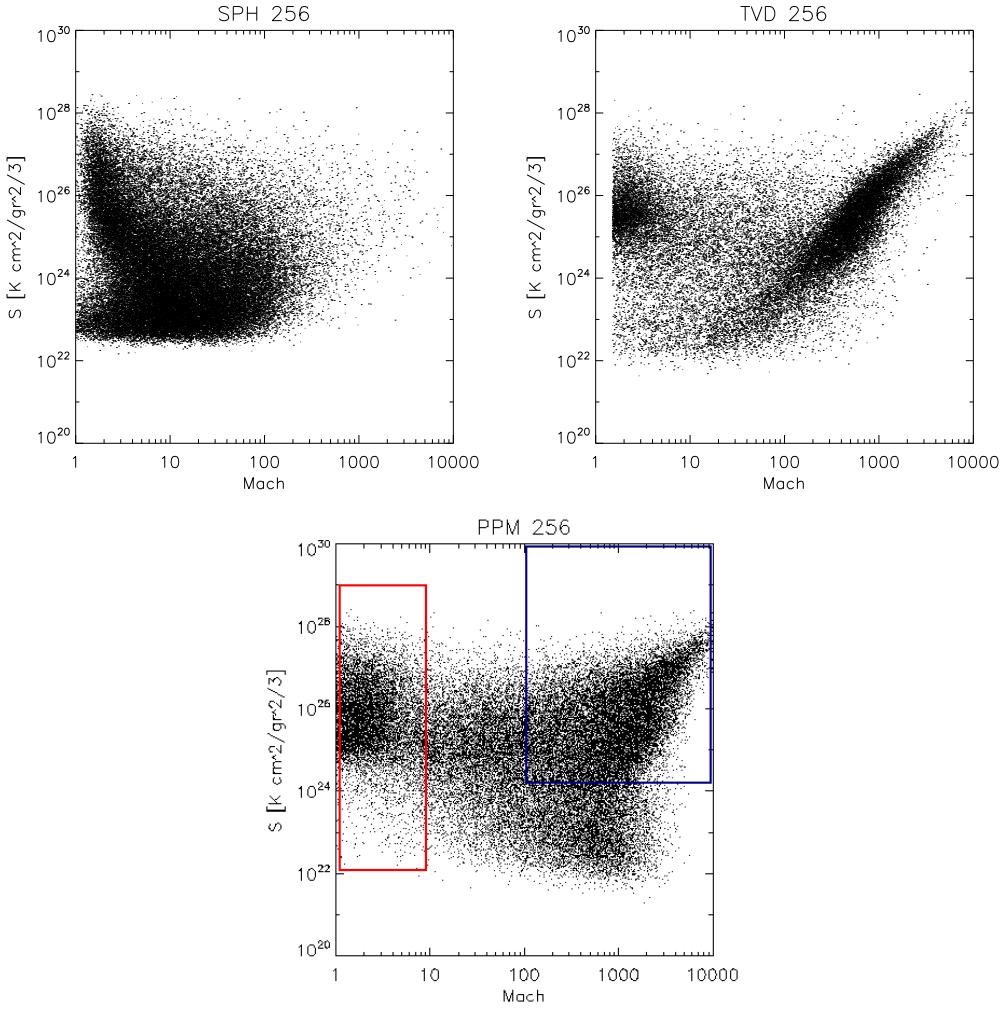

Figure 4.18: Mach vs Entropy diagrams for shocked regions of the 256^3 runs. In the bottom panel, we also highlight in red and blue colors the regions considered to produce maps of Fig.4.19.

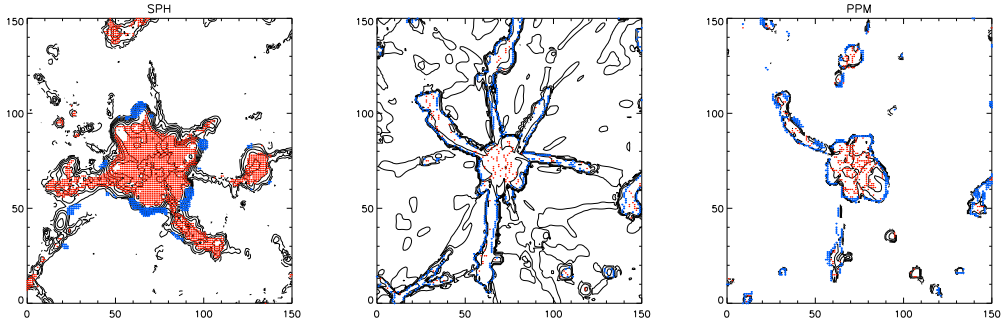

Figure 4.19: Gas temperature (isocontours) for slice of side $60 Mpc/h$ for the 256^3 runs. Color coding shows the location of cells in the different region of the S vs M plane, see text for explanations.

estimate the efficiency of CR injection in cluster A and cluster B. In order to make the comparison the more straightforward as possible, we take the value of M at shocks in all the simulations, and we compute the pre-shock temperature and gas density value by inverting the Rankine-Hugoniot jump conditions Eq.3.3 and Eq.3.4. Finally we apply the $\delta(M)$ and $\eta(M)$ function to calculate the thermal energy flux and the CR energy flux at shocks. As we already pointed out in Sec.3.7.3, this recipe for CR acceleration is quite simple, and do not take into account the back-reaction of accelerated CR on the thermal structure of the shock. However, this choice can be easily applied to all the simulations in our project.

The left panel in Fig.4.22 shows the profiles of the thermal energy flux, f_{th}, and of the CR energy flux, f_{CR}, through shells centered on cluster A. In the merging cluster (B), the different timing makes makes difficult to readily compare the profiles from different codes. The profiles for f_{th} and f_{CR} smoothly increases moving outwards from the center, up to maxima located around $\sim 0.6 - 0.8 R_{vir}$ where most of the energy is processed at shocks(with $f_{th} \sim 3 \cdot 10^{41} erg/s$ and $f_{CR} \sim 10^{41} erg/s$). Inside this radius, GADGET shows always a higher energy profile, with differences up to a factor ~ 10 with respect to grid codes. Inside this region, the average injection efficiency (shown in the Right panel of Fig.4.22) is similar in all codes, and smoothly goes from $f_{CR}/f_{th} < 0.1$ inside $0.1 R_{vir}$ to $f_{CR}/f_{th} \sim 0.7$ at $0.8 - 1 R_{vir}$, implying that the difference between grid and SPH codes inside the cluster is not due to a different Mach number of shocks found in the SPH simulations. Grid codes produce similar thermal and CR energy fluxes at all radii.

4.7 Discussion

In this Section we have presented preliminary results from a comparison project. We simulated a $(100 Mpc/h)^3$ volume at several resolutions, by applying two grid codes (ENZO and the TVD code by D.Ryu) and the SPH code GADGET2 (by V.Springel), and a set of identical cosmological initial conditions. The simulational setup is very simple (no re-ionization, no radiative processes, no Adaptive Mesh Refinement

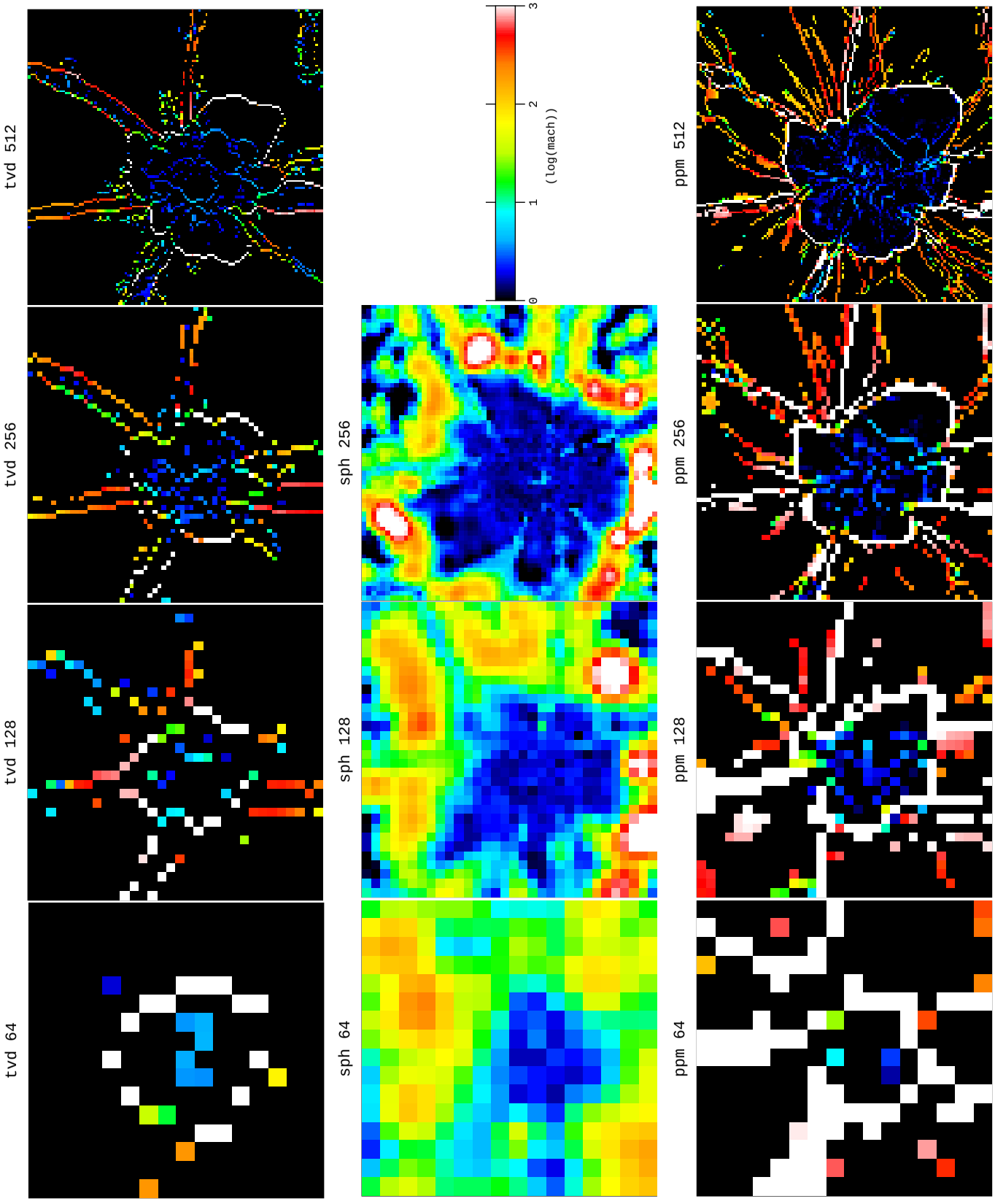

Figure 4.20: Same as in Fig.4.12, but for a $25 Mpc/h$ region around a massive galaxy cluster.

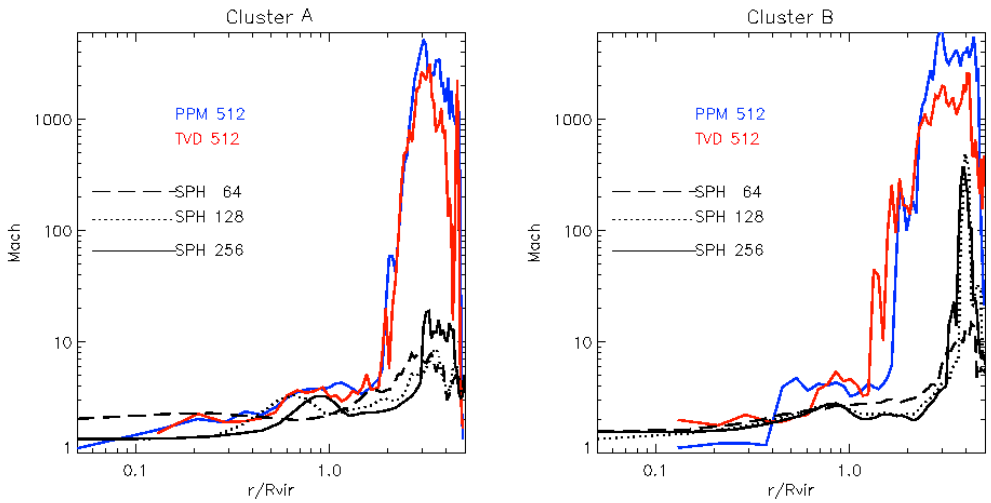

Figure 4.21: Profiles of energy flux-weighted average Mach number for cluster A (*left* panel) and cluster B (*right* panel).

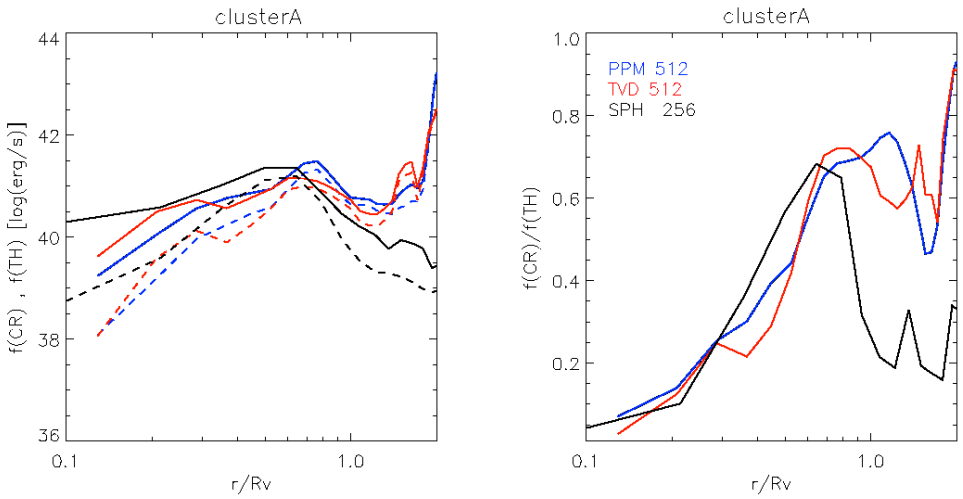

Figure 4.22: *Left:* profiles of thermal energy flux (solid lines) and of CR energy flux (dashed lines) for cluster A. The profiles are the total flux across the shells centered on the clusters. Black lines are for GADGET (256^3), blue lines are for ENZO (512^3) and red lines are for TVD (512^3). *Right:* profiles of the injection efficiency f_{CR}/f_{th} for cluster A.

for grid codes) and thus particularly suitable to study the convergence between complementary numerical approaches, and to explore the reasons for differences.

Thermal Properties:

As expected, an overall agreement between the different codes is measured, provided that the DM mass resolution is large enough (i.e. of the order of $\sim 4 \cdot 10^{10} M_{\odot}/h$). In particular, we find a good cross convergence in the following measures:

* in grid codes, the mass function of halos equals that of GADGET (which is essentially converged at all resolutions) within ≈ 10 per cent for $M \geq 10^{13} M_{\odot}$ with a mesh resolution of $195 kpc/h$, and for $M \geq 10^{14} M_{\odot}$ with a mesh resolution of $390 kpc/h$ (note that TVD uses only 1/8 of DM particles, with respect to ENZO, to achieve the same convergence). The dependence on resolutions we observe in ENZO and GADGET are similar to those found in O'Shea et al.(2005) and in Heitmann et al.(2008);
* the convergence in the position of DM/gas clumps is generally better than 500 kpc for all runs with a DM mass resolution $\leq 4 \cdot 10^{10} M_{\odot}/h$. This scatter is slightly larger than that observed in Heitmann et al.(2008);
* the gas density distribution is in agreement (within $10 - 20$ per cent) for densities in the range $10^{-31} gr/cm^3 < \rho < 10^{-28} gr/cm^3$, for runs with a DM mass resolution $\leq 4 \cdot 10^{10} M_{\odot}/h$. At larger gas densities, the agreement is within a factor $2 - 3$. These results globally agree with Heitmann et al.(2008) findings;
* the gas temperature distribution is in agreement within $5 - 10$ per cent accuracy for $T > 10^6 K$, for runs with a DM mass resolution $\leq 4 \cdot 10^{10} M_{\odot}/h$; this is in line with Kang et al.(1994) findings;
* for the galaxy clusters we analyzed in Sec.4.5.4, gas density and gas temperature profiles inside R_{vir} are in compatible within $10 - 20$ cent scatter. Slight time delays from simulation to simulation are expected to drive relevant differences when comparing outputs at formally the

same cosmic time; this is consistent with Frenk et al.(1999).

On the other hand, large differences are found in the following measures:

* the gas density and gas temperature distribution in regions with $\rho < 10^{-31} gr/cm^3$ and $T < 10^6 K$ are in disagreement by $2-3$ orders of magnitude between simulation (using simulations with DM mass resolution $\leq 4 \cdot 10^{10} M_\odot/h$). For the temperature distributions, a different shape is found between SPH and grid codes;
* outside R_{vir}, grid codes present gas density and gas temperature profiles different to GADGET, which produces higher densities and temperatures (of a factor ≈ 2);
* the entropy profiles in grid codes show a sharp peak at $\sim 2R_{vir}$, while in GADGET the value of entropy at this radius is lower (by a factor ≈ 5) and the profile is relatively smooth;
* the entropy profile inside $0.3R_{vir}$ in GADGET is steeper than in ENZO, where a hint of entropy plateau is observed (within the formal resolution limit); this is consistent with Frenk et al.(1999) findings.

Shocks and CR acceleration:

We also analyzed the properties of shock waves in the different simulations by measuring the Mach number according to the shock detecting scheme specifically conceived for each simulation: the Entropy Jump method (Pfrommer et al.2006) for GADGET, the Temperature Jump method (Ryu et al.2003) for TVD, and the Velocity Jump method for ENZO (Vazza et al.2008). Our main findings are:

* at all resolutions, shocks in PPM and TVD show qualitatively similar morphologies, whereas shocks in GADGET look substantially different (mostly blob-like);
* the average Mach number of shocks in regions with densities $\rho > 10^{-28} gr/cm^3$ in all codes are in the range $1 < M < 3$. For smaller gas densities, all codes show different behaviors with resolution: in general the values of $< M >$ found in grid codes are larger;
* all codes produce steep Mach number distributions. GADGET has the largest number of shocks with $M < 100$ and the smaller number

of shocks with $M > 100$; the total volume occupied by shocks at the highest available resolutions is ~ 20 per cent;

* the distributions of the thermal energy flux processed at shocks calculated in the simulations with the highest resolutions are broadly similar, with a bulk of energy flux at $\sim 10^{41} ergs/s \cdot cm^3 \cdot (Mpc/h)^3$ (within a 5 per cent scatter). Overall the energy flux calculated in grid codes is $5 \div 10$ times larger at $M < 10$ and $2 \div 10$ times lower at $M > 10$ shocks;
* (ρ,T) and (S,M) phase diagrams show that the different codes produce different shock waves in the same cosmic environments (except for the over density and temperature typical of the innermost region of galaxy clusters). In grid codes we find that shocks that form in the outskirts of LSS fill a particular region of the S vs M diagram, showing a clear correlation between the post-shock entropy and M, as expected by Rankine-Hugoniot jump conditions. This region is essentially not populated in SPH simulated data.
* The $< M >$ profiles extracted from the different codes inside clusters are broadly in agreement within $< 0.5 R_{vir}$, with $< M > \sim 2$. For larger radii, the differences are larger: at $\approx 2 R_{vir}$, grid codes produce a sharp increase in terms of shock strength (with $< M > \sim 500$), while a much smoother behavior is found in the case of GADGET;
* we compute the CR injection efficiency at shocks, using the same simplified approach for acceleration (that of Ryu et al.2003). We find that grid codes produce a consistent shocked-thermal energy flux and CR energy flux at all radii. GADGET leads to an overestimate of this flux with respect to grid codes inside $\approx 0.8 R_{vir}$ (up to a factor of 10) and to an underestimate of this flux (up to a factor of 100) outside this radius.

Overall, while some of our findings concerning the DM and baryon properties of the simulated volume are in line with previous works on this issue, a number of interesting new results are found.

Particularly intriguing is the apparent connection between the differences found in the characterization of external accretion shocks and that in the

entropy profiles for the same regions. The implementation of artificial viscosity in GADGET (and, more in general, in SPH) allows to reproduce ideal shock tube tests (e.g. Tasker et al.2008), however a non-negligible amount of pre-shock entropy generation may occur in the much complex case of cosmological numerical simulations (e.g. O'Shea et al.2005).

This picture is qualitatively in agreement with the tests in O'Shea et al.(2005), that used the ZEUS version of ENZO (which employs artificial viscosity to capture shocks) to simulated Zeldovich pancake. In this work it was found that the artificial viscosity makes temperature jumps outside the pancake significantly broader with respect to those found with the standard ENZO PPM, and produces an increase of entropy even during the phase of formally adiabatic compression.

Chapter 5

Turbulence in Simulated Galaxy Clusters

5.1 Introduction

Mergers and infall of halos during the process of galaxy clusters formation can induce large–scale bulk flows with velocities of the order of ~ 1000 km s^{-1} or larger, resulting in complex hydrodynamic flows where most of the kinetic energy is dissipated to heat at shocks, and may excite turbulent gas motions. Unluckily, due to the abrupt breaking of the main instrument on board of the Astro-E2 mission, the direct detection of turbulent fields through the broadening of iron lines profile (e.g. Inogamov & Sunyaev 2003) has to be postponed to the future.

Early numerical simulations of merging clusters (e.g. Schindler Mueller 1993; Roettiger et al.1997; Ricker & Sarazin 2001) provide a detailed description of the gas-dynamics during a merger event.

Despite the potentially significant relevance of turbulence in the ICM (see Sec.2.3, this issue has received attention in hydrodynamical simulations only recently. One reason for this is that 3D turbulence is difficult to resolve in any numerical scheme, because some finite numerical viscosity is always introduced in these schemes, limiting the Reynolds numbers that can still be adequately represented. The lack of spatial resolution within the simulated volume can also artificially suppress small scale chaotic motions naturally induced by accretion processes.

In this Chapter we present detailed studies of turbulent velocity field

in the ICM of simulated galaxy clusters, by using two complementary approaches: SPH (using GADGET2) and PPM (using ENZO) simulations. The comparison between the results obtained with these two different schemes will allow us to better understand at which level present day cosmological codes can describe turbulent fields that should be present in the ICM.

5.2 Turbulent Velocity Field in GADGET.

We present a study of the characterization of turbulent velocity fields in the ICM using a data-set of 21 galaxy clusters simulated with GADGET2. Our study makes use of a method to reduce artificial viscosity in SPH is introduced and of an algorithm to detect turbulent motions in the ICM. Given the fairly large sample of galaxy clusters, we are particularly interested in the scaling laws between the turbulent energy content of the gas particles and the cluster thermal properties and in a comparison between semi-analytical models. In the Appendix (Sec.7) we report an application to the issue of radio halos in galaxy clusters.

5.2.1 Numerical Methods.

The smoothed particle hydrodynamics method treats shocks with an artificial viscosity, which leads to a broadening of shocks and a relatively rapid vorticity decay (Sec.4.2.3). The standard parametrization of this viscosity (Monaghan & Gingold 1983) makes the scheme comparatively viscous; it smooths out small-scale velocity fluctuations and viciously damps random gas motions well above the nominal resolution limit. This hampers the ability of standard SPH to develop fluid turbulence down to the smallest resolved scales.

However, the numerical viscosity of SPH can be reduced by using a more sophisticated parametrization of the artificial viscosity. Ideally, the viscosity should only be present in a hydrodynamical shock, but otherwise it should be negligibly small. To come closer to this goal, Morris & Monaghan (1997) proposed a numerical scheme where the artificial viscosity is treated as an independent dynamical variable for each particle,

with a source term triggered by shocks, and a term that allows the viscosity to decay away from shocks. In this way shocks can still be captured properly, while in the bulk of the simulated volume, the effective viscosity is lower than in standard SPH. We apply this scheme in high-resolution SPH simulations of galaxy clusters formation.

The usual parametrization of the artificial viscosity for an interaction of two particles a and b includes terms to mimic a shear and bulk viscosity. For standard cosmological SPH simulations, it can be written as (e.g. Monaghan & Gingold 1983)

$$\Pi_{ab} = \frac{-\alpha c_{ab}\mu_{ab} + \beta\mu_{ab}^2}{\rho_{ab}} f_{ab}, \tag{5.1}$$

for $\vec{r}_{ab} \cdot \vec{v}_{ab} \leq 0$ and $\Pi_{ab} = 0$ otherwise, i.e. the pair-wise viscosity is only non-zero if the particle are approaching each other. Here

$$\mu_{ab} = \frac{h_{ab}\vec{v}_{ab} \cdot \vec{r}_{ab}}{\vec{r}_{ab}^2 + \eta^2}, \tag{5.2}$$

c_{ab} is the arithmetic mean of the two sound speeds, ρ_{ab} is the average of the densities, h_{ab} is the arithmetic mean of the smoothing lengths, and $\vec{r}_{ab} = \vec{r}_a - \vec{r}_b$ and $\vec{v}_{ab} = \vec{v}_a - \vec{v}_b$ are the inter-particle distance and relative velocity, respectively. We have also included a viscosity-limiter f_{ab}, which is often used to suppress the viscosity locally in regions of strong shear flows, as measure by

$$f_i = \frac{|\left\langle \vec{\nabla} \cdot \vec{v} \right\rangle_i|}{|\left\langle \vec{\nabla} \cdot \vec{v} \right\rangle_i| + |\left\langle \vec{\nabla} \times \vec{v} \right\rangle_i| + \sigma_i}, \tag{5.3}$$

which can help to avoid spurious angular momentum and vorticity transport in gas disks (Steinmetz 1996). Note however that the parameters describing the viscosity with common choices $\alpha = 0.75 - 1.0$, $\beta = 2\alpha$ stay here fixed in time. Additional $\eta = 0.01 h_{ab}$ and $\sigma_i = 0.0001 c_i/h_i$ are the usual choice to avoid singularities in the formulations. This then defines the 'standard' viscosity scheme usually employed in cosmological SPH simulations; we refer to runs performed with this viscosity scheme as *ovisc* simulations.

The idea proposed by Morris & Monaghan (1997) is to give every particle its own viscosity parameter α_i, which is allowed to evolve with time

according to

$$\frac{\mathrm{d}\alpha_i}{\mathrm{d}t} = -\frac{\alpha_i - \alpha_{\rm min}}{\tau} + S_i. \tag{5.4}$$

This causes α_i to decay to a minimum value $\alpha_{\rm min}$ with an e-folding time τ, while the source term S_i is meant to make α_i rapidly grow when a particle approaches a shock. For the decay timescale, Morris & Monaghan (1997) proposed to use

$$\tau = c_i h_i \,/\, l, \tag{5.5}$$

where h_i is the smoothing length, c_i the sound speed and l a free parameter which determines on how many information crossing times the viscosity decays. For an ideal gas and a strong shock, this time scale can be related to a length scale $\delta = 0.447/l$ (in units of the smoothing length h_i) on which the viscosity parameter decays behind the shock front. For the source term S_i, we follow Morris & Monaghan (1997) and adopt

$$S_i = S^* f_i \, \max(0, -|\left\langle \vec{\nabla} \cdot \vec{v} \right\rangle_i|), \tag{5.6}$$

where $\left\langle \vec{\nabla} \cdot \vec{v} \right\rangle_i$ denotes the usual SPH estimate of the divergence around the particle i. Note that it would in principle be possible to use more sophisticated shock detection schemes here, but the simple criterion based on the convergence of the flow is already working well in most cases. We refer to simulations carried our with this 'reduced' viscosity scheme as *lvisc* runs.

Usually we set $S^* = 0.75$ and choose $l = 1$. We also restrict α_i to be in the range $\alpha_{\rm min} = 0.01$ and $\alpha_{\rm max} = 0.75$; increasing S^* can give a faster response of the artificial viscosity to the shock switch without inducing higher viscosity than necessary elsewhere. We also replace α in equation 5.1 by the arithmetic mean α_{ab} of two interacting particles. Depending on the problem, we initialize α_i at the start of a simulation either with $\alpha_{\rm min}$ or $\alpha_{\rm max}$, depending on whether or not there are already shocks present in the initial conditions, respectively.

As a variant of the standard parametrization of the artificial viscosity, GADGET-2 can use a formulation proposed by Morris & Monaghan (1997) based on an analogy with Riemann solutions of compressible gas

dynamics. In this case, μ_{ab} is defined as

$$\mu_{ab} = \frac{\vec{v}_{ab} \cdot \vec{r}_{ab}}{|\vec{r}_{ab}|}, \tag{5.7}$$

and one introduces a signal velocity $v_{ab}^{\rm sig}$, for example in the form

$$v_{ab}^{\rm sig} = c_a + c_b - 3\mu_{ab}. \tag{5.8}$$

The resulting viscosity term then changes into

$$\Pi_{ab} = \frac{-0.5\alpha_{ab} v_{ab}^{sig} \mu_{ab}}{\rho_{ab}} f_{ab}. \tag{5.9}$$

We have performed simulations using this signal velocity based artificial viscosity and found that it performs well in all test problems we examined so far, while in some cases it performed slightly better, in particular avoiding post shock oscillations in a more robust way. We refer to simulations performed using this 'signal velocity' based viscosity scheme as *svisc* simulations.

Studies of the performance of GADGET2 with implemented viscosity can be found in Dolag et al.(2005).

5.2.2 The Sample of Clusters

We have performed high-resolution hydrodynamical re-simulations of the formation of 21 galaxy clusters. The clusters span a mass-range from $10^{14}\,h^{-1}{\rm M}_\odot$ to $2.3 \times 10^{15} h^{-1}{\rm M}_\odot$ and have originally been selected from a DM–only simulation with box-size $479\,h^{-1}$Mpc of a flat ΛCDM model with $\Omega_0 = 0.3$, $h = 0.7$, $\sigma_8 = 0.9$ and $\Omega_{\rm b} = 0.04$. Using the 'Zoomed Initial Conditions' technique (Tormen et al.1997), we then re-simulated the clusters with higher mass and force resolution by populating their Lagrangian regions in the initial conditions with more particles, adding small-scale power appropriately. The selection of the initial region was carried out with an iterative process, involving several low resolution DM-only re-simulations to optimize the simulated volume. The iterative cleaning process ensured that all clusters are free from contaminating boundary effects out to at least 3 - 5 virial radii. Gas was introduced

in the high–resolution region by splitting each parent particle into a gas and a DM particle. The final mass–resolution of these simulations was $m_{\rm DM} = 1.13 \times 10^9\, h^{-1}{\rm M}_\odot$ and $m_{\rm gas} = 1.7 \times 10^8\, h^{-1}{\rm M}_\odot$ for dark matter and gas within the high–resolution region, respectively. The clusters were hence resolved with between 2×10^5 and 4×10^6 particles, depending on their final mass. Tab- 5.1 gives details on the properties of the 9 most massive galaxy clusters in the sample. The gravitational softening length was $\epsilon = 5.0\, h^{-1}$kpc (Plummer–equivalent), kept fixed in physical units at low redshift and switched to constant comoving softening of $\epsilon = 30.0\, h^{-1}$kpc at $z \geq 5$.

We computed three sets of simulations using adiabatic gas dynamics with and extended version of GADGET2, where each cluster was simulated three times with different prescriptions for the artificial viscosity: a standard formulation of artificial viscosity within SPH (*ovisc*), a parametrization based on signal velocity, but with a fixed coefficient for the viscosity (*svisc*), and a the time dependent viscosity scheme, which we expect to lead to lower residual numerical viscosity (*lvisc*).

Table 5.1: Main characteristics of the 9 most massive galaxy clusters in the simulations (data) are referred to the *lvisc* runs. Column 1: identification label. Columns 2 and 3: mass of the dark matter ($M_{\rm DM}$) and gas ($M_{\rm gas}$) components inside the virial radius. Column 4: virial radius $R_{\rm v}$. Column 5: X-ray luminosity inside the virial radius L_x. Columns 6: mass-weighted temperature (T_{MW}).

Clusters	$M_{\rm DM}(10^{14}M_\odot/h)$	$M_{\rm GAS}(10^{13}M_\odot/h)$	$R_{\rm v}$ (kpc/h)	$L_x(10^{44}erg/s)$	T_{MW}(keV)
g1	14.5	17.0	2355	21.3	7.1
g8	22.4	19.8	2705	32.1	9.1
g51	13.0	11.5	2251	17.9	6.3
g72	13.4	11.9	2280	14.1	5.8
g676	1.0	0.91	972	1.4	1.3
g914	1.0	0.91	971	1.7	1.3
g1542	1.0	0.90	967	1.4	1.2
g3344	1.1	0.96	993	1.4	1.3
g6212	1.1	1.00	1006	1.5	1.3

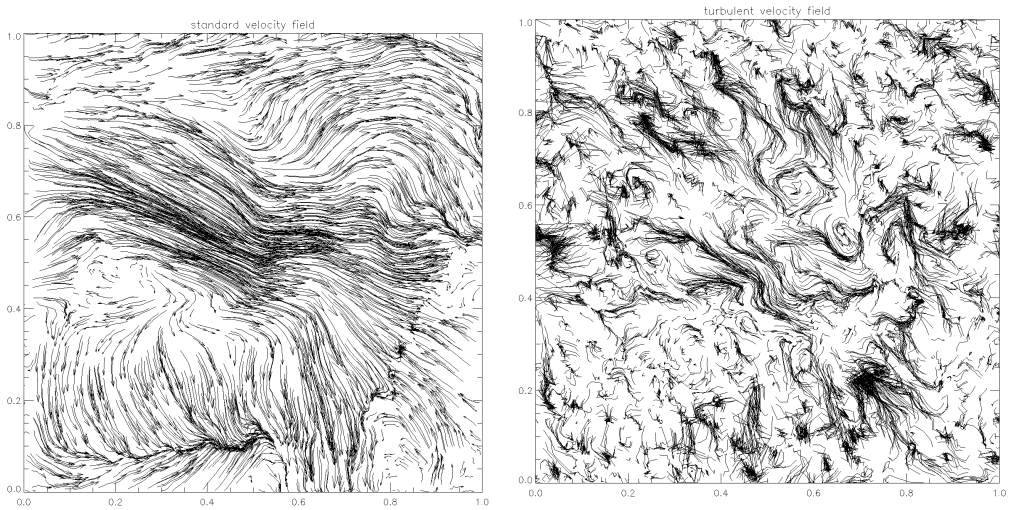

Figure 5.1: Total gas velocity field (*left*) and local velocity dispersion (*right*) for a slice of side $1Mpc$ crossing the center of a simulated galaxy cluster.

5.2.3 Identifying Turbulence

The real case of the ICM is very complex and the gravitational field of the host galaxy cluster drives density and temperature gradients, and also many bulk motions of accreted substructures.

A crucial issue in describing turbulent fields in the ICM is the distinction between large-scale coherent velocity field and small-scale "random" motions. The simplest possible procedure to define a mean velocity field is to take the mean velocity computed for the cluster volume (calculated, for example, within a sphere of radius $R_{\rm vir}$) as the coherent velocity field, and then to define the turbulent velocity component as a residual to this velocity. This simple approach (hereafter *standard* approach) has been widely employed in previous works (e.g. Norman & Bryan 1999, Sunyaev et al.2003) and successfully led to identify turbulence in simulated galaxy clusters. However, an obvious problem with this method is that this global subtraction may fail to distinguish turbulent motions from pure laminar bulk flows, that are quite common in cosmological simulations, where the growth of clusters is driven by the accretion of sub-halos.

In order to avoid this problem, a mean local velocity field (smoothed on scales smaller than the whole box) can be used, and consequently a field of

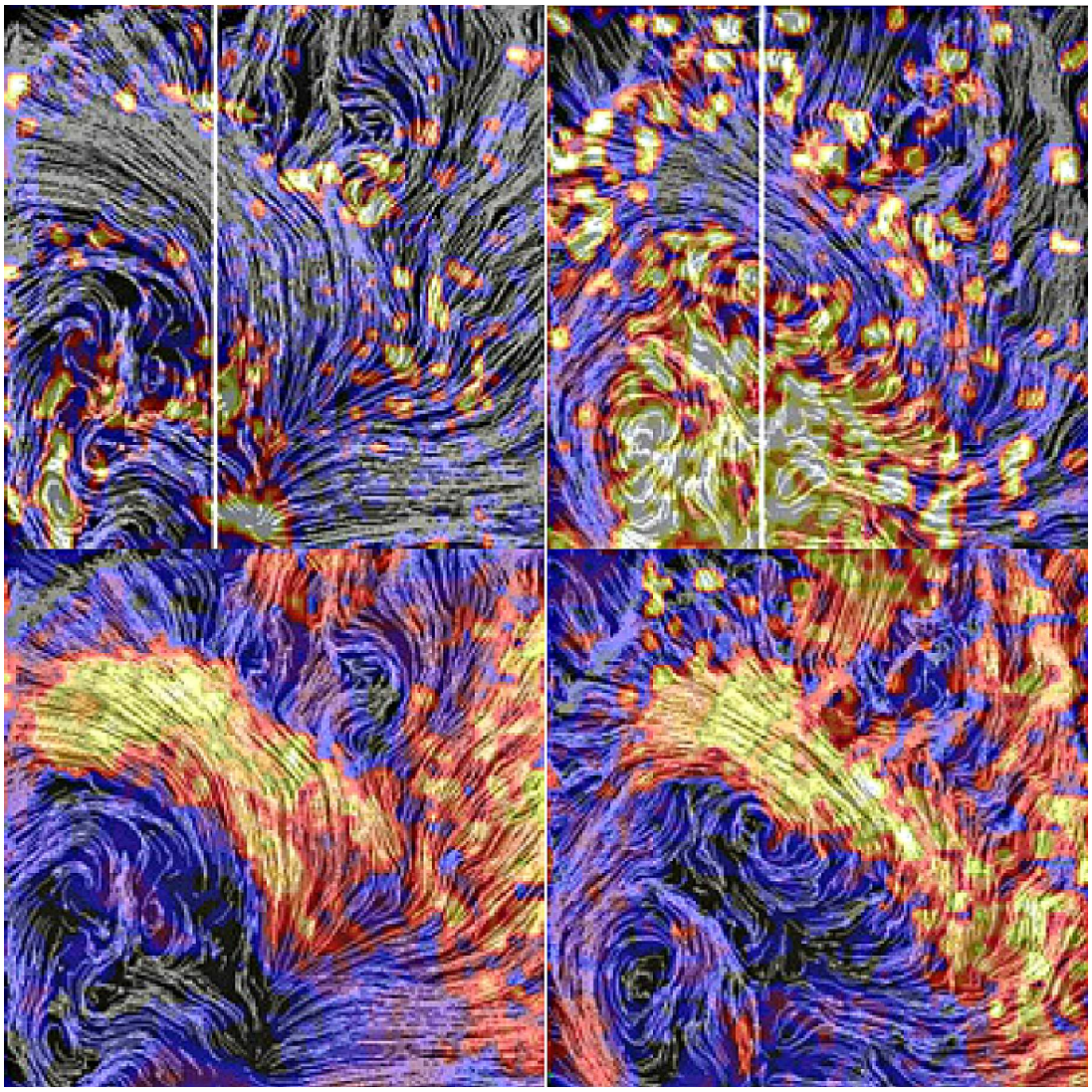

Figure 5.2: Gas velocity field in a slice through the central Mpc of a cluster simulation *g72* after subtracting the *global* mean bulk velocity of the cluster. The panel on the left is for a run with the standard viscosity of SPH while the panel on the right shows the result for the low viscosity scheme. The underlying color maps represent the turbulent kinetic energy content of particles. For both cases, the cluster center is just below the lower-left corner of the images. The vertical lines show where the 1–dimensional profile for the simulated radio–emission of fig.7.5 are taken.

velocity fluctuation can be built by subtracting this mean–local velocity, $\bar{v}(\overline{x})$, to the individual velocities, v_a, of each gas particle a. In general, we note that this approach mimics the "standard" one in the case that the smoothing scale for $\bar{v}(\bar{x})$ is large enough. If the smoothing scale is chosen too small, one may risk loosing large turbulent motions in the system, if they are present, but this does at least not overestimate the level of turbulence.

Following this second approach (hereafter *local–velocity* approach), we construct a mean local velocity field $\bar{v}(\bar{x})$ on a uniform mesh by assigning the individual particles to a mesh with a *Triangular Shape Cloud* (TSC) window function [1]. As a first step we carry out a convergence study by gridding the velocity field in the central comoving Mpc^3 of a massive galaxy cluster, with meshes of increasing resolution: $8-16-32-64^3$ cells (which are all coarse enough to avoid under-sampling effects inside the region under analysis); the equivalent width of the TSC kernel, l, is 3 grid cells in each dimension, i.e. $\approx 360-180-90-45$kpc, respectively. As our analysis is restricted only to the highest–density region in the clusters, the scale for the TSC–interpolation is always above the SPH smoothing length for the gas particles here, which typically spans over the range: $7.5 \div 15h^{-1}$kpc in the box we consider.

The local velocity dispersion at the position $\overline{x}$ of each mesh cell is evaluated over all particles a in the cell by:

$$\sigma^2_{ij}(\overline{x}) \simeq \langle (v_{a,i} - \bar{v}_i(\overline{x}))\,(v_{b,j} - \bar{v}_j(\overline{x})) \rangle_{cell}\,, \tag{5.10}$$

where ij are the indexes for the three spatial coordinates, and $\langle\rangle_{cell}$ denotes the average within each cell; the subtraction of a local velocity from the velocity distribution of the particles is expected to efficiently filter out the contribution from laminar bulk–flows with size ≥ 3 times the size of the cells used in the TSC interpolation. Fig.5.3 shows the mean velocity dispersion in the case of the *lvisc* simulation and its dependence on the resolution of the mesh used in the TSC interpolation. The observed trend

[1] The Triangular Shape Cloud kernel is one of the customary ways of interpolating particle data onto regular grids. Particle fields are interpolated using the most nearby 27 grid nodes in the 3–D volume. One of the main feature of this method, is to produce interpolated fields which are continuous, and whose first order derivatives are continuous too.

is well fitted by a $v^2 \propto l^{1/2}$ dependence. This procedure is also expected to subtract at some level a fraction of the turbulent velocity field, if turbulent eddies exist with scales significantly larger than 3 cells, however Fig.5.3 shows that the increase of the turbulent velocity dispersion with the cell size is not dramatic for cells sized ≥ 100 kpc (and thus for a corresponding FWHM for the TSC interpolation of ~ 300 kpc and since the use of larger cells would not efficiently filter out the contribution from laminar bulk–motions, we can reasonably conclude that a local velocity approach with a grid of 32^3 cells (i.e. having a cell size of 30 kpc and a FWHM of ~ 90 kpc) is able to catch the bulk of turbulent velocity field.

Panels in Fig.5.1 show an example of the total velocity field and of the turbulent velocity field calculated in the central region of a galaxy cluster in the *lvisc* simulation. Note that we here selected a situation where a large (ca. 500 kpc long) laminar flow pattern can be easily identified close to the center of one of our simulated clusters (*g72*). When the mean cluster velocity field is subtracted as in Figure 5.2, large residual bulk flow patterns remain visible, caused by a substructure moving through the cluster atmosphere. Panels in Fig.5.2 give examples of the turbulent velocity field calculated with both the standard and local velocity methods, showing the same galaxy cluster in both cases, but in one case simulated with the signal–velocity variant of the standard viscosity (*svisc*), and in the other with the new time-dependent low-viscosity scheme (*lvisc*). In these panels we color-coded the turbulent kinetic energy of particles, $E_t(x) \sim 1/2\,\rho(x)\sigma_v(x)^2$, after subtracting the local mean velocity field (here interpolated onto a 64^3 mesh). As expected, the strength of this turbulent velocity field is considerably larger in the simulation obtained with the new low-viscosity scheme, providing evidence that such instabilities are less strongly damped in this scheme.

The total kinetic energy in the random gas motions inside our mesh (centered on the cluster center) reaches 30 per cent of the thermal energy for the simulations using the new, low viscosity scheme, whereas it stays at much lower levels ($\approx$2%-10%) when the signal velocity parametrization of the viscosity is used. If the standard viscosity scheme is used, it is

typically at even lower values (≈0.5%-5%).

5.2.4 Effects on the Clusters Profiles

Right panel of Fig.5.3 shows a radial profile of the (volume weighted) relative pressure difference between the standard *svisc* and low viscosity *lvisc* runs, averaged over the three massive clusters (*g1*,*g51* and *g72*) which have comparable masses. The solid line shows the relative difference in radial shells and indicates that the turbulent pressure support can reach even up to 50% in the central part and drops to 0 at approximately 0.2 R_{vir}. The dashed line shows the difference between the two cumulatives of pressure distributions, inside the same radius, which reaches a value of $2-5$ per cent of the total pressure at R_{vir}. Finally, the inlay in right panel of Fig.5.3 gives the contribution to the total pressure inside the radius from turbulent motion assuming the low viscosity *lvisc*, or assuming the standard viscosity in its two variants (*ovisc*, *svisc*) : the signal based viscosity (*svisc*) in general leads already to more turbulence than the 'old" standard viscosity (*ovisc*), but the time-dependent treatment of the viscosity (*lvisc*) works even more efficiently. In Sec.7.0.3 of the Appendix, we will show the application of these numerical simulations to the modeling of radio halos in galaxy clusters.

5.2.5 Scaling laws for Turbulent Kinetic Energy

We investigate in this section the scaling laws between the mass (gas and DM particles) of clusters/groups, $M_{\rm tot}$, and the thermal, kinetic and turbulent energy of the ICM.

Due to computational limitations we restricted our analysis to a cubic region, centered onto the center of the clusters, of equivalent volume $V_{\rm box} = (R_{\rm vir})^3$. This ensures that we consider in any case a number of gas particles ranging from several thousands to nearly 1 million. After the velocity decomposition is performed (section 5.2.3), we evaluate the turbulent energy content as:

$$E_{\rm TUR} = \frac{1}{2} m_{\rm gas} \sum_{\rm BOX} \delta v_i^2 \tag{5.11}$$

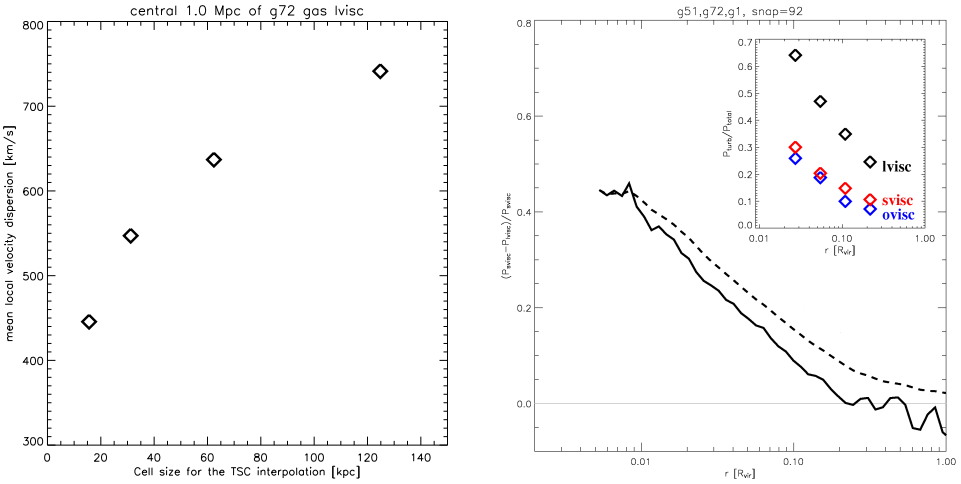

Figure 5.3: *Left:*mean local velocity dispersion for the central $500^3 kpc^3$ box as a function of the resolution adopted for the TSC–smoothing of the local mean field. Results are plotted for a low viscosity simulation.*Right:* Radial profile of the relative pressure difference averaged over three nearly equally massive clusters (*g1*,*g51* and *g72*), comparing the standard viscosity (based on signal velocity) and low viscosity runs (lines). The dashed line is the cumulative difference, whereas the solid line marks the profile in radial shells. The inlay shows the absolute value inferred from the local velocity dispersion from the different viscosity parametrization, respectively.

where the sum is done over the module of the velocity fluctuation, δv_i, of the gas particles. This calculation was repeated at three different resolutions of the TSC–kernel used to define the local mean velocity field: l =16, 32 and 64 kpc.

The total kinetic and thermal energies were evaluated as:

$$E_{\rm TH} = \frac{3}{2} m_{\rm gas} \sum_{\rm BOX} \frac{f_e k_B T_i}{\mu m_p}, \tag{5.12}$$

where k_B is Boltzmann's constant, T_i the gas particle temperature, $\mu = 0.59$ the mean molecular weight in AMU, m_p the proton mass and $f_e = 0.58$ the fraction of free electrons per molecule, assuming a primordial mixture of $x_H = 0.76$, and

$$E_{\rm K} = \frac{1}{2} m_{\rm gas} \sum_{\rm BOX} v_i^2, \tag{5.13}$$

where the module of velocity, v_i, has been reduced to the center of mass velocity frame (as in Norman & Bryan 1998).

In Figure 5.4 we report the time evolution of four representative clusters in our sample in the $E_{\rm TUR,TH,K}$–$M_{\rm tot}$ plane. The most "relaxed" structures

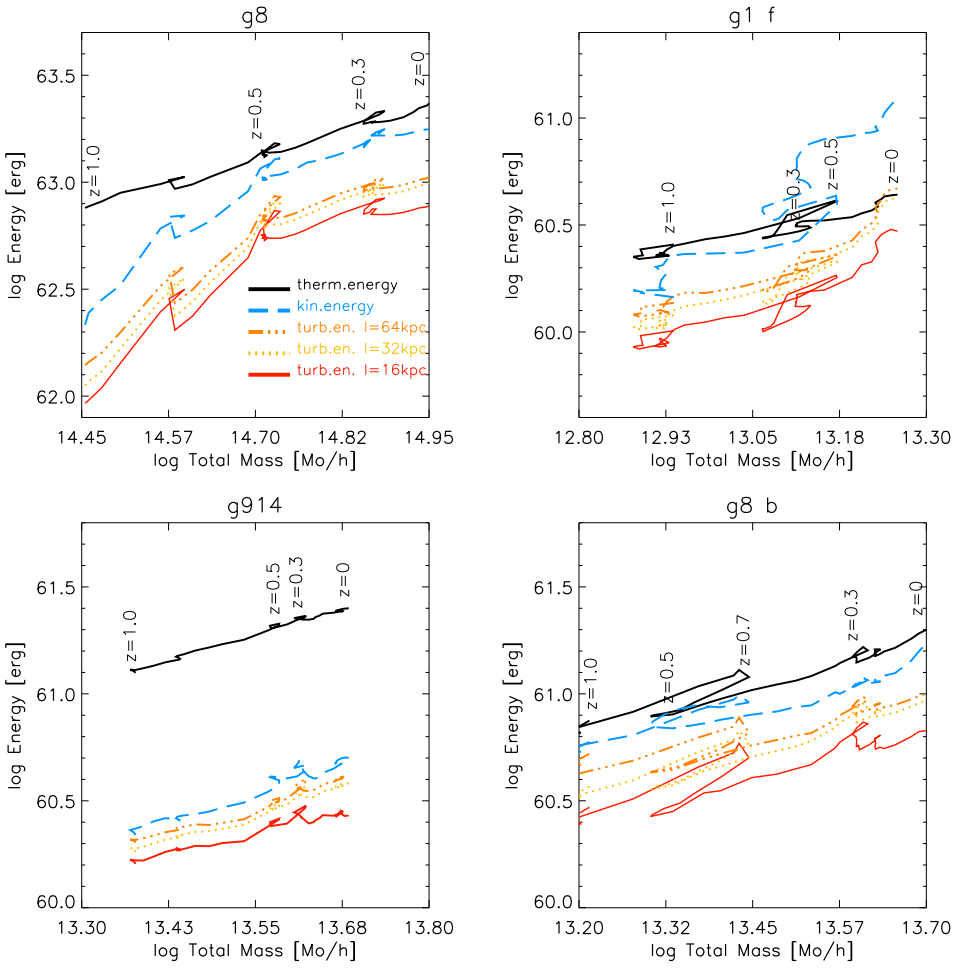

Figure 5.4: Individual paths for fours clusters of the sample, in the $\log \mathrm{Energy} - \log \mathrm{M_{tot}}$ plane. The upper two panels show the evolution of the most and of the less massive cluster within our catalog, whereas the lower two panels show the evolution of two clusters with a nearly equal final mass ($\simeq 5 \times 10^{13} M_{\odot} h^{-1}$), but very different "relaxation" state: left panel is for the "relaxed" (i.e. $\xi < 0.5$ at z=0) cluster g914 while the right one is for the "perturbed" one, g8 b ($\xi \geq 0.5$ at z=0).

(as the cluster g914, bottom left panel) present a fairly smooth evolution, whereas "perturbed" structures (as g8b and g1f, right panels) show a more complex evolution with episodic jumps in turbulent and kinetic energies, and have a high ratio, ξ, between kinetic and total (thermal plus kinetic) energy. This reflects the significant difference in the ratio between the kinetic and the potential energy of these clusters (e.g. Tormen et al. 1997), which is higher for the perturbed ones.

Since our cluster sample is extracted from re–simulations centered on 9 massive and fairly isolated clusters, smaller systems generally correspond to structures about to be accreted by larger ones. As such, small systems are often perturbed, and this introduces a bias in the dynamical properties of the cluster population. This bias can however be alleviated by restricting our analysis only to the most "'relaxed" objects in our sample, as we will see below.

In general, we find the following power law scaling between cluster energy (thermal, kinetic or turbulent) and cluster mass:

$$E_j \sim A_j(\frac{M_{\rm tot}}{10^{15}M_{\odot}h^{-1}})^{D_j}, \tag{5.14}$$

with $j = TH$, K, TUR, and where A_j and D_j are the zeroth point and the slope of the correlations, respectively.

We find that the scaling of thermal energy with mass is always consistent with that expected in the virial case, $D_{\rm TH} \sim 5/3$, while the values of D_K and D_{TUR} slightly depend on the number of "perturbed" small systems included in the analysis. With all system included, the slope of the scaling between turbulent energy and cluster mass is flatter than that between thermal energy and mass by ~ 0.2. As we remove more and more small perturbed systems, the turbulent slope approaches the thermal value. We find that the flattening of the turbulent scaling with respect to the thermal scaling is statistically significant only if objects with $\xi \geq 0.5$ (nine at z=0) are included.

Most importantly, we also find that the slopes of these scalings do not depend on the value of the TSC-kernel, l, used to subtract the laminar motions; this is shown left panel of Fig. 5.5, that also provide a confirmation of the $E_{TUR} \propto l^{1/2}$ scaling found in Sec.5.2.3.

Table 5.2: Values for the slopes of the kinetic and turbulent scaling laws at zero redshift, for the whole sample of data and the "relaxed" sub sample, with 1σ errors.

l	$D_{\rm TUR}$ **(all)**	$D_{\rm TUR}$ **(relax)**	$D_{\rm K}$ **(all)**	$D_{\rm K}$ **(relax)**
16 kpc	1.43 ± 0.06	1.63 ± 0.04	1.38 ± 0.04	1.72 ± 0.03
32 kpc	1.49 ± 0.04	1.72 ± 0.01	1.38 ± 0.04	1.72 ± 0.03
64 kpc	1.49 ± 0.03	1.73 ± 0.05	1.38 ± 0.04	1.72 ± 0.03

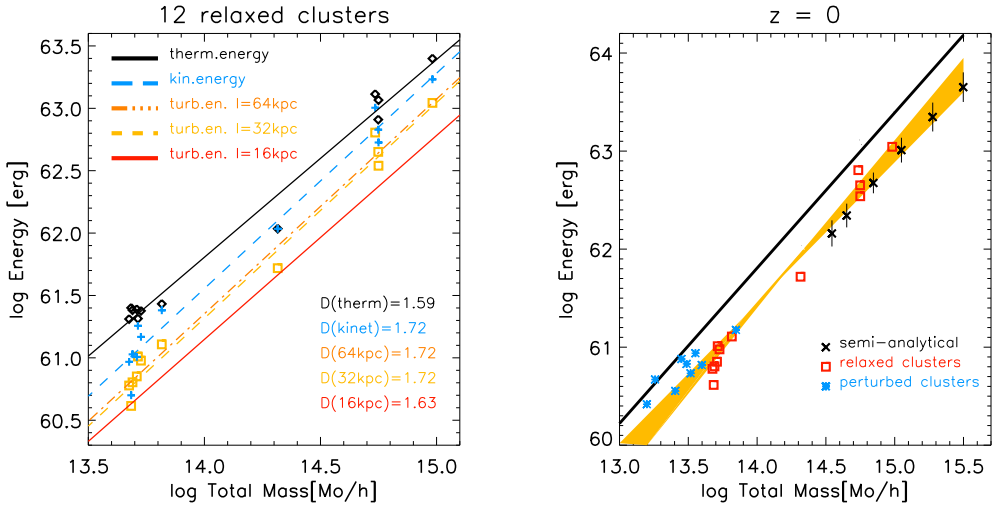

Figure 5.5: *Left:* scaling laws at redshift $z = 0$ for the 12 most relaxed clusters ($\xi < 0.5$); the values of the slopes for the different relations are reported in the panel. For the sake of displaying, only the data points of the $l = 32kpc$ grid turbulence are drawn. *Right:* comparison between the thermal and turbulent scaling at zero redshift, for 12 "relaxed" (i.e. $\xi < 0.5$) galaxy clusters, 9 "perturbed" (i.e. $\xi \geq 0.5$) clusters and semi-analytical average data with 1σ errors. The black line shows the thermal scaling of the whole simulated sample, while the orange band encloses, within 1σ errors, the scaling of the "relaxed" sample alone and the scaling with the 9 "perturbed" object added.

Finally, Figure 5.6 shows the redshift evolution of the slopes, D_j, and of the zero points, A_j, of the five correlations (Eq. 5.14). It is clear that the slopes are relatively constant with redshift, unless very "perturbed" groups, with $\xi \geq 0.5$, are considered in the analysis. In this last case a systematic flattening ($\Delta D_{\rm K,TUR} \sim 0.2$) of the scaling of the kinetic and turbulent energies with cluster mass at low redshift is found: this is caused by the interactions between objects, which makes the smaller systems more and more perturbed as time proceeds.

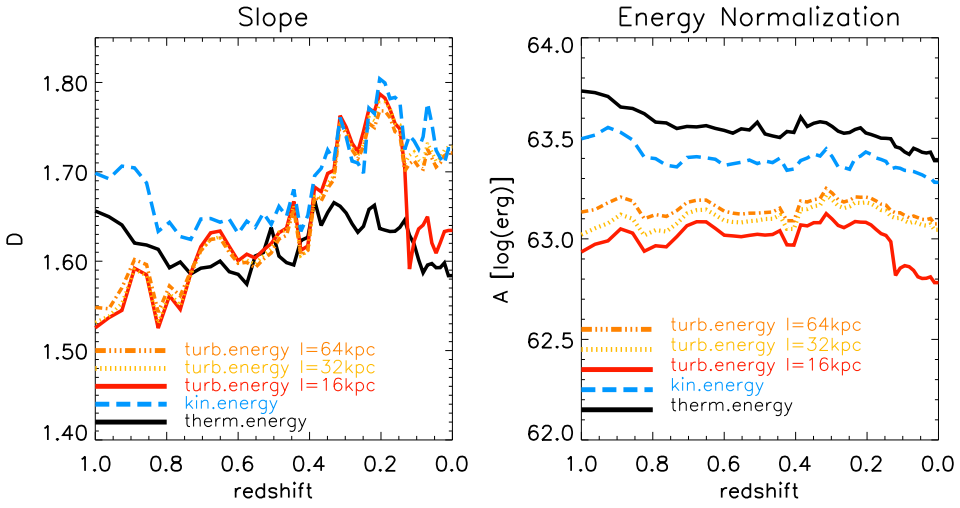

Figure 5.6: Redshift evolution of slope(*left*) and zero point (*right*) of the scaling law Eq.(5.14), for the sample of objects with $\xi < 0.5$.

5.2.6 Comparison with semi–analytical results

In the previous section we reported on the scaling between the turbulent energy and the thermal (and kinetic) energy as measured in simulated clusters, without motivating their physical origin. It is clear that we cluster mergers are likely to be the responsible for most of the injection of turbulent velocity fields in the ICM.

A comprehensive approach to follow the injection of merger–turbulence during cluster life is also given by semi–analytical calculations: C&B05 used merger trees to follow the merger history of a synthetic population of galaxy clusters (using the Press & Schechter 1974 model) and calculated the energy of the turbulence injected in the ICM during the mergers experienced by each cluster.

Although simplified, this semi–analytical approach allows a simple and physical understanding of the scaling laws reported in the previous Section. Indeed, since the in-falling sub-clusters are driven by the gravitational potential, the velocity of the infall should be $\sim 1.5-2$ times the sound speed of the main cluster; consequently, the energy density of the turbulence injected during the cluster–crossing should be proportional to the thermal energy density of the main cluster. In addition, the fraction of the volume of the main cluster in which turbulence is injected (the

volume swept by the in-falling sub clusters) depends only on the mass ratio of the two merging clusters, provided that the distribution of the accreted mass–fraction does not strongly depend on the cluster mass (Lacey & Cole 1993). The combination of this two items yields a self–similarity in the injection of turbulence in the ICM: the energy of such turbulence should scale with the cluster thermal energy and the turbulent energy should scale with virial mass with a slope $D_{sem} \sim 1.67$ (C&B05).

In the Right panel of Fig.5.5 we compare the integral of the turbulent energy (injected in the ICM up to the present time) versus the cluster mass, as estimated under the C&B05 approach with 360 merging trees of massive galaxy clusters, with that measured in our simulated clusters: the two scalings are consistent within 1σ errors. We also note that the two approaches are complementary since semi–analytical calculations can follow the properties of $> 10^{15}\mathrm{M}_{\odot}$ clusters which are rare in numerical simulations due to the limited simulated cosmic volume. These results strengthen our claim that the turbulent velocity fields detected in simulated clusters are actually real turbulent fields supplied by the mass accretion process acting in galaxy clusters.

Both numerical and semi-analytical approach derive an estimate in the ranges of 25 per cent to 35 per cent of the thermal one (in the $(R_{\rm vir})^3$ region). Formally in the case of our simulations this should be considered as an upper limit of the turbulent energy content at a given time, because present simulations do not contain appropriate recipes for the dissipation of the turbulent eddies at the smallest scales.

Fig.5.2.6 highlights the different behavior of "perturbed" (i.e. $\xi \geq 0.5$) and "relaxed" clusters in the turbulent energy – mass plane. As discussed in Section 5.2.5 the presence of "perturbed" clusters/groups introduces a bias in the properties of the overall simulated cluster population. In this case the complete sample of our simulations would be more representative of rich environments and super clusters, with the smaller structures being more perturbed (and turbulent) than those in other environments.

5.3 Turbulent Velocity Fields in AMR Simulations with ENZO.

As extensively discussed in Chap.4, the Eulerian approach presents complementary properties to Lagrangian SPH numerical simulations. Due to its high order accuracy in following fluid dynamics through conservative equations and fluxes balances, it is expected to be a valuable tool to follow purely hydro-dynamical processes in the ICM. In Chap.3 we showed detailed results from the characterization of shocks in LSS of the Universe, using a fixed resolution of 125 kpc. The above mesh resolution is accurate enough to model the bulk of accretion processes around galaxy clusters, groups and filaments, but it is less efficient in the study of shocks and turbulent motions in the innermost regions of GC, with respect to SPH approaches discussed in Sec.5.2, that provide much better resolution.

For these reasons, we have implemented a novel Adaptive Mesh Refinement criterion in ENZO that is explicitly designed to increase spatial resolution both in the cluster central regions and around discontinuities in the velocity field. The aim of this technique is to follow with adequate resolution the inner regions of cluster, but also to follow shocks and turbulent eddies with unprecedented spatial resolution, even at large distances from the clusters center. In this Section we will apply this technique to reference galaxy cluster in order to investigate the spectral properties of turbulent fields of the gas, their time evolution and the properties of shocks and their connection with chaotic motions.

5.3.1 Numerical Code and Setup

For the simulations presented here, we assume a ΛCDM cosmology with parameters $\Omega_0 = 1.0$, $\Omega_{BM} = 0.0441$, $\Omega_{DM} = 0.2139$, $\Omega_\Lambda = 0.742$, Hubble parameter $h = 0.72$ and a normalization of $\sigma_8 = 0.8$ for the primordial density power spectrum.

We present here the simulation of a cubic volume of side $75Mpc$ starting from $z = 30$, and applying AMR within a sub-volume of side $7.5Mpc$, centered on a $\sim 2 \cdot 10^{14} M_\odot$ galaxy cluster. We re-simulate this volume under different configurations, as reported in Tab.1. The mass resolution

Table 5.3: Main characteristics of the runs. "D" stands for AMR triggered by gas/DM over-density, while "V" stands for AMR triggered by velocity jumps. Δ is the peak gas spatial resolution. δ specifies the value adopted to trigger AMR, see Sec.3 for explanations.

ID	N_{grid}	Mdm $[M_\odot/h]$	Δ [kpc]	AMR
v256-4	256^3	$6.76 \cdot 10^8$	18	D+V($\delta > 10$)
v256-3	256^3	$6.76 \cdot 10^8$	36	D+V($\delta > 3$)
v128-3	128^3	$5.39 \cdot 10^9$	36	D+V($\delta > 3$)
v64-3	64^3	$4.32 \cdot 10^{10}$	36	D+V($\delta > 3$)
d128	128^3	$5.39 \cdot 10^9$	36	D
v128-10	128^3	$5.39 \cdot 10^9$	36	D+V($\delta > 10$)
v128-1	128^3	$5.39 \cdot 10^9$	36	D+V($\delta > 1$)
v128-z2	128^3	$5.39 \cdot 10^9$	36	D+V($\delta > 3$,$z > 2$)

of Dark Matter (DM) particles ranges from $6.76 \cdot 10^8 M_\odot$ (v256-3 and v256-4) to $4.32 \cdot 10^{10} M_\odot$ (v64-3), corresponding to minimum root grid spatial resolutions from $292kpc$ to $1.172Mpc$. The maximum spatial resolution in the region where AMR in applied is $\Delta = 36kpc$ in all the simulations except for the case of v256-4, where $\Delta = 18kpc$. In these simulations, the $\sim 2 \cdot 10^{14} M_\odot$ cluster is formed through a major merger at $0.8 < z < 1$.

5.3.2 Adaptive Mesh Refinement technique for Turbulent Motions

The first application of AMR to the study of turbulence in the inter stellar medium was reported in Kritsuk, Norman & Padoan (2006); then Iapichino & Niemeyer (2008) applied a refinement criterion based on based on the gas velocity field (analyzing curl and divergence of velocity), in order to study turbulence in cosmological ENZO simulations. Motivated by the above results, here we report on first results from an exploratory study where 1–D velocity jumps are used to trigger the grid refinement in ENZO. In Chapter 3 (and in Vazza, Brunetti & Gheller, 2009) we presented the application of a shock–detecting scheme relying on the analysis of the jump of the velocity, Δv, field across cells. Small scale velocity fluctuations are also expected in the case of turbulent motions, induced by merging processes and therefore we propose to use $\delta \equiv |\Delta v / v_m|$ across 1–D patches of cells in the simulation (v_m is the minimum velocity over the cells in the patch) to trigger grid refinement and follow in detail

small scale chaotic motions driven by accretion processes. In detail we recursively analyze the velocity jumps across three adjacent cells at a given AMR level, and increase the resolution (by a factor 2 in cell size) for the cells of the patch whenever δ is larger than a threshold value. At the same time, also the standard AMR method triggered by gas/DM over-density is applied (e.g. Norman et al.2007); the over-density threshold is kept at the conservative choice of = 2 for all runs. We adopt as reference value $\delta = 3$ and allow for a number of AMR levels up to the maximum resolution of $\Delta = 36kpc$. We also present results for $\delta = 10$ (v128-10) and $\delta = 1$ (v128-1), in order to assess the convergence of our results (Sec.5.3.4-5.3.5). Finally, we performed a run using the same setup of the v256-3 run, but allowing for one more AMR level (4 levels instead of 3), reaching the peak resolution of $18kpc$ (v256-4). In order to compare with a reference standard simulation, we also produced a run where only the gas/DM over-density criterion is used to trigger mesh refinements (d128). For comparison we also present a test run where the AMR criterion triggered by velocity jumps is added to the standard one only starting from $z \leq 2$ (v128-z2). Fig.5.7 shows 2–D slices of gas density and temperature comparing runs v128-3 and d128 at $z = 0.1$. Unlike refining on over-density (standard) AMR, with the velocity/over-density criterion shocks and chaotic motions are followed with high resolution, $\Delta = 36kpc$, even at large ($\sim$ 3 Mpc) distance from the cluster center. To highlight the improvement due to the new AMR scheme, Fig.5.8 shows the time evolution of the gas temperature within the same cut, in the case of the standard AMR criterion and in the new one, and the most importantly the evolution of the difference in temperature between the two. Relevant differences are found around expanding shocks even at large distance from the cluster center.

5.3.3 Detection of turbulent motions.

As discussed in Sec.5.2 the turbulent gas velocity field can be extracted by removing a *"local"* mean velocity field, whose value is obtained by interpolating the 3–D gas velocity on large enough scales. Following this

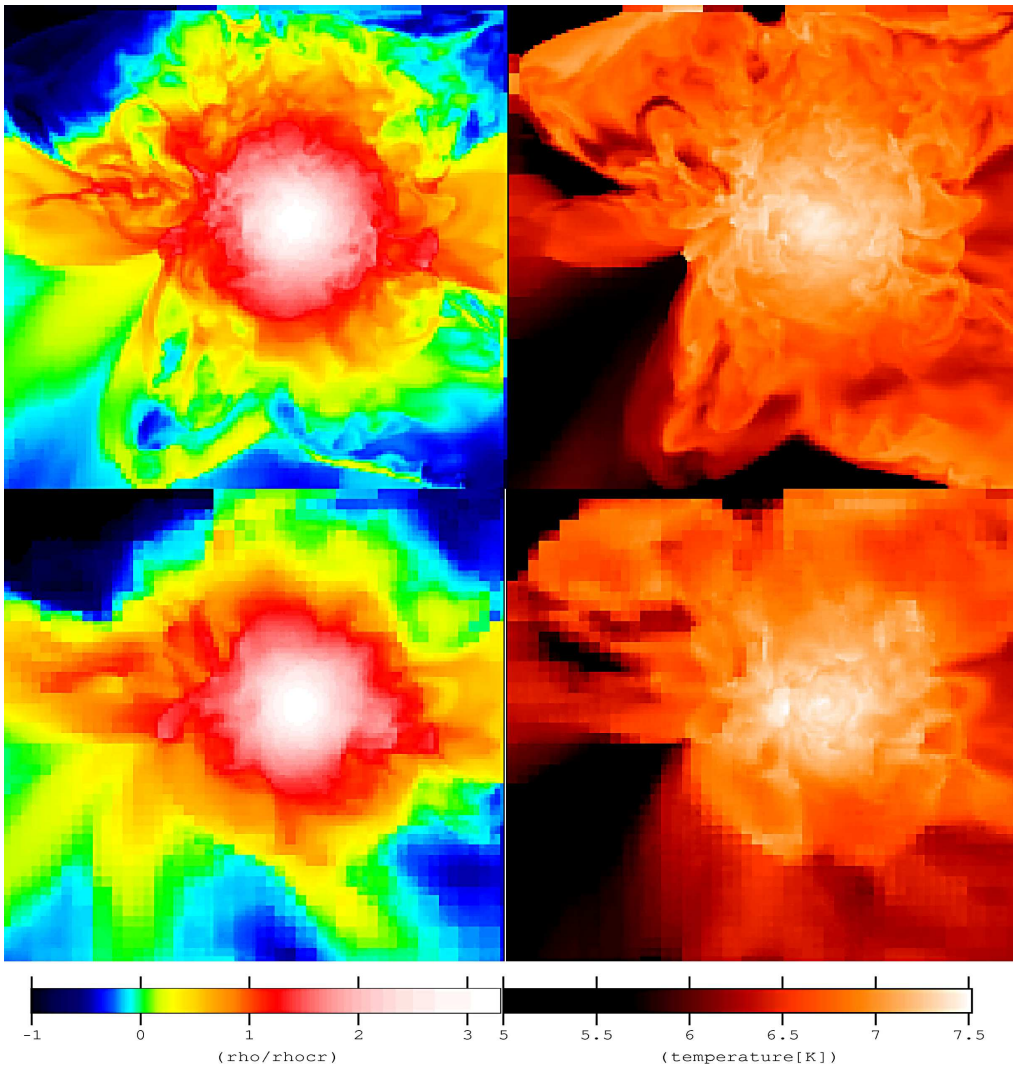

Figure 5.7: Gas density and temperature slices for the AMR region of the v128-3 run (upper panels), and of the d128 run (lower panel). The side of the image is $7.5Mpc$ and the depth along the line of sight is $36kpc$. The gas density is normalized to the critical density of the universe, rescaled to the cosmic baryon fraction.

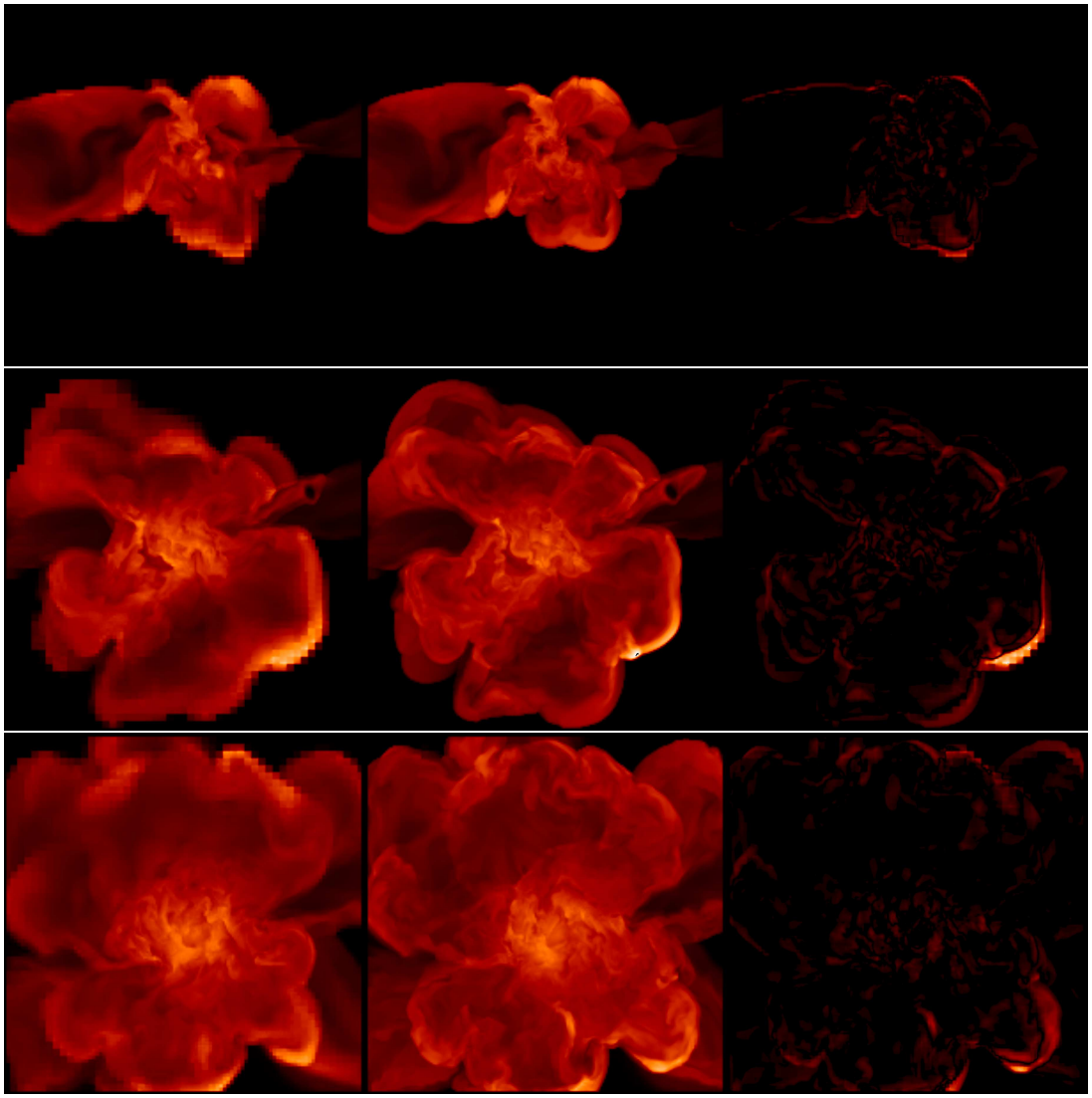

Figure 5.8: Temperature maps for a central slice in the simulated AMR region, at for different redshifts ($z = 2$,$z = 1$ and z=0.2) by using the standard AMR criterion (*left panels*), the new AMR criterion (*central panels*); the right panels show the cell by cell difference, as $T_{new} - T_{standard}$.

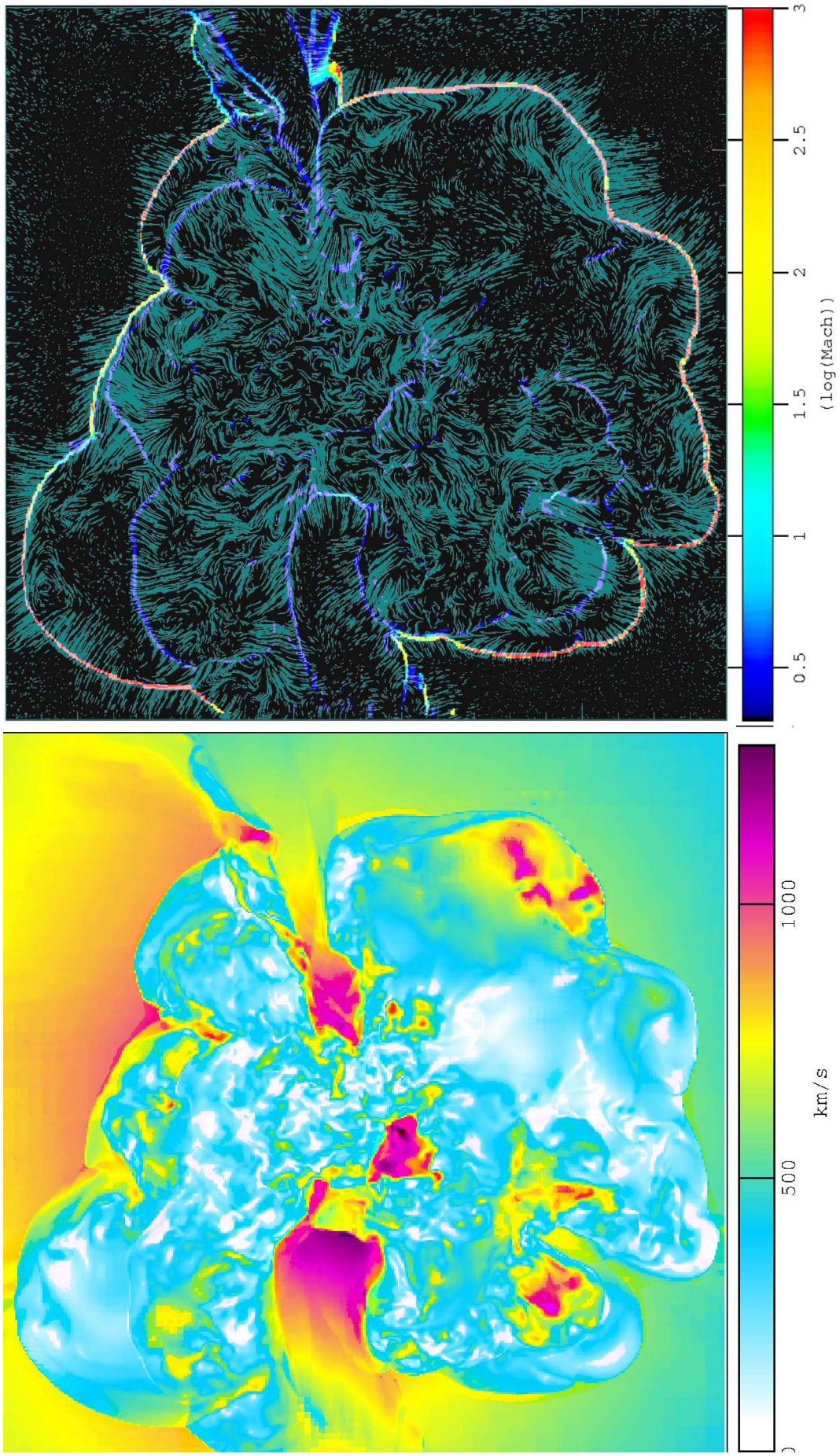

Figure 5.9: *Left:* modulus of total gas velocity in a slice of side $7.5Mpc$ and depth $18kpc$, for the v256-4 run at $z = 0.6$. *Right:* map of Mach number (in colors) and turbulent gas velocity field (arrows).

approach, we use here the ENZO implementation of the PPM scheme (based on parabolic interpolations on cells) to map the 3–D local mean velocity field, V_L, and for each cell we measure the turbulent velocity as $\Delta v = v - V_L$; v is the gas velocity at the maximum AMR level, while V_L is measured at a coarser resolution (for the v256-3 and v256-4 runs this is $\Delta = 292kpc$, while for the other runs we consider the AMR level corresponding to this scale). We notice that this procedure implies a largest possible scale of ~ 300 kpc for turbulent motions, and therefore in presence of significant turbulent motions on larger scales our procedure would lead to a lower estimate on the total turbulent energy budget. This choice is more conservative than that in Sec.5.2. Indeed in the case of SPH we adopted as a reference scale ~ 100 kpc. On the other hand, as already discussed, Fig.5.5 in Sec 5.2 shows that quasi convergence i already achieved for about $l \sim 100kpc$, and a larger value of l is not expected to greatly affect our results.

5.3.4 Turbulent Energy Budget

In all runs, the total mass of the cluster at the center of the AMR region is $M \sim 2.1 \cdot 10^{14} M_{\odot}$ at $z = 0$, which corresponds to a virial radius of $R_{vir} = 1.4$ Mpc. Fig.5.9 shows the total and turbulent velocity fields at $z = 0.6$ for a slice crossing the AMR region. The laminar infall patterns, due to accretion of sub-clumps from filaments (see left panel), are almost completely removed by our filtering of the velocity field, and small scale curling motions, injected along accreted clumps, and around shocks, are well highlighted (see right panel). The uppermost panels in Fig.5.10 show the gas density profile and the gas entropy profiles of the cluster in all runs. The lower panels in the same Figure show the profiles of thermal, turbulent and kinetic energy, and the ratio between turbulent (or kinetic) energy and the total energy E_{TOT} (kinetic plus thermal) inside a given radius. The turbulent energy, E_{TUR}, is measured as $\rho \Delta v^2/2$, the total kinetic energy is $E_K = \rho v^2/2$ and the thermal energy in the cell is $E_{TH} = (3/2) k_B \rho T/\mu m_p$. All velocities are corrected for the velocity of the cluster center of mass. The standard AMR run (i.e. over-

density based refinement, d128) shows the highest central density and the steepest entropy profile, while all runs produced with velocity/over-density refinement have flatter profiles. This feature is likely due to the fact that, in runs with the velocity/over-density velocity/over-density refinement, merger shocks are simulated with high accuracy and can propagate more deeply towards the inner regions of the cluster. At all radii, the runs with the velocity/over-density refinement show larger energy budget in turbulent motions, with a $E_{TUR}/E_{TOT} \sim 3-4$ percent at $r = 0.1R_{vir}$ ($E_{TUR}/E_{TH} \sim 5$ per cent within the same radius) and $E_{TUR}/E_{TOT} \sim 5-8$ percent inside R_{vir} ($E_{TUR}/E_{TH} \sim 10-20$ per cent within the same radius); as already stressed the amount of turbulence always refers to motions with scales $\leq$ 300kpc. As expected the adoption of a larger threshold for δ (v128-10) decreases the budget of turbulent motions in the simulated volume, gradually approaching the results of standard AMR(d128), except for the outermost regions, where strong shocks occur and the threshold $\delta = 10$ still triggers refinement. Decreasing δ (v128-1) increases the turbulent energy budget, yet convergence is already reached at $\geq 0.2R_{vir}$ for $\delta = 3$ (v128-3).

In the cases where the AMR peak resolution is fixed at $\Delta = 36kpc$ (v256-3,v128-3,v64-3), the adoption of a larger mass resolution in DM particles causes a significant decrease in the turbulent budget at large radii(the kinetic energy profiles, however, are almost unaffected by that). Understanding this trend is not trivial, and we speculate the following: in the cluster outskirts, where strong accretion shocks are located, a coarse DM resolution produces satellites with smaller gas and DM density concentration, which are more easily stripped and inject more turbulence in the peripheral cluster regions.

The total kinetic energy within R_{vir} in these ENZO AMR simulations is in line with SPH results with reduced artificial viscosity (Vazza et al.2006) and other AMR results obtained with ENZO (Iapichino & Niemeyer 2008). However the radial profile of the turbulent energy is different with respect to that in SPH simulations (Sec.5.2.4). On one hand it seems that the progressive increase of the DM mass and force resolution in ENZO AMR

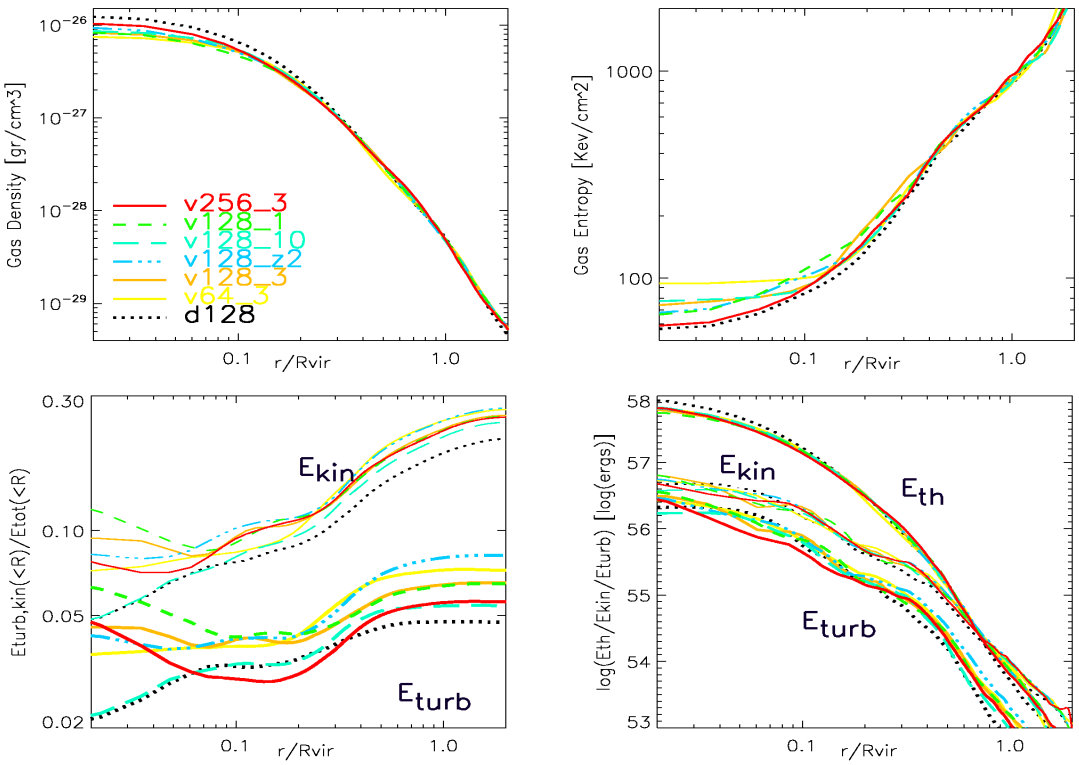

Figure 5.10: Gas density profiles (*top left*), gas entropy profiles (*top right*), $E_{TUR}/E_{TOT}$and E_K/E_{TOT} profiles (*lower left*) and E_{TUR},E_K and E_{TH} profiles (*lower right*) for all runs of the paper. The color coding is all the same as in the first panel; E_{TUR} refers to turbulent motions on scales $< 300kpc$.

simulations causes the increase of turbulence in the innermost region, on the other hand the turbulent energy budget in these regions is still smaller by a factor $\sim 5-6$ than that in SPH. Whether or not this is related to the different clusters under observation (and to their dynamical states) or if this is this a more fundamental issue caused by differences between AMR and SPH simulations, is a topic that deserves more accurate investigations.

5.3.5 Power Spectra and Structure Functions of the Turbulent Velocity Field

We characterize the cluster velocity field through it 3D power spectrum, $E(k)$, defined as:

$$E(\mathbf{k}) = \frac{1}{2}|\tilde{\mathbf{v}}(\mathbf{k})|^2, \tag{5.15}$$

where $\tilde{\mathbf{v}}(\mathbf{k})$ is the Fourier transform of the velocity field:

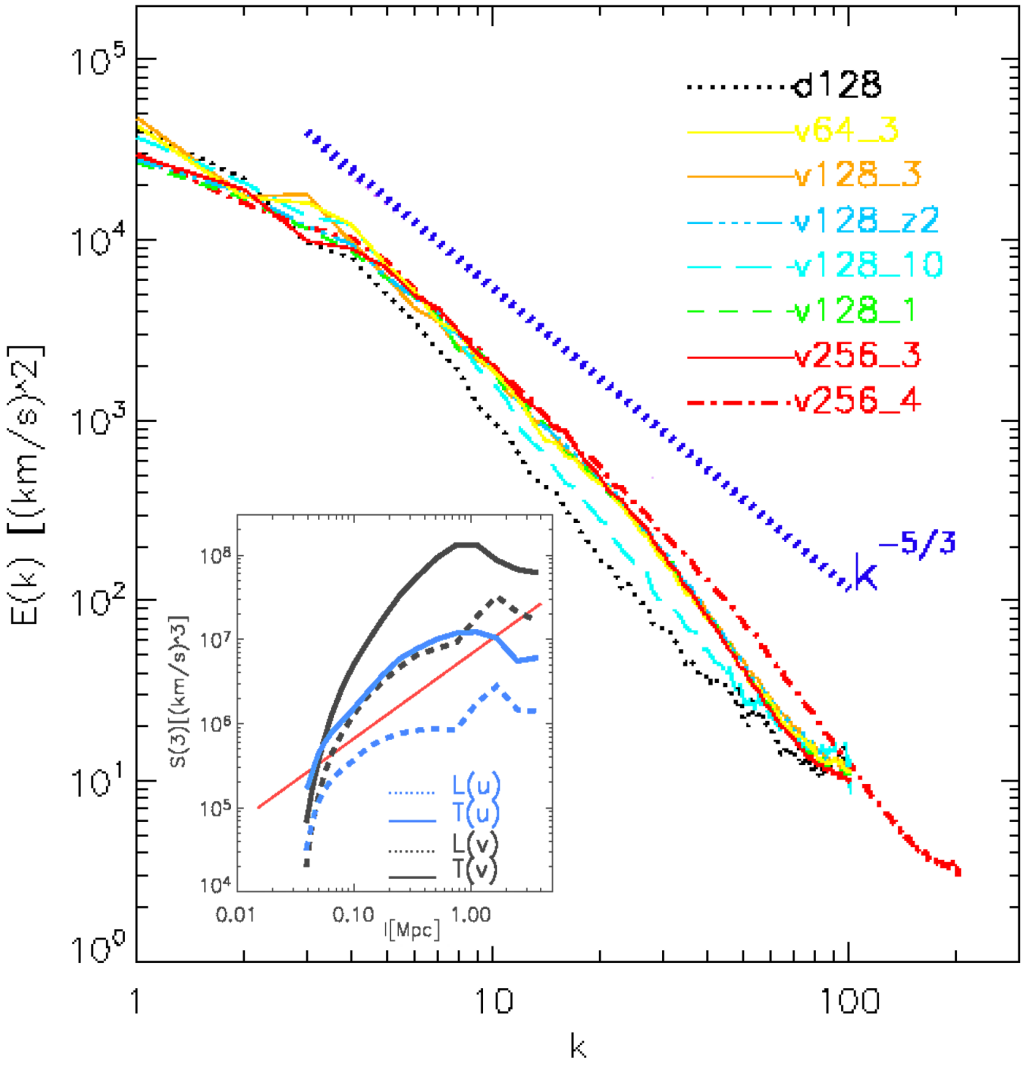

Figure 5.11: 3D power spectra for the velocity field of the various run at $z = 0.1$. The spectra are shown up to their Nyquist frequency; the purple dashed lines shows the $-5/3$ slope to guide the eye. The inlay shows the longitudinal and transverse third–order structure functions for velocity field, v, and for the density=weighted velocity field, $u \equiv \rho^{1/3} v$ for a sub volume in the v128-3 run. The additional red line shows the expected scaling for the Kolmogorov model.

$$\tilde{\mathbf{v}}(\mathbf{k}) = \frac{1}{(2\pi)^3} \int_V \mathbf{v}(\mathbf{x}) e^{-2\pi i\, \mathbf{k}\cdot\mathbf{x}} d^3x. \quad (5.16)$$

$E(k)$ is calculated with standard FFT algorithm and with a zero-padding technique to deal with the non-periodicity of the considered volume. Differently from SPH and standard AMR simulations, the velocity plus density refinement allows us to enter into an unexplored territory for cosmological numerical simulations, since for the first time we can study the cluster velocity field with high spatial resolution in lower density regions, with consequences on the capability to describe its spectral properties over a wide range of scales.

Fig.5.11 shows the 3–D power calculated for all runs at $z = 0.1$. $E(k)$ is approximately described by a simple power law over more than one order of magnitude in k, with a slope not far from a standard Kolmogorov model ($E(k) \propto k^{-5/3}$). At large scales ($k < 4$) a flattening in the spectrum is observed in all runs, at a wave number roughly corresponding to the virial diameter of the cluster, which likely identifies the outer scale of turbulent motions connected with accretion processes; we remark that, for spatial scales $\leq 32\Delta$, the slope of the power spectrum may be affected by the non-uniform numerical dissipation that PPM adopts to increase resolution in shocks and contact discontinuities (Porter & Woodward, 1994). As in the case of the turbulent energy budget, the v128-10 run falls in between the standard AMR run and all the other runs with velocity/over-density refinement, while there is almost no difference by adopting $\delta = 3$ or $\delta = 1$ as threshold. Remarkably due to its larger peak resolution, the v256-4 shows a regular power law for almost two orders of magnitude, which is an unprecedented result in cosmological numerical simulations, thus supporting the picture that the simulated IGM is globally turbulent starting from sub–Mpc scales. This is also further suggested by the inlay in Fig.5.11, which shows the third order velocity structure functions for the v128-3 run, calculated as in Kritsuk et al.(2007):

$$S_p(l) \equiv < |\mathbf{u}(\mathbf{r}+\mathbf{l}) - \mathbf{u}(\mathbf{r})|^p >, \quad (5.17)$$

where $\mathbf{l}$ is the separation between cells and $\mathbf{p}$ defines of the structure

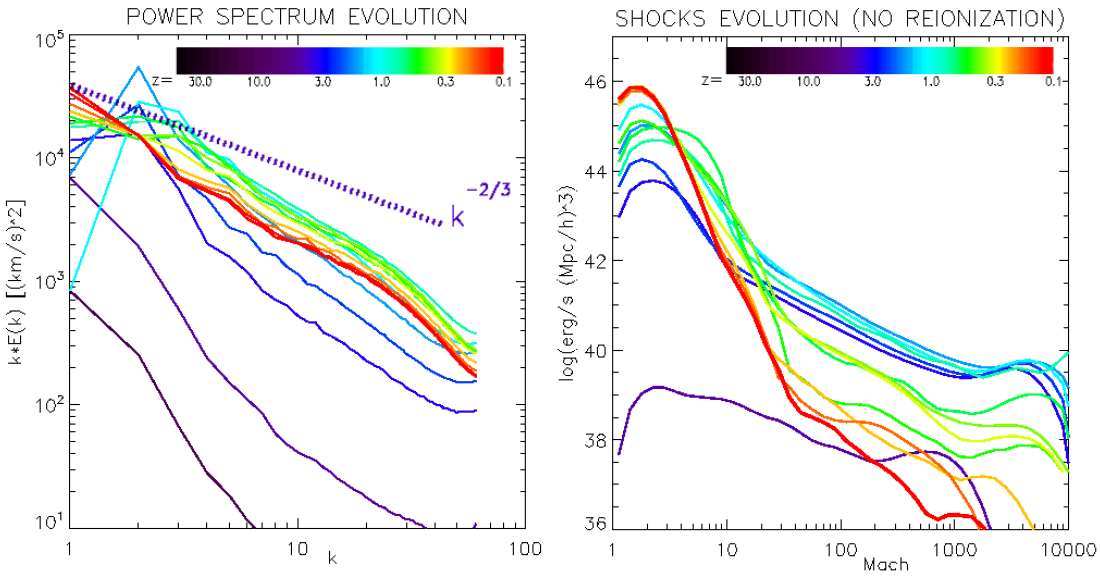

Figure 5.12: *Left:* time evolution from of the $kE(k)$ for a sub-volume of side $3.5Mpc$ in the v256-3 run. The additional dashed line shows the slopes for the Kolmogorov model. *Right:* time evolution of the thermal energy flux at shocks for the same volume. The color coding for the liens is shown in the color bar.

function. Shown are the transverse ($\mathbf{v} \perp \mathbf{l}$) and longitudinal ($\mathbf{v} \parallel \mathbf{l}$) structure functions extracted from a random sub-sample of $\sim 10^5$ cells in the simulated volume. The same structure functions are also calculated for the density-weighted velocity, $\mathbf{u} \equiv \rho^{1/3}\mathbf{v}$, which was introduced by Kritsuk et al.(2007) to study scaling relations for simulated supersonic turbulence. All signals show a peak at $\sim Mpc$ scales, thus implying that the maximum outer scale for the drive of turbulence should of the order of R_{vir}.

5.3.6 Time Evolution

Fig.5.12 (top left panel) shows the evolution with cosmic time of $kE(k)$ within a sub-volume of $3.5Mpc$ centered on the cluster center, for a sub-sample of outputs of the v256-3 run. The bulk of turbulence is driven at the epoch of the major merger, at $z \sim 1$, at scales in the range $\sim 1 - 2Mpc$. At smaller redshifts, the spectrum gradually approaches the shape in Fig.5.11. In order to explore the connection between turbulence injection and shocks generation, we also plot in the top right panel of Fig.5.12 the evolution of the thermal energy flux through shocks for the

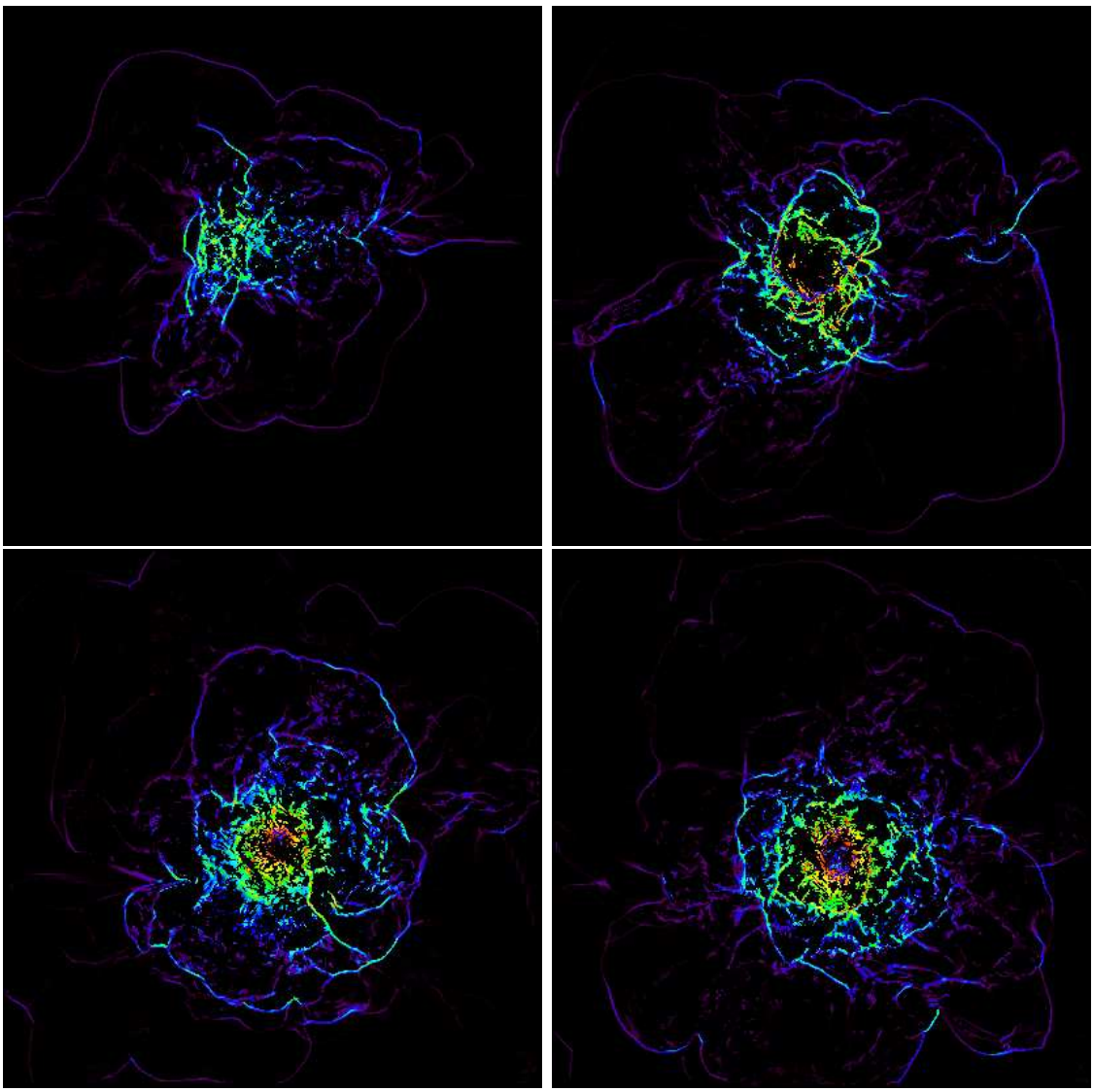

Figure 5.13: Slices of side $7.5Mpc$, showing the evolution of the thermalized energy flux at shocks, for different epochs ($z = 1$,$z = 0.8$,$z = 0.5$ and z=0.1) of the $v256 - 4$ run. The resolution of the image is $18kpc$ per pixel. The color coding is approximately: *red*=$f_{th} > 10^{46} ergs/s$, *green*= $10^{45} ergs/s < f_{th} < 10^{46} ergs/s$ and *blue*= $f_{th} < 10^{45} ergs/s$.

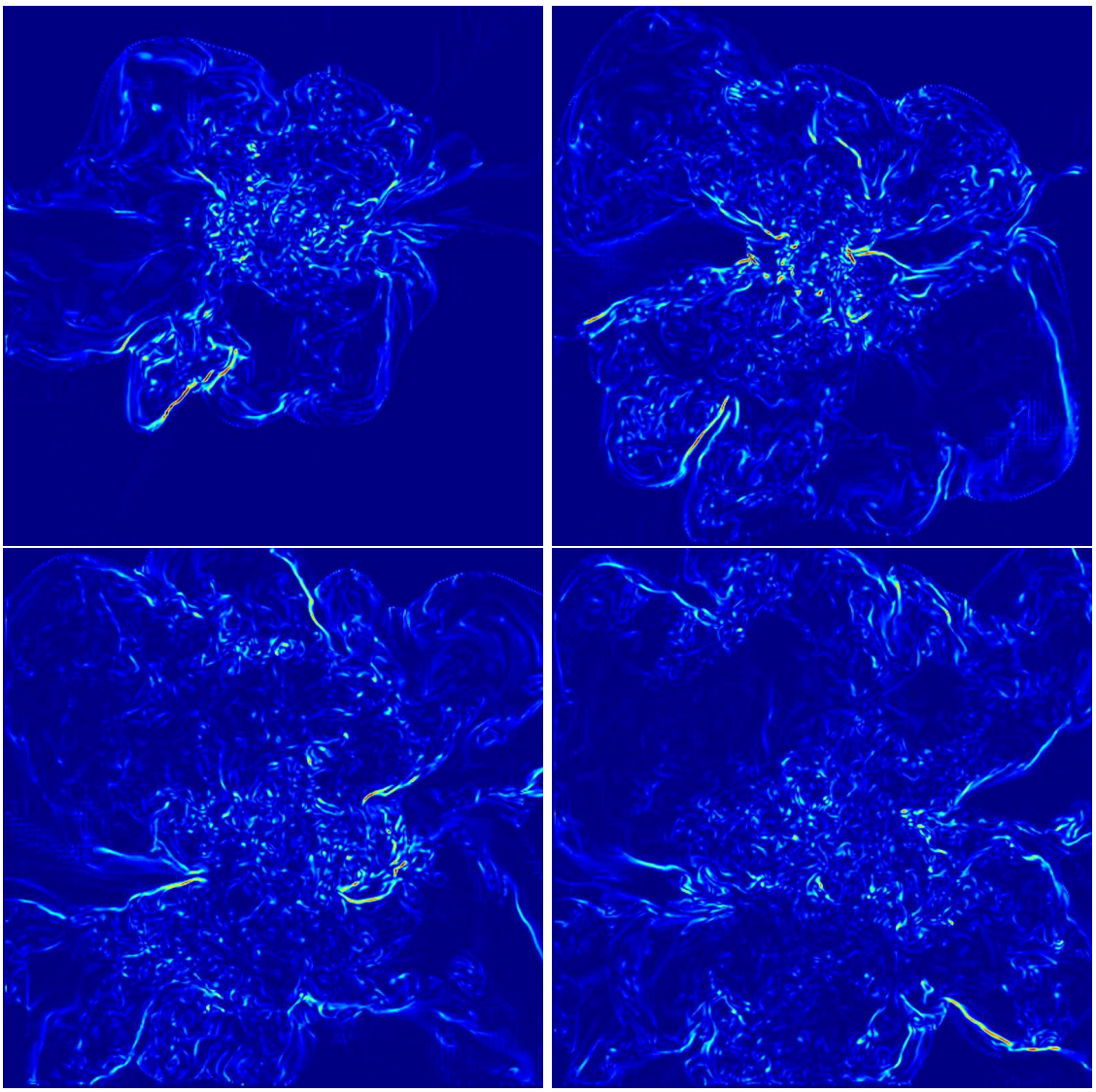

Figure 5.14: Slices of side $7.5Mpc$, showing the evolution of the modulus of curl of velocity, for different epochs ($z = 1$,$z = 0.8$,$z = 0.5$ and z=0.1) of the $v256 - 4$ run. The resolution of the image is $18kpc$ per pixel, the red/green colors locate the largest value of the curl of velocity.

same sub-volume (a map of Mach numbers in the v256-4 run is shown in colors in the right panel of Fig.5.9). Mach numbers and energy fluxes are calculated according to Eqs.7 and 10 in Vazza, Brunetti & Gheller (2009), using the information of the velocity jump and the speed of sound of pre-shock cells (note that due to the absence of a re-ionization background, the sound speed in under-dense cells can be unrealistically low). A bump of thermal energy flux marks the epoch of the major merger, when thermal energy is being pumped within the cluster by strong $M \sim 3-6$ shocks. After virialization occurs, extremely strong shocks become rare and the shocks energy distribution reaches the typical steep shape which is usually measured in evolved galaxy clusters (e.g. Pfrommer et al.2007, Vazza et al.2009). Lower panels in Fig.5.12 present the complete time evolution for the $kE(K)$, the Mach number distribution and the energy flux distribution, for all outputs of the simulation. As shown in Fig.5.9, the tight connection between the pattern of shock waves in the galaxy cluster and the turbulent velocity field is clear. This is further suggested by looking at the Maps in Figures 5.13-5.14, where we present cuts showing the energy flux at shocks and the modulus of curl of velocity for four different epochs ($z = 1$,$z = 0.8$,$z = 0.5$ and z=0.1) in the central region of the simulated galaxy clusters in the v256-4 run. The spatial correlation between high energy shocks and injection of vorticity at small scale is quite evident; this further suggests the idea that the driving mechanism of turbulent injection in the simulated ICM is the (mildly supersonic) drive of in-falling structures, and qualitatively confirms the picture sketched in Sec.5.2.6.

5.3.7 Discussion

A simple implementation of a new refinement criterion in ENZO simulations allows to follow shocks and turbulent motions with unprecedented detail, even at large distances from cluster centers. This refinement criterion is successful in catching the bulk of turbulent motions developed in the ICM by cluster formation processes, allows us to measure velocity power spectra across two orders of magnitude in spatial scales,

and to follow shocks evolution over time with great detail. In all the analyzed AMR runs, the simulated ICM is found to host turbulent motions (on scales $< 300kpc$) accounting for a $\sim 5-25$ per cent of the gas thermal energy within R_{vir}. Compared to refinement on over-density, the new criterion shows lower inner gas density, flatter entropy profiles and significantly larger turbulence budget at all radii. This is likely due to the sharper representation of shock waves and turbulent motions, and highlights the importance of highly resolving these phenomena in discussing accretion processes in the ICM of galaxy clusters.

5.4 Conclusions

In this Chapter we presented results from two numerical studies aiming at the characterization of turbulent motions in the ICM of simulated galaxy clusters. We used two of the most diffused cosmological codes on the market, GADGET2 and ENZO, and we developed recipes to efficiently disentangle laminar bulk motions from chaotic small scale motions.

These approaches allow us to investigate the still poorly explored issue of the injection of turbulent motions in galaxy clusters in connection with their cosmological formation process, and a strict comparison between the above works is currently not feasible: the first was focused on a sample of simulated galaxy clusters in various dynamical states, while the second was focused at the re-simulation of the same (merging) galaxy cluster adopting different AMR criteria. Moreover, the slightly different setup of cosmological parameter (due to the fact the the two set of simulations were produced after different releases of the WMAP data) may cause some additional effects, e.g. the higher σ_8 normalization adopted in GADGET simulations (Sec.5.2) is expected to produce significantly more evolved galaxy clusters than in ENZO AMR simulations (and in Vazza et al.2009).

In both the numerical approaches followed in this Section, the dissipation of turbulent motions is expected to happen due to artificial viscosity, at spatial scales of the order of the spatial resolution of the simulations. Thus the study of turbulent motions con only be done for scales well above the formal spatial resolutions of the codes.

In both of the numerical approaches, the process of galaxy clusters formation is found to be a natural source of turbulent motions in the ICM, through the injection of fluid instabilities at scales generally $< 1 Mpc$. Since the outer drive of turbulence is related to the process of accretion of substructures, and the injection of chaotic energy happens approximately at a constant fraction of the infall velocity (which is related to the total mass of the host galaxy cluster), one should expect that the total turbulent energy in the ICM scales with the total thermal energy of the host galaxy cluster (e.g. Cassano & Brunetti 2005). This is quantitatively measured across a wide range of cluster masses in SPH, and qualitatively found also in AMR results by looking at the associations between shocks and turbulent motions.

The total turbulent energy within R_{vir} is $\sim 20 \div 30$ per cent of the thermal energy within the same radius, when only turbulent motions are considered on scales $\leq 100 \div 300$ kpc. An additional budget might come from larger scales and the above estimate should be considered as conservative.

In both codes, as soon as numerical techniques are adopted to reduce the artificial viscosity that suppresses turbulent motions (e.g. by switching off artificial viscosity outside shocks in SPH, and by increasing the spatial resolution where chaotic velocity field are measured in ENZO), the level of turbulence increases and also the innermost properties of the ICM are found to be affected by this additional energy/pressure budget (increasing entropy and temperature, and decreasing gas density), up to a ~ 10 per cent level.

We stress that a discrepancy is presently found by comparing the turbulent energy profile for $r < 0.1 R_{vir}$, when results with GADGET *lvisc* are compared to ENZO AMR runs. The innermost profile in GADGET is found to be steeply increasing towards the cluster center, and the level of turbulent energy inside $0.1 R_{vir}$ is about one order of magnitude larger in SPH than in ENZO. However, we observe that the increase in DM mass resolution in ENZO causes a progressive change of slope in the inner turbulent energy profile, and that in the case of runs with the

the highest DM resolution that we adopted in ENZO (run $v256-3$) the shape of the profile is more similar (compared to re-simulation with a lower DM resolution) to that found in SPH. Most importantly, we note that the higher spatial resolution achieved in GADGET runs (compared to ENZO run) in the innermost region of the simulated galaxy clusters is "counter-balanced" by the much higher resolution achieved in ENZO in the outermost region ($r \geq 0.5R_{vir}$). Since the injection of turbulent motions is expected to be more efficient with increasing resolution, we believe that part of the difference between AMR ENZO and GADGET is due to the fact that the injection of cluster turbulence in ENZO happens at larger radii through stripping and shocks mechanisms and that these turbulent motions are lost in GADGET due to the relatively poor resolution of SPH in the external regions.

We note that the inclusion of cooling processes within the simulations is not expected to modify much our conclusions outside cluster cores, because the average cooling time for the large cluster regions considered here is longer than an Hubble time. Cooling may play an important role in innermost regions, where however only a small fraction of the turbulent energy is stored, yet the inclusion of cooling in simulations would also require the implementation of feedback mechanisms – like galactic winds and bubble inflation by AGNs – in order to prevent un–physical massive cooling flows. These complex processes may induce additional turbulent motions and future studies are required to understand their importance.

Chapter 6

Conclusions & Perspectives

6.1 Summary of Results

This thesis presents results on the characterization of shocks and turbulence in the Intra Cluster Medium using cosmological numerical simulations (the Eulerian code ENZO and the SPH code GADGET), with the aim of improving our understanding of the connection between these two phenomena and the cluster-formation process. The final goal of these studies is to contribute to the theoretical modeling of non–thermal components in the Intra Cluster Medium and of the related non-thermal emissions observed in galaxy clusters.

Using some of the most diffuse cosmological numerical codes on the market, we applied numerical simulations of galaxy clusters formation to the study of the generation of shocks waves, turbulent motions and CR injection in a detailed way. Simulations have a relevant impact in the theoretical understanding of non–thermal processes in galaxy clusters, because they allow to follow complex phenomena in a time-dependent way, providing an important tool to compare theoretical hypothesis with observations.

We conceived original numerical algorithms to detect and characterize the properties of shocks and turbulent motions and performed extensive comparison between our results and those in the literature.

In this respect we provide two innovative approaches:

* we propose a novel approach, based on measured gas velocity jumps,

to characterize shocks with grid codes, and extensively apply this approach to ENZO simulations. We have shown that this approach provides a more solid characterization of shocks in cosmological simulations, with respect to the usual adopted one, that is based on the analysis of temperature jumps; we find that this is particulary important in the case of the low density environments in the simulated universe;

* we propose a novel approach to trigger Adaptive Mesh Refinement in grid codes. This is based on a combination of the standard AMR criterion (triggered by over-density) with a new AMR criterion triggered by gradients in the gas velocity field. We have shown that this new AMR criterion allows to follow galaxy clusters in cosmological simulations with high spatial resolution both in the central regions and in the external regions where accretion shocks come into play. We applied this scheme to ENZO simulations and we were able to study, for the first time, the power spectrum of turbulent motions over 2 orders of magnitude in spatial scale, and to highlight the connection between turbulent motions and large scale shocks.

Moreover, we presented preliminary results from a comparison project carried out between different cosmological codes (e.g. ENZO, GADGET and TVD) that are used to study shocks in the simulated large scale structures. We discussed the environmental and numerical regimes where the best agreement between the codes is found, and we explored the possible reasons for the disagreement.

In the following, we summarize the most important results of the present thesis:

* we find that different numerical approaches (ENZO, TVD, GADGET) predict similar properties of large scale structures of the universe, such as: mass distribution of halos, large scale morphology, distribution of gas density and gas temperature, baryon fraction of halos, profiles of thermal properties of galaxy clusters inside R_{vir}. The typical scatter on the simulated quantities analyzed in this thesis (once that a suitable minimum resolution criterion is adopted) is of the order of ~ 10 per

cent (Sec.4.4 -4.5.4).

* The process of structure formation in the universe is an ubiquitous source of shock waves, that are found to fill a $10-20$ per cent of the total volume of the simulated universe (Sec.3.7.1). The bulk of the kinetic energy is dissipated in thermal energy at shocks with Mach number $M \sim 2$ inside virialised structures, and the distribution of the energy flux through shocks in the universe can be broadly described by a steep power law. The average Mach number of shocks increases in more rarefied environments, and tails of very strong shocks (i.e. $M > 100$) are also found in accretion regions, outside clusters and at the boundary of filaments. These findings are common to all numerical codes analyzed in this thesis (see Chap. 3 - 4).

* Different numerical algorithms to capture shocks in different simulations are discussed (Sec.3.5-4.6.1). On average, we find that the different approaches are in broad agreement within the high temperature and dense region of clusters, while they disagree outside these regions. When different methods are applied to the same simulation (Sec.3.6.4), we obtained stronger shocks in the case of the temperature-based method (TJ) with respect to the velocity-based method (VJ). The differences in the characterization of shocks and of their statistical properties in the simulated volume become larger when comparing different codes (Sec.4.6.2-4.6.5) and this suggests that the details of how gas-dynamics is modeled cause an important source of uncertainty to characterize shocks; we conclude that an important source of uncertainty to derive shock statistics is specific implementation of the re-ionization background in the simulations (Sec.3.6.3).

* In the innermost region of galaxy clusters shocks are found to be weak on average, with $< M > \leq 2$ up to $\sim 0.5-1 R_{vir}$ in all numerical codes (Sec.3.7.4). Approaching R_{vir}, we observe a steep increase of the value of the mean Mach number in the case of grid-based simulations, while a smooth increase is found in the clusters simulated with SPH. This comes from the fact that accretion shocks in grid codes are sharp,

while in SPH they smoothed out into extended clumps. Importantly, this is found to correlate also with the different distribution of entropy at $\approx R_{vir}$ (which is much peaked in grid codes, see Sec.4.5.4).

* Galaxy clusters are likely powerful sources of CR via the shock acceleration mechanism. We investigated the issue of CR injection at shocks in numerical simulations using several theoretical models (Sec.3.7.3, Sec.4.6.6) and found that the average injection rate in massive galaxy clusters is ≤ 10 per cent of the energy injection rate in form of thermal energy. Importantly, since this process is mainly provided by $M \sim 2 \div 3$ shocks, the spectrum of the accelerated CR is relatively steep, providing a contribution to the non-thermal emission in the radio band (via synchrotron emission from secondary electrons) and in the gamma rays (via decay of secondary π^0), that is in line with present upper limits from radio and gamma rays observations (Sec.3.8.3). The differences found in the statistical properties of shocks in external regions (low density environments) in the different simulations drive large differences in the estimate of the injection rate of CR in these regions. We thus concluded that present simulations are not suitable to firmly address the properties of CR injected at shocks in these regions.

* Accretion processes during the formation of cosmic structures inject turbulent motions in galaxy clusters (Chap.5). Using complementary numerical approaches (i.e. SPH and ENZO AMR simulations), we showed that the amount of turbulent energy inside the virial region of galaxy clusters is ≈ 30 per cent of the total thermal energy (Sec.5.2.5-5.3.4). We also found that the energy support of turbulence slightly affects the thermal properties of simulated galaxy clusters, when these properties are compared to those from standard simulations where turbulent motions are suppressed due to large numerical viscosity (Sec.5.2.4 and 5.3.4).

* Using an implemented AMR criterion for ENZO simulations, we studied in detail the spectral properties of 3-D gas velocity field of a reference galaxy cluster, achieving a high spatial resolution (i.e. 18

kpc) across the whole cluster volume (Sec.5.3.5). Remarkably, the power spectrum of the gas velocity field is broadly described by a steep power law behaviors, in the scale range $40kpc \div 1Mpc$. The use of velocity structure functions confirms a maximum coherence length of the cluster velocity field $\approx$ 1Mpc.

6.2 Future Developments

Overall the results of this thesis suggest that present numerical simulations provide a powerful (even though not yet convergent, when different techniques are compared) tool to study shocks and chaotic motions in galaxy clusters. These are crucial processes in our theoretical understanding of non-thermal processes in galaxy clusters and large scale structures of the universe.

This thesis represents a first, exploratory step in a self-consistent description of the interplay between thermal and non-thermal components in the intra cluster medium, by the extensive use of numerical codes. The necessary second step would be to include CR in the simulations.

In Chap.3 and 4 we have shown that CR protons are likely dynamically important in low density environments of the universe, and this requires to include this component in the next generation of numerical simulations. We plan to implement ENZO to model in run time the feedback of these CR protons on gas dynamics. First approaches in this direction have been carried out by Pfrommer et al.(2006) with SPH simulations. Given the large discrepancy that we find when comparing the outer regions of clusters simulated with grid codes and with SPH, it is crucial to explore CR dynamics also in Eulerian simulations with ENZO. Moreover, it would be important to treat in detail the issue of the back-reaction of accelerated CR on the thermal structure of the shock itself, and this can be done by means of non-linear semi-analytical methods available in literature. This is an unexplored territory in cosmological numerical simulations, since the approach adopted so far is that of modeling only the dynamical feedback of CR hadrons on the thermal gas, and to apply diffusive shock acceleration also even in the presence of sizable CR pressure in the simulated structures

(e.g. Ensslin et al.2007).

A different case is that of CR electrons. These particles are believed to be energetically sub-dominant with respect to protons and in addition their fast evolution with time (due to radiative losses) makes impossible to follow this component in run-time with cosmological numerical simulations. Yet relativistic electrons and their interplay with shocks and turbulence drive the non thermal radio and hard-X emission in galaxy clusters, where many observations are now available. We thus plan to follow electrons as passive tracers in ENZO simulations. During this PhD thesis, we already developed and tested a post processing pipeline, which uses the 3-D gas velocity fields to follow the evolution of tracers (see Fig.6.1). This approach opens the possibility to model the injection of CR particles and to follow the time evolution of their energy spectrum due to radiative and Coulomb losses, and the re-acceleration from shocks and turbulence.

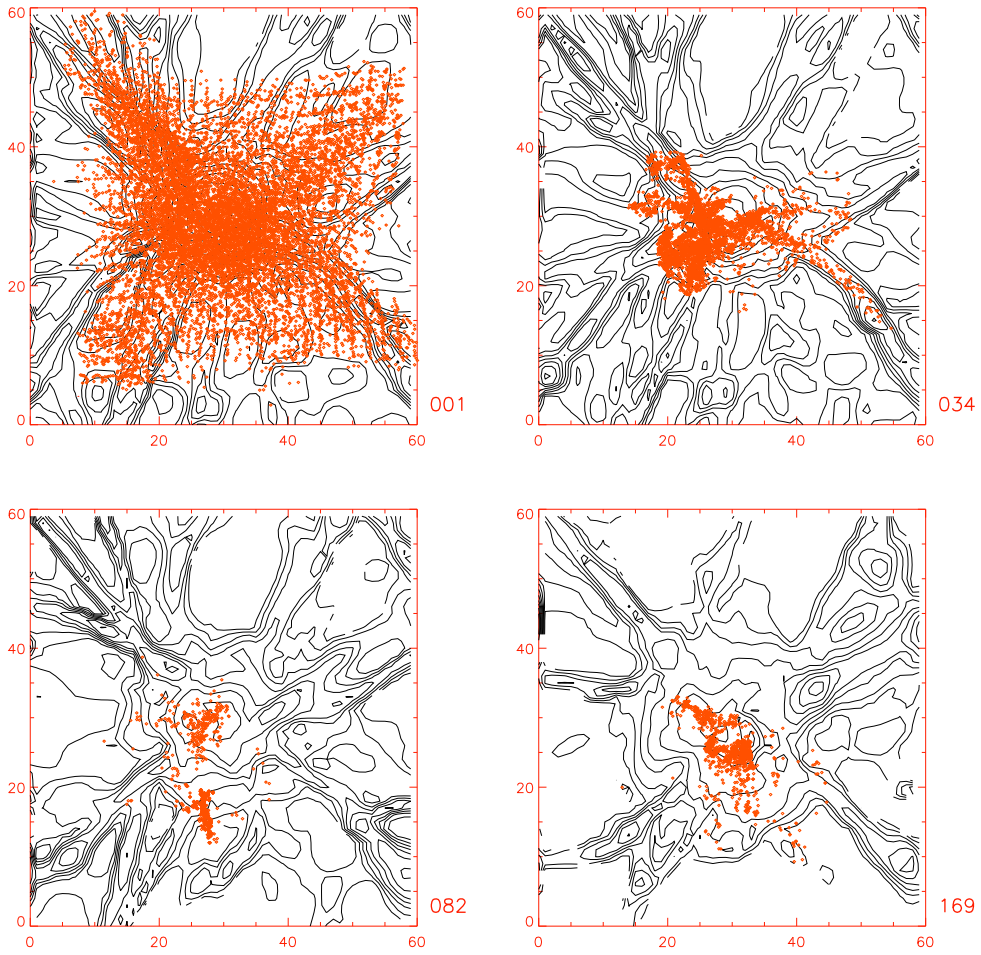

Figure 6.1: 2–dimensional cuts of 4 evolutionary time steps in the density distribution (isocontours) and tracers (red points) of a galaxy cluster. The side of the image is 8 Mpc. The redshift of the panel are z=1, z=0.8, z=0.5 and z=0, respectively.

Chapter 7

Appendix

7.0.1 The effect of spatial resolution on shocks properties.

We investiagated the effect of resolution on the properties of detected shocks by re–simulating the same initial conditions and cosmic volume of the $AD125$ simulations of Chapter 3 at resolutions of $800kpc$, $500kpc$ and $250kpc$.

Even if most of the graphs and statistics presented in the paper are done by using $n = 1$ for the shock detecting scheme (see Sec.5.3) and thus assuming that the best reconstructing of the shock discontinuity is achieved by considering a jump of 2 cells between pre-shock and post-shock, here we prefer to keep this jump smaller (i.e. $n = 0$). This is in order minimize

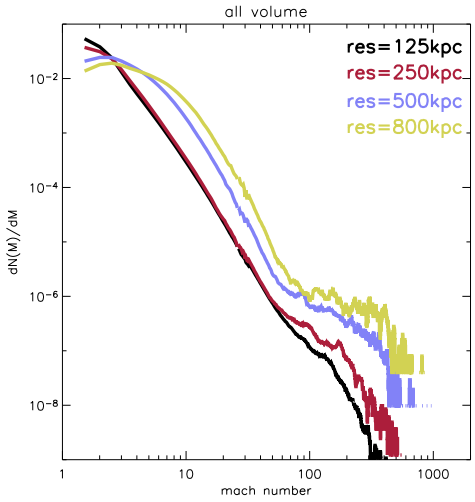

Figure 7.1: Mach numbers distribution for the total $80Mpc$ box at 4 different numerical resolutions.

any confusion coming from the fact that in poorly resolved runs shocks have sizes of typical cluster halos (i.e. for $n = 1$ in the $AD800$ one would reconstruct shocks across $1.6Mpc$). This is fair enough to reconstruct the trend with resolution within our simulations, and the comparison to the $n = 1$ case can be recovered in Fig.14.

We find that at all these resolutions Eq. 3.1 provides a good fit to the density–temperature distributions obtained with run time re–ionization. Thus we use this relation to model the reionization in our post processing approach at all resolutions. We then analyse the outputs at $z = 0$ and derive statistical properties of shocks in the simulated volumes, following the procedures given in the previous Sections.

The number distributions of shocked cells as a function of their Mach number are given in Fig. 7.1 for the different resolutions. We find that the results converge at higher resolutions, in particular the shape of the distribution and integral number of shocked cells obtained with $125kpc$ and with $250kpc$ resolution are consistent within ≈ 20 percent. A relevant point here is that the excess of shocks with high Mach number found at low resolution is progressively reduced with increasing resolution.

The case of the thermal energy flux and CR energy flux dissipated at shocks is reported Figures 7.2 This case is more unclear as it depends on the combination of the properties of shocks with the local baryon overdensity. Despite the properties of shocks statistically converge with resolution, the overdensity in the simulated volume increases with spatial resolution and this causes the increase of the dissipated energy at higher resolutions. Anyhow also in this case some level of convergence is obtained in line with previous studies (Ryu et al. 2003; Pfrommer et al. 2006a). The hardest case is that of galaxy clusters, where the dissipation of the energy dissipation at shocks increases by one order of magnitude between lower and higher resolution datasets (this still inceases by ≈ 1.5 times between the 250 and 125 kpc datasets).

Despite this slow convergence with resolution, the value of the ratio f_{CR}/f_{th} is not found to change significantly with resolution since the spatial resolution affects the two quantities in a similar way.

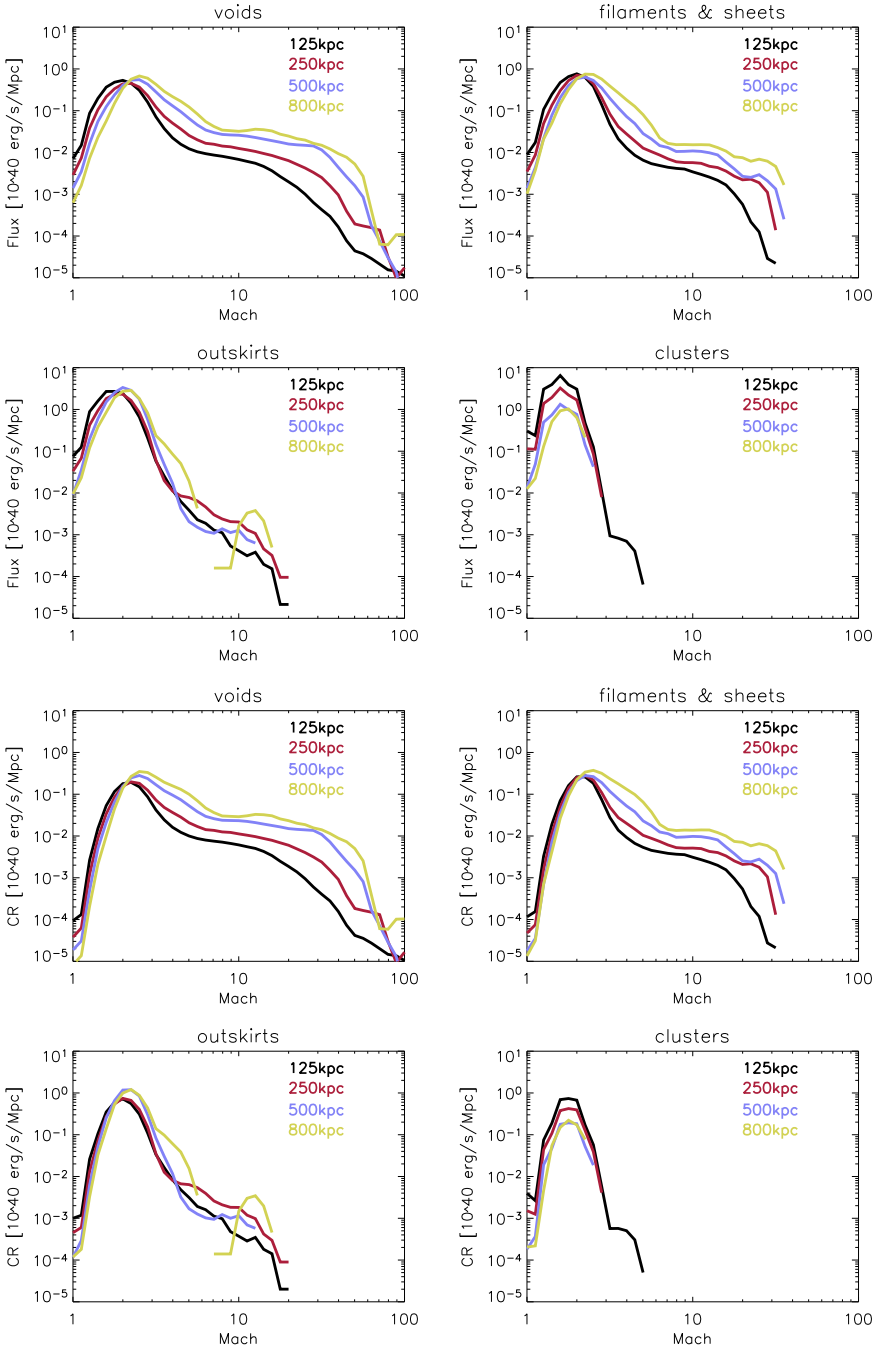

Figure 7.2: Distribution of the thermalised energy flux (*Top*) and CR flux (*Bottom*) in different overdensity bins, for 4 different numerical resolution.

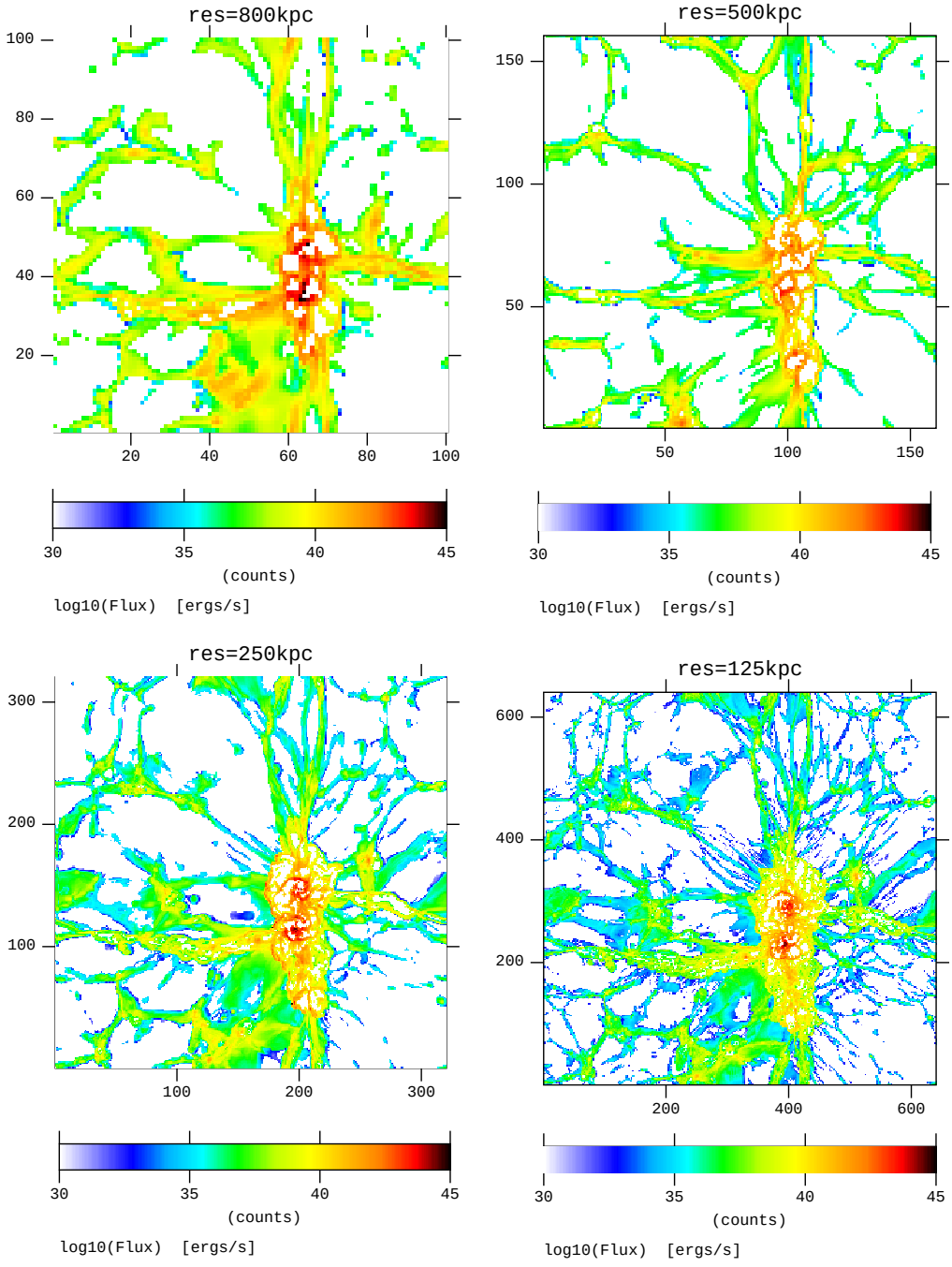

Figure 7.3: 2–dimensional cuts of the thermalized energy flux through shocks, for the same $80Mpc$ simulated volume at four different numerical resolutions. The width along the line sight is kept constant as $\sim 500kpc$ ($800kpc$ for the $CO800$ run).

7.0.2 The effect of a variation of the σ_8 parameter.

The value of the σ_8 parameter (the normalization in the power spectrum of primordial overdensity fluctutations) crucially affects the abundance of collapsed objects in the universe at a given epoch. This value is not presently well constrained: very recent CMB analysis give a relatively small value, $\sigma_8 = 0.74$ (Spergel et al.2007), with respect to that derived from previous CMB data–analysis (Spergel et al.2003) and to the constraints from the observed abundance of galaxy clusters (e.g. Evrard et al.2007). In this Appendix we briefly discuss the effect of the σ_8 parameter on the statistical properties of the shocks as measured in our simulated datasets (adopting as in the previous Section $n = 0$ for the reconstruction of shocks). We thus resimulated the *CO250* run with $\sigma_8 = 0.74$ (*S8250*) and applied all the procedures discussed in the previous Sections to derive the properties of the shocks (note that the CO250 and S8250 simulations have run–time re-ionization).

Theoretically, the population of shocks in a universe with larger σ_8 is expected to evolve faster as more power is associated with the primordial overdensity fluctuations. Thus, at a fixed redshift, universes with larger σ_8 host more evolved structures, which are characterized by typically higher internal sound speeds at higher densities, and low temperatures in low density regions.

The distribution of thermalised energy at shocks in the two simulations is given in Fig.B1. Although modifying the value of σ_8 has some effect on the properties of the shocks in the simulations, the net result is that, within the presently allowed region of the values of the σ_8 parameter, no clear difference in the properties of the shocks are found. Globally we find that the energy dissipated at the present time in the *S8250* simulation is ≈ 2 times smaller than that in the *CO250* simulation, and the distribution with Mach number of the dissipated energy in underdense regions is slightly flatter with decreasing σ_8.

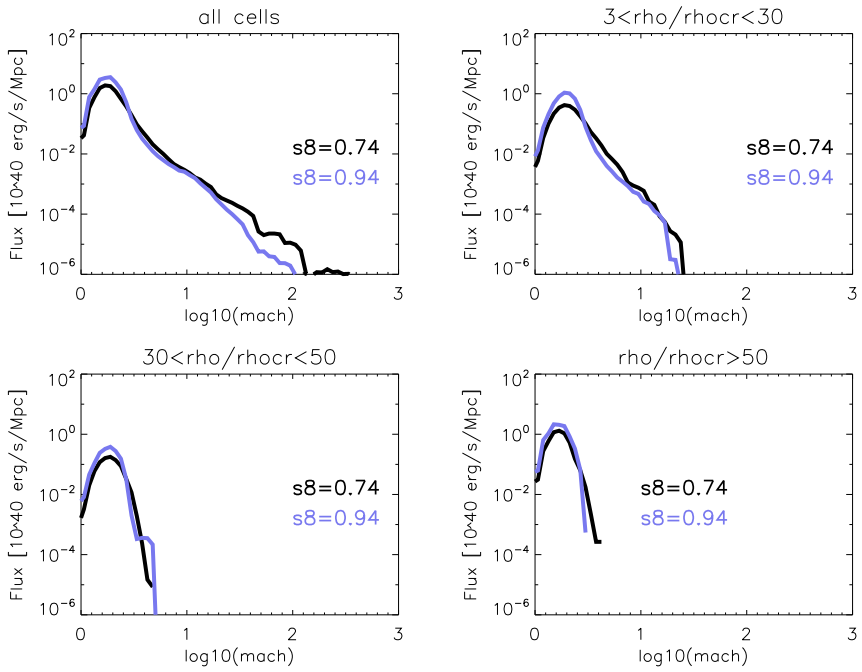

Figure 7.4: Effect of the variation of the σ_8 parameter on the distribution of thermalised flux, in different overdensity bins.

7.0.3 The Application of Simulated Turbulence to Radio Halos

As discussed in the Introduction (Sec.2.3.1) One promising possibility to explain radio halos is electron acceleration by cluster turbulence (e.g. Brunetti & Lazarian 2007).

Starting from the results obtained in Sec.5.2.3, in this Section, we carry out a first exploratory analysis of the efficiency of electron acceleration that is expected in the ICM, based on the turbulent energy we inferred from our SPH simulations performed with the low viscosity (*lvisc*) scheme. We focus on the case of Fast Modes in the ICM, since in this theoretical case relativistic electrons are mainly accelerated by coupling with large scale modes (e.g., $k^{-1} \geq$ kpc, k being the wave number) whose energy density can hopefully be constrained with the numerical simulations in a reliable fashion. In addition, the damping and time evolution of Fast Modes basically depends only on the properties of the thermal plasma and it is not sensitive to the presence of cosmic ray protons in the ICM (e.g. Brunetti & Lazarian 2007).

Relativistic particles couple with Fast Modes via magnetic Landau damping. The necessary condition for Landau damping (Melrose 1968; Eilek 1979) is

$$\omega - k_{\parallel} v_{\parallel} = 0, \quad (7.1)$$

where ω is the frequency of the wave, $k_{\parallel}$ is the wavenumber projected along the magnetic field, and $v_{\parallel} = v\mu$ is the projected electron velocity. Large scale fluid turbulence is resolved by our simulations and therefore we assume that Fast Modes can be described as a fraction η_m of the fluid turbulence, measured by the local velocity dispersion (e.g. equation 5.10) as described in Section 5. A simplified formula giving the gain of momentum (p) of particles subject to non-linear interaction with Fast Modes is given by Cassano & Brunetti (2005):

$$\frac{\mathrm{d}p}{\mathrm{d}t} \sim 180 \frac{v_{\mathrm{M}}^2}{c} \frac{p}{B^2} \int \mathrm{k} W^B(\mathbf{k}) \mathrm{d}k, \quad (7.2)$$

where B is the magnetic field, v_{M} is the magneto–sonic velocity, and $W^B(\mathbf{k})$ is the power spectrum of the magnetic field fluctuations (e.g. Barnes & Scargle 1973; Cassano & Brunetti 2005).

We estimate the rate of injection of Fast Modes, I_k^{FM}, assuming that a fraction, η_m, of fluid turbulence is associated with these modes and that turbulence is injected and dissipated in galaxy clusters within a crossing time, τ_{cross}. One has :

$$I_k^{FM} \sim \eta_m \frac{E_t}{\tau_{cross}} \sim \frac{1}{2} \eta \rho_{gas} \sigma_v^2 \tau_{cross}^{-1} \quad (7.3)$$

Following Cassano & Brunetti (2005) the spectrum of the magnetic fluctuations associated with Fast Modes is computed under stationary conditions by taking into account the damping rate of these modes with thermal electrons, $\Gamma_k = \Gamma_o k$; one has :

$$W_k^B \sim \frac{B_o^2}{8\pi} \frac{1}{P_{gas}} \frac{I_k^{FM}}{\Gamma_o k} \quad (7.4)$$

Thus the integral in Eq.(7.2) at each position of the grid in our simulated clusters can be readly estimated through:

$$\int kW_k^B dk \sim \eta \frac{B^2(\mathbf{x})}{16\pi} \frac{\rho_{\rm gas}(\mathbf{x})\sigma_{ii}^2(\mathbf{x})}{P_{\rm gas}(\mathbf{x})} \frac{\left\langle k\hat{E}(k)\right\rangle}{\Gamma_o \tau_{cross}} \tag{7.5}$$

where $\hat{E}(k)$ is the normalized power spectrum of turbulence, $\left\langle k\hat{E}(k)\right\rangle \sim 1$, and Γ_o depends on the temperature of the ICM (Cassano & Brunetti 2005). Here we are primarily interested in the maximum energy of accelerated electrons, given the energy density for Fast Modes in our simulations. This maximum energy of electrons is determined reached by the balance between radiative losses and acceleration. The radiative synchrotron and inverse Compton losses are given by (e.g. Sarazin 1999)

$$\begin{aligned} \left(\frac{{\rm d}p}{{\rm d}t}\right)_{\rm rad} &= -4.8\times 10^{-4} p^2 \left[\left(\frac{B_{\mu G}}{3.2}\right)^2 \frac{\sin^2\theta}{2/3} + (1+z)^4\right] \\ &= -\frac{\beta p^2}{m_e\, c}, \end{aligned} \tag{7.6}$$

where $B_{\mu G}$ is the magnetic field strength in μG, and θ is the pitch angle of the emitting electrons. If an efficient isotropisation of electron momenta can be assumed, it is possible to average over all possible pitch angles, so that $\left\langle \sin^2\theta\right\rangle = 2/3$, and the maximum Lorentz factor of electrons comes out:

$$\gamma_{max} \approx 180 \frac{v_M^2}{\beta c B_{\mu G}^2} \cdot \int kW_k^B dk. \tag{7.7}$$

In Figure 7.5 we report the distribution of the maximum Lorentz factor of the fast electrons obtained via Eq.7.7 along the line through the cluster atmosphere drawn in upper panels of Fig.5.1. The two different lines are obtained in the case of the *lvisc* and *ovisc* schemes. This highlights the importance of the new scheme with "low" viscosity(*lvisc*): when the *lvisc* scheme is used, enough turbulence is resolved to maintain high energy electrons almost everywhere out to a distance of ≈1 Mpc from the cluster center.

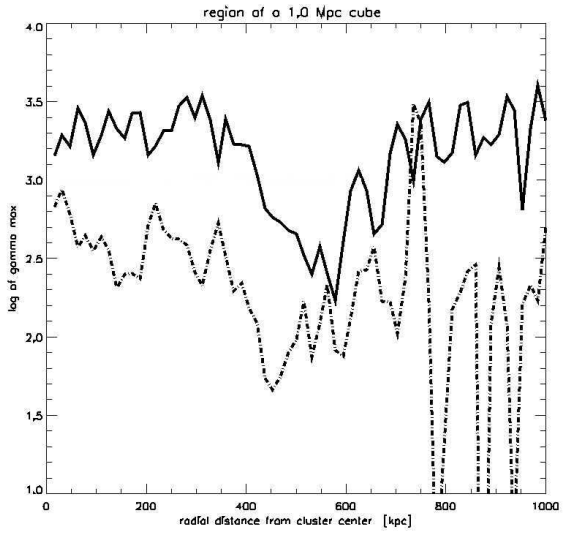

Figure 7.5: One-dimensional profile of the maximum energy of the electrons accelerated via the turbulent-magneto-sonic model, along the same vertical lines drawn in Figure 5.1. Dashed lines are for the standard viscosity run, while solid lines are for the low viscosity scheme.

Chapter 8

Bibliography

[1] Agertz O., et al., 2007, MNRAS, 380, 963

[2] Aharonian F., et al., 2009, ApJ, 691, 175

[3] Amato E., Blasi P., 2006, MNRAS, 371, 1251

[4] Arimoto, N. & Yoshii, Y. 1987, , 173, 23

[5] Ascasibar, Y., Yepes, G., Müller, V., & Gottlöber, S. 2003, , 346, 731

[6] Bagchi, J., Durret, F., Lima Neto, G.B., & Paul, S., 2006, Science, 314, 791

[7] Bagla J. S., 2002, JApA, 23, 185

[8] Bagla J. S., Prasad J., 2006, MNRAS, 370, 993

[9] Bagla J. S., Ray S., 2005, MNRAS, 358, 1076

[10] Bartlett, J.G., 2006, astro-ph/0606241

[11] Belsole E., Pratt G. W., Sauvageot J.-L., Bourdin H., 2004, A&A, 415, 821

[12] Belsole, E., Sauvageot, J.-L., Pratt, G.W., & Bourdin, H., 2005, Adv. Sp. Res., 36, 630

[13] Berezinsky V. S., Blasi P., Ptuskin V. S., 1997, ApJ, 487, 529

[14] Berger M. J., Colella P., 1989, JCoPh, 82, 64

[15] Berrington R. C., Dermer C. D., 2003, ApJ, 594, 709

[16] Blandford R. D., Ostriker J. P., 1978, ApJ, 221, L29

[17] Blandford, R. & Eichler, D. 1987, , 154, 1

[18] Blasi P., Colafrancesco S., 1999, APh, 12, 169

[19] Blasi P., 2001, APh, 15, 223

[20] Blasi P., 2002, APh, 16, 429

[21] Blasi P., 2004, APh, 21, 45

[22] Blasi P., 2004, NuPhS, 136, 208

[23] Blasi P., Gabici S., Brunetti G., 2007, IJMPA, 22, 681

[24] Bonafede A., Giovannini G., Feretti L., Govoni F., Murgia M., 2009, A&A, 494, 429

[25] Borgani S., Tornatore L., 2003, Ap&SS, 285, 225

[26] Borgani, S., Murante, G., Springel, V., et al., MNRAS ,2004,348,1078

[27] Borgani, S., Diaferio, A., Dolag, K., & Schindler, S., 2008a, SSR

[28] Borgani, S., Fabjan, D., Tornatore, L., et al., 2008b, SSR

[29] Brighenti F., Mathews W. G., 2003, ApJ, 587, 580

[30] Brüggen, M., Ruszkowski, M., Simionescu, A., Hoeft, M., & Dalla Vecchia, C. 2005, ApjL, 631, L21

[31] Brunetti G., Setti G., Feretti L., Giovannini G., 2001, MNRAS, 320, 365

[32] Brunetti G., 2003, ASPC, 301, 349

[33] Brunetti, G., 2004, JKAS, 37, 493

[34] Brunetti G., Blasi P., Cassano R., Gabici S., 2004, MNRAS, 350, 1174

[35] Brunetti G., Blasi P., 2005, MNRAS, 363, 1173

[36] Brunetti G., Venturi T., Dallacasa D., Cassano R., Dolag K., Giacintucci S., Setti G., 2007, ApJ, 670, L5

[37] Brunetti G., Lazarian A., 2007, HiA, 14, 97

[38] Brunetti G., et al., 2008, Natur, 455, 944

[39] Bryan G. L., Norman M. L., Stone J. M., Cen R., Ostriker J. P., 1995, CoPhC, 89, 149

[40] Bryan G. L., Norman M. L., 1998, ApJ, 495, 80

[41] Bryan G. L., Norman M. L., 1997, ASPC, 123, 363

[42] Bryan G. L., Abel T., Norman M. L., 2001, astro, arXiv:astro-ph/0112089

[234] Buote D.A, 2001, ApJ 553, 15

[44] Buote, D.A., & Tsai, J.C., ApJ,1996,458,27

[45] Burns J. O., Hallman E. J., Gantner B., Motl P. M., Norman M. L., 2007, hvcg.conf, 349

[46] Bykov, A. M. 2001, SSR, 99, 317

[47] Bykov, A., Dolag, K., & Durret, F. 2008

[234] Cassano R., Brunetti G. 2005, MNRAS 357, 1313

[234] Cassano R., Brunetti G., Setti G., 2006, MNRAS 369,1577

[234] Cassano R., Brunetti G., Setti G. et al. 2007, MNRAS 378, 1565

[51] Cassano R., Gitti M., Brunetti G., 2008, A&A, 486, L31

[52] Cassano R., 2009, arXiv, arXiv:0902.2971

[53] Cavagnolo K. W., Donahue M., Voit G. M., Sun M., 2009, arXiv, arXiv:0902.1802

[54] Cavaliere, A. & Fusco-Femiano, R. 1976, ApJ, 49, 137

[55] Cen R., Ostriker J. P., 1999, ApJ, 514, 1

[56] Churazov, E., Brüggen, M., Kaiser, C. R., Böhringer, H., & Forman, W. 2001, ApJ, 554, 261

[57] Churazov E., Forman W., Jones C., Böhringer H., 2003, ApJ, 590, 225

[58] Clarke, T.E., & Enßlin, T.A., ApJ,2006,131,2900

[59] Collins D. C., Xu H., Norman M. L., Li H., Li S., 2009, arXiv, arXiv:0902.2594

[60] Comparato M., Becciani U., Costa A., Larsson B., Garilli B., Gheller C., Taylor J., 2007, PASP, 119, 898

[61] Couchman H. M. P., Thomas P. A., Pearce F. R., 1995, ApJ, 452, 797

[62] Davé, R., Katz, N., & Weinberg, D. H. 2002, ApJ, 579, 23

[63] De Grandi, S. & Molendi, S. 2002, ApJ, 567, 163

[234] Dennison B., 1980, ApJ 239L

[65] Diaferio, A., MNRAS,1999,309,610

[66] Dolag, K., Bartelmann, M., & Lesch, H. 1999, A&A, 348, 351

[67] Dolag K., Enßlin T. A., 2000, A&A, 362, 151

[108] Dolag, K., Bartelmann, M., & Lesch, H. 2002, , 387, 383

[69] Dolag K., Vazza F., Brunetti G., Tormen G., 2005, MNRAS, 364, 753

[70] Dolag K., Meneghetti M., Moscardini L., Rasia E., Bonaldi A., 2006, MNRAS, 370, 656

[71] Dolag K., Borgani S., Schindler S., Diaferio A., Bykov A. M., 2008, SSRv, 134, 229

[72] Dolag K., Bykov A. M., Diaferio A., 2008, SSRv, 134, 311

[234] Dolag K., Vazza F., Ryu D., Kang H., Brunetti G., Gheller C., Pfrommer C., in prep.

[73] Donahue, M., Horner, D. J., Cavagnolo, K. W., & Voit, G. M. 2006, ApJ, 643, 730

[74] Donnert J., Dolag K., Lesch H., Müller E., 2009, MNRAS, 392, 1008

[75] Drury L. O., Voelk J. H., 1981, ApJ, 248, 344

[76] Eisenstein D. J., Hu W., 1999, ApJ, 511, 5

[77] Ellison D. C., Baring M. G., Jones F. C., 1995, ApJ, 453, 873

[78] Ensslin T. A., Biermann P. L., Klein U., Kohle S., 1998, A&A, 332, 395

[79] Enßlin, T.A., & Gopal-Krishna, A&A,2001,366,26

[80] Enßlin, T.A., & Röttgering, H.J.A., A&A, 2002,396,83

[81] Enßlin T. A., Pfrommer C., Springel V., Jubelgas M., 2007, A&A, 473, 41

[82] Ettori, S., Tozzi, P., & Rosati, P. 2003, , 398, 879

[83] Ettori, S., Tozzi, P., Borgani, S., & Rosati, P., A&A,2004,417,13

[84] Ettori S., Dolag K., Borgani S., Murante G., 2006, MNRAS, 365, 1021

[85] Evrard A. E., Henry J. P., 1991, ApJ, 383, 95

[86] Evrard A. E., et al., 2007, astro, arXiv:astro-ph/0702241

[87] Fabian A. C., Sanders J. S., Crawford C. S., Ettori S., 2003, MNRAS, 341, 729

[88] Fan X., Carilli C. L., Keating B., 2006, ARA&A, 44, 415

[89] Feretti, L., Fusco-Femiano, R., Giovannini, G., & Govoni, F., 2001373106

[90] Feretti L., 2005, AdSpR, 36, 729

[91] Feretti, L., & Neumann, D.M., 2006450L21

[92] Ferrari, C., Govoni, F., Schindler, S., Bykov, A., & Rephaeli, Y., 2008, SSR

[93] Finoguenov A., Reiprich T. H., Böhringer H., 2001, A&A, 368, 749

[94] Frenk, C. S., White, S. D. M., Bode, P., et al. 1999, , 525, 554

[95] Fryxell B., et al., 2000, ApJS, 131, 273

[234] Fusco-Femiano R., Orlandini M., Brunetti G., et al. 2004, ApJ 602, 73

[97] Fukugita M., Kawasaki M., 1994, MNRAS, 269, 563

[98] Fusco-Femiano, R., Dal Fiume, D., Feretti, L., et al., ApJ,1999,513,L21

[99] Fusco-Femiano, R., Landi, R., & Orlandini, M., ApJ,2007,654,9

[100] Gabici S., Blasi P., 2003, ApJ, 583, 695

[101] Gardini A., Rasia E., Mazzotta P., Tormen G., De Grandi S., Moscardini L., 2004, MNRAS, 351, 505

[102] Gheller C., Pantano O., Moscardini L., 1998, MNRAS, 296, 85

[103] Giacintucci, S., Venturi, T., Brunetti, G., et al., A&A,2005,440,867

[104] Gingold R. A., Monaghan J. J., 1983, MNRAS, 204, 715

[234] Giovannini G., Tordi M., Feretti L., 1999, NewA 4, 141

[106] Giovannini, G., & Feretti, L., 2000, New Astron., 5, 335

[107] Gnedin N. Y., 1998, MNRAS, 294, 407

[108] Dolag, K., Bartelmann, M., & Lesch, H. 2002, A&A, 387, 383

[234] Godunov, S. K. 1959, Mat. Sbornik, 47, 271

[110] Govoni F., Feretti L., 2004, IJMPD, 13, 1549

[111] Govoni, F., Murgia, M., Feretti, L., et al., A& A 2006,460,425

[112] Guo F., Oh S. P., 2008, MNRAS, 384, 251

[113] Gursky, H., Levinson, R., Kellogg, E., et al., ApJ,1972, 173, L99

[114] Hallman E. J., Ryu D., Kang H., Jones T. W., 2003, AAS, 35, 1348

[115] Haardt F., Madau P., 1996, ApJ, 461, 20

[116] Haiman Z., Holder G. P., 2003, ApJ, 595, 1

[117] Heinz S., Brüggen M., Young A., Levesque E., 2006, MNRAS, 373, L65

[118] Heitmann K., et al., 2008, CS&D, 1, 015003

[119] Henry J. P., Finoguenov A., Briel U. G., 2004, ApJ, 615, 181

[120] Hoeft, M., & Brüggen, M., MNRAS,2007,375,77

[121] Inogamov N. A., Sunyaev R. A., 2003, AstL, 29, 791

[122] Jaffe, W.J., Apj, 1977,212,1

[123] Jeltema, T.E., Canizares, C.R., Bautz, M.W., & Buote, D.A., ApJ,2005,624,606

[124] Jubelgas M., Springel V., Ensslin T. A., Pfrommer C., 2006, astro, arXiv:astro-ph/0603485

[125] Kaiser, N., MNRAS, 1986, 222, 323

[126] Kang H., Ostriker J. P., Cen R., Ryu D., Hernquist L., Evrard A. E., Bryan G. L., Norman M. L., 1994, ApJ, 430, 83

[127] Kang H., Jones T. W., Gieseler U. D. J., 2002, ApJ, 579, 337

[128] Kang H., Jones T. W., 2002, JKAS, 35, 159

[129] Kang H., Jones T. W., 2005, ApJ, 620, 44

[130] Kang H., Ryu D., Cen R., Ostriker J. P., 2007, ApJ, 669, 729

[131] Katz N., Weinberg D. H., Hernquist L., 1996, ApJS, 105, 19

[234] Kempner J.C., Sarazin C.L., 2001, ApJ, 548, 639

[133] Keshet U., Waxman E., Loeb A., Springel V., Hernquist L., 2003, ApJ, 585, 128

[134] Kim, K.-T., Kronberg, P.P., & Tribble, P.C., ApJ,1991,379,80

[135] Kolmogorov A., 1941, DoSSR, 30, 301

[136] Kravtsov A. V., Klypin A. A., Khokhlov A. M., 1997, ApJS, 111, 73

[137] Kravtsov A. V., Nagai D., Vikhlinin A. A., 2005, ApJ, 625, 588

[138] Kravtsov, A. V., Vikhlinin, A., & Nagai, D. 2006, , 650, 128

[139] Kempner, J.C., & Sarazin, C.L., 2001548639

[140] Kritsuk A. G., Norman M. L., Padoan P., Wagner R., 2007, ApJ, 665, 416

[141] Kronberg, P. P., Lesch, H., & Hopp, U. 1999, ApJ, 511, 56

[142] Lacey C., Cole S., 1993, MNRAS, 262, 627

[143] Landau L. D., Lifshitz E. M., 1966, hydr.book,

[144] Li S., Li H., Cen R., 2006, astro, arXiv:astro-ph/0611863

[145] Lin Y.-T., Mohr J. J., Stanford S. A., 2003, ApJ, 591, 749

[146] Loeb A., Barkana R., 2001, ARA&A, 39, 19

[147] Loeb A., Waxman E., 2000, Natur, 405, 156

[148] Malkov M. A., 1997, ApJ, 485, 638

[149] Markevitch, M. 1998, , 504, 27

[150] Markevitch M., Sarazin C. L., Vikhlinin A., 1999, ApJ, 521, 526

[151] Markevitch M., Gonzalez A. H., David L., Vikhlinin A., Murray S., Forman W., Jones C., Tucker W., 2002, ApJ, 567, L27

[152] Markevitch, M., Govoni, F., Brunetti, G., & Jerius, D., ApJ,2005,627,733

[153] Markevitch M., Vikhlinin A., 2007, PhR, 443, 1

[154] Mazzotta P., Rasia E., Moscardini L., Tormen G., 2004, MNRAS, 354, 10

[234] McNamara B.R., Nulsen P.E.J., 2007, ARA&A 45, 117

[156] Mellema G., Iliev I. T., Pen U.-L., Shapiro P. R., 2006, MNRAS, 372, 679

[157] Miniati F., Ryu D., Kang H., Jones T. W., Cen R., Ostriker J. P., 2000, ApJ, 542, 608

[158] McNamara B. R., Nulsen P. E. J., Wise M. W., Rafferty D. A., Carilli C., Sarazin C. L., Blanton E. L., 2005, Natur, 433, 45

[159] Miniati F., Jones T. W., Kang H., Ryu D., 2001, ApJ, 562, 233

[160] Miniati, F. 2001, Computer Physics Communications, 141, 17

[161] Miniati F., 2003, MNRAS, 342, 1009

[162] Mitchell N. L., McCarthy I. G., Bower R. G., Theuns T., Crain R. A., 2008, arXiv, arXiv:0812.1750

[163] Monaghan J. J., 1992, ARA&A, 30, 543

[164] Moore B., Katz N., Lake G., 1996, IAUS, 171, 203

[165] Murgia, M., Govoni, F., Feretti, L., et al., A&A,2004,424,429

[166] Nagai D., Kravtsov A. V., 2005, ApJ, 618, 557

[167] Nagai D., Kravtsov A. V., Vikhlinin A., 2007, ApJ, 668, 1

[168] Norman M. L., Bryan G. L., 1999, LNP, 530, 106

[169] Norman M. L., Bryan G. L., Harkness R., Bordner J., Reynolds D., O'Shea B., Wagner R., 2007, arXiv, 705, arXiv:0705.1556

[170] Orrù, E., Murgia, M., Feretti, L., et al., A&A,2007,467,943

[171] O'Shea B. W., Bryan G., Bordner J., Norman M. L., Abel T., Harkness R., Kritsuk A., 2004, astro, arXiv:astro-ph/0403044

[172] O'Shea B. W., Nagamine K., Springel V., Hernquist L., Norman M. L., 2005, ApJS, 160, 1

[173] Omma, H., Binney, J., Bryan, G., & Slyz, A. 2004, , 348, 1105

[174] Padmanabhan T., 1993, sfu..book,

[175] Pen U.-L., 1998, ApJ, 504, 601

[176] Petrosian V., 2001, ApJ, 557, 560

[177] Porter D. H., Woodward P. R., 1994, ApJS, 93, 309

[178] Power C., Navarro J. F., Jenkins A., Frenk C. S., White S. D. M., Springel V., Stadel J., Quinn T., 2003, MNRAS, 338, 14

[179] Pfrommer C., Enßlin T. A., 2004, JKAS, 37, 455

[180] Pfrommer C., Springel V., Enßlin T. A., Jubelgas M., 2006, MNRAS, 367, 113

[181] Pfrommer C., Enßlin T. A., Springel V., Jubelgas M., Dolag K., 2007, MNRAS, 378, 385

[182] Pfrommer C., 2008, MNRAS, 385, 1242

[183] Ponman, T. J., Sanderson, A. J. R., & Finoguenov, A. 2003, , 343, 331

[184] Pratt, G. W., Böhringer, H., Croston, J. H., et al. 2007, , 461, 71

[185] Press, W.H., & Schechter, P., ApJ,1974,187,425

[186] Quilis, V., Ibanez, J. M. A., & Saez, D. 1998, , 502, 518

[187] Rasia E., et al., 2006, MNRAS, 369, 2013

[188] Regan J. A., Haehnelt M. G., Viel M., 2007, MNRAS, 374, 196

[189] Reimer O., 2004, JKAS, 37, 307

[190] Reiprich T. H., Böhringer H., 2002, ApJ, 567, 716

[191] Rephaeli, Y., Gruber, D., & Blanco, P., 1999,ApJ, 511,21

[192] Rephaeli, Y., Nevalainen, J., Ohashi, T., & Bykov, A., 2008, SSR

[193] Ricker P. M., Sarazin C. L., 2001, ApJ, 561, 621

[194] Roettiger K., Loken C., Burns J. O., 1997, ApJS, 109, 307

[195] Rosati, P., Borgani, S., & Norman, C. 2002, ARAA, 40, 539

[196] Rossetti, M., & Molendi, S., A&A,2004,414,L41

[197] Röttgering, H.J.A., Wieringa, M.H., Hunstead, R.W., & Ekers, R.D., MNRAS ,1997,290,577

[198] Ryu D., Ostriker J. P., Kang H., Cen R., 1993, ApJ, 414, 1

[199] Ryu D., Kang H., Hallman E., Jones T. W., 2003, ApJ, 593, 599

[234] Sanders, J.S.; Fabian, A.C.; Dunn, R.J. H. 2005, MNRAS 360, 133

[201] Sanderson, A. J. R., Ponman, T. J., Finoguenov, A., Lloyd-Davies, E. J., & Markevitch, M. 2003, , 340, 989

[202] Sarazin C. L., 1999, ApJ, 520, 529

[203] Schekochihin A. A., Cowley S. C., Dorland W., Hammett G. W., Howes G. G., Quataert E., Tatsuno T., 2007, arXiv, arXiv:0704.0044

[204] Schindler S., Mueller E., 1993, A&A, 272, 137

[205] Schindler S., et al., 2005, A&A, 435, L25

[206] Schlickeiser R., Sievers A., Thiemann H., 1987, A&A, 182, 21

[207] Schneider, P., 2006, in Gravitational lensing: strong, weak and micro. Saas-Fee Advanced Course 33, eds. G. Meylan, P. Jetzer & P. North, Springer, Berlin, p. 1

[208] Schuecker P., Finoguenov A., Miniati F., Böhringer H., Briel U. G., 2004, A&A, 426, 387

[209] Shen J., Abel T., Mo H. J., Sheth R. K., 2006, ApJ, 645, 783

[210] Sheth R. K., Tormen G., 1999, MNRAS, 308, 119

[211] Sijacki, D., Springel, V., Di Matteo, T., & Hernquist, L. 2007, , 380, 877

[212] Skillman S. W., O'Shea B. W., Hallman E. J., Burns J. O., Norman M. L., 2008, arXiv, 806, arXiv:0806.1522

[213] Spergel D. N., et al., 2003, ApJS, 148, 175

[214] Spergel D. N., et al., 2007, ApJS, 170, 377

[215] Springel V., Hernquist L., 2002, MNRAS, 333, 649

[216] Springel V., 2005, MNRAS, 364, 1105

[217] Springel V., Farrar G. R., 2007, MNRAS, 380, 911

[218] Steinmetz M., 1996, MNRAS, 278, 1005

[219] Stone J. M., Norman M. L., 1992, ApJ, 389, 297

[220] Subramanian K., Shukurov A., Haugen N. E. L., 2006, MNRAS, 366, 1437

[221] Sunyaev R. A., Norman M. L., Bryan G. L., 2003, AstL, 29, 783

[222] Takizawa M., Naito T., 2000, ApJ, 535, 586

[223] Tasker E. J., Brunino R., Mitchell N. L., Michielsen D., Hopton S., Pearce F. R., Bryan G. L., Theuns T., 2008, MNRAS, 390, 1267

[224] Thierbach, M., Klein, U., & Wielebinski, R., 2003,397,53

[225] Tormen G., Moscardini L., Yoshida N., 2004, MNRAS, 350, 1397

[226] Tornatore, L., Borgani, S., Springel, V., et al. 2003, MNRAS, 342, 1025

[227] Valageas P., Schaeffer R., Silk J., 2002, A&A, 388, 741

[228] Valdarnini, R., 2003, MNRAS ,339,1117

[229] Vazza F., Tormen G., Cassano R., Brunetti G., Dolag K., 2006, MNRAS, 369, L14

[230] Vazza F., Brunetti G., Gheller C., 2008, arXiv, arXiv:0808.0609 accepted by MNRAS

[231] Vazza F., Brunetti G., Gheller C., 2008, arXiv, arXiv:0805.4214

[232] Vazza F., Brunetti G., Kritsuk A., Wagner R., Gheller C., Norman M. L., 2009, submitted to MNRAS Letters

[234] Vazza F., Dolag K., Ryu D., Brunetti G., Gheller C., Kang H., Pfrommer C., in prep.

[234] Venturi T., Giacintucci S., Brunetti G. et al. 2007, A&A 463, 937

[234] Venturi T., Giacintucci S., Dallacasa D. et al. 2008, A&A 484, 327

[235] Vladimirov, A., Ellison, D. C., & Bykov, A. 2006, ApJ, 652, 1246

[236] Vogt, C., & Enßlin, T.A., 200543467

[237] Voit, G. M. & Bryan, G. L. 2001, Nat., 414, 425

[238] Voit, G. M., Balogh, M. L., Bower, R. G., Lacey, C. G., & Bryan, G. L. 2003, ApJ, 593, 272

[239] Voit, G. M., Kay, S. T., & Bryan, G. L. 2005, MNRAS, 364, 909

[240] Völk H. J., Aharonian F. A., Breitschwerdt D., 1996, SSRv, 75, 279

[241] Völk, H., Aharonian, F.A., & Breitschwerdt, D., Space S.,1996,75,279

[242] Völk, H., & Atoyan, A.M., 1999, Astrop. Phys., 11, 73

[243] White, S. D. M., Navarro, J. F., Evrard, A. E., & Frenk, C. S. 1993, Nat., 366, 429

[244] Woodward P., Colella P., 1984, JCoPh, 54, 115

[247] Younger, J. D. & Bryan, G. L. 2007, ApJ, 666, 647

[246] Xu G., 1995, ApJS, 98, 355

[247] Younger, J. D. & Bryan, G. L. 2007, Apj, 666, 647

[248] Zwicky, F., ApJ,1937,86,217

Chapter 9

Acknowledgments

Just technical thanks and acknowledgments here, that I would like to address to the people who have been very useful (or fundamental!) during these three years of work (?).

My honor mention goes to Gianfranco B. e Claudio G., who have been patient, motivating and helpful advisers for these three years. Thanks guys, it has been an extremely enjoyable period!

Thanks to Annalisa B. for providing me colors.

Thanks to Simona G., Rossella C. and all the other young, or less young, students, phds and post docs I have met at IRA, for the many helps (and coffees) that I received.

Thanks to Mike Norman for the enjoyable hospitality at San Diego, and many thanks to the other people met at CASS: especially Rick Wagner, Dave Collins, Stephen Skory and Alexei Kritsuk, who did not (visibly) lose their patience while dealing with my numerical problems.

Thanks to Lauro M. and Bepi T. for many answers to my questions (some were correct).

Thanks to Dongsu Ryu and Hyesung Kang for providing useful materials for the comparison work, and for the enjoyable hospitality in South Korea.

Thanks to Riccardo B., Carlo G., Andrea N., Marco M., Emiliano M. for many inspiring chats, and for a sizable number of questions with no answers.

Thanks to Mauro N. and Franco T. for the helpful assistance with computing at IRA.

...and many thanks to Klaus (for a number of technical helps, suggestions and beautiful trips around the world).